

HARVARD UNIVERSITY
Graduate School of Arts and Sciences



DISSERTATION ACCEPTANCE CERTIFICATE

The undersigned, appointed by the
Department of Physics
have examined a dissertation entitled

Search for pair production of Higgs bosons in the four b quark final state
with the ATLAS detector

presented by Baojia Tong

candidate for the degree of Doctor of Philosophy and hereby
certify that it is worthy of acceptance.

Signature

A handwritten signature in black ink.

Typed name: Professor Melissa Franklin, Chair

Signature

A handwritten signature in black ink.

Typed name: Professor Howard Georgi

Signature

A handwritten signature in black ink.

Typed name: Professor Masahiro Morii

Date: April 27, 2018

Search for pair production of Higgs bosons in the four b quark final state with the ATLAS detector

A DISSERTATION PRESENTED
BY
BAOJIA TONG
TO
THE DEPARTMENT OF PHYSICS

IN PARTIAL FULFILLMENT OF THE REQUIREMENTS
FOR THE DEGREE OF
DOCTOR OF PHILOSOPHY
IN THE SUBJECT OF
PHYSICS

HARVARD UNIVERSITY
CAMBRIDGE, MASSACHUSETTS
MAY 2018

©2017-2018 – BAOJIA TONG
ALL RIGHTS RESERVED.

Search for pair production of Higgs bosons in the four b quark final state with the ATLAS detector

ABSTRACT

This thesis presents a search for Higgs boson pair production, in the $b\bar{b}b\bar{b}$ final state. This search uses the full 2015 and 2016 datasets collected by the ATLAS Collaboration at center of mass energy $\sqrt{s} = 13$ TeV, corresponding to $3.2 \pm 0.2 \text{ fb}^{-1}$ in 2015 and $32.9 \pm 1.1 \text{ fb}^{-1}$ in 2016 of proton-proton collision data. Improvements with respect to the previous analysis come from the a larger dataset, detailed background estimation and additional signal regions. Search sensitivity is particularly enhanced for resonance signals between 2500 GeV and 3000 GeV. The data is found to be compatible with the Standard Model predictions and no signs of new physics have been observed. The results are interpreted in the context of the bulk Randall-Sundrum warped extra dimension model with a Kaluza-Klein graviton $k/\bar{M}_{\text{Pl}} = 1.0$ or 2.0 decaying to two Higgs bosons, and the Type 2 two-Higgs doublet model (2HDM) where the neutral heavy CP-even scalar decays to two Higgs bosons.

Contents

o INTRODUCTION	I
1 THEORY AND MOTIVATION	4
1.1 The Standard Model and the Higgs boson	4
1.2 Standard Model di-Higgs production	6
1.3 Beyond the Standard Model di-Higgs production	8
1.4 Di-Higgs decay and LHC previous search results	13
1.5 Resolved and Boosted	16
2 LHC AND ATLAS	18
2.1 The Large Hadron Collider	19
2.2 A Toroidal LHC ApparatuS	22
3 RECONSTRUCTION AND OBJECTS	27
3.1 ID Tracks and Vertices	28
3.2 Jets	29
3.3 Flavor Tagging	34
3.4 Leptons	38
4 DATA AND SIMULATION	39
4.1 Data	39
4.2 MC	41
5 EVENT SELECTION	45
5.1 Data Cleaning	45
5.2 Trigger	46
5.3 Object Selection	48
5.4 Resolved Veto	54
5.5 2D Higgs Mass Cut	56
5.6 Number of b -tagged track jet requirements	58

5.7	Signal efficiency and cutflow	59
6	BACKGROUND ESTIMATION	63
6.1	Overview	63
6.2	Definition of the sideband and control regions	65
6.3	QCD multi-jet	68
6.4	$t\bar{t}$	69
6.5	Fitting procedure for QCD and $t\bar{t}$ normalization	71
6.6	QCD reweighting	73
6.7	m_{2J} in the sideband region	77
6.8	m_{2J} in the control region	78
6.9	m_{2J} rescale and smoothing in the signal region	79
6.10	Yields	80
7	SYSTEMATICS	85
7.1	Overview	85
7.2	Theoretical uncertainties	87
7.3	Uncertainties on detector and reconstruction	88
7.4	Uncertainty on $t\bar{t}$ generator	90
7.5	Uncertainty on μ_{qcd} estimation	91
7.6	Validation in low mass and high mass signal region	94
7.7	Uncertainty on the shape of $t\bar{t} m_{2J}$ in the $4/3b$ signal region	99
7.8	Uncertainty on the shape of the QCD distribution in the signal region	99
7.9	Uncertainty on smoothing function in the signal region	100
7.10	Summary of systematics	103
8	RESULT	107
8.1	Boosted signal region	107
8.2	Resolved signal region	109
8.3	Statistical analysis	112
8.4	Boosted and resolved combined limits	115
9	CONCLUSION	121
APPENDIX A	BOOSTED SIDEBAND REGION KINEMATIC DISTRIBUTIONS	123

APPENDIX B BOOSTED CONTROL REGION KINEMATIC DISTRIBUTIONS	136
APPENDIX C BOOSTED SIGNAL REGION KINEMATIC DISTRIBUTIONS	149
APPENDIX D CONSTANT μ_{qcd} VALIDATION	164
APPENDIX E REWEIGHTING DETAILS	171
APPENDIX F EFFECTS ON YIELD PREDICTION FROM VARIATIONS OF THE SIDEBAND AND CONTROL REGIONS	193
REFERENCES	212

Listing of figures

1.1	Fermions and bosons of the Standard Model and their properties ¹ , where all values are measured experimentally.	5
1.2	Leading order Feynman diagrams contributing to di-Higgs production via gluon-gluon fusion, through the Higgs-fermion Yukawa interactions in Figure 1.2a and the Higgs boson self-coupling in Figure 1.2b. Only Figure 1.2b probes λ_{hhh}	6
1.3	Leading order Feynman diagrams contributing to Higgs pair production via VBF.	7
1.4	Total cross sections (y-axis) at the NLO in QCD for the six largest di-Higgs production channels at pp colliders for different energy (x-axis). Gluon-gluon fusion, VBF, top-pair, W^\pm, Z and single-top associated di-Higgs productions are shown. The thickness of the lines corresponds to the uncertainties added linearly. H refers to the SM Higgs.	7
1.5	BSM Higgs boson pair production: non-resonant production proceeds through changes in the SM Higgs couplings in Figure 1.5a and Figure 1.5b, resonant production proceeds through Figure 1.5c an intermediate resonance, X . H and h both refers to the SM Higgs.	9
1.6	Total cross sections (y-axis) at the LO and NLO in QCD for di-Higgs production channels, at the LHC $\sqrt{s} = 14$ TeV as a function of the self-interaction coupling λ (x-axis) . The dashed (solid) lines and light- (dark-) color bands correspond to the LO (NLO) results and to the scale and PDF uncertainties added linearly. The SM values of the cross sections are obtained at $\frac{\lambda}{\lambda_{SM}} = 1$, indicated by the red vertical line. H refers to the SM Higgs.	9
1.7	Parton luminosity ratios as a function of resonance mass, M_X , for 13/8 TeV ¹³ . 1, 2, and 3 TeV M_X ratios are indicated by red lines. For a 2 TeV X , the luminosity ratio is almost 10.	10
1.8	Reach of ATLAS searches for new phenomena. Only a representative selection of the available results is shown. Blue (green) bands indicate 7 TeV (8 TeV) data results.	12

1.9	Regions of the $[m_A, \tan\beta]$ plane excluded in the hMSSM model via direct searches for heavy Higgs bosons and fits to the measured rates of observed Higgs boson production and decays. Limits are quoted at 95% CL and are indicated for the data (solid lines) and the expectation for the SM Higgs sector (dashed lines). The light shaded or hashed regions indicate the observed exclusions.	13
1.10	Summary of di-Higgs final states and their ratios. Top left, $b\bar{b}b\bar{b}$, has the largest branching ratio.	14
1.11	The observed and expected 95% CL upper limits of $\sigma(gg \rightarrow H) \times BR(H \rightarrow hh)$ at $\sqrt{s} = 8\text{TeV}$ as functions of the heavy Higgs boson mass, m_H , combining resonant searches in Higgs boson pair to $b\bar{b}\tau^+\tau^-$, $W^+W^-\gamma\gamma$, $b\bar{b}\gamma\gamma$, and $b\bar{b}b\bar{b}$ final states. The expected limits from individual searches are also shown. The green and yellow bands represent $\pm 1\sigma$ and $\pm 2\sigma$ uncertainty ranges of the expected combined limits. The improvement above $m_H = 500\text{ GeV}$ reflects the sensitivity of the $b\bar{b}b\bar{b}$ analysis. The results beyond 1TeV are from the $b\bar{b}b\bar{b}$ final state alone.	14
1.12	Cartoon for $X \rightarrow hh \rightarrow b\bar{b}b\bar{b}$, with resolved event topology (left) and boosted event topology (right).	16
2.1	A schematic view of the LHC ring ²⁷ . LINAC ₂ , Booster, PS, SPS, and LHC accelerate the protons in order. Four main experiments are located at interaction points along the ring. ATLAS and CMS are general purpose experiments, while ALICE focuses on heavy ion collisions and LHC _b is dedicated to B physics.	19
2.2	The luminosity-weighted distribution of the mean number of interactions per bunch crossing for 2015 and 2016 pp collision data at $\sqrt{s} = 13\text{ TeV}$. ³¹	21
2.3	A detailed, computer-generated image of the ATLAS detector and its systems.	22
2.4	Geometry of IBL, PIXEL and SCT detectors in Run 2.	24
2.5	The overall layout of the ATLAS muon spectrometer.	24
2.6	Cumulative luminosity vs. time delivered to (green) and recorded by ATLAS (yellow) during stable beams for pp collisions at $\sqrt{s} = 13\text{ TeV}$	25
3.1	Illustration of particle interactions in ATLAS.	28
3.2	Two collision events recorded in June 2015 with a high leading jet p_T shown in pseudorapidity-azimuthal angle parameter space. The dots are calorimeter-cell clusters with positive energy. Only the two leading jets are shown, with their area demarcated by a colored circle, with gray regions denoting the corresponding k_t sub-jets of size $R_{sub} = 0.2$. The color of both jets and clusters corresponds to their p_T	30

3.3	For the trimming algorithm using calorimeter cell clusters as inputs to the anti- k_t jet reconstruction algorithm with $R = 1.0$, a comparison of the jet mass distribution for QCD background jets and W boson jets low p_T kinematic regions, as determined by the untrimmed truth jet p_T	31
3.4	For the trimming algorithm using calorimeter cell clusters as inputs to the anti- k_t jet reconstruction algorithm with $R = 1.0$, a comparison of the jet mass distribution for QCD background jets and W boson jets high p_T kinematic regions, as determined by the untrimmed truth jet p_T	31
3.5	Uncalibrated (dashed line) and calibrated (solid line) reconstructed jet mass distribution Figure 3.5a, and the jet mass resolution vs jet p_T Figure 3.5b for calorimeter-based jet mass, m_{calo} (red), track-assisted jet mass m_{TA} (black) and the invariant mass of four-vector sum of tracks associated to the large-radius calorimeter jet m_{track} (blue) for W/Z-jets ⁴⁹	33
3.6	Secondary vertex reconstruction rate and MV2c10 output for b -jets (solid blue), c -jets (dashed green) and light-jets (dotted red) evaluated with simulated $t\bar{t}$ events.	35
3.7	b -jet efficiency for the fixed cut working point with a b -jet efficiency of 77% as a function of jet p_T for the comparison between the MV2c10 b -tagging algorithm employed for the 2016 analyses (2016 config) and the previous version of the tagger, MV2c20 (2015 config), which has 15% c -fraction in the training.	36
3.8	Light-flavor jet and c -jet rejection as a function of jet p_T for the previous (2015 config) MV2c20 and the current MV2c10 configuration (2016 config). A fixed cut at 77% b -jet efficiency operating point is used ⁵⁰	37
4.1	Trigger efficiencies following the full resolved analysis selection as a function of the resonance signal mass. The efficiencies of the triggers used in 2015 and 2016 are shown. In both graphs, the green line shows the efficiency of the “2b4j” trigger; the blue line represents the “2b3j” trigger; the red line represents the “ibij” trigger. The 2016 triggers are less efficient due to a bug in the online primary vertex reconstruction.	40
5.1	2015 ATLAS boosted di-Higgs event candidate’s event display. The data is taken in run 282712, lumiblock 503 and has event number 595661746. ID is in gray, ECAL is in green, HCAL is in red and MS is in blue. Only tracks with $p_T > 25$ GeV are shown. Jets are gray cones, and ID tracks are colored lines in the ID.	46
5.2	Different trigger efficiencies as a function of the resonance signal mass with respect to all events without additional selections (left) and with respect to events passing the two large- R jets and leading (subleading) jet $p_T > 400(250)$ GeV(right).	47

5.3	Large- R jet trigger (<code>HLT_j360_a10_lcw</code> , left and <code>HLT_j420_a10_lcw</code> , right) efficiencies with respect to the large- R jet p_T , defined as the ratio between events that fired the trigger and the all the simulated events, measured in 2015 and 2016 data and G_{KK}^* with $c = 1.0$ MC.	48
5.4	Percentages of truth Higgs boson contained by a large- R jet with $\Delta R_{\text{Higgs,jet}} < 1.0$ as a function of G_{KK}^* masses. The three cases listed in the legend are orthogonal. Two Higgs bosons almost never match to the same large- R jet.	49
5.5	Normalized ΔR between the truth Higgs (leading on left, subleading on right) and the truth children b -quarks for G_{KK}^* MC. Lines are drawn at $\Delta R = 0.4$ (R of small- R jets) and $\Delta R = 1.0$ (R of large- R jets).	50
5.6	Percentage of $\Delta R < 0.2$ matching truth b 's to track jets (leading Higgs on the left, subleading Higgs on the right) for different G_{KK}^* masses. The cases listed in the legend are orthogonal to each other. The cases not listed on the legend (including when a truth b is not contained in the large- R jet) happen in total at most 1.6% of the total for a given G_{KK}^* mass.	51
5.7	Kinematics of 1TeV G_{KK}^* MC before (blue) and after (red) muon-in-jet corrections. The reconstructed Higgs masses (top row, left for leading large- R jet, right for subleading large- R jet) are closer to 125GeV after the correction, which improves the signal efficiency for the signal region selection by $\sim 10\%$ (bottom row, left for m_{JJ} , right for event distribution differences on the leading-subleading large- R jet mass plane.).	52
5.8	After large- R jet requirements, normalized $\Delta\eta_{JJ}$ distribution in 1.5 TeV G_{KK}^* and data, where the data consists of mostly multijet events ($> 90\%$). Higgs candidate refers to the two large- R jets. The background multijet events are more forward in $\Delta\eta_{JJ}$ distribution.	53
5.9	Event display of the same event in 2015 data using resolved 5.9a and boosted 5.9b topologies. The resolved reconstruction gives a m_{4J} of 873 GeV, and the boosted reconstruction gives m_{2J} of 852 GeV.	54
5.10	For RSG $c = 1.0$ samples, the number of events as a function of leading Higgs candidate mass and subleading Higgs candidate mass, for 1.2 TeV (left) signal and 2 TeV (right) signal samples. The red dotted line in the center correspond to the signal region, passing $X_{bb} < 1.6$	57
5.11	Signal fraction in different b -tag categories (left) and detailed fraction in different number of track jet and b -tag categories (right) as a function of signal resonance mass hypothesis for selection cuts. The efficiencies are relative to the total number of events passing the 2D mass cut.	58

5.12 Selection efficiency (left) and relative efficiency with respect to the previous cut (right) as a function of RSG c=1.0 signal resonance mass hypothesis for selection cuts. The relative efficiency is defined from the previous cut, where the order of cuts is given by the legend. PassTrig means the event passes the trigger selection; PassDiJetPt means the event passes the leading and sub-leading jet p_T cuts; PassDiJetEta means the event passes the leading and sub-leading jet η cuts; PassDetaH means the events passes the $ \Delta\eta < 1.7$ cut; PassBJetSkim means the event contains at least two b -tagged track jets, inclusive of $2b$, $2bs$, $3b$ and $4b$ configurations; PassSignal means the event passes the signal region cut $X_{bb} < 1.6$	60
6.1 The m_J^{lead} vs m_J^{subl} distribution of data in $2bs$ region. The signal region is the area surrounded by the inner (red) dashed contour line, centered on ($m_J^{\text{lead}} = 12.4$ GeV, $m_J^{\text{subl}} = 11.5$ GeV). The control region is the area between the signal region and the intermediate (orange) contour line. The sideband region is the area between the control region and the outer (yellow) contour line.	66
6.2 Detailed signal efficiency in different signal/control/sideband regions in n -tagged channels and the inclusive b -tagged channel, which includes $2b$, $1b$, and $0b$ as well, (bottom right) as a function of G_{KK}^* resonance mass for selection cuts. The efficiencies are relative to the total number of events in the preselection.	67
6.3 Normalized $2bs$, $3b$, and $4b$ $t\bar{t}$ MC m_{2J} (mHH) distribution in the signal region. The uncertainties are statistical.	70
6.4 Simultaneous fit of μ_{qcd} and $\alpha_{t\bar{t}}$ in $4b$, $3b$ and $2bs$ sideband regions using the leading large- R jet mass.	72
6.5 Comparison of track jet p_T distributions in different b -tag channels. Data are shown in the plots. They contain inclusive SB/CR/SR regions for $0b$ and $1b$, and only the SB region for $2bs$. At the bottom of the plots, all the ratios are taken with respect to the $0b$ tagged distribution.	74
6.6 The m_{2J} distributions in the sideband region of the boosted analysis for the data and the predicted background for $4b$, $3b$, and $2bs$ channels. The data-to-background ratio (bottom panels) shows the statistical uncertainties as the gray hatched band.	77
6.7 The m_{2J} distributions in the control region of the boosted analysis for the data and the predicted background for $4b$, $3b$, and $2bs$ channels. The data-to-background ratio (bottom panels) shows the statistical uncertainties as the gray hatched band.	78

6.8 Normalized scaled m_{2J} distributions for the $4b$ (left), $3b$ (middle), and $2bs$ (right) signal regions. For comparison, the unscaled m_{2J} distributions are shown on the same plot.	79
6.9 Fits for scaled background smoothing are shown for the $4b$ signal region. The figures show the distributions with the fit central value and the fit variations determined by varying the fit parameters within uncertainties and taking into account parameter correlations.	81
6.10 Fits for scaled background smoothing are shown for the $3b$ signal region. The figures show the distributions with the fit central value and the fit variations determined by varying the fit parameters within uncertainties and taking into account parameter correlations.	81
6.11 Fits for scaled background smoothing are shown for the $2bs$ signal region. The figures show the distributions with the fit central value and the fit variations determined by varying the fit parameters within uncertainties and taking into account parameter correlations.	82
6.12 Background predictions for $4b$ signal region using scaled m_{2J} before and after smoothing. The uncertainty band includes only fit statistical uncertainties.	82
6.13 Background predictions for $3b$ signal region using scaled m_{2J} before and after smoothing. The uncertainty band includes only fit statistical uncertainties.	83
6.14 Background predictions for $2bs$ signal region using scaled m_{2J} before and after smoothing. The uncertainty band includes only fit statistical uncertainties.	83
7.1 Impact of efficiency scale factor w_{sf} and inefficiency scale factor w_{sf}^{anti} on 2 TeV G_{KK}^* with $c = 1.0$. $4b$ signal region (left), $3b$ signal region (middle), and $2bs$ signal region are shown.	90
7.2 Total background estimation ($\text{QCD} + t\bar{t}$) with different $t\bar{t}\text{MC}$ variations. The different variations agree with the default within the statistical uncertainties.	91
7.3 Illustration of ZZ (left) and TT (right) signal region as shown in the orange shaded region. Control region shown in green, and sideband region in blue. The white circle in the middle is the real signal region, and it is blinded.	95
7.4 ZZ signal region distribution of m_{2J} (left column) and leading large-R jet mass (right column), for $4b$ (top row), $3b$ (middle row) and $2b$ split (bottom row). Only statistical uncertainties are shown.	97
7.5 TT signal region distribution of m_{2J} (left column) and leading large-R jet mass (right column), for $4b$ (top row), $3b$ (middle row) and $2b$ split (bottom row). Only statistical uncertainties are shown.	98

7.6	The shape of $t\bar{t}$ m_{2J} in the sideband region, comparing the $3b$ shape with that of the $2bs$, in order to assess the systematic effect of additional b -tags changing the dijet mass distribution. The m_{2J} distributions is shown on the left, and the ratio of $3b$ to $2bs$ distributions on the right.	99
7.7	Dijet mass distribution in the CR along with the prediction (left) and the ratio of the prediction to the CR distribution (right) for the $2bs$ (top) $3b$ (middle) and $4b$ (bottom) samples. Ratios are from the smoothed distributions, the data uncertainty band contains the smoothing parameter variations, and the prediction uncertainty band also contains smoothing parameter variations.	101
7.8	Dijet mass distribution SR prediction fit with several fit ranges (left) and the ratio of nominal to fits with different fit ranges (right) for the $2bs$ (top) $3b$ (middle) and $4b$ (bottom) samples.	102
7.9	Dijet mass distribution SR prediction fit with several fit functions (left) and the ratio of nominal to fits with different fit functions (right) for the $2bs$ (top) $3b$ (middle) and $4b$ (bottom) samples. The additional fit functions are from Table 7.6.	104
7.10	Impact of each systematic on the signal prediction as a function of the signal mass, in the $4b$ (left) and $3b$ (middle) and $2bs$ (right) signal regions.	105
8.1	Unscaled m_{2J} distributions in the $4b$ signal region after unblinding.	108
8.2	Unscaled m_{2J} distributions in the $3b$ signal region after unblinding.	109
8.3	Unscaled m_{2J} distributions in the $2bs$ signal region after unblinding.	109
8.4	Scaled m_{2J} distributions in the $4b$ signal region after unblinding.	110
8.5	Scaled m_{2J} distributions in the $3b$ signal region after unblinding.	110
8.6	Scaled m_{2J} distributions in the $2bs$ signal region after unblinding.	111
8.7	Distributions of m_{4j} in the signal region of the resolved analysis for (a) 2015 data and (b) 2016 data, compared to the predicted backgrounds. The hatched bands shown in the bottom panels represent the combined statistical and systematic uncertainties in the total background estimates. The expected signal distributions of G_{KK}^* resonances with masses of 800 and 1200 GeV, the 280 GeV scalar sample and SM non-resonant di-Higgs production ($\times 100$) are also shown. The scalar sample is normalized to a cross section times branching ratio of 2.7 pb.	112
8.8	Local p_0 of the (a) scalar, (b) G_{KK}^* with $c = 1$, and (c) G_{KK}^* with $c = 2$	114

8.9	The impact of nuisance parameters on the fitted cross section, ranked by their post-fit impact. The signal mass used in these fits is 2000 GeV, and the signal model is (a) narrow scalar, (b) G_{KK}^* with $c = 1$, and (c) G_{KK}^* with $c = 2$	115
8.10	Post-fit signal region scaled m_{2j} distributions after fitting the data with the 2 TeV G_{KK}^* with $c = 1.0$ hypothesis. The signal strength is slightly positive.	116
8.11	The expected and observed 95% CL upper exclusion limits for the boosted analysis calculated including all systematic uncertainties for the narrow scalar model. The dot-dashed line shows the expected limit when only statistical uncertainties are included. The limits are derived with the asymptotic approximation.	117
8.12	The expected and observed 95% CL upper exclusion limits for the boosted analysis calculated including all systematic uncertainties for the $c = 1.0$ Graviton. The dot-dashed line shows the expected limit when only statistical uncertainties are included. The limits are derived with the asymptotic approximation.	117
8.13	The expected and observed 95% CL upper exclusion limits for the boosted analysis calculated including all systematic uncertainties for the $c = 2.0$ Graviton. The dot-dashed line shows the expected limit when only statistical uncertainties are included. The limits are derived with the asymptotic approximation.	118
8.14	The expected and observed 95% CL upper exclusion limits for the combined analysis calculated including all systematic uncertainties for the narrow scalar model. The dot-dashed line shows the expected limit when only statistical uncertainties are included. The limits are derived with the asymptotic approximation.	119
8.15	The expected and observed 95% CL upper exclusion limits for the combined analysis calculated including all systematic uncertainties for the $c = 1.0$ G_{KK}^* . The dot-dashed line shows the expected limit when only statistical uncertainties are included. The limits are derived with the asymptotic approximation.	119
8.16	The expected and observed 95% CL upper exclusion limits for the combined analysis calculated including all systematic uncertainties for the $c = 2.0$ G_{KK}^* . The dot-dashed line shows the expected limit when only statistical uncertainties are included. The limits are derived with the asymptotic approximation.	120
A.1	Kinematics (p_T , mass, η , ϕ) of the lead large- R jet in data and prediction in the sideband region after requiring 4 b -tags.	124
A.2	Kinematics (p_T , mass, η , ϕ) of the subleading large- R jet in data and prediction in the sideband region after requiring 4 b -tags.	125

A.3	First two rows show the p_T of the lead (left) and sub-lead (right) small- R track jets associated to the lead (first-row) and sub-lead (second-row) large- R jet in data and prediction in the sideband region after requiring 4 b -tags. Third row shows the ΔR between two leading small- R track-jets associated to the leading (left) and sub-leading (right) large- R jet.	126
A.4	Kinematics (invariant mass, ΔR , $\Delta\eta$ and $\Delta\phi$) of two large- R jets in data and prediction in the sideband region after requiring 4 b -tags.	127
A.5	Kinematics (p_T , mass, η , ϕ) of the lead large- R jet in data and prediction in the sideband region after requiring 3 b -tags.	128
A.6	Kinematics (p_T , mass, η , ϕ) of the subleading large- R jet in data and prediction in the sideband region after requiring 3 b -tags.	129
A.7	First two rows show the p_T of the lead (left) and sub-lead (right) small- R track jets associated to the lead (first-row) and sub-lead (second-row) large- R jet in data and prediction in the sideband region after requiring 3 b -tags. Third row shows the ΔR between two leading small- R track-jets associated to the leading (left) and sub-leading (right) large- R jet.	130
A.8	Kinematics (invariant mass, ΔR , $\Delta\eta$ and $\Delta\phi$) of two large- R jets in data and prediction in the sideband region after requiring 3 b -tags.	131
A.9	Kinematics (p_T , mass, η , ϕ) of the lead large- R jet in data and prediction in the sideband region after requiring 2 b -tags split.	132
A.10	Kinematics (p_T , mass, η , ϕ) of the subleading large- R jet in data and prediction in the sideband region after requiring 2 b -tags split.	133
A.11	First two rows show the p_T of the lead (left) and sub-lead (right) small- R track jets associated to the lead (first-row) and sub-lead (second-row) large- R jet in data and prediction in the sideband region after requiring 2 b -tags split. Third row shows the ΔR between two leading small- R track-jets associated to the leading (left) and sub-leading (right) large- R jet.	134
A.12	Kinematics (invariant mass, ΔR , $\Delta\eta$ and $\Delta\phi$) of two large- R jets in data and prediction in the sideband region after requiring 2 b -tags split.	135
B.1	Kinematics (p_T , mass, η , ϕ) of the lead large- R jet in data and prediction in the control region after requiring 4 b -tags.	137
B.2	Kinematics (p_T , mass, η , ϕ) of the subleading large- R jet in data and prediction in the control region after requiring 4 b -tags.	138

B.3	First two rows show the p_T of the lead (left) and sub-lead (right) small- R track jets associated to the lead (first-row) and sub-lead (second-row) large- R jet in data and prediction in the control region after requiring 4 b -tags. Third row shows the ΔR between two leading small- R track-jets associated to the leading (left) and sub-leading (right) large- R jet.	139
B.4	Kinematics (invariant mass, ΔR , $\Delta\eta$ and $\Delta\phi$) of two large- R jets in data and prediction in the control region after requiring 4 b -tags.	140
B.5	Kinematics (p_T , mass, η , ϕ) of the lead large- R jet in data and prediction in the control region after requiring 3 b -tags.	141
B.6	Kinematics (p_T , mass, η , ϕ) of the subleading large- R jet in data and prediction in the control region after requiring 3 b -tags.	142
B.7	First two rows show the p_T of the lead (left) and sub-lead (right) small- R track jets associated to the lead (first-row) and sub-lead (second-row) large- R jet in data and prediction in the control region after requiring 3 b -tags. Third row shows the ΔR between two leading small- R track-jets associated to the leading (left) and sub-leading (right) large- R jet.	143
B.8	Kinematics (invariant mass, ΔR , $\Delta\eta$ and $\Delta\phi$) of two large- R jets in data and prediction in the control region after requiring 3 b -tags.	144
B.9	Kinematics (p_T , mass, η , ϕ) of the lead large- R jet in data and prediction in the control region after requiring 2 b -tags split.	145
B.10	Kinematics (p_T , mass, η , ϕ) of the subleading large- R jet in data and prediction in the control region after requiring 2 b -tags split.	146
B.11	First two rows show the p_T of the lead (left) and sub-lead (right) small- R track jets associated to the lead (first-row) and sub-lead (second-row) large- R jet in data and prediction in the control region after requiring 2 b -tags split. Third row shows the ΔR between two leading small- R track-jets associated to the leading (left) and sub-leading (right) large- R jet.	147
B.12	Kinematics (invariant mass, ΔR , $\Delta\eta$ and $\Delta\phi$) of two large- R jets in data and prediction in the control region after requiring 2 b -tags split.	148
C.1	Kinematics (p_T , mass, η , ϕ) of the lead large- R jet in data and prediction in the signal region after requiring 4 b -tags.	152
C.2	Kinematics (p_T , mass, η , ϕ) of the subleading large- R jet in data and prediction in the signal region after requiring 4 b -tags.	153

C.3	First two rows show the p_T of the lead (left) and sub-lead (right) small- R track jets associated to the lead (first-row) and sub-lead (second-row) large- R jet in data and prediction in the signal region after requiring 4 b -tags. Third row shows the ΔR between two leading small- R track-jets associated to the leading (left) and sub-leading (right) large- R jet.	154
C.4	Kinematics (invariant mass, ΔR , $\Delta\eta$ and $\Delta\phi$) of two large- R jets in data and prediction in the signal region after requiring 4 b -tags.	155
C.5	Kinematics (p_T , mass, η , ϕ) of the lead large- R jet in data and prediction in the signal region after requiring 3 b -tags.	156
C.6	Kinematics (p_T , mass, η , ϕ) of the subleading large- R jet in data and prediction in the signal region after requiring 3 b -tags.	157
C.7	First two rows show the p_T of the lead (left) and sub-lead (right) small- R track jets associated to the lead (first-row) and sub-lead (second-row) large- R jet in data and prediction in the signal region after requiring 3 b -tags. Third row shows the ΔR between two leading small- R track-jets associated to the leading (left) and sub-leading (right) large- R jet.	158
C.8	Kinematics (invariant mass, ΔR , $\Delta\eta$ and $\Delta\phi$) of two large- R jets in data and prediction in the signal region after requiring 3 b -tags.	159
C.9	Kinematics (p_T , mass, η , ϕ) of the lead large- R jet in data and prediction in the signal region after requiring 2 b -tags split.	160
C.10	Kinematics (p_T , mass, η , ϕ) of the subleading large- R jet in data and prediction in the signal region after requiring 2 b -tags split.	161
C.11	First two rows show the p_T of the lead (left) and sub-lead (right) small- R track jets associated to the lead (first-row) and sub-lead (second-row) large- R jet in data and prediction in the signal region after requiring 2 b -tags split. Third row shows the ΔR between two leading small- R track-jets associated to the leading (left) and sub-leading (right) large- R jet.	162
C.12	Kinematics (invariant mass, ΔR , $\Delta\eta$ and $\Delta\phi$) of two large- R jets in data and prediction in the signal region after requiring 2 b -tags split.	163
D.1	$1b$ over ob μ_{qcd} values evaluated in data, with the N_{event} weighted mean and the Gaussian fit mean listed.	165
D.2	$2b$ over $1b$ μ_{qcd} values evaluated in data, with the N_{event} weighted mean and the Gaussian fit mean listed.	165

D.3	$2b$ s over $1b$ μ_{qcd} values evaluated in data, with the N_{event} weighted mean and the Gaussian fit mean listed.	166
D.4	$3b$ over $2b$ μ_{qcd} values evaluated in data, with the N_{event} weighted mean and the Gaussian fit mean listed. SR is blinded.	166
D.5	$4b$ over $2b$ μ_{qcd} values evaluated in data, with the N_{event} weighted mean and the Gaussian fit mean listed. SR is blinded.	167
D.6	$1b$ over $0b$ μ_{qcd} values evaluated in dijet MC, with the N_{event} weighted mean and the Gaussian fit mean listed.	168
D.7	$2b$ over $1b$ μ_{qcd} values evaluated in dijet MC, with the N_{event} weighted mean and the Gaussian fit mean listed.	168
D.8	$2b$ s over $1b$ μ_{qcd} values evaluated in dijet MC, with the N_{event} weighted mean and the Gaussian fit mean listed.	169
D.9	$3b$ over $2b$ μ_{qcd} values evaluated in dijet MC, with the N_{event} weighted mean and the Gaussian fit mean listed.	169
D.10	$4b$ over $2b$ μ_{qcd} values evaluated in dijet MC, with the N_{event} weighted mean and the Gaussian fit mean listed.	170
E.I	For $2b$ s background estimate: the fits to the ratio of the data in the $1b$ category, of the sub-leading Higgs candidate $1b$ -tagged events' subleading Higgs candidate distributions(black point), over the leading Higgs candidate $1b$ -tagged events' subleading Higgs candidate distributions(yellow). Distributions and fits to the estimated QCD background for large- R jet p_T (left), the large- R jet's leading track jet p_T (middle), and large- R jet's subleading track jet p_T (right) are shown. Figures are before reweighting (top row), after the first iteration(second row), after the fourth iteration(third row), and after the last iteration (bottom row). The green line is the spline fit; the red line is a polynomial fit; the blue line is the spline interpolation.	173

E.11	Reweighted $3b$ control region predictions comparison. Top row is the dijet Mass, second row is leading large- R jet p_T , third row is the leading large- R jet's leading track jet p_T and the last row subleading large- R jet's leading track jet p_T . On the left are the distributions before reweighting, and on the right are the distributions after reweighting.	183
E.12	Reweighted $4b$ control region predictions comparison. Top row is the dijet Mass, second row is leading large- R jet p_T , third row is the leading large- R jet's leading track jet p_T and the last row subleading large- R jet's leading track jet p_T . On the left are the distributions before reweighting, and on the right are the distributions after reweighting.	184
E.13	Reweighted $2bs$ (left column), $3b$ (middle column), and $4b$ (right column) sideband (top row), control (middle row) and signal (bottom row) region predictions comparison, for MJJ. The Signal region is blinded, and the data distribution is replaced with the non-reweighted background predictions.	187
E.14	Reweighted $2bs$ sideband (top row), control (middle row) and signal (bottom row) region predictions comparison, for leading Higgs Candidate leading track jet p_T (first column), leading Higgs Candidate subleading track jet p_T (second column), subleading Higgs Candidate leading track jet p_T (third column), subleading Higgs Candidate subleading track jet p_T (fourth column). The signal region is blinded, where the distribution is replaced with the non-reweighted predictions.	188
E.15	Reweighted $3b$ sideband (top row), control (middle row) and signal (bottom row) predictions comparison, for leading Higgs Candidate leading track jet p_T (first column), leading Higgs Candidate subleading track jet p_T (second column), subleading Higgs Candidate leading track jet p_T (third column), subleading Higgs Candidate subleading track jet p_T (fourth column). The signal region is blinded, where the distribution is replaced with the non-reweighted predictions.	189
E.16	Reweighted $4b$ sideband (top row), control (middle row) and signal (bottom row) region predictions comparison, for leading Higgs Candidate leading track jet p_T (first column), leading Higgs Candidate subleading track jet p_T (second column), subleading Higgs Candidate leading track jet p_T (third column), subleading Higgs Candidate subleading track jet p_T (fourth column). The signal region is blinded, where the distribution is replaced with the non-reweighted predictions.	190

E.17	Reweighted $2bs$ inclusive region predictions comparison in dijet MC, for leading Higgs Candidate leading track jet p_T (top left), leading Higgs Candidate subleading track jet p_T (top right), subleading Higgs Candidate leading track jet p_T (bottom left), subleading Higgs Candidate subleading track jet p_T (bottom right). $1b$ and reweighted $1b$ distributions are normalized to $2bs$	191
E.18	Reweighted $2bs$ sideband (top) / control (middle) / signal (bottom) region predictions comparison, for MJJ. The signal region is not blinded, since it is dijet MC distribution. $1b$ and reweighted $1b$ distributions are normalized to $2bs$	192
F.1	In $1b$ data, with low-mass CR variation, new SB and CR $m_J^{\text{lead}} - m_J^{\text{subl}}$ distribution.	195
F.2	In $1b$ data, with high-mass CR variation, new SB and CR $m_J^{\text{lead}} - m_J^{\text{subl}}$ distribution.	196
F.3	In $1b$ data, with signal-depletion (small) CR variation, new SB and CR $m_J^{\text{lead}} - m_J^{\text{subl}}$ distribution.	196
F.4	In $1b$ data, with low-mass SB variation, new SB and CR $m_J^{\text{lead}} - m_J^{\text{subl}}$ distribution.	197
F.5	In $1b$ data, with high-mass SB variation, new SB and CR $m_J^{\text{lead}} - m_J^{\text{subl}}$ distribution.	197
F.6	In $1b$ data, with small SB variation, new SB and CR $m_J^{\text{lead}} - m_J^{\text{subl}}$ distribution.	198
F.7	In $1b$ data, with large SB variation, new SB and CR $m_J^{\text{lead}} - m_J^{\text{subl}}$ distribution.	198
F.8	Comparisons of the nominal QCD shape prediction (black) with the results of control and sideband region variations (red). The ratio of the shape from each variation to the nominal shape is shown in the lower panel. The left column shows the relevant distributions for the $4b$ signal region, the middle column is for the $3b$ signal region, and the left column is for the $2bs$ signal region. The top row is for high CR variation, the middle row is for the low CR variation, and the bottom row is for the small CR variation.	209
F.9	Comparisons of the nominal QCD shape prediction (black) with the results of control and sideband region variations (red). The ratio of the shape from each variation to the nominal shape is shown in the lower panel. The left column shows the relevant distributions for the $4b$ signal region, the middle column is for the $3b$ signal region, and the left column is for the $2bs$ signal region. The top row is for high SB variation, the second row is for the low SB variation, the third row is for the small SB variation and the large raw is for the large SB variation.	210

Listing of tables

2.1	LHC nominal and operational parameters	21
5.1	Physics objects and their technical names in the boosted analysis.	48
5.2	List of kinematic selection used in the boosted analysis. These cuts are generally efficient for signal events.	49
5.3	The selection efficiency for $G_{KK}^* \rightarrow hh \rightarrow b\bar{b}b\bar{b}$ events ($c = 1.0$) at each stage of the event selection. Uncertainties are the MC stat uncertainty only.	61
5.4	The selection efficiency for $G_{KK}^* \rightarrow hh \rightarrow b\bar{b}b\bar{b}$ events ($c = 2.0$) at each stage of the event selection. Uncertainties are the MC stat uncertainty only.	61
5.5	The selection efficiency for $H \rightarrow hh \rightarrow b\bar{b}b\bar{b}$ events at each stage of the event selection.	62
6.1	Definitions of the signal region, the control region, and the sideband region.	65
6.2	Definitions of the QCD background estimation sample for $4b/3b/2bs$. $n_b^{lead/sublj}$ stands for the number of b -tagged track jets in the leading/subleading large- R jet.	68
6.3	Background scaling parameters (μ_{qcd} and α_{tt}) estimated from fits to the m_j^{lead} distributions in $4b/3b/2bs$ sideband regions pre-reweighting. $\varrho(\mu_{qcd}, \alpha_{tt}) = \frac{\text{Cov}(\mu_{qcd}, \alpha_{tt})}{\sigma_{\mu_{qcd}} \sigma_{\alpha_{tt}}}.$	73
6.4	Definitions of the $1b$ subsamples.	75
6.5	Background scaling parameters (μ_{qcd} and α_{tt}) estimated from fits to the m_j^{lead} distributions in $4b/3b/2bs$ sideband regions post reweighting. $\varrho(\mu_{qcd}, \alpha_{tt}) = \frac{\text{Cov}(\mu_{qcd}, \alpha_{tt})}{\sigma_{\mu_{qcd}} \sigma_{\alpha_{tt}}}.$	76
6.6	Smoothing parameters in $4b$, $3b$, and $2bs$ signal regions for scaled mass distributions, the correlation between parameters is almost always 0.99.	80
6.7	Expected yields for backgrounds in the $4b$ signal region, control region, and sideband region, along with the observed number of data events. The signal predictions for $G_{KK}^* m = 1.0, 1.5, 2.0$ TeV with $c = 1.0$. The uncertainty listed is statistical, without fit uncertainty.	84

6.8	Expected yields for backgrounds in the $3b$ signal region, control region, and sideband region, along with the observed number of data events. The signal predictions for $G_{KK}^* m = 1.0, 1.5, 2.0$ TeV with $c = 1.0$. The uncertainty listed is statistical, without fit uncertainty.	84
6.9	Expected yields for backgrounds in the $2bs$ signal region, control region, and sideband region, along with the observed number of data events. The signal predictions for $G_{KK}^* m = 1.0, 1.5, 2.0$ TeV with $c = 1.0$. The uncertainty listed is statistical, without fit uncertainty.	84
7.1	Agreement between data and prediction in $4b$ tag CR. Showing stat uncertainty only.	93
7.2	Agreement between data and prediction in $3b$ tag CR. Showing stat uncertainty only.	93
7.3	Agreement between data and prediction in $2bs$ tag CR. Showing stat uncertainty only.	94
7.4	Data and prediction in ZZ SR in $4b$, $3b$ and $2bs$ regions.	96
7.5	Data and prediction in TT SR in $4b$, $3b$ and $2bs$ regions.	96
7.6	Functions used to fit the QCD dijet mass distributions, where $x = m_{jj}/\sqrt{s}$.	103
7.7	Percent impact of the dominant systematics on the background acceptance and on the signal acceptance of G_{KK}^* with $c = 1.0$ in the $4b$ signal region.	105
7.8	Percent impact of the dominant systematics on the background acceptance and on the signal acceptance of G_{KK}^* with $c = 1.0$ in the $3b$ signal region.	106
7.9	Percent impact of the dominant systematics on the background acceptance and on the signal acceptance of G_{KK}^* with $c = 1.0$ in the $2bs$ signal region.	106
8.1	Unblinded signal region predictions and results. All systematic uncertainties are included for backgrounds. The Poisson uncertainty in data is shown for comparison.	108
8.2	The number of predicted background events in the signal region for the resolved analysis compared to the data, for the 2015 and 2016 datasets. The yields for three potential signals, an 800 GeV G_{KK}^* resonance with $c = 1$, a scalar with a mass of 280 GeV, and SM non-resonant Higgs boson pair production, are also shown. The scalar sample is normalized to a cross section times branching ratio of 2.7 pb. The quoted uncertainties include both the statistical and systematic uncertainties, and the total uncertainty considers correlations. The numbers of observed and predicted events are also given in the control region.	III
8.3	95% CL exclusion limits for SM non-resonant di-Higgs production, in units of the SM predicted value for $\sigma(pp \rightarrow hh \rightarrow b\bar{b}b\bar{b})$.	118

C.1	$4b$ unblinded signal region predictions and results. All systematic uncertainties included for backgrounds. For Data, the statistical uncertainty is shown. Mass range is broken into greater than 1 TeV, 1.5 TeV, 2 TeV, 2.5 TeV, and 3 TeV intervals.	150
C.2	$3b$ unblinded signal region predictions and results. All systematic uncertainties included for backgrounds. For Data, the statistical uncertainty is shown. Mass range is broken into greater than 1 TeV, 1.5 TeV, 2 TeV, 2.5 TeV, and 3 TeV intervals.	150
C.3	$2bs$ unblinded signal region predictions and results. All systematic uncertainties included for backgrounds. For Data, the statistical uncertainty is shown. Mass range is broken into greater than 1 TeV, 1.5 TeV, 2 TeV, 2.5 TeV, and 3 TeV intervals.	150
C.4	$4b$ unblinded scaled dijet mass signal region predictions and results. All systematic uncertainties included for backgrounds. For Data, the statistical uncertainty is shown. Mass range is broken into greater than 1 TeV, 1.5 TeV, 2 TeV, 2.5 TeV, and 3 TeV intervals. . .	151
C.5	$3b$ unblinded scaled dijet mass signal region predictions and results. All systematic uncertainties included for backgrounds. For Data, the statistical uncertainty is shown. Mass range is broken into greater than 1 TeV, 1.5 TeV, 2 TeV, 2.5 TeV, and 3 TeV intervals. . .	151
C.6	$2bs$ unblinded scaled dijet mass signal region predictions and results. All systematic uncertainties included for backgrounds. For Data, the statistical uncertainty is shown. Mass range is broken into greater than 1 TeV, 1.5 TeV, 2 TeV, 2.5 TeV, and 3 TeV intervals. . .	151
F.1	Background prediction in SR/CR/SB for High CR in $4b$ region.	199
F.2	Background prediction in SR/CR/SB for Low CR in $4b$ region.	199
F.3	Background prediction in SR/CR/SB for Small CR in $4b$ region.	200
F.4	Background prediction in SR/CR/SB for High SB in $4b$ region.	200
F.5	Background prediction in SR/CR/SB for Low SB in $4b$ region.	200
F.6	Background prediction in SR/CR/SB for Large SB in $4b$ region.	201
F.7	Background prediction in SR/CR/SB for Small SB in $4b$ region.	201
F.8	Background prediction in SR/CR/SB for High CR in $3b$ region.	202
F.9	Background prediction in SR/CR/SB for Low CR in $3b$ region.	202
F.10	Background prediction in SR/CR/SB for Small CR in $3b$ region.	203
F.11	Background prediction in SR/CR/SB for High SB in $3b$ region.	203
F.12	Background prediction in SR/CR/SB for Low SB in $3b$ region.	203
F.13	Background prediction in SR/CR/SB for Large SB in $3b$ region.	204
F.14	Background prediction in SR/CR/SB for Small SB in $3b$ region.	204
F.15	Background prediction in SR/CR/SB for High CR in $2bs$ region.	205

F.16	Background prediction in SR/CR/SB for Low CR in $2bs$ region.	205
F.17	Background prediction in SR/CR/SB for Small CR in $2bs$ region.	206
F.18	Background prediction in SR/CR/SB for High SB in $2bs$ region.	206
F.19	Background prediction in SR/CR/SB for Low SB in $2bs$ region.	206
F.20	Background prediction in SR/CR/SB for Large SB in $2bs$ region.	207
F.21	Background prediction in SR/CR/SB for Large SB in $2bs$ region.	207
F.22	Variations in Prediction in $4b$ SR region.	208
F.23	Variations in Prediction in $3b$ SR region.	208
F.24	Variations in Prediction in $2bs$ SR region.	211

VERITAS VOS LIBERABIT.

Acknowledgments

I have many people to thank. Without them I would not have finished this thesis or my Ph.D. in physics. Thanks to:

- **MELISSA FRANKLIN**, the best adviser ever. Every time I get stuck, Melissa is always there to guide me and show me the light at the end of the tunnel. She always pushes me to understand the details I ignore and think about every result I get. Her encouragement, advice, and commentary have always been inspirational and keep me moving ahead.
- **MASAHIRO MORII**, for being on my committee, and offering physics guidance and discussions. You have always been insightful.
- **HOWARD GEORGI**, for being on my committee, and having me teach Physics 16 with you.
- **JOÃO GUIMARÃES DA COSTA**, for your enthusiasm about physics. I have always enjoyed talking about LHC physics with you. You got me interested in di-Higgs and have always been very supportive.
- **PAOLO GIROMINI**. You taught me how to work on Micromegas, always have great comments on physics and scolding, and ask for the White Rabbits.
- **JOHN HUTH**, for all your support and great stories.
- **THE CHINESE, THE U.S., AND THE E.U. GOVERNMENTS**. Without their generous support, I couldn't study and live in different countries.

- CERN. CERN is a unique and special place with the streets named after physicists. Without the support from the IT department, I could not log into Lxplus, check the Twikis, or finish my work. CERN user's office also made traveling to Europe a much nicer and easier experience for me.
- LHC. Without a fully functional accelerator, there would have been no data for me to study. The LHC has performed outstandingly since 2015, and all the data in this thesis is produced from it.
- **EVERYONE IN THE ATLAS COLLABORATION.** They have supported this remarkable program and have contributed enormously to my thesis. Without the excellent work on detector design, commissioning, operational work, reconstruction, data processing, performance studies and recommendations, software support, computing support, and analysis discussions and guidance, I could not have completed this thesis. I sincerely thank all ATLAS members for their work.
- **ATLAS MUON EXPERTS.** Thanks to Christoph Amelung for his support. Thanks to Ioannis Nomidis, for his guidance on Athena and Muon Monitoring Software. Thanks to Philipp Fleischmann and TieSheng Dai for teaching me about the ATLAS control room and Muon detectors, and for bringing me down to the detector. Thanks to Niels van Eldik, for his guidance on Hough Transform, segment reconstruction and seeding. Thanks to Jochen Meyer, for his patience, help, and discussions on Muon reconstruction and software writing.
- **ATLAS DI-HIGGS TO $4b$ GROUP.** Thanks to Mel Shochet for his support. Thanks to Michael Kagan, for his guidance, patience, and pushing. Thanks to John Allison, for always doing great and ambitious work. Thanks to David Wardrope, for his help on statistical analysis. Thanks to Jana Schaarschmidt, for finishing the paper. Thanks to Qi Zeng, for the his help and useful discussions. Thanks to Patrick Bryant, for finishing the resolved di-Higgs analysis. Without them, I would not have completed the di-Higgs analysis.
- **HARVARD ATLAS GROUP POST-DOCS.** I want to thank Alex Tuna, for his patience, help, and kind support in Muon work and di-Higgs analysis. He always gives good advice on talks and activities. I want to thank Pierluigi Catastini, for working on early di-Higgs searches with

me in summer 2014; Hugh Skottowe, for his help on Micromegas and C code; David Lopez Mateos, for his discussions on physics and asking for plots and espressos; Chris Rogan, for his passion and great insights in analysis; Valerio Ippolito, for following up on questions; Geraldine Conti, Stefano Zambito and Larry Lee, for their discussions and help.

- **STEPHEN CHAN**, for his great company as a roommate and awesome-o discussions. He edited this thesis more than his own.
- **HARVARD ATLAS GRADUATE STUDENTS**. Thanks to Tomo Lazovich and Emma Tolley for being great elder graduate students. Thanks to Karri Di Petrillo and Ann Wang for great discussions and support. I want to also thank Laura Jeanty, Giovanni Zevi Della Porta, Kevin Mercurio, William Spearman, Andy Yen, Brian Clark, Siyuan Sun, Jennifer Roloff, and Julia Gonski. And Gareth Kafka, even though you did neutrinos.
- **HARVARD ATLAS UNDERGRADUATE STUDENTS**. I want to thank Michael Albergo and Gray Putnam, the two undergraduates I have worked with.
- **HARVARD PHYSICS STAFF**. I want to thank Lisa Cacciabuado, Carol Davis, Jacob Barandes, Korin Watras, and Angela Allen for always having open doors and being the most kind, helpful people in the Physics department.
- **CALTECH AND MY UNDERGRADUATE ADVISERS**. Dr. Thomas Tombrello, thanks for teaching me to do research. Stephen Padin, thanks for teaching me how to do an experiment in a lab. Gil Rafeal, thanks for being a great friend and great discussions. Harvey Newman, thanks for teaching me EM and special relativity, and all the help on my research. And Maria Spiropulu, thanks for showing me how exciting particle physics is. Coach Clinton Dodd, for teaching me how to swim. I also want to thank Yi Chen, who taught me a lot when I was a junior on CMS.
- **CHI FENG, HELENA ZHANG, PETER KOCH, JENNIFER HU**. Thanks for being my wonderful friends from Caltech.

- XINYU YANG, CHI ZHANG, RUNDONG NING, BoQI ZHU, YIZHOU JIN. Thanks for being my wonderful friends from Beijing High School Four.
- WEIDONG TONG, my father. You have always been the smartest person I know.
- LIPING SUN, my mother. You have always been the wisest person I know.
- XUYANG MA. I didn't find a new particle, but I found you.

*It was the best of times, it was the worst of times, it was
the age of wisdom, it was the age of foolishness, it was
the epoch of belief, it was the epoch of incredulity, it was
the season of Light, it was the season of Darkness, it was
the spring of hope, it was the winter of despair, we had
everything before us, we had nothing before us, we were
all going direct to Heaven, we were all going direct the
other way. In short, the period was so far like the present
period, that some of its noisiest authorities insisted on
its being received, for good or for evil, in the superlative
degree of comparison only.*

Charles Dickens

O

Introduction

In 2012, the Higgs boson was discovered by the ATLAS and CMS experiments at the LHC. The particle physics community faced a period just like at the beginning of *A Tale of Two Cities*. The Higgs discovery completes the Standard Model and leaves very few experimental clues for physics beyond the Standard Model at the LHC. But with the LHC's increase in collision energy, it is a great time to search for beyond the Standard Model physics. The newly discovered Higgs boson can be used as a tool in these searches. Higgs boson pair production is particularly interesting. While having a low cross-section in the Standard Model, new physics can modify its production in multiple ways. In particular, two Higgs bosons can be produced through heavy particle resonances which give clear signatures at collider experiments.

This search focuses on the dominant $h \rightarrow b\bar{b}$ decay mode to search for two Higgs bosons production. The “resolved” analysis is used for hh systems in which the Higgs bosons have Lorentz boosts low enough that four b -jets can be reconstructed. The “boosted” analysis is used for those hh systems in which the Higgs bosons have higher Lorentz boosts, which prevents the Higgs boson decay products from being resolved in the detector as separate b -jets. Instead, each Higgs boson candidate consists of a single large-radius jet, and b -decays are identified using smaller-radius jets built from charged-particle tracks. The two analyses are complementary in their acceptance, each employing a unique technique to reconstruct the Higgs boson. This thesis focuses on the boosted analysis due to its greater sensitivity to heavy resonance signals.

The dataset for the boosted analysis corresponds to 36.1 fb^{-1} data collected in 2015 and 2016. The results are obtained using the resolved analysis for a resonance mass between 260 GeV and 1400 GeV, and the boosted analysis between 800 GeV and 3000 GeV. The main background is multijet production, which is estimated from data; the sub-leading background is $t\bar{t}$, which is estimated using both data and simulation. The two analyses employ orthogonal selections, and a statistical combination is performed in the mass range where they overlap. The final discriminants are the four-jet and two-jet invariant mass distributions in the resolved and boosted analyses, respectively. Limits are set for the following benchmark signals: a spin-2 graviton decaying into Higgs bosons, a scalar resonance decaying into two Higgs bosons, and SM non-resonant Higgs boson pair production. In the boosted analysis, the improvements with respect to the preceding ATLAS analysis comes from an additional signal region and novel background estimation techniques.

This thesis begins by discussing the status of di-Higgs searches. Chapter 1 gives an overview of double Higgs production in the Standard Model and beyond. Chapter 2 presents details regarding the Large Hadron Collider and the ATLAS experiment. Chapter 3 discusses reconstruction of physics objects. Chapter 4 lists the dataset and simulation samples. Chapter 5 shows the event selec-

tion. Chapter 6 discusses the background estimation in details. Chapter 7 presents the systematic uncertainties. Finally, the results are shown in Chapter 8. A brief summary and outlook is presented in the conclusion. Many detailed plots and supporting material are shown in the appendices.

Knowledge knows no bounds.

1

Theory and Motivation

1.1 THE STANDARD MODEL AND THE HIGGS BOSON

The Standard Model (SM)^{1,2,3,4} is a quantum field theory describing the interactions of elementary particles through the strong, weak, and electromagnetic forces. The elementary particles and their properties are shown in Figure 1.1. So far, the SM predictions of particle interactions agree extremely well with almost all experimental observations.

In the SM, the Higgs mechanism introduces a complex scalar Higgs field, φ , with nonzero vacuum expectation values. The scalar Higgs potential is $V(\varphi) = -v^2\lambda_v\varphi^\dagger\varphi + \lambda_v(\varphi^\dagger\varphi)^2$. Through spontaneous symmetry breaking, W^\pm and Z bosons acquire their masses. This process also predicts an extra scalar, the Higgs boson. The SM Lagrangian containing Higgs couplings, $\mathcal{L}_{\text{Higgs}}$, is shown

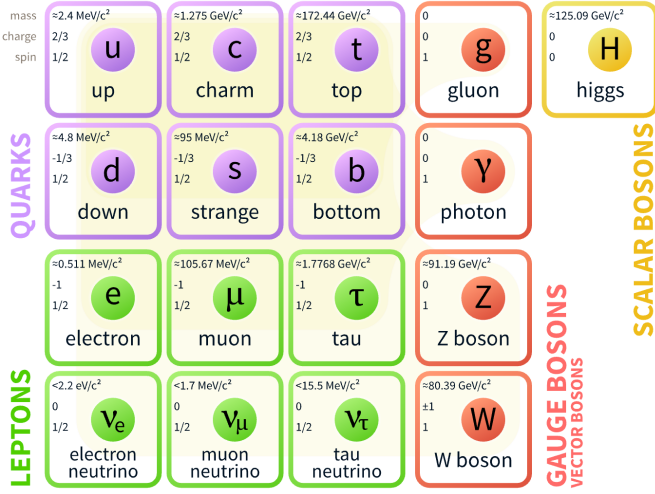


Figure 1.1: Fermions and bosons of the Standard Model and their properties¹, where all values are measured experimentally.

in Equation 1.1.

$$\mathcal{L}_{\text{Higgs}} = -\lambda_{h\bar{f}f} h\bar{f}f + \delta_V V_\mu V^\mu (\lambda_{hvv} b + \lambda_{hhvv} b^2) + \lambda_{hh} b^2 + \lambda_{hhh} b^3 + \lambda_{hhhh} b^4 \quad (1.1)$$

where

- $v \sim 246 \text{ GeV}$, is the non-zero expectation value of the Higgs field;
- $\lambda_v \sim -0.13$, the coefficient for the quartic potential term, is constrained from Higgs mass;
- $m_h = \sqrt{2\lambda_v v} = 125.09 \pm 0.24 \text{ GeV}$, is the Higgs mass; this was discovered in 2012^{5,6};
- $V = W^\pm$ or Z , $\delta_W = 1$, $\delta_Z = \frac{1}{2}$;
- $\lambda_{h\bar{f}f} = \frac{m_f}{v}$, is the Higgs to fermion coupling; m_f is the mass of the fermion;
- $\lambda_{hvv} = \frac{2m_v^2}{v}$, is the Higgs to boson coupling; m_v is the mass of the boson;
- $\lambda_{hhvv} = \frac{m_v^2}{v^2}$, is the Higgs-Higgs to boson-boson coupling;
- $\lambda_{hh} = \frac{m_h^2}{2}$, is the Higgs mass term;

- $\lambda_{hhh} = \frac{m_h^2}{2\nu} = \lambda_{\nu\nu}$, or λ_{hhh} , is the Higgs self-coupling;
- $\lambda_{hhhh} = \frac{m_h^2}{8\nu^2}$, is the Higgs quartic-coupling.

λ_{hhh} in Equation 1.1 has not been experimentally measured. The SM predicts $\lambda_{hhh} = \frac{m_h^2}{2\nu}$, which is referred to as λ_{SM} in this thesis. Measuring λ_{hhh} directly probes the quartic term in the Higgs potential. Also, the $\lambda_{hhh} h^3$ term enables a double Higgs production channel within the SM. Double Higgs production is also known as *di-Higgs* or *Higgs pair production*.

1.2 STANDARD MODEL DI-HIGGS PRODUCTION

There are two main di-Higgs production diagrams at the LHC, both shown in Figure 1.2. In the gluon-gluon fusion process, di-Higgs are produced through a box or a triangle loop. Only the triangle loop Figure 1.2b probes the λ_{hhh} . In the triangle diagram, the middle Higgs boson acts as a propagator (off-shell), and the two Higgs bosons in the final state are on-shell. The diagram with an on-shell middle Higgs and two off-shell Higgs bosons in the final state is strongly suppressed¹. The box and triangle diagrams interfere destructively, which makes the overall production rate smaller than what would be expected in the absence of a λ_{hhh} term.

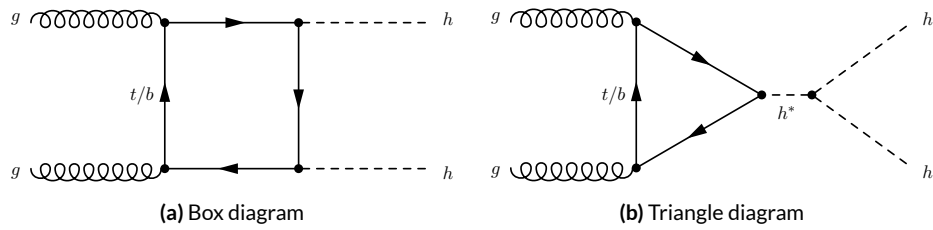


Figure 1.2: Leading order Feynman diagrams contributing to di-Higgs production via gluon-gluon fusion, through the Higgs-fermion Yukawa interactions in Figure 1.2a and the Higgs boson self-coupling in Figure 1.2b. Only Figure 1.2b probes λ_{hhh} .

Many other different production modes of di-Higgs exist. The Feynman diagrams for VBF production are shown in Figure 1.3. Figure 1.4⁷ compares the cross sections of gluon-gluon fusion, vector boson fusion (VBF), top-pair, W^\pm , Z and single-top associated di-Higgs production. It shows that gluon-gluon fusion is the dominant production channel for di-Higgs at pp colliders.

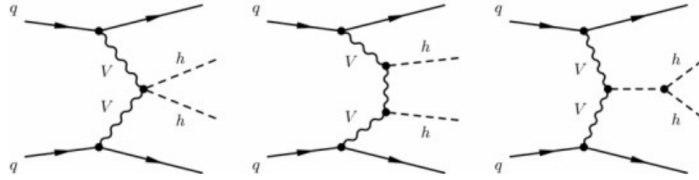


Figure 1.3: Leading order Feynman diagrams contributing to Higgs pair production via VBF.

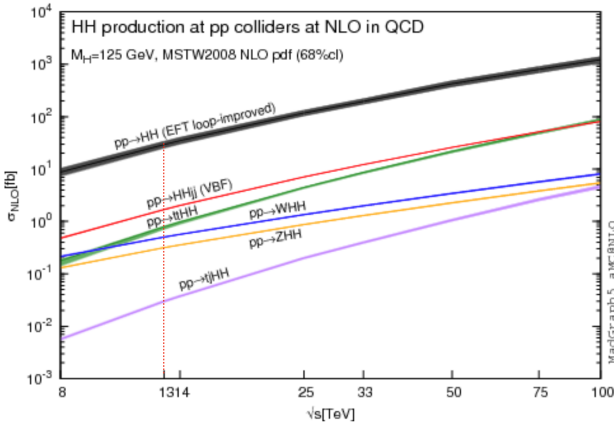


Figure 1.4: Total cross sections (y-axis) at the NLO in QCD for the six largest di-Higgs production channels at pp colliders for different energy (x-axis). Gluon-gluon fusion, VBF, top-pair, W^\pm , Z and single-top associated di-Higgs productions are shown. The thickness of the lines corresponds to the uncertainties added linearly. H refers to the SM Higgs.

For pp collisions at $\sqrt{s} = 13$ TeV, the total cross section for SM di-Higgs production⁸ is evaluated at next-to-next-to-leading order (NNLO) with the summation of logarithms at next-to-next-leading-logarithm (NNLL) accuracy and including finite top-quark mass effects at next-to-leading

order (NLO). There are uncertainties from energy scale and parton distributions functions (PDF).

The production cross section, broken down by different production modes, are as follows:

- Gluon gluon fusion: $\sigma_{gg \rightarrow HH} = 33.49^{+4.3\%}_{-6.0\%} \pm 2.1\% \text{ fb.}$
- Vector boson fusion: $\sigma_{VBF \rightarrow HH} = 1.62^{+2.3\%}_{-2.7\%} \pm 2.3\% \text{ fb.}$
- Gluon gluon fusion to Triple-Higgs: $\sigma_{gg \rightarrow HHH} = 0.06332^{+16.1\%}_{-14.1\%} \pm 3.4\% \text{ fb.}$

A femtobarn (fb) is a unit of area equal to 10^{-43} m^2 . This means with the full 2015 and 2016 36 fb^{-1} dataset, the SM expectation is around one thousand di-Higgs events and only two triple Higgs events.

1.3 BEYOND THE STANDARD MODEL DI-HIGGS PRODUCTION

The SM has had many successful experimental predictions, yet the Higgs boson mass at 125 GeV requires extreme fine-tuning for radiative corrections¹. The presence of new physics at the TeV scale would help solve this unnatural fine-tuning problem.

Beyond the Standard Model (BSM) physics could significantly enhance both resonant and non-resonant production of di-Higgs at the LHC. Non-resonant production generally refers to modifications of the Higgs couplings, either the Higgs self-coupling or the Higgs-top couplings. Resonant production refers to the case when a particle with invariant mass greater than twice the Higgs mass decays directly into two Higgs bosons. Non-resonant and resonant production also translate to different di-Higgs invariant mass distributions at truth level. In the non-resonant case, the invariant mass distribution has no clear peak, whereas in the resonant case, the invariant mass distribution usually forms a peak with a model dependent width.

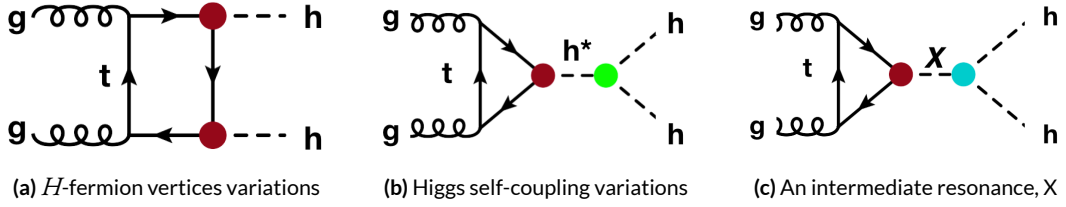


Figure 1.5: BSM Higgs boson pair production: non-resonant production proceeds through changes in the SM Higgs couplings in Figure 1.5a and Figure 1.5b, resonant production proceeds through Figure 1.5c an intermediate resonance, X . H and h both refers to the SM Higgs.

1.3.1 BSM NON-RESONANT DI-HIGGS

Enhanced non-resonant Higgs boson pair production is predicted in many models. BSM models featuring direct $t\bar{t}hh$ vertices^{9,10} or new light colored scalars¹¹ could augment the vertex strength, shown as red circles in Figure 1.5. A direct modification of the Higgs self-coupling coefficient in Eq 1.1, from $\lambda_{\text{sm}} hhh$ to λhhh , is also possible. This is shown as a green circle in Figure 1.5b.

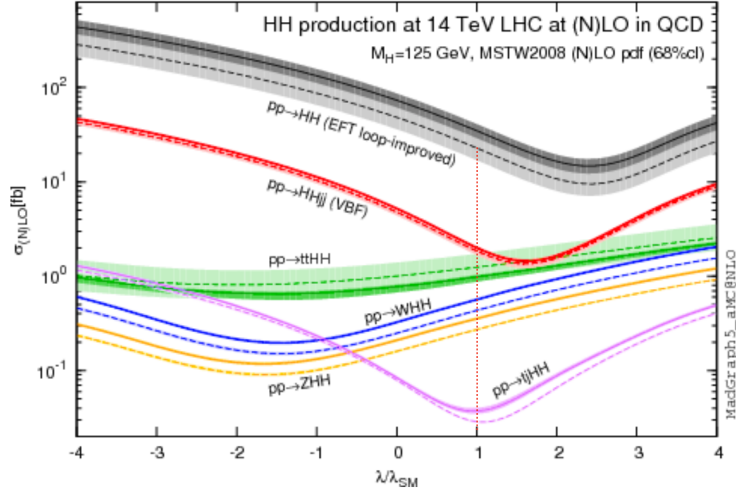


Figure 1.6: Total cross sections (y-axis) at the LO and NLO in QCD for di-Higgs production channels, at the LHC $\sqrt{s} = 14$ TeV as a function of the self-interaction coupling λ (x-axis). The dashed (solid) lines and light- (dark-) color bands correspond to the LO (NLO) results and to the scale and PDF uncertainties added linearly. The SM values of the cross sections are obtained at $\frac{\lambda}{\lambda_{\text{SM}}} = 1$, indicated by the red vertical line. H refers to the SM Higgs.

The non-resonant di-Higgs enhancement is usually described by the di-Higgs cross section ratio between a BSM λ coupling scenario and the λ_{SM} coupling scenario. $\frac{\lambda}{\lambda_{\text{SM}}}$ indicates the ratio between the BSM model λ and λ_{SM} . From SM electroweak measurements, the self coupling term is constrained to $-14 \leq \frac{\lambda}{\lambda_{\text{SM}}} \leq 17.4$ ¹². Variations of λ have a non-trivial effect on di-Higgs production cross section, shown in Figure 1.6⁷. In the regime of relatively high trilinear coupling, $10 < |\frac{\lambda}{\lambda_{\text{SM}}}|$, the interference between the two diagrams is dominated by the trilinear coupling term. A simple limit on $\frac{\lambda}{\lambda_{\text{SM}}}$ can be set based on the observed cross section limit.

1.3.2 BSM RESONANT DI-HIGGS

Theoretically, it is relatively easy to introduce new heavy resonances that interact with the SM through the Higgs as a mediator. This usually results in resonant di-Higgs production. With the increase in center of mass collision energy from 8 TeV to 13 TeV in Run 2 of the LHC, the production cross section for particles with TeV mass grows dramatically, as shown in Figure 1.7. In the case of a 2 TeV M_X , the cross section gain is almost a factor of 10. Therefore, it is particularly important to focus on resonant searches in the region above 1 TeV.

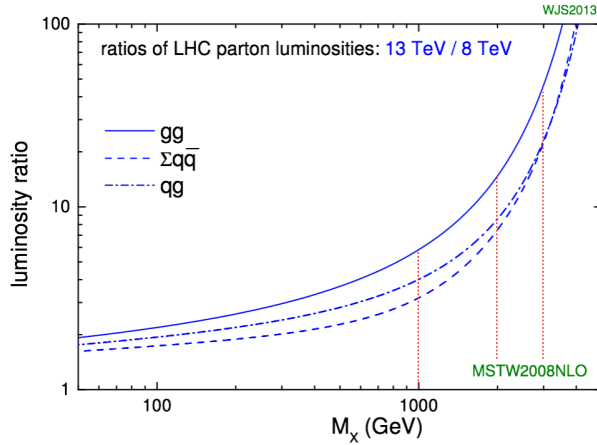


Figure 1.7: Parton luminosity ratios as a function of resonance mass, M_X , for 13/8 TeV¹³. 1, 2, and 3 TeV M_X ratios are indicated by red lines. For a 2 TeV X , the luminosity ratio is almost 10.

Resonant Higgs boson pair production is also predicted by many models. Extensions of the Higgs sector, such as two-Higgs-doublet models (2HDM)^{14,15}, propose the existence of a heavy spin-0 scalar H that can decay into two Higgs bosons. The bulk Randall-Sundrum model^{16,17}, which features spin-2 Kaluza-Klein gravitons, G_{KK}^* , could also subsequently decay to pairs of Higgs bosons. These proposed heavy particles, heavy CP-even scalar H and G_{KK}^* , are represented as X in Figure 1.5c. In model dependent searches, based on fixed assumptions of the resonant particles' branching ratio, other searches for resonances decaying into VV or $t\bar{t}$ are more sensitive compared to di-Higgs searches¹⁸. In order to fully constrain the BSM physics production and decay phase space, di-Higgs search results are interpreted in different models, covering both narrow and wide resonances.

The Randall-Sundrum model proposes a five-dimensional warped space-time that contains two manifolds: one where the force of gravity is very strong and a second manifold at the TeV scale corresponding to the known SM sector. The experimental consequence of this theory is a series of widely mass-spaced Kaluza-Klein graviton resonances, G_{KK}^* . In cases where the fermions are localized to the SM manifold, production of gravitons from fermion pairs is suppressed and the primary mode of production of G_{KK}^* is gluon-gluon fusion. These gravitons further decay to two Higgs bosons, with branching fraction ranging from 6.43% for gravitons with a mass of 500 GeV to 7.66% at 3 TeV. Randall-Sundrum models have two free parameters — the mass of the graviton and $c = k/\bar{M}_{\text{pl}}$, where \bar{M}_{pl} is the reduced Planck mass and k is the curvature scale of the extra dimension. The width of the graviton increases with both mass and c . In Run 1, the G_{KK}^* with $c = 1.0$ is excluded by searches in di-boson and di-Higgs channels up to 760 GeV, as shown in Figure 1.8. Therefore, probing the TeV region is promising in the LHC Run 2.

The 2HDM is a simple extension of the SM which has large resonance effects⁸. The 2HDM consists of 5 physical Higgs bosons: b (light scalar Higgs), H (heavy scalar Higgs), A (heavy pseudoscalar Higgs), and H^\pm (two charged Higgs). The 2HDM can introduce tree level flavor changing

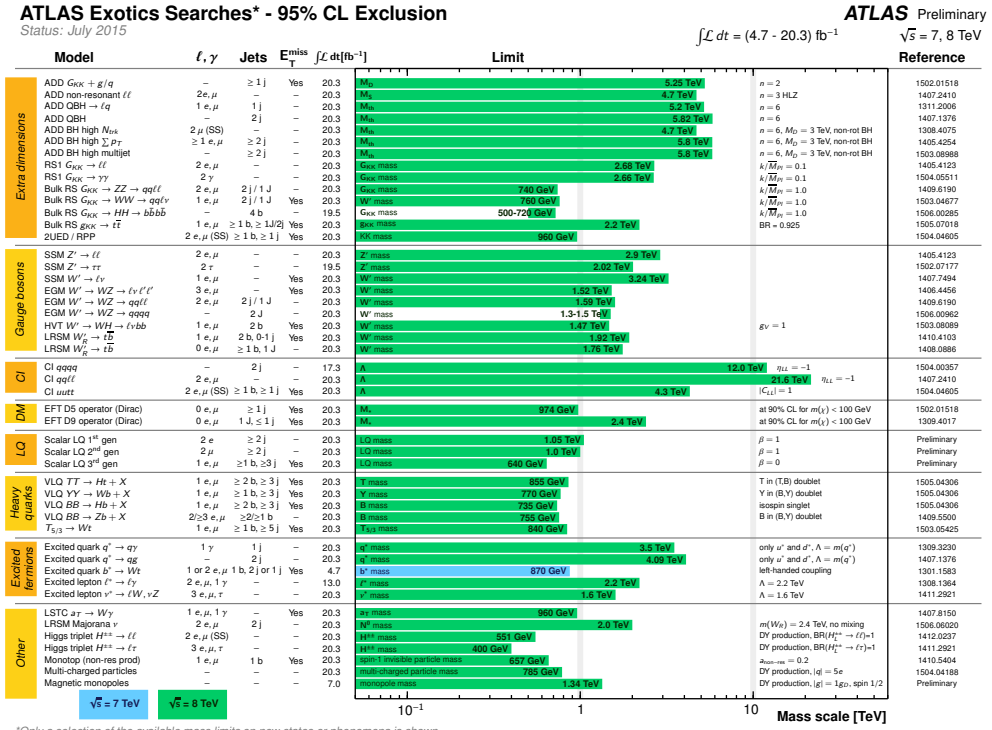


Figure 1.8: Reach of ATLAS searches for new phenomena. Only a representative selection of the available results is shown. Blue (green) bands indicate 7 TeV (8 TeV) data results.

neutral currents. To avoid this obvious contradiction with the SM, models impose discrete symmetries in which the charged fermions only couple to one of the Higgs doublets. One class of such models is type II 2HDM, in which all positively charged quarks couple to one doublet and the negatively charged quarks and leptons couple to the other. The type II model is consistent with the Minimal Supersymmetric Standard Model (MSSM). Resonant di-Higgs production in 2HDM models can proceed through decays of the heavy CP-even Higgs $H \rightarrow hh$. The branching ratio for $H \rightarrow hh$ depends on the model type as well as the values of $\tan \beta$ and $\cos(\beta - \alpha)$. $\tan \beta = \frac{v_{\text{doublet}_2}}{v_{\text{SM}}}$ is the ratio of the vacuum expectation values of the two Higgs doublets. α is the mixing angle between the heavy H and light h fields. The limit where $\cos(\beta - \alpha) = 0$ is called the alignment limit, where the

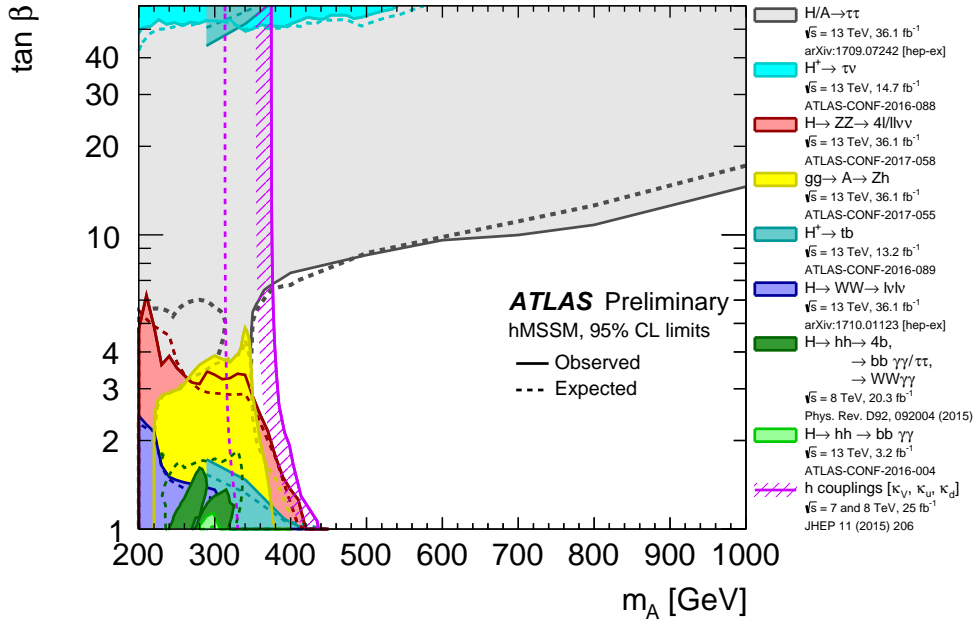


Figure 1.9: Regions of the $[m_A, \tan \beta]$ plane excluded in the hMSSM model via direct searches for heavy Higgs bosons and fits to the measured rates of observed Higgs boson production and decays. Limits are quoted at 95% CL and are indicated for the data (solid lines) and the expectation for the SM Higgs sector (dashed lines). The light shaded or hashed regions indicate the observed exclusions.

light Higgs h has the same couplings as a SM Higgs. For a fixed range of $\tan \beta$, the phase space close to the alignment limit is unexplored, as shown in Figure 1.9. Di-Higgs searches have only excluded the low m_A mass regions in Run 1. It is of particular interest in BSM searches at the LHC Run 2.

1.4 DI-HIGGS DECAY AND LHC PREVIOUS SEARCH RESULTS

The Higgs boson has a short lifetime of 1.56×10^{-22} s. It decays into other elementary particles as soon as it is produced in pp collisions. Therefore, searching for di-Higgs productions requires reconstructing the Higgs boson from its decay products. Di-Higgs decay modes is a combination of two single Higgs boson decay modes. The branching ratios of different di-Higgs final states are shown in Figure 1.10.

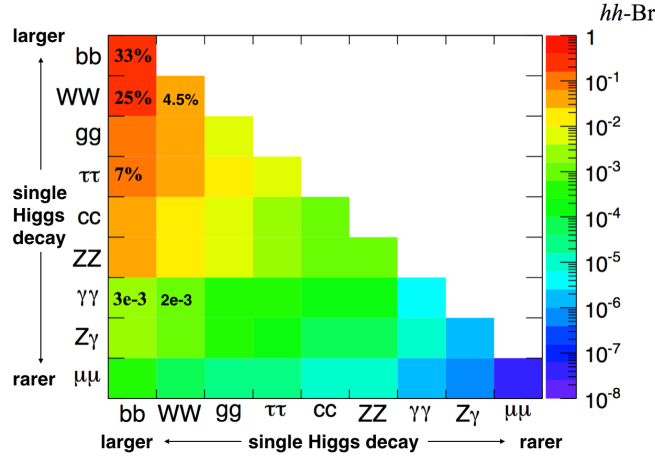


Figure 1.10: Summary of di-Higgs final states and their ratios. Top left, $b\bar{b}b\bar{b}$, has the largest branching ratio.

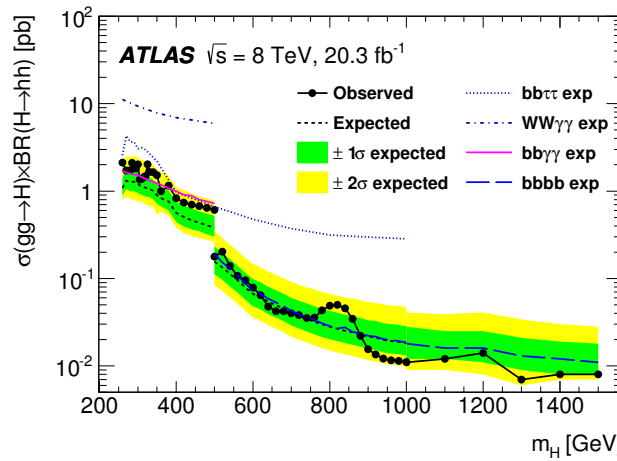


Figure 1.11: The observed and expected 95% CL upper limits of $\sigma(gg \rightarrow H) \times BR(H \rightarrow hh)$ at $\sqrt{s} = 8 \text{ TeV}$ as functions of the heavy Higgs boson mass, m_H , combining resonant searches in Higgs boson pair to $b\bar{b}\tau^+\tau^-$, $W^+W^-\gamma\gamma$, $b\bar{b}\gamma\gamma$, and $b\bar{b}b\bar{b}$ final states. The expected limits from individual searches are also shown. The green and yellow bands represent $\pm 1\sigma$ and $\pm 2\sigma$ uncertainty ranges of the expected combined limits. The improvement above $m_H = 500 \text{ GeV}$ reflects the sensitivity of the $b\bar{b}b\bar{b}$ analysis. The results beyond 1 TeV are from the $b\bar{b}b\bar{b}$ final state alone.

Previous searches for Higgs boson pair production have not found any significant signals. Using 8 TeV data, ATLAS examined the $b\bar{b}b\bar{b}$ ¹⁹, $b\bar{b}\gamma\gamma$ ²⁰, $b\bar{b}\tau^+\tau^-$ and $W^+W^-\gamma\gamma$ channels, all of which were combined²¹. The resonant search combination result is shown in Figure 1.11. The best non-resonant $\sigma(pp \rightarrow hh)$ cross section limit in Run 1 of the LHC is the ATLAS combination, at 0.69 pb. This corresponds to $|\frac{\lambda}{\lambda_{SM}}| < 70$. Different di-Higgs search challenges and perspectives are summarized below:

- $b\bar{b}b\bar{b}$: This channel is the most sensitive channel for high mass resonance searches. The b -jet trigger efficiency limits the low mass resonance searches, but for high mass resonances above 500 GeV, the branching ratio of this channel provides a decisive advantage. It is sensitive for non-resonant searches as well.
- $b\bar{b}W^+W^-$: This channel has the second largest branching ratio, yet the large background from $t\bar{t}$ limits the search sensitivity.
- $b\bar{b}\gamma\gamma$: This channel benefits from high double photon trigger efficiency, a good photon reconstruction efficiency, and a low SM background. This is more sensitive at resonance masses $m_X \leq 350$ GeV. At higher masses, the smaller branching ratio and the merging of photons hurt the search sensitivity. It is also sensitive for non-resonant searches.
- $b\bar{b}\tau^+\tau^-$: This channel is complimentary between $b\bar{b}b\bar{b}$ and $b\bar{b}\gamma\gamma$ for resonance searches. It contributes to the non-resonant result significantly.
- $W^+W^-\gamma\gamma$: This channel suffers from much lower branching ratio and lower reconstruction efficiency of the W^+W^- compared to $b\bar{b}$.
- $W^+W^-\tau\tau, W^+W^-W^+W^-, b\bar{b}ZZ$: These channels have not been searched for yet. But because of the large yield and clean leptonic signatures, it is possible that they will be explored in the future.

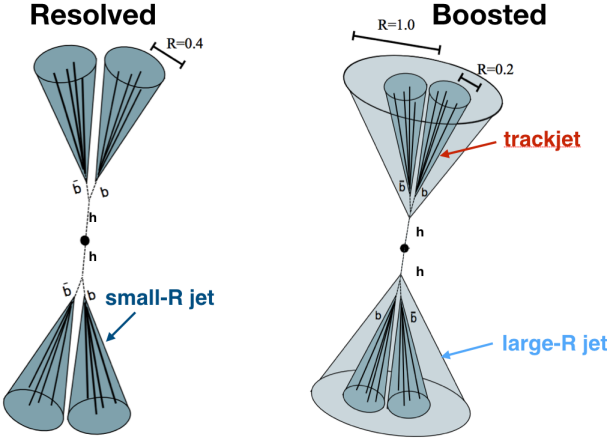


Figure 1.12: Cartoon for $X \rightarrow hh \rightarrow b\bar{b}b\bar{b}$, with resolved event topology (left) and boosted event topology (right).

1.5 RESOLVED AND BOOSTED

The thesis focuses on searching for a TeV scale resonance $X \rightarrow hh \rightarrow b\bar{b}b\bar{b}$. The invariant mass of the two-Higgs-boson-candidate system, m_{2J} , is used as the final discriminant between Higgs boson pair production and the SM backgrounds. The Higgs boson reconstruction affects the m_{2J} invariant mass resolution. Fully reconstructed b -quarks are also necessary to separate the signal from the multi quark production backgrounds.

When the Higgs bosons have Lorentz low boosts, four small- R b -jets with $R = 0.4$ can be reconstructed. This final state is called the *resolved* state, shown on the left of Figure 1.12. The resolved strategy is effective for resonance M_X from 260 GeV up to 1.2 TeV. The resolved state is also sensitive for non-resonant di-Higgs searches.

A different reconstruction strategy is used for di-Higgs systems with higher Lorentz boosts from heavier resonances. For a Higgs boson produced with momentum p_H , the angular separation between the b and \bar{b} quarks, $\Delta R_{bb} = \sqrt{(\Delta\eta_{bb})^2 + (\Delta\phi_{bb})^2}$, scales roughly as $\frac{2m_H}{p_H}$. For example, a 1.5 TeV resonance G_{KK}^* is produced roughly at rest in a $p\bar{p}$ collision. In the lab frame, the two Higgs

bosons each have ~ 625 GeV momentum. The ΔR_{bb} is ~ 0.4 . This means the $b\bar{b}$ system will be contained in two overlapping the standard $R = 0.4$ b -jets. The background rejection power is reduced, and the resolved analysis is not sensitive in this case. Therefore, a different analysis strategy is required. Instead, each $b\bar{b}$ system is reconstructed as a single, large-radius jet. The large-radius jet contains the decay products of the Higgs boson. The presence of b -quarks is inferred using smaller-radius track jets built from charged-particle tracks. This final state is called the *boosted* state, shown on the right of Figure 1.12. This strategy works for resonance M_X from 1 GeV up to 3 TeV.

In summary, di-Higgs production is very rare in the SM, but could be significantly enhanced in BSM scenarios. In particular, a heavy resonance spin-0 or spin 2 particle could decay into Higgs boson pair directly. The search sensitivity for massive resonances increases as the collision center of mass energy. For resonance signals above 1 TeV decaying into Higgs boson pair, $b\bar{b}b\bar{b}$ channel has the best discovery potential in Run 2. In order to fully reconstruct these $X \rightarrow hh \rightarrow b\bar{b}b\bar{b}$, boosted techniques have to be used. Searching for TeV scale resonant production of di-Higgs $\rightarrow b\bar{b}b\bar{b}$ in the boosted regime is the goal of thesis.

Pain teaches lessons no scholar can.

2

LHC and ATLAS

The Large Hadron Collider (LHC) is a proton-proton (pp) collider at the European Organization for Nuclear Research (CERN) laboratory in Geneva, Switzerland²². ATLAS (A Toroidal LHC ApparatuS), CMS (the Compact Muon Solenoid), ALICE (A Large Ion Collider Experiment), and LHC b (Large Hadron Collider beauty experiment)^{23,24,25,26} are the four main experiments. They are located at the interaction points (IPs) of the accelerator. Figure 2.1 shows a schematic of the LHC ring and its experiments.

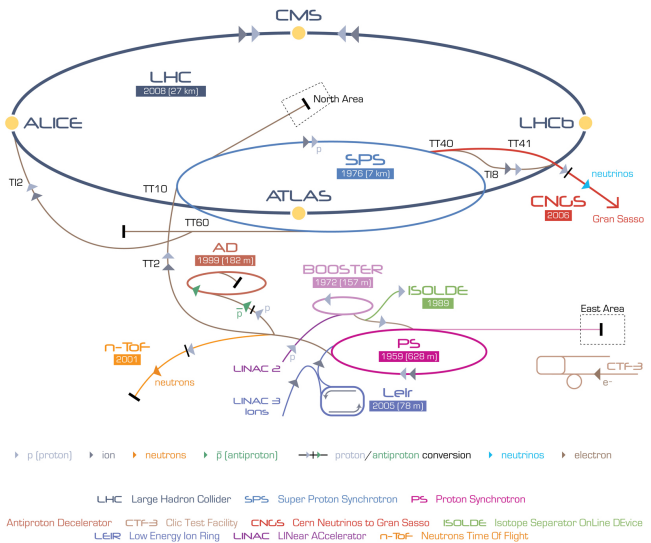


Figure 2.1: A schematic view of the LHC ring²⁷. LINAC2, Booster, PS, SPS, and LHC accelerate the protons in order.

Four main experiments are located at interaction points along the ring. ATLAS and CMS are general purpose experiments, while ALICE focuses on heavy ion collisions and LHC b is dedicated to B physics.

2.1 THE LARGE HADRON COLLIDER

Protons accelerated around the LHC originate in a red bottle of hydrogen gas. The 25 minute acceleration of the protons from rest to 6.5 TeV is accomplished in multiple steps:

- Electrons are stripped from the hydrogens to create protons;
- A linear particle accelerator, Linac 2, accelerates the protons to 50 MeV;
- The Proton Synchrotron Booster (PSB) accelerates the protons to 1.4 GeV;
- The Proton Synchrotron (PS) accelerates the protons to 25 GeV;
- The Super Proton Synchrotron (SPS) accelerates the protons to 450 GeV;
- The 16.7 kilometer LHC accelerates the protons to the final TeV energies.

The instantaneous luminosity, $L (m^{-2}s^{-1})$, at the LHC is defined in Equation 2.1 ²⁷:

$$L = \frac{n_b N_b^2 f_{\text{rev}} \gamma_r}{4\pi \epsilon_n \beta^*} F \quad (2.1)$$

In the above Eq2.1:

- n_b is the number of bunches per beam;
- N_b is the number of protons per bunch;
- f_{rev} is the proton revolution frequency;
- γ_r is the relativistic Lorentz factor for the protons;
- ϵ_n is the normalized transverse beam emittance, or the average beam spread length;
- β^* is the transverse beam size; $\sigma_{\text{beam}} = \sqrt{\epsilon \cdot \beta}$;
- F is a reduction factor for the angle beams are colliding.

In $p\bar{p}$ collisions, the rate of a certain physics process is $R_{\text{phy}} = L\sigma$, where $\sigma(m^2)$ is the cross section.

The instantaneous luminosity can also be written as the ratio of the rate of inelastic collisions to the inelastic cross section σ_{inel} ²⁸:

$$L = \frac{R_{\text{inel}}}{\sigma_{\text{inel}}} = \frac{\mu n_b f_{\text{rev}}}{\sigma_{\text{inel}}} \quad (2.2)$$

where μ is the number of interactions per bunch crossing. For each bunch crossing, there is one main collision used for physics analysis with the highest center of mass energy, and many other lower energy collisions called “pileup” interactions. Larger “pileup” requires higher detector resolution and faster reconstruction techniques.

Table 2.1: LHC nominal²² and operational parameters in 2015²⁹ and 2016³⁰.

Parameter [unit]	Nominal design value	2015 Operating value	2016 Operating value
Beam Energy [TeV]	7	6.5	6.5
Peak Luminosity [$10^{34} \text{ cm}^{-2} \text{ s}^{-1}$]	1	0.5	1.25
Bunch spacing [ns]	25	25	25
f_{rev} [kHz]	11245	11245	11245
n_b [10^{11} p/bunch]	1.15	1.15	1.12
N_b [bunch]	2808	1825	2220
ϵ_n [mm mrad]	3.5	3.5	2
β^* [cm]	55	40	40
F	0.84	0.84	0.59
$\langle \mu \rangle$	19	13	41

The main parameters of the LHC beam and performance are shown in Table 2.1. The target peak instantaneous luminosity for both the ATLAS and CMS experiments is $L = 10^{34} \text{ cm}^{-2} \text{ s}^{-1}$ ²², which was already been exceeded in 2016. This is partly due to the improved β^* and F . The number of “pileup” interactions also increases, shown in Figure 2.2.

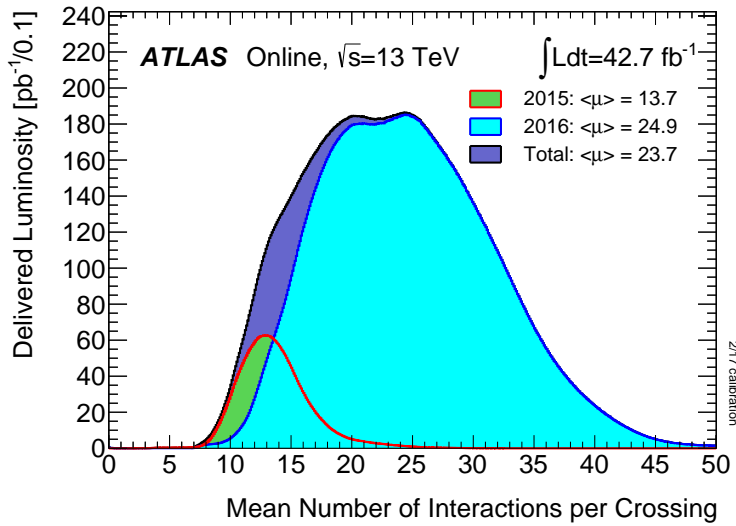


Figure 2.2: The luminosity-weighted distribution of the mean number of interactions per bunch crossing for 2015 and 2016 $p\bar{p}$ collision data at $\sqrt{s} = 13 \text{ TeV}$.³¹

2.2 A TOROIDAL LHC APPARATUS

The ATLAS experiment³² at the LHC is a general-purpose particle detector with near 4π coverage in solid angle and a forward-backward symmetric cylindrical geometry. The ATLAS detector (Figure 2.3) consists of an inner tracking detector (ID) surrounded by a 2.3 m diameter, thin superconducting solenoid providing a 2T axial magnetic field, electromagnetic (EM) and hadronic calorimeters (HCAL), and a muon spectrometer (MS). Three extra air-core toroid magnets generate the magnetic field in the MS.

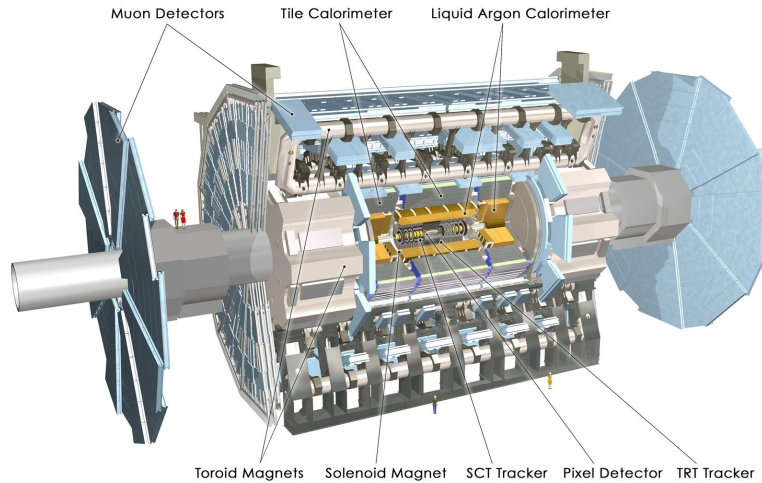


Figure 2.3: A detailed, computer-generated image of the ATLAS detector and its systems.

2.2.1 COORDINATE SYSTEM

ATLAS uses a right-handed coordinate system with its origin at the nominal IP in the center of the detector and the z -axis along the beam pipe. The positive x -axis points from the IP to the center of the LHC ring; the positive y -axis points towards the sky; and the z -axis points straight (like bridges) towards the Geneva airport (A side), back from the Charlie's pub in France (C side). Cylindrical coordinates (r, ϕ) are used in the transverse plane, ϕ being the azimuthal angle around the

z -axis. The pseudorapidity is defined in terms of the polar angle ϑ as $\eta = -\ln \tan(\vartheta/2)$. η the massless approximation of rapidity $y = \frac{1}{2} \ln \frac{E+p_z}{E-p_z}$. ϑ is the angle parameterizing special relativity's boosts along the z -axis. The angular distance is measured in units of $\Delta R = \sqrt{(\Delta\eta)^2 + (\Delta\phi)^2}$.

The region with $|\eta| < 1.5$ is called the “central” region. It consists of the “barrel” elements, which are arranged in a cylindrical fashion around the beam line. In the “endcap” region, with $|\eta| > 1.5$, the detector elements are arranged as disks perpendicular to the beam line. The “forward” region of the detector has $|\eta| > 2.5$.

2.2.2 INNER DETECTOR

The ID is important for track reconstruction and heavy flavor b -tagging. The ID covers the pseudorapidity range $|\eta| < 2.5$. It consists of three sub-detectors: the silicon pixel detector (PIXEL), the silicon microstrip detector (SCT), and the straw-tube transition-radiation tracking detector (TRT). An additional pixel detector layer (IBL)³³, positioned at a mean radius of 3.3 cm, was inserted before the Run-2 data-taking and improves the identification of b -jets³⁴. A 10 GeV charged particle in the barrel region will produce 1 IBL hits, 3 PIXEL hits, 8 SCT hits and 36 TRT hits. Figure 2.4a³⁵ shows the R - z distribution of the material for a quadrant of the barrel region PIXEL and SCT. Figure 2.4b shows the distribution of hadronic-interaction vertex candidates in $|\eta| < 2.4$ and $|z| < 400$ mm for 13 TeV data.

2.2.3 CALORIMETERS

The calorimeters are important for measuring the energy of the Higgs boson decay products. A lead and liquid argon (LAr) sampling calorimeter with finely segmented layers provides EM energy measurements. A steel/scintillator-tile hadronic calorimeter covers the central pseudorapidity range ($|\eta| < 1.7$) and provides hadronic energy measurements. The endcap and forward regions

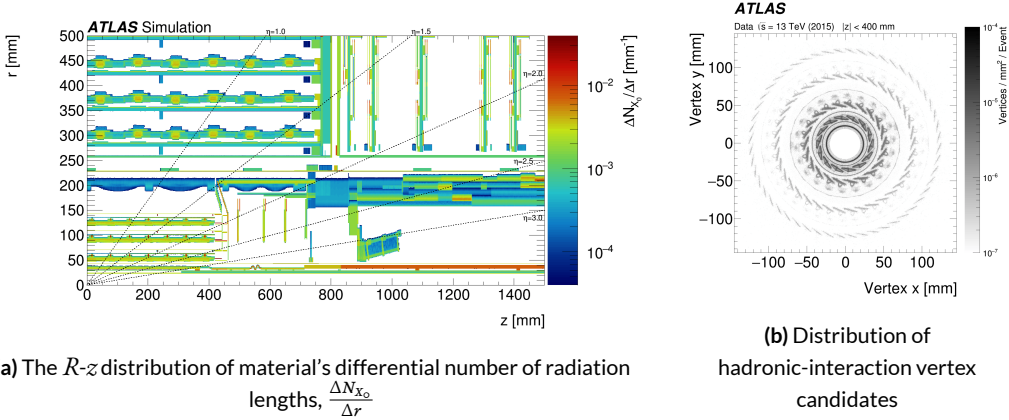


Figure 2.4: Geometry of IBL, PIXEL and SCT detectors in Run 2.

are instrumented with copper/tungsten and LAr calorimeters, respectively, for both the EM and hadronic energy measurements up to $|\eta| = 4.9$. The calorimeters also provide basic EM/hadronic trigger information, with fast, analog summing in coarse granularity.

2.2.4 MUON SPECTROMETER

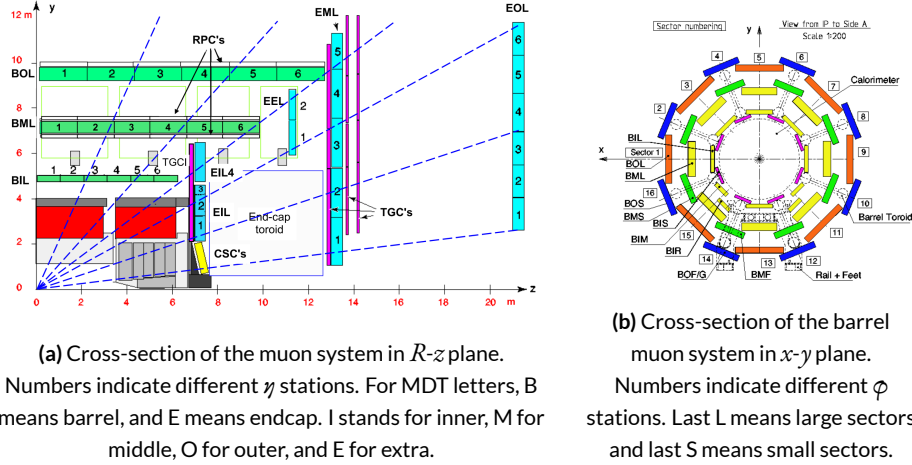


Figure 2.5: The overall layout of the ATLAS muon spectrometer.

The muon spectrometer (Figure 2.5) is the largest component of the ATLAS detector. It surrounds the calorimeters and includes three, large superconducting air-core toroids. The field integral of the toroids ranges between 2 and 6 T/m for most of the detector. Because of this bending power, the MS measures muon momentum with $\sigma_{p_T}/p_T \sim 10\%$ at $p_T = 1\text{TeV}$. Muon Drift Tubes (MDT) and Cathode Strip Chambers (CSC) are the precision tracking detectors. Resistive Plate Chambers (RPC) in the barrel and Thin Gap Chambers (TGC) are the triggering detectors, with 1.5-5 ns timing resolution.

2.2.5 TRIGGER AND DATA ACQUISITION

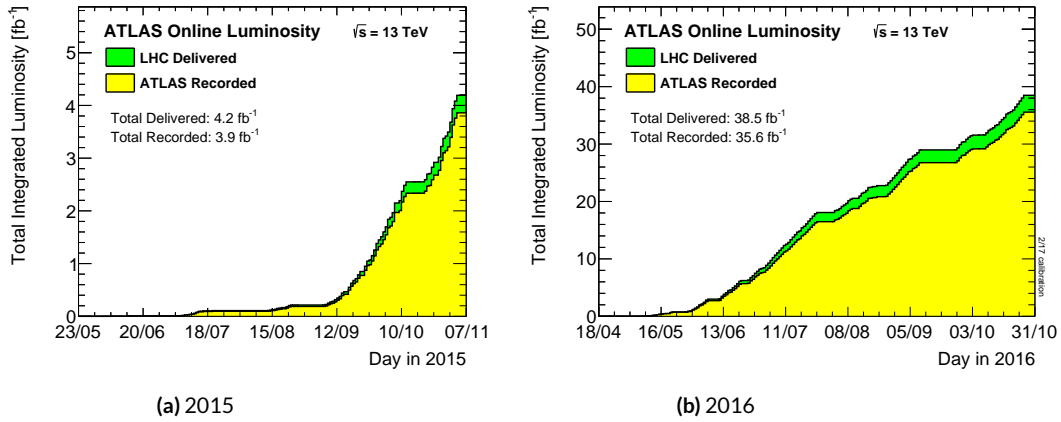


Figure 2.6: Cumulative luminosity vs. time delivered to (green) and recorded by ATLAS (yellow) during stable beams for pp collisions at $\sqrt{s} = 13\text{ TeV}$.

A dedicated trigger system is used to select interesting physics collision events³⁶. The first-level trigger (L1) is implemented in hardware and uses the calorimeter and muon detectors to seed regions of interest (RoI) and reduce the accepted event rate to 100 kHz. This is followed by a software-based high-level trigger (HLT) that reduces the accepted event rate from 40 MHz to 1 kHz on average. To avoid high rates for certain triggers, the triggers are often prescaled, which means some accepted

events get rejected. For example, a prescale of two means only every second event passing all trigger conditions gets accepted.

Over 2015 and 2016, both the LHC and the ATLAS performed outstandingly ³¹. The total data recording efficiency for ATLAS is around 92%, shown in Figure 2.6.

A picture is worth a thousand swords.

3

Reconstruction and Objects

Reconstruction is the process of turning raw detector readouts into particle identification and measurements. In each pp collision recorded by ATLAS, charged particles bend in the magnetic field and leave tracks in the ID; electrons and photons deposit their energies in ECAL; hadrons are absorbed in HCAL; muons leave extra tracks in the MS; and neutrinos are inferred by the conservation of momentum in the transverse plane. Figure 3.1 gives an overview of the different sub-detectors that each type of particle will interact with in ATLAS. Quark reconstruction is particularly important for this $b\bar{b}b\bar{b}$ final state analysis.

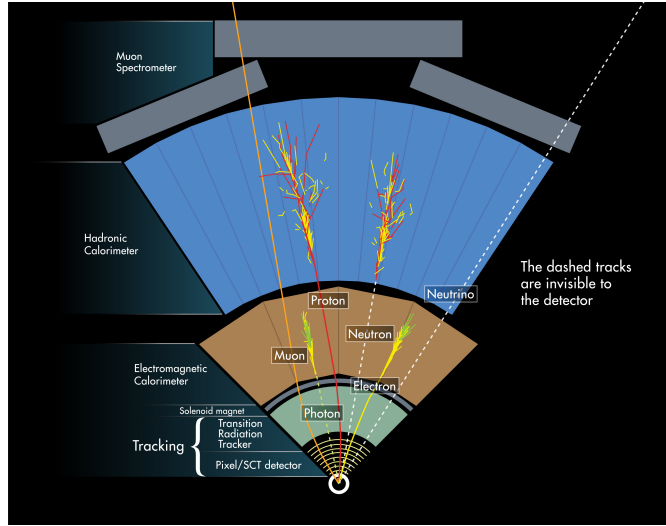


Figure 3.1: Illustration of particle interactions in ATLAS.

3.1 ID TRACKS AND VERTICES

Each beam crossing generates multiple track vertices, and the vertices are reconstructed from the available ID tracks. The primary vertex (PV), or the hard-scatter vertex, is selected as the one with the largest $\sum p_T^2$, where the sum is over all associated tracks. The ID tracks are usually required to have at least 1 PIXEL hit and 6 SCT hits, and to be tightly matched to the primary vertex. The tracks are required to have $p_T > 0.4 \text{ GeV}$ and $|\eta| < 2.5$.

The track reconstruction performance is highly dependent on the momentum of the particle. The decay tracks from a highly boosted parent particle have smaller separations in the inner detector, hindering the cluster process, and thus degrading the track identification efficiency. For a 1 TeV b -hadron, the reconstruction track efficiency is 83%, compared to 95% for a 200 GeV b -hadron ³⁷.

3.2 JETS

When a quark or gluon is produced in pp collisions, it produces a collimated spray of hadrons, which is known as a jet³⁸. Jets are built from topological clusters of energy deposits in calorimeter cells³⁹, using a four-momentum reconstruction scheme with massless clusters as input. The directions of jets are corrected to point back to the primary vertex. Typically, jets are reconstructed using the anti- k_t algorithm⁴⁰ with different values of the radius parameter, R . This algorithm favors clusterings that involve hard particles, and the jets grow outwards around hard “seeds”. R appears in the denominator of the clustering distance metric. It determines the radial size of the jet in η - ϕ plane. The standard $R = 0.4$ jets are used for b -quark reconstruction in the resolved topology. The large $R = 1.0$ jets are used for Higgs boson reconstruction in the boosted topology. The small fixed $R = 0.2$ track jets are used for b -quark identification inside the large- R jets.

3.2.1 SMALL- R JETS

The jets with $R = 0.4$ (“small- R jets”) are reconstructed from clusters calibrated at the electromagnetic (EM) scale. The jets are corrected for additional energy deposited from pile-up interactions using an area-based correction⁴¹. They are then calibrated using p_T - and η -dependent calibration factors derived from simulation, before global sequential calibration⁴² is applied, which reduces differences in calorimeter responses to gluon or quark-initiated jets. The final calibration is based on in situ measurements in collision data⁴³.

Small- R jets are required to be consistent with the primary vertex, in order to avoid contamination from pileup interactions. The jet vertex fraction (JVF) is a useful variable for this purpose. It is the ratio of tracks associated with a primary vertex to the total number of tracks inside a jet. Jets from the PV should have most tracks consistent with the PV and therefore have a large JVF value.

3.2.2 LARGE- R JETS

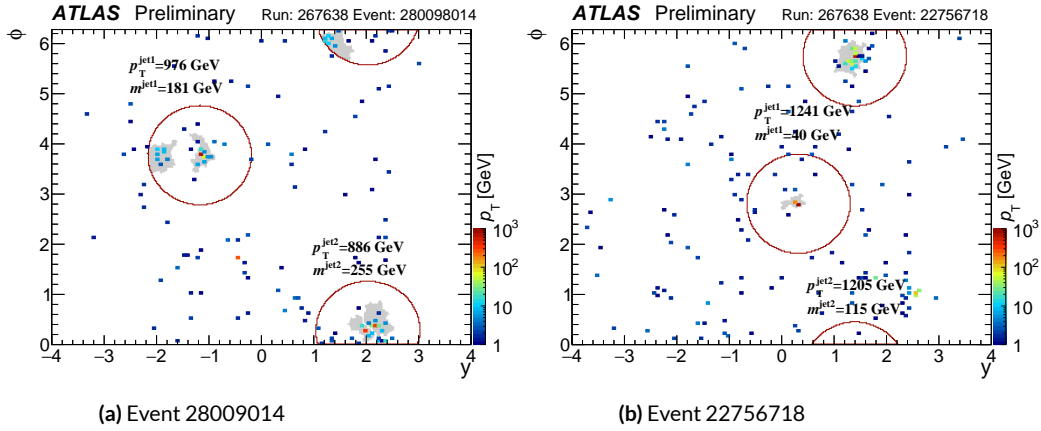


Figure 3.2: Two collision events recorded in June 2015 with a high leading jet p_T shown in pseudorapidity-azimuthal angle parameter space. The dots are calorimeter-cell clusters with positive energy. Only the two leading jets are shown, with their area demarcated by a colored circle, with gray regions denoting the corresponding k_t sub-jets of size $R_{sub} = 0.2$. The color of both jets and clusters corresponds to their p_T .

The jets with $R = 1.0$ (“large- R jets”) are built from locally calibrated⁴² topological clusters.

Two examples are shown in Figure 3.2⁴⁴. Large- R jets are trimmed⁴⁵ to minimize the impact of contamination from non-perturbative effects associated with beam-remnants (“pile-up” events).

Trimming proceeds by re-clustering the jet with the k_t algorithm⁴⁶ into $R_{sub} = 0.2$ sub-jets and then removing those sub-jets with $p_T^{\text{subjet}}/p_T^{\text{jet}} < 0.05$, where p_T^{subjet} is the transverse momentum of the sub-jet and p_T^{jet} that of the original jet. Trimming improves the jet mass resolution, as shown in Figure ?? and ??⁴⁷. The trimming parameter choices shown here are $R_{sub} = 0.1, 0.2$, and 0.3 for a fixed cut at 5%. The energy and mass scales of the trimmed jets are then calibrated using p_T - and η -dependent calibration factors derived from simulation⁴⁸.

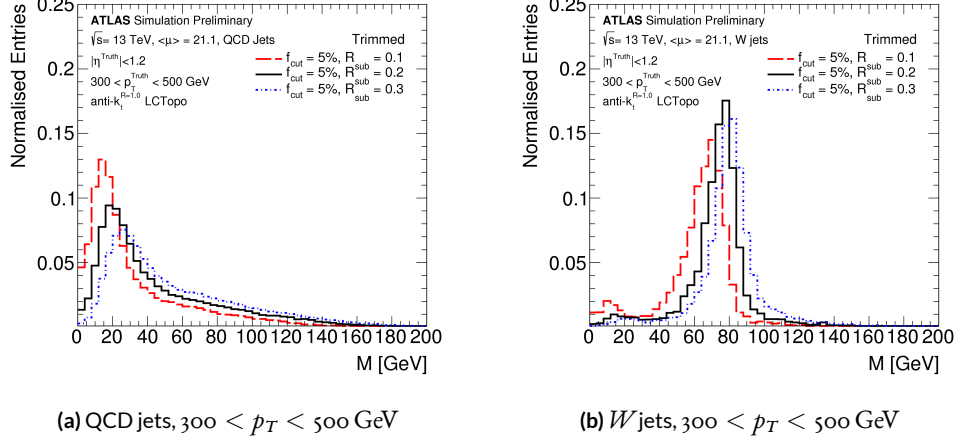


Figure 3.3: For the trimming algorithm using calorimeter cell clusters as inputs to the anti- k_t jet reconstruction algorithm with $R = 1.0$, a comparison of the jet mass distribution for QCD background jets and W boson jets low p_T kinematic regions, as determined by the untrimmed truth jet p_T .

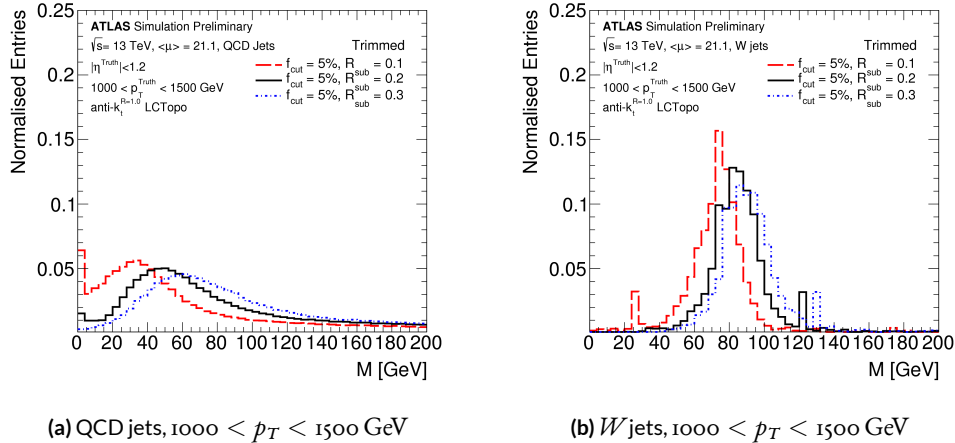


Figure 3.4: For the trimming algorithm using calorimeter cell clusters as inputs to the anti- k_t jet reconstruction algorithm with $R = 1.0$, a comparison of the jet mass distribution for QCD background jets and W boson jets high p_T kinematic regions, as determined by the untrimmed truth jet p_T .

The calorimeter-based jet mass m^{calo} for a large-radius calorimeter jet J is computed from the calorimeter cell cluster constituents i with energy E_i and momentum \vec{p}_i :

$$m^{calo} = \sqrt{\left(\sum_{i \in J} E_i\right)^2 - \left(\sum_{i \in J} \vec{p}_i\right)^2}. \quad (3.1)$$

Tracking information is used to improve the mass resolution. The track-assisted jet mass, m^{TA} , is defined as:

$$m^{TA} = \frac{p_T^{calo}}{p_T^{track}} \cdot m^{track}. \quad (3.2)$$

where p_T^{calo} is the transverse momentum of the large- R calorimeter jet, p_T^{track} is the transverse momentum of the four-vector sum of tracks associated to the large- R calorimeter jet, and m^{track} is the invariant mass of this four-vector sum. This ratio corrects for charged-to-neutral hadron fluctuations and therefore improves the resolution with respect to track-only jet mass.

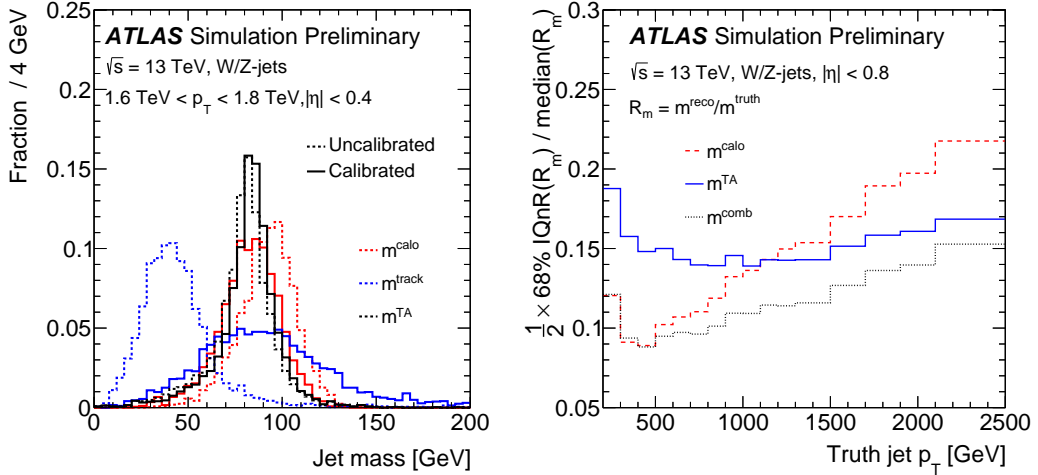
The above two jet mass definitions are only weakly correlated with each other, so they can be linearly combined to the combined mass, m^{comb} , by weighting the components with w :

$$m^{comb} = w \cdot m^{calo} + (1 - w) \cdot m^{TA}. \quad (3.3)$$

where w is determined for each large- R jet from the resolution functions of the calibrated track and calo mass terms. This results in a smaller mass resolution and better estimate of the median mass value than obtained using only calorimeter energy clusters, as shown in Figure 3.5.

3.2.3 TRACK JETS

Track jets are essentially clustered charged hadron tracks. They are reconstructed from ID tracks using the anti- k_t algorithm with a fixed $R = 0.2$. Once the track jet axis is determined, an extra



(a) Uncalibrated (dashed line) and calibrated (solid line) jet mass distribution.

(b) The fractional jet mass resolution vs. the truth jet mass transverse momentum.

Figure 3.5: Uncalibrated (dashed line) and calibrated (solid line) reconstructed jet mass distribution Figure 3.5a, and the jet mass resolution vs jet p_T Figure 3.5b for calorimeter-based jet mass, m_{calo} (red), track-assisted jet mass m_{TA} (black) and the invariant mass of four-vector sum of tracks associated to the large-radius calorimeter jet m_{track} (blue) for W/Z-jets⁴⁹.

step of track association is performed to select tracks with looser impact parameter requirements, in order to collect the tracks needed for effectively running the b -tagging algorithms. Only track jets with at least two tracks are kept. Track jets are also required to have $p_T > 10$ GeV and $|\eta| < 2.5$, in order to suppress light flavor track jets.

Track jets are associated to large- R jets using Ghost-Association. “Ghosts” are track jet 4-vectors, with each track jet’s p_T set to an infinitesimal amount, essentially keeping only the direction of the 4-vector. This ensures that the large- R jet reconstruction is not altered by the ghosts when the calorimeter clusters plus ghosts are reclustered. Re-clustering is then performed using the anti- k_t algorithm with $R = 1.0$. The calorimeter jets after re-clustering are identical to the parents of the trimmed jets used in this analysis, with the addition of the associated track jets retained as constituents. In addition, the track jets corresponding to the ghosts that survive the trimming pro-

cedure (and thus are clustered into one of the surviving sub-jets) are the track jets ghost-associated to the trimmed jet. The small radius parameter of the track-jets enables two nearby b -hadrons to be identified when their ΔR separation is small, which is beneficial when reconstructing high- p_T Higgs boson candidates.

3.3 FLAVOR TAGGING

Some jets are formed from quarks with different flavors. Identifying the flavor of the jet parent quark is called flavor tagging. Jets originating from b -quarks are referred as b -jets, from c -quarks is referred as c -jets, and from other quarks other than the t -quark are referred as light jets. b -tagging is particularly useful for this analysis, since there are four b -quarks in the final state.

B -hadrons have a lifetime, τ , on the order of 1.5×10^{-12} seconds, which gives a flight path length $c\tau \sim 0.45 \text{ mm}^{\text{†}}$ without significant boost. The mean flight path is $\beta\gamma c\tau$, where $\beta = \frac{v}{c}$ and γ is the Lorenz factor. With a higher boost, like $p_T = 50 \text{ GeV}$, the average transverse displacement is 3mm. This results in a displaced decay vertex that can be identified in vertex reconstruction. This allows b -jets with sufficient transverse boost to be distinguished from other flavors of jets.

ATLAS uses three different basic b -tagging algorithms, which provide complementary information:

- Impact parameter based algorithm: this algorithm uses the signed transverse and longitudinal impact parameters d_0 and $z_0 \sin\theta$ of the tracks inside a jet to determine their consistency with the primary vertex. The algorithm uses simulated templates of $\frac{d_0}{\sigma_{d_0}}$ and $\frac{z_0 \sin\theta}{\sigma z_0 \sin\theta}$ for light, c , and b jets to evaluate the likelihood of the jet coming from each of these types.
- Secondary vertex (SV) reconstruction algorithm: this algorithm uses tracks inside the jet to look for vertices that are displaced from the primary vertex. The algorithm provides information on the invariant mass of tracks pointing to a displaced vertex, the number of two track vertices, and the angular separation between the jet axis and the PV \rightarrow SV direction. The

fraction of jets which have a reconstructed secondary vertex are shown in Figure 3.6a. The increase of tracks from fragmentation in the high p_T region is the main reason for the performance degradation. The number of fake vertices is increasing with jet p_T in light jets, while the secondary vertex reconstruction efficiency for b/c -jets slightly decreases with jet p_T .

- Decay chain multi-vertex reconstruction algorithm, or JetFitter (JF): this algorithm reconstructs the full flight path of the b -hadron by looking for multiple displaced vertices along the same direction. A Kalman filter is used to find a common trajectory for the b and c vertices, and hence the algorithm exploits the topology of the weak b/c -hadron decay chain. Leptonic decays of b/c are not considered.

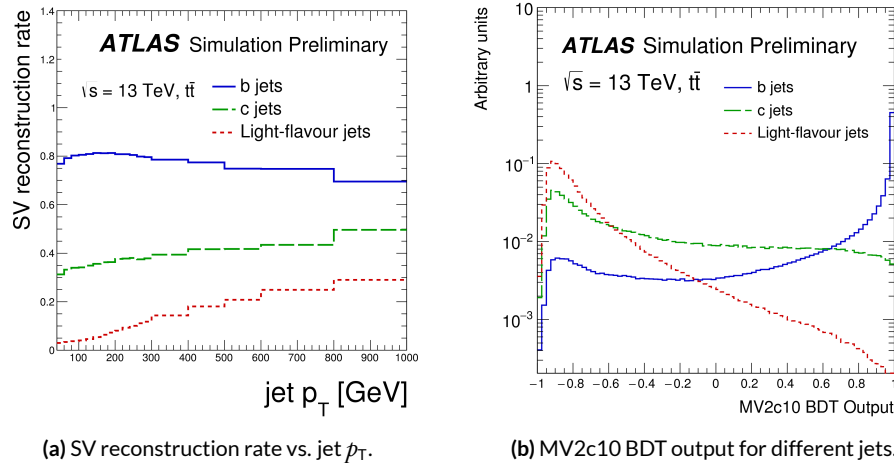


Figure 3.6: Secondary vertex reconstruction rate and MV2c10 output for b -jets (solid blue), c -jets (dashed green) and light-jets (dotted red) evaluated with simulated $t\bar{t}$ events.

Jets containing b -hadrons are identified using a score value computed from a boosted decision tree (BDT) algorithm MV2c10^{so,rt}, which makes use of observables provided by the three algorithms above. A BDT consists of a forest of decision trees. A number of individual decision trees are trained sequentially, with a boosting process in between each training. Boosting adjusts the weights of individual events depending on whether the previously trained tree classifies them correctly. The MV2c10 algorithm is trained on a $t\bar{t}$ sample, with b -jets as signal and a mixture of 93% light-jets and

7% c-jets as backgrounds. It is applied to a set of charged-particle tracks that satisfy quality and impact parameter criteria and are matched to each jet. The MV2c10 algorithm works on both small- R jets or track jets.

The b -tagging working point (wp) is a fixed cut on the MV2c10 value that lead to an efficiency of 70% for b -jets with $p_T > 20$ GeV when evaluated in a sample of simulated $t\bar{t}$ events. This working point corresponds to an acceptance rate of light-jets or jets originating from gluons at $\frac{1}{380}$ for the jets with $R = 0.4$ and $\frac{1}{120}$ for the track jets. The acceptance of jets from c -quarks is $\frac{1}{12}$ for the $R = 0.4$ jets and $\frac{1}{7}$ for the track jets.

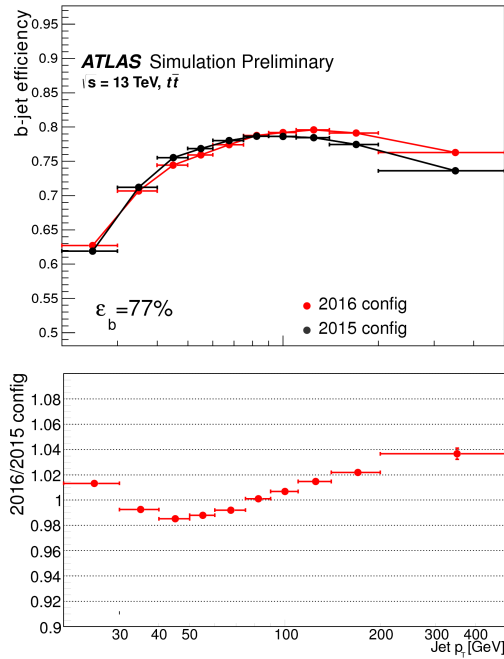


Figure 3.7: b -jet efficiency for the fixed cut working point with a b -jet efficiency of 77% as a function of jet p_T for the comparison between the MV2c10 b -tagging algorithm employed for the 2016 analyses (2016 config) and the previous version of the tagger, MV2c20 (2015 config), which has 15% c -fraction in the training.

In this thesis, the track-jets have a wide p_T ranges, between $10 - 400$ GeV, and the same working point leads to b -tagging efficiencies varying from 40% at low p_T , to 80% for p_T values of about 150 GeV, to 60% at high p_T . This can be seen in Figure 3.7, and the b -tagging efficiency varies from 60% to 80% for an average efficiency of 77%. The increase of tracks from fragmentation in the high jet p_T region is the main reason for the performance degradation. As the jet p_T increases, the number of vertices from the random combination of high multiplicity tracks is increasing, while the secondary vertex reconstruction efficiency for b and c -jets decreases with jet p_T . This is shown in Figure 3.8, and the light-jet acceptance rate could range from $\frac{1}{120}$ to $\frac{1}{250}$. This non-trivial jet p_T dependence of b -tagging performance is one of the major challenges of this analysis.

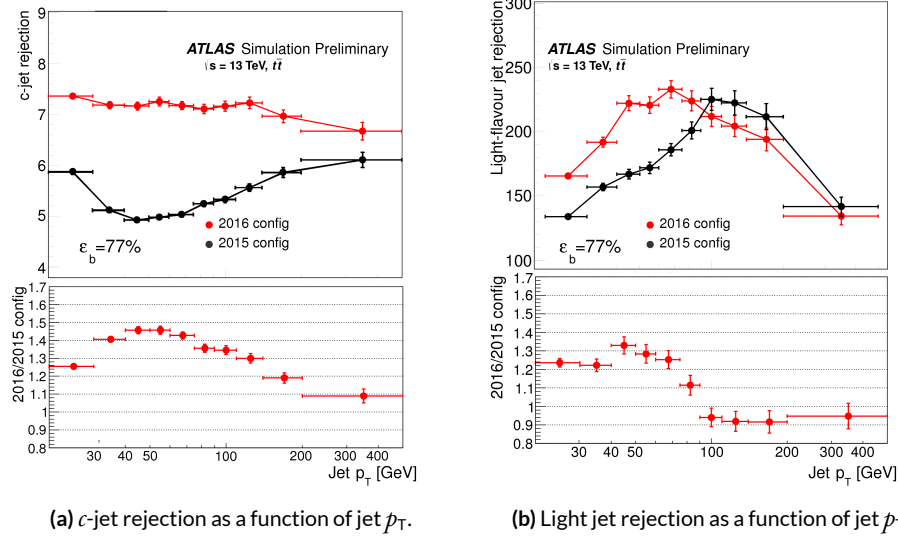


Figure 3.8: Light-flavor jet and c -jet rejection as a function of jet p_T for the previous (2015 config) MV2c20 and the current MV2c10 configuration (2016 config). A fixed cut at 77% b -jet efficiency operating point is used⁵⁰.

Correction factors are applied to the simulated MC samples to compensate for differences between data and simulation in the b -tagging efficiency for b , c and light-jets. The correction for b -jets is derived from $t\bar{t}$ events with final states containing two leptons, and the corrections are consistent

with unity with uncertainties at the level of a few percent over most of the jet p_T range.

3.4 LEPTONS

Muons are identified by matching ID tracks with reconstructed MS tracks³². For this thesis, muons must have $p_T > 4$ GeV, $|\eta| < 2.5$ and to satisfy “medium” muon identification criteria³². Muons are used in this thesis because b hadrons decay to muons with $\sim 20\%$ probability. This is described in section 5.3.

Ugliness is in a way superior to beauty because it lasts.

Serge Gainsbourg

4

Data and Simulation

4.1 DATA

This analysis uses 2015 and 2016 LHC $p\bar{p}$ collision datasets at $\sqrt{s} = 13$ TeV recorded by the ATLAS experiment. Data were collected during stable beam conditions and when all relevant detector systems were functional. A Good Run List (GRL) is generated after gathering on-line and off-line data quality reviews of the dataset after reconstruction. Typically, any $> 10\%$ defect in any detector subsystem makes the corresponding Lumiblocks (LB) fail the GRL requirement. The integrated luminosity of the 2015 dataset passing the GRL requirement is 3.2 fb^{-1} , and the 2016 dataset passing the GRL requirement is 32.9 fb^{-1} . These values are 82% and 92% of the data ATLAS recorded, respectively, as shown in Figure 2.6.

In the resolved analysis, a combination of three b -jet triggers is used:

- “2b4j”: this trigger requires two b -tagged jets and two non- b -tagged jets, all with $p_T > 35 \text{ GeV}$. This trigger is most sensitive for resonance mass between 260 GeV and 500 GeV.
- “2b3j”: this trigger requires two b -tagged jets with $p_T > 55 \text{ GeV}$, and one non- b -tagged jet with $p_T > 100 \text{ GeV}$. This trigger is efficient for resonance mass above 600 GeV.
- “1bj”: this trigger requires one b -tagged jet with $p_T > 225 \text{ GeV}$.

Due to a change in the on-line b -tagging algorithm between 2015 and 2016, the two datasets are treated independently until they are combined in the final statistical analysis. After the resolved selection described later, this combination of triggers is estimated to be 65% efficient for simulated signals with mass above 280 GeV, rising to 95% efficiency for resonance masses greater than 600 GeV, as shown in Figure 4.1.

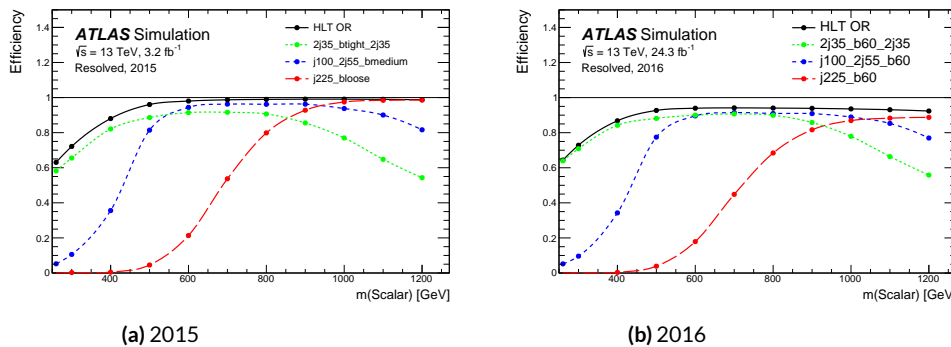


Figure 4.1: Trigger efficiencies following the full resolved analysis selection as a function of the resonance signal mass. The efficiencies of the triggers used in 2015 and 2016 are shown. In both graphs, the green line shows the efficiency of the “2b4j” trigger; the blue line represents the “2b3j” trigger; the red line represents the “1b1j” trigger. The 2016 triggers are less efficient due to a bug in the online primary vertex reconstruction.

During 2016 data-taking, a fraction of the data was affected by a bug. The movement of the beam spot was not accounted for in the on-line vertex reconstruction. This reduced the efficiency of the algorithms used to identify b -jets. That fraction of data is not used and this reduces the integrated luminosity of the 2016 dataset for the resolved analysis to 24.3 fb^{-1} .

In the boosted analysis, events were selected from the 2015 dataset using a trigger that required a single anti- k_t jet with radius parameter $R = 1.0$ and with $p_T > 360$ GeV. In 2016, a similar trigger was used but with a higher threshold of $p_T > 420$ GeV. The efficiency of these triggers is 100% for simulated signals passing the jet requirements as described later, so the 2015 and 2016 datasets were combined into one dataset.

The data is further skimmed (removing objects) into the Derived Analysis Object Data (DAOD). The ATLAS off-line software 20.7.8.7 derivation cache is used, with version p -tags $p2950$. The boosted slimming (removing events) keeps events with at least two large- R jets with $p_T > 200$ GeV. The final input data file has name format:

$dataYR_{\text{15}}TeV.periodPR.physics_Main.PhysCont.DAOD_EXOT8.grpYR_vo1_p2950$, where YR is 15 and PR is [DEFGHJ] for 2015 data, and YR is 16 and PR is [ABCDEFGHIKL] for 2016 data.

4.2 MC

All Monte Carlo (MC) samples used in this analysis are produced with full ATLAS detector simulation. For all simulated samples, charm-hadron and bottom-hadron decays were handled by EVTGEN 1.2.0⁵³. To simulate the impact of multiple low momentum pp interactions that occur within the same or nearby bunch crossings, minimum-bias events generated with PYTHIA 8⁵⁴ using the A2 set of tuned parameters⁵⁵ were overlaid on the hard-scatter event. This pile-up effect is simulated with a μ of 25. Although this is different from the pile-up level in data, it has little effect on the analysis, so the pile-up reweighting is not adopted. The detector response was simulated with GEANT 4^{56,57}, and the events were processed with the same reconstruction software as that used for the data. Simulated data samples from the ATLAS MC15c campaign are be used, corresponding to p -tags $p2952-p2949$.

4.2.1 SIGNAL

In all signal samples, the mass of the Higgs boson (m_H) was set to 125 GeV. The signal MC contains truth-level information, such as the two Higgs and the b -quark four-momenta before detector interactions. This enables a ΔR truth matching between the reconstructed objects and the Higgs.

SM non-resonant production of Higgs boson pairs via the gluon–gluon fusion process was simulated at NLO with `MG5_aMC@NLO`, using form factors for the top-quark loop from HPAIR^{58,59}. The simulated events are reweighted to reproduce the m_{hh} spectrum obtained^{60,61}. This spectrum is calculated at NLO in QCD while fully accounting for the top-quark mass. Interference effects between di-Higgs resonant production and SM non-resonant di-Higgs production are not included in the simulated samples.

Signal $G_{KK}^* \rightarrow hh \rightarrow b\bar{b}b\bar{b}$ events were generated at leading order (LO) with `MG5_aMC@NLO 2.2.2`⁶² interfaced with `PYTHIA 8.186` for parton-showering, hadronization and underlying-event simulation. The NNPDF2.3 LO parton distribution function (PDF) set⁶³ was used for both `MG5_aMC@NLO` and `PYTHIA`. The A14 set of tuned underlying-event parameters was used. These signal samples were generated with $k/\bar{M}_{Pl} = 1$ or 2 . Relative to the resonance mass, widths of the graviton signals range from 3% (at low mass) to 13% (at the highest mass) for $k/\bar{M}_{Pl} = 1$, and 6% to 25% for $k/\bar{M}_{Pl} = 2$. The graviton samples were normalized using fixed cross sections⁶⁴.

Signal 2HDM Scalar $\rightarrow HH \rightarrow b\bar{b}b\bar{b}$ events were generated at LO in QCD with `MG5_aMC@NLO 2.2.3` interfaced with `HERWIG++`⁶⁵ for parton-showering, hadronization, and simulation of the underlying event. CT10⁶⁶ PDF sets were used for `MG5_aMC@NLO` and CTEQ6L1⁶⁷ for `HERWIG++`. The UE-EE-5-CTEQ6L1 set of tuned underlying-event parameters⁶⁸ was used. The scalar signals were generated with a width of 1 GeV, which represent generic, narrow-width scalar signals. Because the

width and branching ratios depend on 2HDM parameters, each mass point generated with this fixed width corresponds to a different point in the 2HDM parameter phase space.

Resonant signal samples for the scalar and $k/\bar{M}_{\text{Pl}} = 1$ models were produced in 10 GeV steps between 260 and 300 GeV, in 100 GeV steps up to 1600 GeV, in 200 GeV steps up to 2000 GeV, and in 250 GeV steps up to 3000 GeV. Signal samples for the $k/\bar{M}_{\text{Pl}} = 2$ model were produced with the same spacings but omitting the masses of 270 GeV, 290 GeV, and 2750 GeV due to the larger generated width. Unless specified, the MC signal sample used as benchmark is $k/\bar{M}_{\text{Pl}} = 1 G_{\text{KK}}^*$, since its width is medium among the three signal models.

4.2.2 BACKGROUNDS

A very small fraction of the background arises from $Z + \text{jets}$ events. The $Z+\text{jets}$ sample was generated using PYTHIA 8.186 with the NNPDF2.3 LO PDF set.

The $t\bar{t}$ background is modeled using large all-hadronic and non-all-hadronic samples that have both been generated with Powheg-Box v1⁶⁹ using the CT10 PDF set. The parton shower, hadronization, and the underlying event were simulated using PYTHIA 6.428 with the CTEQ6L1 PDF set and the corresponding Perugia 2012 set of tuned underlying-event parameters⁷⁰. The t -quark mass in both samples is set to 172.5 GeV. Higher-order corrections to the $t\bar{t}$ cross section were computed with Top++ 2.0⁷¹. These incorporate NNLO corrections in QCD, including re-summation of NNLL soft gluon terms. The $t\bar{t}$ MC samples are normalized to the NNLO+NLL predicted inclusive $t\bar{t}$ cross-section of 1821.87 pb multiplied by the all-hadronic branching ratio of 0.457 and non-all-hadronic of 0.543.

In order to minimize statistical fluctuations across the dijet invariant mass spectrum, especially for large values of m_{tt} , additional $t\bar{t}$ samples are generated in slices of $t\bar{t}$ invariant mass. The cross-

section of the $t\bar{t}$ process is normalized to NNLO+NNLL in QCD, as calculated by Top++ 2.0.

Overlap with the inclusive $t\bar{t}$ samples is removed by a fixed cut on the truth value of $m_{t\bar{t}}$ at 1100 GeV.

A PYTHIA dijet sample is used to understand the multi-jet background and characteristics of the event selection. This MC sample is generated without a heavy flavor filter, and hence is limited by the total generated number of events, given the high background rejection of the analysis selection.

You gotta have a swine to show you where the truffles are.

Edward Albee

5

Event Selection

An $X \rightarrow hh \rightarrow b\bar{b}b\bar{b}$ boosted event candidate observed in 2015 data is shown in Figure 5.1. There are $2b$ tagged tracks within in each of the large- R jets. The one large- R jet has 119 GeV mass and 543 GeV p_T , and the other one has 127 GeV mass and 413 GeV p_T . The ΔR between the two large- R jet is 3.54 and the invariant mass of the two large- R jets is 1336 GeV. This chapter explains why and how this event is selected as an $X \rightarrow hh \rightarrow b\bar{b}b\bar{b}$ candidate.

5.1 DATA CLEANING

The following data cleaning requirements are made:

- Events with problems in SCT/TileCal/LAr are removed.

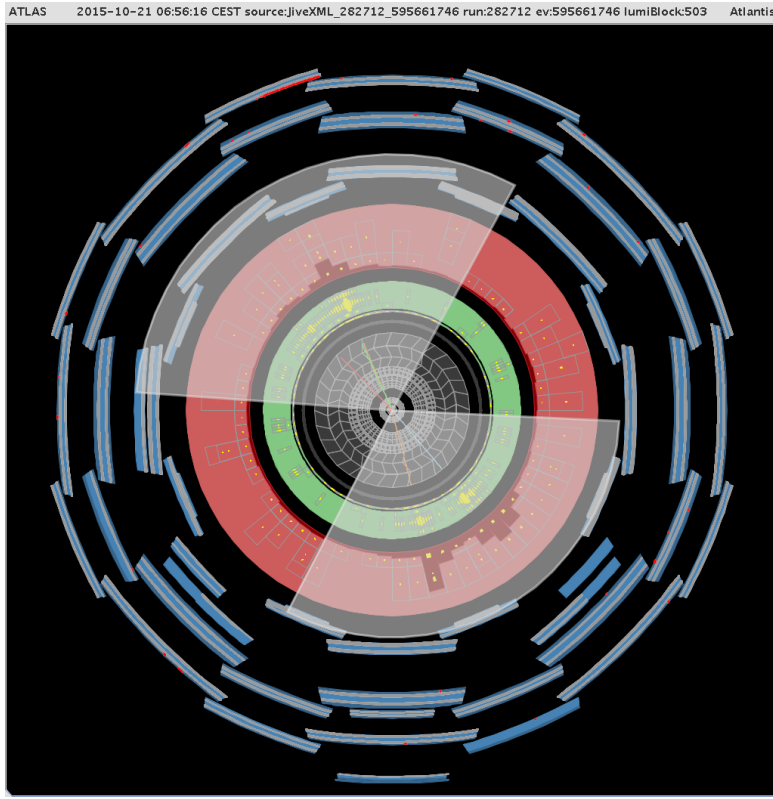


Figure 5.1: 2015 ATLAS boosted di-Higgs event candidate's event display. The data is taken in run 282712, lumiblock 503 and has event number 595661746. ID is in gray, ECAL is in green, HCAL is in red and MS is in blue. Only tracks with $p_T > 25$ GeV are shown. Jets are gray cones, and ID tracks are colored lines in the ID.

- Events that fail the jet cleaning procedure are removed. This is designed to exclude jets caused by detector noise, non-collision background, and cosmic rays.
- Incomplete events are removed.

The analysis also runs over the debug stream, which contains events recorded that could not be reconstructed on-line due to CPU time constraints. No event passing the full signal selection is found.

5.2 TRIGGER

Events in data and MC are required to pass the lowest unprescaled large- R jet trigger:

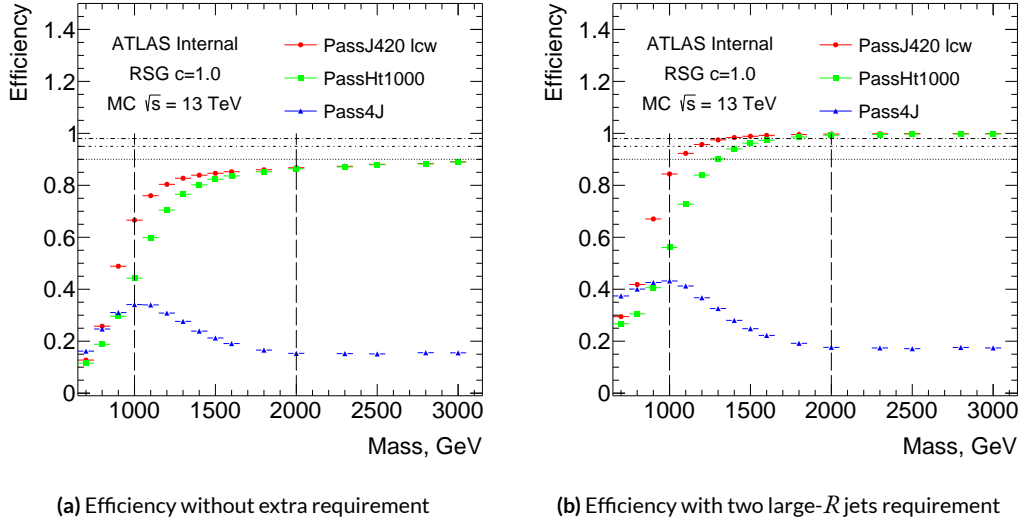


Figure 5.2: Different trigger efficiencies as a function of the resonance signal mass with respect to all events without additional selections (left) and with respect to events passing the two large- R jets and leading (subleading) jet $p_T > 400(250)$ GeV(right).

HLT_j360_a10_lcw in 2015 and HLT_j420_a10_lcw in 2016, where LCW stands for locally clustered weighted. The triggered jets are topo-cluster jets with local calibration weights and pile-up subtraction. They are seeded by the lowest unprescaled L1 jet trigger, L1_J100. LCW cluster triggers are chosen, because the alternative option, reclustered large- R jet trigger, has a slower jet momentum turn-on in multi-jet events. Other options such as the lowest unprescaled transverse energy trigger, HLT_ht1000, have a much slower turn-on compared to large- R jet triggers. Another trigger option is a four jet trigger HLT_4j100, but because of boosted jet merging, the trigger efficiency decreases rapidly as the signal mass increases. The trigger efficiencies with respect to all events and events with two large- R jets are shown in Figure 5.2. For 1.4 TeV signal with two large- R jets, the large- R jet trigger efficiency is about 98%. The trigger turn-on curve in 2015 and 2016 data, as a function of leading jet p_T , is shown in Figure 5.3. Based on this figure, the large- R jet p_T is required to be above 450 GeV, which is above the trigger turn-on threshold.

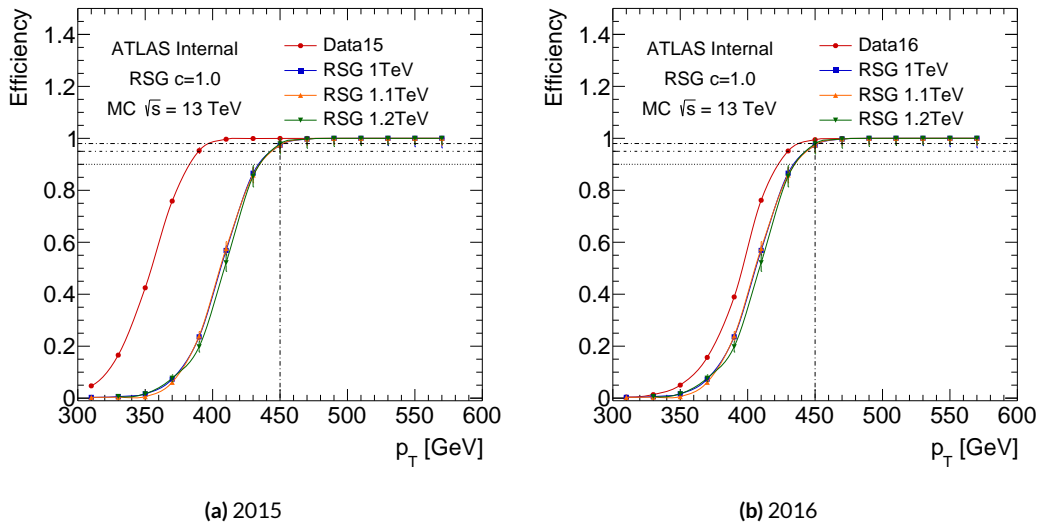


Figure 5.3: Large- R jet trigger (HLT_j360_a10_lcw , left and HLT_j420_a10_lcw , right) efficiencies with respect to the large- R jet p_T , defined as the ratio between events that fired the trigger and the all the simulated events, measured in 2015 and 2016 data and G_{KK}^* with $c = 1.0$ MC.

5.3 OBJECT SELECTION

Table 5.1: Physics objects and their technical names in the boosted analysis.

object	technical name
large- R calorimeter jets	AntiKt10LCTopoTrimmedPtFrac5SmallR20Jets
small- R track jets	AntiKt2PV0TrackJets
b-tagging	on track jets, MV2c10, 70% b-tagging wp

The specific physics objects used in the boosted analysis are described in previous sections and reiterated in Table 5.1. The selection cuts are listed in Table 5.2 and are explained in detail.

Each event must have at least two high momentum large- R jets, defined in section 3.2.2. They are sorted by p_T . The leading large- R jet, also referred to as the leading Higgs candidate (leadJ), is

Table 5.2: List of kinematic selection used in the boosted analysis. These cuts are generally efficient for signal events.

kinematic selection

-
- leading large- R jet must have $p_T > 450$ GeV, $|\eta| < 2$, $m > 50$ GeV
 - sub-leading large- R jet must have $p_T > 250$ GeV, $|\eta| < 2$, $m > 50$ GeV
 - track jets must have $p_T > 10$ GeV, $|\eta| < 2.5$
 - $|\Delta\eta| = |\eta_{\text{leadjet}} - \eta_{\text{subjet}}| < 1.7$

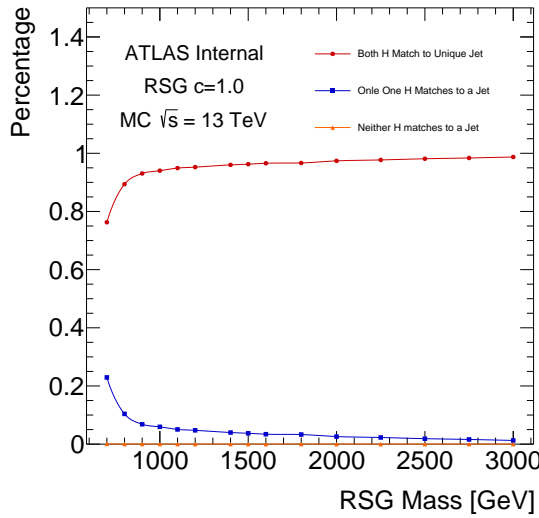


Figure 5.4: Percentages of truth Higgs boson contained by a large- R jet with $\Delta R_{\text{Higgs},\text{jet}} < 1.0$ as a function of G_{KK}^* masses. The three cases listed in the legend are orthogonal. Two Higgs bosons almost never match to the same large- R jet.

defined to be the large- R jet with the highest p_T . The second highest p_T large- R jet is called the sub-leading large- R jet, also referred to as the subleading Higgs Candidate, or sublJ. The large- R jets are required to have $p_T > 250 \text{ GeV}$, $|\eta| < 2$ to guarantee the tracking acceptance, and mass $> 50 \text{ GeV}$ to reduce the size of data and simulations. The leading large- R jet is also required to have $p_T > 450 \text{ GeV}$ to be above the trigger turn on threshold. Only the leading and subleading large- R jets are considered in the rest of this thesis. Both truth-level Higgs bosons are matched to the two large- R jets $\sim 95\%$ of the time for 1.2 TeV signal MC, shown as the red curve in Figure 5.4. Requiring $R = 1.0$ ensures that the two b quarks and their decay products are very likely to be contained within the large- R jet, as shown in Figure 5.5.

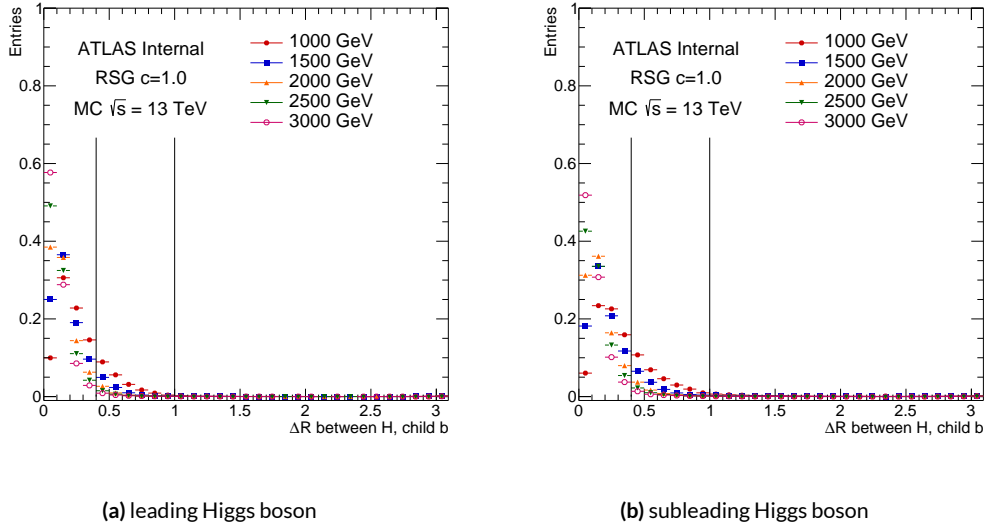


Figure 5.5: Normalized ΔR between the truth Higgs (leading on left, subleading on right) and the truth children b -quarks for G_{KK}^* MC. Lines are drawn at $\Delta R = 0.4$ (R of small- R jets) and $\Delta R = 1.0$ (R of large- R jets).

The track jets, defined in section 3.2.3, are required to have $p_T > 10 \text{ GeV}$, $|\eta| < 2.5$ and at least two associated tracks. A track jet is considered b -tagged if it has $\text{MV}_{2c10} > 0.6455$ (see Section 3.3 for details). Each large- R jet is required to have at least one ghost-associated track jet. Allowing only one ghost-associated track jet is motivated by the kinematic signatures of signals with masses above

2.5 TeV, where the resulting $R = 0.2$ track jets merge due to large Lorentz boosts. If there is more than one track jet contained in the large- R jet, they are also sorted by p_T . The highest p_T track jet is defined to be the leading track jet, and the second highest p_T one is defined to be the subleading track jet. Only the two leading p_T track jets are considered in this thesis. One or two track jets are ΔR matched to the truth b quarks 80% of the time, as shown in Figure 5.6. In the Figure, red means the truth Higgs doesn't match the large- R jet. Blue means both truth b s match the two track jets. Orange means two truth b s match the same track jet. Green indicates one b quark has $\Delta R < 0.2$ for both the leading and subleading track jets, and the other b is matched to one of the two track jets. Pink means one b matches to one of the two track jets, while the other b doesn't match to the two leading track jets.

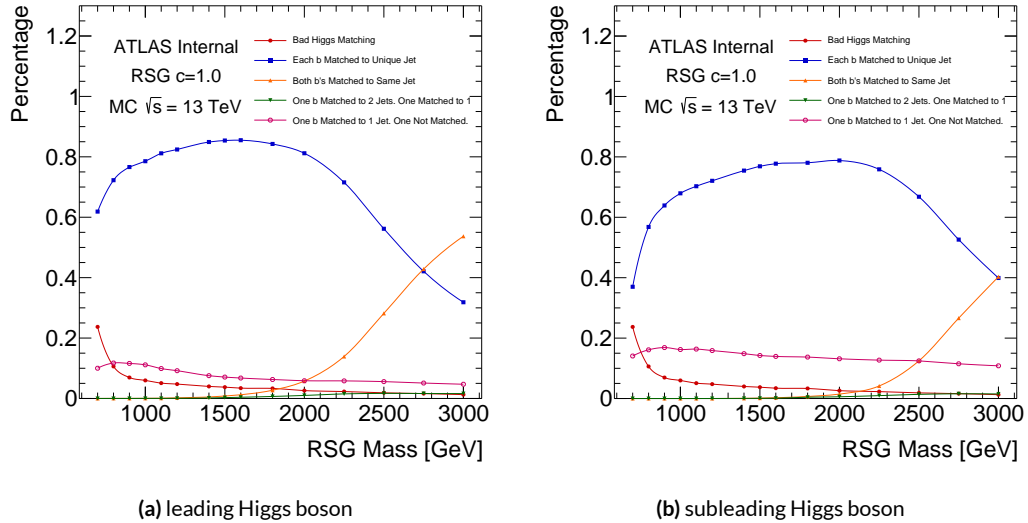


Figure 5.6: Percentage of $\Delta R < 0.2$ matching truth b 's to track jets (leading Higgs on the left, subleading Higgs on the right) for different G_{KK}^* masses. The cases listed in the legend are orthogonal to each other. The cases not listed on the legend (including when a truth b is not contained in the large- R jet) happen in total at most 1.6% of the total for a given G_{KK}^* mass.

Muon correction to the large- R jet four-momenta is applied. b -hadrons decay to a muon and a muon neutrino through a W boson with 20% probability. The energy carried by the muon is not

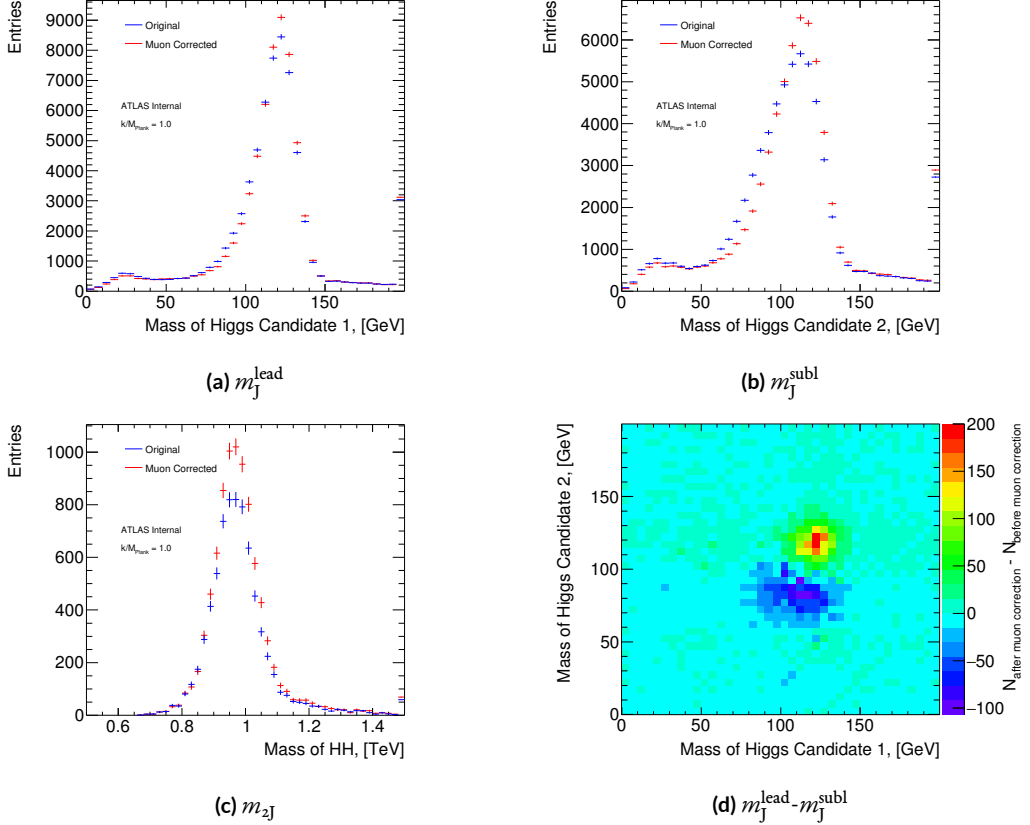


Figure 5.7: Kinematics of $1 \text{ TeV } G_{\text{KK}}^*$ MC before (blue) and after (red) muon-in-jet corrections. The reconstructed Higgs masses (top row, left for leading large- R jet, right for subleading large- R jet) are closer to 125 GeV after the correction, which improves the signal efficiency for the signal region selection by $\sim 10\%$ (bottom row, left for m_{2J} , right for event distribution differences on the leading-subleading large- R jet mass plane.).

measured in the large- R jet. A further muon correction on large- R jet four-momentum accounts for this energy loss. The muon-in-jet corrections are applied only after the fiducial large- R jet requirements on p_T and η . The muons are required have $\Delta R < 0.2$ with the b -tagged track jets within each large- R jet. In the case where more than one muon is found within a track jet, only the muon with the smallest ΔR is considered. If two b -tagged track jets are found to have muons, both corrections are considered. The four-momenta of the matched muon is added to the large- R jet four-momentum, with the muon calorimeter energy deposits subtracted. This correction is only applied

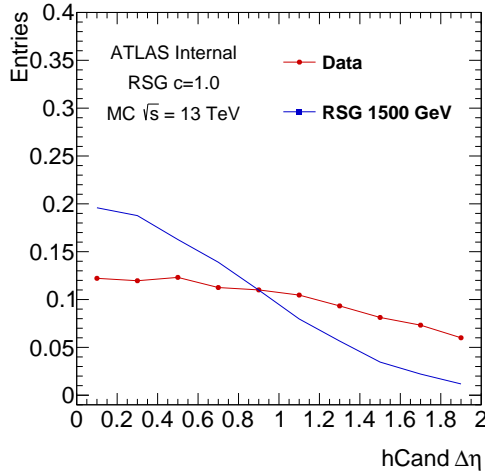


Figure 5.8: After large- R jet requirements, normalized $\Delta\eta_{JJ}$ distribution in $1.5 \text{ TeV } G_{KK}^*$ and data, where the data consists of mostly multijet events ($> 90\%$). Higgs candidate refers to the two large- R jets. The background multijet events are more forward in $\Delta\eta_{JJ}$ distribution.

to the calorimeter mass portion of the combined mass, because the track mass calculation already contains the muon track. The muon-in-jet correction improves the overall large- R jet mass resolution by approximately 5%, and Figure 5.7 shows the impact of this correction on the $1\text{TeV } G_{KK}^*$.

Finally, the Higgs candidates (large- R jets) are also required to have $|\Delta\eta| = |\eta_{\text{leadJ}} - \eta_{\text{subJ}}| < 1.7$. This is because the spin 2 G_{KK}^* production is mostly s -channel with a more central distribution in η , while the multi-jet events have larger t -channel or u -channel productions with a more forward distribution. Figure 5.8 shows the $\Delta\eta_{JJ}$ distribution for signal MC and data in inclusive b -tag channels. This cut is not entirely optimal for scalar signals due to the different spin, but it is fixed for both G_{KK}^* and scalar selections.

5.4 RESOLVED VETO

Sometimes one event can be reconstructed in both the resolved method as four small- R jets and the boosted method as two large- R jets with track jets. Figure 5.9 shows an example event display of collision data recorded in 2015.

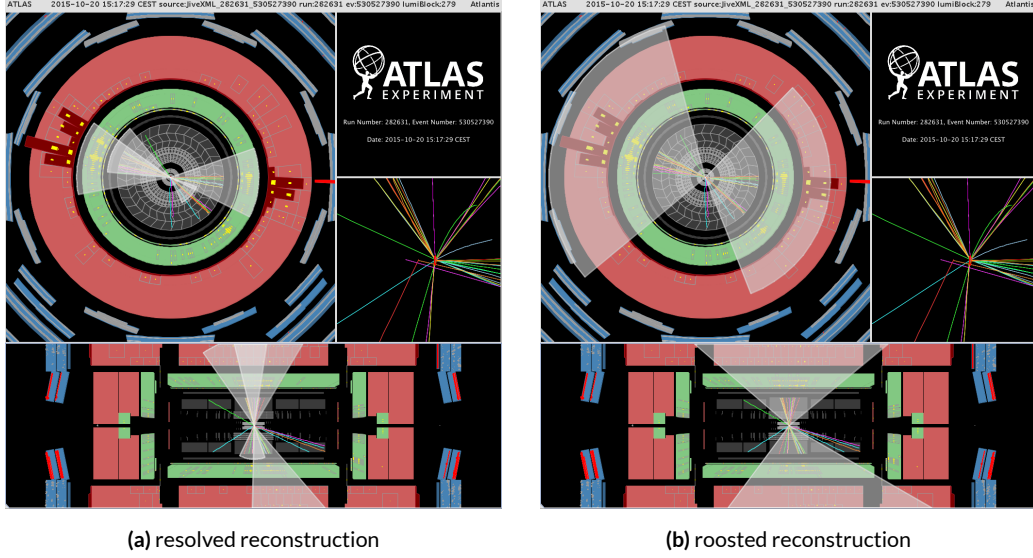


Figure 5.9: Event display of the same event in 2015 data using resolved 5.9a and boosted 5.9b topologies. The resolved reconstruction gives a m_{4J} of 873 GeV, and the boosted reconstruction gives m_{2J} of 852 GeV.

In order to avoid events being reconstructed by both the resolved and the boosted analysis, events that pass the resolved signal region selections are vetoed in the boosted analysis. This is an ATLAS political decision, and the effect of vetoing boosted event selection in the resolved analysis was never tested. The gain is a full statistical combination of the resolved and boosted result. This veto reduces the boosted analysis sensitivity in the resonant mass region up to 1.5 TeV, which is recovered in the statistical combination with the resolved analysis. Hence, it is necessary to introduce the resolved selection⁷².

For the resolved analysis, the four small- R jets with the highest b -tagging score are paired to construct two Higgs boson candidates. Each jet must have $p_T > 40 \text{ GeV}$, $|\eta| < 2.5$, $\text{MV2c10} > 0.8244$ (small- R jet 70% b -tagging working point). Pairings of jets are only accepted as Higgs candidates if they satisfy the following requirements, where m_{4j} is expressed in GeV:

if $m_{4j} < 1250 \text{ GeV}$:

$$\frac{360 \text{ GeV}}{m_{4j}} - 0.5 < \Delta R_{jj}^{lead} < \frac{653 \text{ GeV}}{m_{4j}} + 0.475; \quad \frac{235 \text{ GeV}}{m_{4j}} < \Delta R_{jj}^{subl} < \frac{875 \text{ GeV}}{m_{4j}} + 0.35 \quad (5.1)$$

if $m_{4j} > 1250 \text{ GeV}$:

$$0 < \Delta R_{jj}^{lead} < 1; \quad 0 < \Delta R_{jj}^{subl} < 1 \quad (5.2)$$

In these expressions, $\Delta R_{jj,lead}$ is the angular distance between jets in the leading Higgs boson candidate and $\Delta R_{jj,subl}$ for the sub-leading candidate. The leading Higgs boson candidate is defined to be the candidate with the highest scalar sum of jet p_T . This ΔR requirement efficiently rejects jet-pairings where one of the b -tagged jets did not originate from a Higgs boson decay.

Also, mass-dependent requirements are made on the leading Higgs boson candidate p_T and the sub-leading Higgs boson p_T :

$$p_T^{lead} > 0.5m_{4j} - 105 \text{ GeV}, \quad p_T^{subl} > 0.33m_{4j} - 75 \text{ GeV} \quad (5.3)$$

where m_{4j} is again expressed in GeV.

A further (m_{4j} -independent) requirement is placed on the pseudorapidity difference between the two Higgs boson candidates, $|\Delta\eta_{bb}| < 1.5$, which rejects multi-jet events.

$$|\Delta\eta_{bb}| < 1.1 \quad \text{if } m_{4j} < 850 \text{ GeV}, \quad |\Delta\eta_{bb}| < 2 \times 10^{-3}m_{4j} - 0.6 \quad \text{if } m_{4j} > 850 \text{ GeV} \quad (5.4)$$

Events that have multiple Higgs boson candidates satisfying these requirements (which happens often when $m_{4j} < 500$ GeV) necessitate an algorithm to choose the correct pairs. The optimal choice would be the combination most consistent with the decays of two Higgs bosons of equal mass. To account for energy loss in measurement and reconstruction resolution, the requirement of equal masses is modified. The distance, D_{hh} , of the leading and subleading Higgs boson candidate masses, $(m_{2j}^{\text{lead}}, m_{2j}^{\text{subl}})$ from the line connecting (0 GeV, 0 GeV) and (120 GeV, 110 GeV) is computed, and the pairing with the smallest value of D_{hh} is chosen. The values of 120 GeV and 110 GeV are chosen because they correspond to the median values of the narrowest large- R jet mass intervals that contain 90% of the signal in simulations. D_{hh} can be expressed as follows:

$$D_{hh} = \frac{\left| m_{2j}^{\text{lead}} - \frac{120}{110} m_{2j}^{\text{subl}} \right|}{\sqrt{1 + \left(\frac{110}{120} \right)^2}}. \quad (5.5)$$

A requirement on the Higgs boson candidate mass is used to define the resolved signal region:

$$X_{hh-\text{resolved}} = \sqrt{\left(\frac{m_{2j}^{\text{lead}} - 120 \text{ GeV}}{0.1m_{2j}^{\text{lead}}} \right)^2 + \left(\frac{m_{2j}^{\text{subl}} - 110 \text{ GeV}}{0.1m_{2j}^{\text{subl}}} \right)^2} < 1.6, \quad (5.6)$$

where the $0.1m_{2j}$ terms represent the widths of the leading and sub-leading Higgs boson candidate mass distributions, derived from simulation. In summary, any event is rejected in the boosted selection if the D_{hh} minimized Higgs candidate passes the resolved signal region $X_{hh-\text{resolved}}$ cut.

5.5 2D HIGGS MASS CUT

To separate di-Higgs decays from background productions like QCD multi-jets and top, requirements on the leading and subleading large- R jet masses are imposed. Figure 5.10 shows the G_{KK}^* MC $m_J^{\text{lead}} - m_J^{\text{subl}}$ 2D distribution. The signal is centered around the Higgs boson mass 125 GeV in the 2D plane.

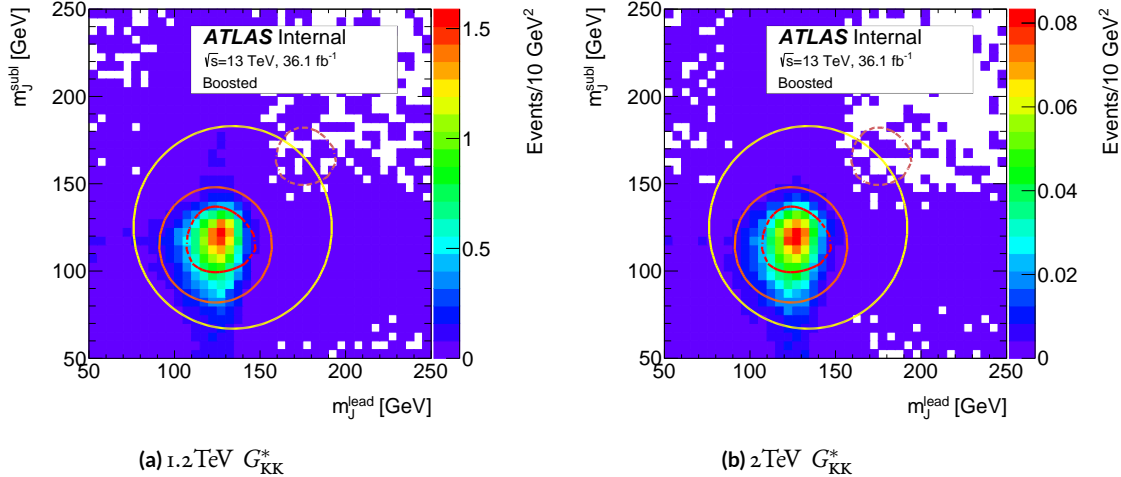


Figure 5.10: For RSG $c = 1.0$ samples, the number of events as a function of leading Higgs candidate mass and subleading Higgs candidate mass, for 1.2 TeV (left) signal and 2 TeV (right) signal samples. The red dotted line in the center correspond to the signal region, passing $X_{hh} < 1.6$.

The signal region is defined using the expression 5.7:

$$X_{hh} = \sqrt{\left(\frac{m_j^{\text{lead}} - 124 \text{ GeV}}{\text{o.1}(m_j^{\text{lead}})}\right)^2 + \left(\frac{m_j^{\text{subl}} - 115 \text{ GeV}}{\text{o.1}(m_j^{\text{subl}})}\right)^2} \quad (5.7)$$

The denominator of each term in X_{hh} represents the resolution of the reconstructed leading and subleading jet masses. Hence X_{hh} can be interpreted as a χ^2 compatibility with the di-Higgs hypothesis. The subleading large- R jet typically has a biased downward reconstructed mass. Because it is the subleading jet and hence has lower boost. The jet decay constituents are sometimes outside of the jet cone. The energy losses from neutrinos in leptonic b decays and cracks in the calorimeter also contribute. The subleading jet mass center value of 115 GeV accounts for the larger energy loss in subleading jets. The signal region requires $X_{hh} < 1.6$. This cut keeps $\sim 40\%$ of signal events passing all selections. A more optimal signal region definition, using asymmetric signal jet mass resolution and a momentum dependent cut accounting for the higher mass resolution of larger p_T jets, can improve the overall search sensitivity by 2 – 8%. Since the gain in sensitivity is small, the signal region

is kept to be consistent with the $X_{hh\text{-resolved}}$.

5.6 NUMBER OF b -TAGGED TRACK JET REQUIREMENTS

In addition to requirements for basic object selection and the X_{hh} cut, the signal regions are defined by further requiring multiple b -tags which are consistent with the di-Higgs decay. The MC events passing all signal region selections are sorted into different b -tagging categories. This is shown in Figure 5.11.

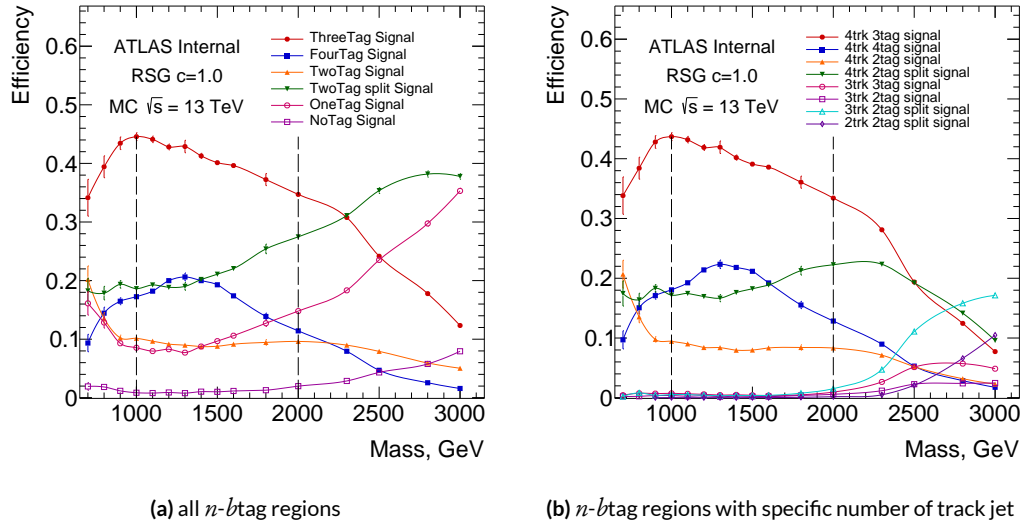


Figure 5.11: Signal fraction in different b -tag categories (left) and detailed fraction in different number of track jet and b -tag categories (right) as a function of signal resonance mass hypothesis for selection cuts. The efficiencies are relative to the total number of events passing the 2D mass cut.

$X \rightarrow hh \rightarrow b\bar{b}b\bar{b}$ results in four b -quarks, which ideally leads to four track jets passing b -tagging requirements. This is defined as the $4b$ channel. The $4b$ requirement has an overall efficiency of roughly ϵ^4 , where ϵ is the b -tagging efficiency chosen to be 70%. This means an overall $0.7^4 \sim 0.24$ probability, but having one actual b -jet failing b -tagging while the other three passing has probability $3 \times 0.7^3 \times (1 - 0.7) \sim 0.31$. Therefore, a $3b$ selection is also introduced to recover the signal efficiency.

An event with $3b$ -tags must have at least $3b$ -tagged track jets, but can have any number of additional un-tagged track jets. In $4b$ and $3b$, each Higgs candidate can have at most two b -tagged track jets, hence $\geq 3b$ -tagged track jets cannot be in the same large- R jet.

At the highest resonance mass, the Lorentz boost of the Higgs boson can be large enough to collimate the b -quarks, resulting in $\Delta R_{bb} < 0.2$. The two b -quarks decay products are therefore contained inside only one $R = 0.2$ track jet instead of two. This decreases the selection efficiency in $4b$ and $3b$ channels. A third signal channel is added to account for this, denoted by two-tag-split or simply $2bs$. It requires that exactly one b -tagged track jet is found in each Higgs candidate, plus an arbitrary number of track jets that must fail the b -tag. For masses above 2.5 TeV, the $2bs$ channel (where each large- R jet has exactly one b -tagged track jet) significantly improves signal acceptance.

$4b$, $3b$, and $2bs$ channels are chosen as three signal channels, also referred to as n - b tag channels. The other b -tagging channels, also referred to as lower- b tag channels, are also sorted and studied. $2b$ channel is defined as one large- R jet has two b -tagged track jets, and the other large- R jet has no b -tagged track jet. $1b$ channel is defined as one large- R jet has one and only one b -tagged track jets, and the other large- R jet has no b -tagged track jet. $0b$ channel is defined as both large- R jets have no b -tagged track jet. They all have relatively small signal acceptance.

5.7 SIGNAL EFFICIENCY AND CUTFLOW

Acceptance means the geometric fiducial volume of the detector. Efficiency refers to the detector effectiveness in finding objects. The signal efficiency as a function of G_{KK}^* resonance mass is shown in Figure 5.12, both for the absolute signal efficiency and for the efficiency relative to the previous cut in the selection. Above a mass of ~ 1 TeV, the reconstruction of high momentum large- R jets with small $\Delta\eta$ is efficient, as shown in the orange-triangle curve. The biggest limitation of the boosted

analysis is b -tagging inefficiency for track jets with momentum above 500 GeV, as shown in the pink-circle curve. The second biggest limitation is the large- R jet mass resolution, as shown in the purple-square curve. Across the mass range considered, the signal jet masses requirement (X_{hh}) and b -tagging requirements are $\mathcal{O}(40\%)$ efficient relative to the previous cuts.

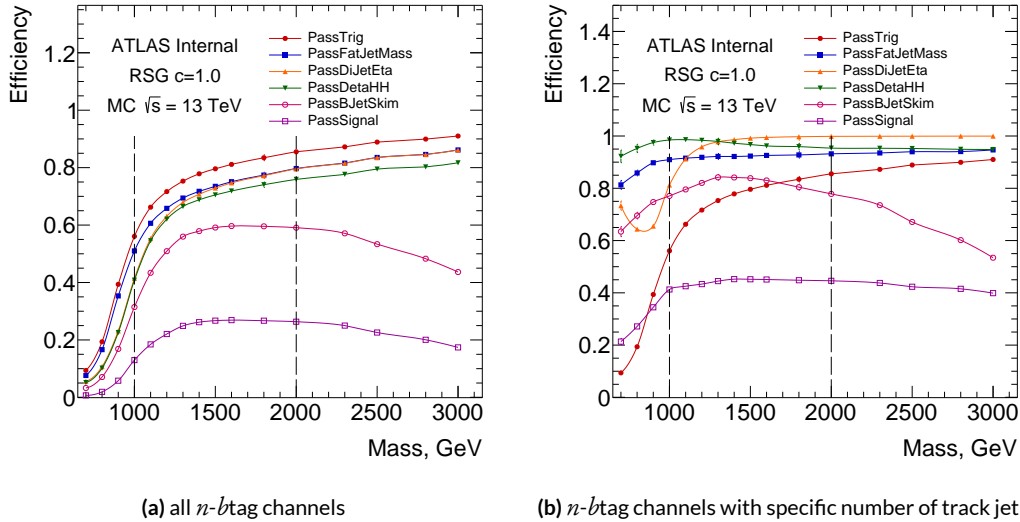


Figure 5.12: Selection efficiency (left) and relative efficiency with respect to the previous cut (right) as a function of RSG $c=1.0$ signal resonance mass hypothesis for selection cuts. The relative efficiency is defined from the previous cut, where the order of cuts is given by the legend. PassTrig means the event passes the trigger selection; PassDiJetPt means the event passes the leading and sub-leading jet p_T cuts; PassDiJetEta means the event passes the leading and sub-leading jet η cuts; PassDeltaH means the events passes the $|\Delta\eta| < 1.7$ cut; PassBJetSkim means the event contains at least two b -tagged track jets, inclusive of $2b$, $2bs$, $3b$ and $4b$ configurations; PassSignal means the event passes the signal region cut $X_{hh} < 1.6$.

The selection efficiency at various stages for G_{KK}^* with $c = 1.0$, G_{KK}^* with $c = 2.0$, and Heavy Scalar signal samples of all mass points can be found in Tables 5.3, 5.4 and 5.5. The signal production cross section is monotonically decreasing as a function of signal mass.

Table 5.3: The selection efficiency for $G_{KK}^* \rightarrow hh \rightarrow b\bar{b}b\bar{b}$ events ($c = 1.0$) at each stage of the event selection. Uncertainties are the MC stat uncertainty only.

Resonance Mass [GeV]	Mini-ntuple Skimming	2 large-R jets	$\Delta\eta$	Xhh < 1.6	2bs SR	3b SR	4b SR
500	317.31 ± 6.0	295.75 ± 5.79	164.5 ± 4.32	8.45 ± 0.99	1.08 ± 0.37	2.14 ± 0.52	0 ± 0
600	269.07 ± 3.64	247.94 ± 3.5	136.31 ± 2.59	11.31 ± 0.76	2.57 ± 0.37	3.84 ± 0.45	0.66 ± 0.19
700	253.68 ± 3.35	226.93 ± 3.16	124.83 ± 2.35	16.79 ± 0.86	3.74 ± 0.42	6.99 ± 0.56	1.91 ± 0.29
800	286.26 ± 2.28	245.36 ± 2.11	129.2 ± 1.53	24.41 ± 0.67	5.11 ± 0.31	11.27 ± 0.46	4.13 ± 0.27
900	306.51 ± 1.61	275.57 ± 1.52	158.03 ± 1.15	40.72 ± 0.59	8.81 ± 0.28	19.76 ± 0.41	7.5 ± 0.25
1000	238.2 ± 0.98	226.98 ± 0.96	165.2 ± 0.82	52.86 ± 0.47	10.87 ± 0.22	26.0 ± 0.33	10.07 ± 0.2
1100	164.5 ± 0.63	160.94 ± 0.63	132.53 ± 0.57	45.26 ± 0.34	9.55 ± 0.16	21.88 ± 0.23	9.03 ± 0.14
1200	109.24 ± 0.41	107.92 ± 0.4	93.45 ± 0.38	33.53 ± 0.23	6.96 ± 0.11	15.8 ± 0.16	7.38 ± 0.1
1300	72.72 ± 0.59	72.2 ± 0.59	63.74 ± 0.56	24.19 ± 0.35	5.02 ± 0.17	11.33 ± 0.24	5.45 ± 0.16
1400	48.83 ± 0.17	48.61 ± 0.17	42.96 ± 0.16	16.62 ± 0.1	3.72 ± 0.052	7.61 ± 0.07	3.68 ± 0.046
1500	33.13 ± 0.12	33.02 ± 0.12	29.25 ± 0.11	11.31 ± 0.07	2.67 ± 0.036	5.08 ± 0.047	2.44 ± 0.031
1600	22.81 ± 0.08	22.75 ± 0.08	20.16 ± 0.075	7.74 ± 0.048	1.93 ± 0.025	3.48 ± 0.032	1.53 ± 0.02
1800	11.2 ± 0.1	11.18 ± 0.1	9.93 ± 0.094	3.71 ± 0.059	1.1 ± 0.034	1.6 ± 0.038	0.6 ± 0.022
2000	5.72 ± 0.021	5.71 ± 0.021	5.07 ± 0.019	1.83 ± 0.012	0.6 ± 0.0072	0.76 ± 0.0076	0.25 ± 0.0041
2250	2.61 ± 0.0088	2.61 ± 0.0088	2.32 ± 0.0083	0.78 ± 0.005	0.31 ± 0.0032	0.3 ± 0.003	0.078 ± 0.0014
2500	1.24 ± 0.0054	1.24 ± 0.0054	1.11 ± 0.0051	0.33 ± 0.0028	0.16 ± 0.002	0.11 ± 0.0016	0.021 ± 0.00066
2750	0.6 ± 0.0026	0.6 ± 0.0026	0.54 ± 0.0025	0.14 ± 0.0013	0.081 ± 0.00099	0.038 ± 0.00065	0.0055 ± 0.00024
3000	0.3 ± 0.0011	0.3 ± 0.0011	0.27 ± 0.0011	0.058 ± 0.00051	0.039 ± 0.00041	0.013 ± 0.00023	0.0016 ± 8e-05

Table 5.4: The selection efficiency for $G_{KK}^* \rightarrow hh \rightarrow b\bar{b}b\bar{b}$ events ($c = 2.0$) at each stage of the event selection. Uncertainties are the MC stat uncertainty only.

Resonance Mass [GeV]	Mini-ntuple Skimming	2 large-R jets	$\Delta\eta$	Xhh < 1.6	2bs SR	3b SR	4b SR
500	3705.15 ± 40.86	3479.44 ± 39.59	2325.18 ± 32.37	568.04 ± 16.17	122.56 ± 7.76	253.49 ± 10.78	100.7 ± 6.53
600	2549.14 ± 22.55	2374.01 ± 21.76	1591.92 ± 17.82	396.96 ± 9.03	89.01 ± 4.46	178.63 ± 6.05	74.31 ± 3.71
700	1928.4 ± 13.57	1782.85 ± 13.04	1183.86 ± 10.63	320.53 ± 5.62	71.38 ± 2.76	148.41 ± 3.81	59.31 ± 2.31
800	1595.14 ± 8.82	1457.71 ± 8.43	958.89 ± 6.84	268.75 ± 3.67	64.14 ± 1.86	123.48 ± 2.47	49.43 ± 1.51
900	1264.78 ± 5.77	1179.88 ± 5.58	819.75 ± 4.65	251.29 ± 2.61	55.63 ± 1.27	119.44 ± 1.79	48.72 ± 1.11
1000	891.0 ± 3.66	856.95 ± 3.59	662.54 ± 3.15	219.04 ± 1.84	49.45 ± 0.91	104.31 ± 1.26	42.97 ± 0.78
1100	595.58 ± 2.98	581.72 ± 2.95	481.67 ± 2.68	167.96 ± 1.61	37.64 ± 0.79	78.28 ± 1.09	34.59 ± 0.7
1200	390.84 ± 1.69	385.41 ± 1.68	330.23 ± 1.55	118.0 ± 0.94	26.23 ± 0.46	54.18 ± 0.64	25.34 ± 0.42
1300	257.66 ± 0.94	255.35 ± 0.94	222.37 ± 0.88	82.11 ± 0.54	19.04 ± 0.27	37.8 ± 0.37	16.99 ± 0.23
1400	172.09 ± 0.72	171.02 ± 0.71	150.22 ± 0.67	56.23 ± 0.42	13.6 ± 0.22	25.36 ± 0.28	11.78 ± 0.18
1500	116.25 ± 0.41	115.72 ± 0.41	101.92 ± 0.39	38.5 ± 0.24	9.94 ± 0.13	17.04 ± 0.16	7.64 ± 0.1
1600	80.09 ± 0.28	79.82 ± 0.28	70.48 ± 0.26	26.24 ± 0.16	7.01 ± 0.09	11.62 ± 0.11	4.92 ± 0.067
1800	38.99 ± 0.14	38.9 ± 0.14	34.39 ± 0.13	12.65 ± 0.081	3.82 ± 0.047	5.46 ± 0.053	2.02 ± 0.03
2000	19.94 ± 0.088	19.91 ± 0.088	17.68 ± 0.083	6.17 ± 0.05	2.15 ± 0.031	2.52 ± 0.032	0.85 ± 0.017
2250	9.02 ± 0.031	9.01 ± 0.031	7.99 ± 0.029	2.62 ± 0.017	1.03 ± 0.011	1.02 ± 0.01	0.28 ± 0.0051
2500	4.28 ± 0.016	4.28 ± 0.016	3.8 ± 0.015	1.13 ± 0.0083	0.52 ± 0.0058	0.4 ± 0.0048	0.098 ± 0.0022
3000	1.07 ± 0.004	1.07 ± 0.004	0.96 ± 0.0038	0.23 ± 0.0019	0.13 ± 0.0015	0.062 ± 0.00097	0.013 ± 0.00043

Table 5.5: The selection efficiency for $H \rightarrow hh \rightarrow b\bar{b}b\bar{b}$ events at each stage of the event selection.

Resonance Mass [GeV]	Mini-ntuple Skimming	2 large-R jets	$\Delta\eta$	Xhh < 1.6	2bs SR	3b SR	4b SR
500	1557.94 ± 136.12	1022.77 ± 110.29	95.14 ± 33.64	11.69 ± 11.69	0 ± 0	11.69 ± 11.69	0 ± 0
600	3289.78 ± 123.99	2542.11 ± 108.99	485.99 ± 47.66	54.55 ± 15.77	18.73 ± 9.39	9.17 ± 6.49	0 ± 0
700	4655.21 ± 94.59	3855.64 ± 86.09	1237.8 ± 48.78	142.42 ± 17.03	28.55 ± 7.74	52.6 ± 10.75	7.69 ± 3.85
800	7506.31 ± 81.79	6020.56 ± 73.25	2150.64 ± 43.78	320.63 ± 17.02	67.63 ± 7.83	139.97 ± 11.23	47.57 ± 6.75
900	9732.89 ± 61.17	8400.91 ± 56.83	3574.63 ± 37.07	866.13 ± 17.76	188.71 ± 8.71	377.92 ± 12.12	127.7 ± 6.99
1000	7516.07 ± 37.72	7033.18 ± 36.49	4496.85 ± 29.18	1351.1 ± 16.2	303.71 ± 7.88	650.89 ± 11.19	234.2 ± 6.57
1100	4731.39 ± 21.54	4563.4 ± 21.15	3485.58 ± 18.49	1135.18 ± 10.7	251.77 ± 5.18	539.51 ± 7.36	215.39 ± 4.5
1200	2853.51 ± 12.23	2782.42 ± 12.07	2253.95 ± 10.87	786.92 ± 6.53	175.53 ± 3.21	366.01 ± 4.44	158.29 ± 2.8
1300	1700.83 ± 7.01	1668.05 ± 6.94	1362.91 ± 6.27	494.36 ± 3.84	107.0 ± 1.86	224.19 ± 2.58	107.55 ± 1.7
1400	1016.14 ± 4.03	999.98 ± 4.0	802.44 ± 3.59	296.46 ± 2.22	65.49 ± 1.1	133.86 ± 1.49	65.58 ± 0.99
1500	621.34 ± 2.41	613.46 ± 2.39	484.92 ± 2.13	179.29 ± 1.32	42.75 ± 0.68	79.32 ± 0.88	36.77 ± 0.56
1600	386.3 ± 1.46	382.44 ± 1.46	297.63 ± 1.28	109.99 ± 0.8	27.68 ± 0.42	49.3 ± 0.53	20.92 ± 0.32
1800	154.8 ± 0.58	153.5 ± 0.57	116.52 ± 0.5	42.24 ± 0.31	12.41 ± 0.18	18.2 ± 0.2	6.66 ± 0.11
2000	65.4 ± 0.24	65.02 ± 0.24	48.57 ± 0.2	16.89 ± 0.12	5.64 ± 0.076	7.01 ± 0.079	2.18 ± 0.041
2250	23.84 ± 0.085	23.73 ± 0.085	17.44 ± 0.073	5.57 ± 0.042	2.25 ± 0.028	2.11 ± 0.025	0.52 ± 0.012
2500	9.2 ± 0.032	9.17 ± 0.032	6.72 ± 0.028	1.9 ± 0.015	0.92 ± 0.011	0.64 ± 0.0086	0.11 ± 0.0034
2750	3.73 ± 0.013	3.73 ± 0.013	2.71 ± 0.011	0.63 ± 0.0054	0.37 ± 0.0042	0.17 ± 0.0027	0.021 ± 0.00093
3000	1.59 ± 0.0054	1.59 ± 0.0054	1.15 ± 0.0046	0.22 ± 0.0021	0.15 ± 0.0017	0.044 ± 0.0009	0.0038 ± 0.00025

*Even in the darkest night. Stars and angels still shine
bright.*

6

Background Estimation

6.1 OVERVIEW

The invariant mass of the two-Higgs-boson-candidate system, m_{2J} , is used as the final discriminant between Higgs boson pair production and SM backgrounds. Multi-jet (QCD) is the dominant background. About 40% of the total QCD events are $gg \rightarrow b\bar{b}b\bar{b}$, and the rest 60% are $gg \rightarrow c\bar{c}c\bar{c}$ or $gg \rightarrow q\bar{q}q\bar{q}$ where the quark-jets fake multiple b -jets. There are neither accurate nor high-statistics MC samples with three or four b -tagged track jets contained in two high- p_T large- R jets. A data-driven method is used for estimating both the yield and kinematic distribution of the QCD events. For $t\bar{t}$ backgrounds, MC samples are available, which provide $t\bar{t}$ kinematic distributions. The $t\bar{t}$ yield is also estimated using the same data-driven method to avoid mis-modeling in the

MC. The Z +jets background is small, and it is estimated by the Z +heavy flavor jets MC. The SM $ZZ \rightarrow b\bar{b}b\bar{b}$ has been estimated to be completely negligible using a MC based analysis. For the three signal channels $4b/3b/2bs$, the fraction of expected backgrounds are:

- $4b$: $\underline{\text{QCD}} \sim 95\%$, $\bar{t}\bar{t} \sim 5\%$, $Z+\text{jets} < 1\%$.
- $3b$: $\underline{\text{QCD}} \sim 90\%$, $\bar{t}\bar{t} \sim 10\%$, $Z+\text{jets} < 1\%$.
- $2bs$: $\underline{\text{QCD}} \sim 80\%$, $\bar{t}\bar{t} \sim 20\%$, $Z+\text{jets} < 1\%$.

All of the kinematic distributions of the $\underline{\text{QCD}}$ background are estimated from low signal yield data b -tag channels. These channels use the signal region selection, with the exception of having a different number of b -tagged track jets. The differences in kinematic distributions between the fewer b -tagged and n -tagged signal channels are corrected by reweighting the fewer b -tagged samples.

The fewer b -tagged channels estimate the shapes of the expected background, but do not estimate the total yield. The *sideband region* (SB), with the same number of b -tags as the signal regions but a cut on $m_{\text{J}}^{\text{lead}} - m_{\text{J}}^{\text{subl}}$ different from the X_{bb} cut, is used to estimate the yield. A third region, called the *control region* (CR), is used to validate the background estimations. The sideband and control regions are optimized to accurately estimate the rate of $\underline{\text{QCD}}$ and $\bar{t}\bar{t}$ backgrounds.

The definitions of sideband region and control region are introduced in section 6.2. The $\underline{\text{QCD}}$ and $\bar{t}\bar{t}$ background shape templates are introduced in section 6.3 and section 6.4. The normalization estimation for $\underline{\text{QCD}}$ and $\bar{t}\bar{t}$ is introduced in section 6.5. The reweighting procedure is explained in section 6.6. The sideband region and control region distributions are shown in section 6.7 and section 6.8. The signal region prediction rescaling and smoothing are discussed in section 6.9. The yields are listed section 6.10.

6.2 DEFINITION OF THE SIDEBAND AND CONTROL REGIONS

A circular variable R_{hh} is defined in the 2D $m_J^{\text{lead}}\text{-}m_J^{\text{subl}}$ mass plane. It has the same central values as X_{hh} , but without resolution terms in the denominators:

$$R_{hh} = \sqrt{(m_J^{\text{lead}} - 124 \text{ GeV})^2 + (m_J^{\text{subl}} - 115 \text{ GeV})^2} \quad (6.1)$$

Similarly, R_{hh}^{high} , the circular region with the previous central values shifted up by 10 GeV, is defined as:

$$R_{hh}^{\text{high}} = \sqrt{(m_J^{\text{lead}} - 134 \text{ GeV})^2 + (m_J^{\text{subl}} - 125 \text{ GeV})^2} \quad (6.2)$$

The definitions of the sideband region, control region, and signal region in the 2D $m_J^{\text{lead}}\text{-}m_J^{\text{subl}}$ plane are listed in Table 6.1. These regions are shown in Figure 6.1. This Figure also shows that the QCD background rate is decreasing from the low $m_J^{\text{lead}}\text{-}m_J^{\text{subl}}$ mass region to high $m_J^{\text{lead}}\text{-}m_J^{\text{subl}}$ mass region in the 2D plane. The $t\bar{t}$ events are also distinguishable as the vertical cyan band where $m_J^{\text{lead}} \sim 173 \text{ GeV}$.

Table 6.1: Definitions of the signal region, the control region, and the sideband region.

Region	Definition
signal region (SR)	$X_{hh} < 1.6$
control region (CR)	$R_{hh} < 33 \text{ GeV}$ and $X_{hh} > 1.6$
sideband region (SB)	$33 \text{ GeV} < R_{hh}$ and $R_{hh}^{\text{high}} < 58 \text{ GeV}$

The control region is as close to the signal region as possible. The ring shape around the SR allows a good test for the background predictions with different $m_J^{\text{lead}}\text{-}m_J^{\text{subl}}$ combinations, and avoids too few or too many $t\bar{t}$ events. The current control region gives $N_{CR} \sim 2N_{SR}$, which contains good statistics and does not affect the sideband region design.

The sideband region must be a reasonable approximation for the QCD events contained in the control region and signal region. It is therefore chosen as the ring outside the control region. The shift upwards in the center of R_{hh}^{high} helps to contain more $t\bar{t}$ events in the normalization estimates. A larger SB will potentially increase the kinematic differences between different QCD processes in CR/SR and SB. Different $m_J^{\text{lead}} - m_J^{\text{subl}}$ reflects of different fractions of $g \rightarrow b\bar{b}$ and $g \rightarrow c\bar{c}/q\bar{q}$ events. This kinematic bias should be reduced as much as possible. However, a smaller SB will introduce larger statistical uncertainties in the normalization estimation. This is a bias-variance trade off. The current design gives roughly $N_{\text{SB}} \sim 4N_{\text{SR}}$ and $N_{\text{SB}} \sim 2N_{\text{CR}}$, which provides a good balance between the bias and variance in the background estimation.

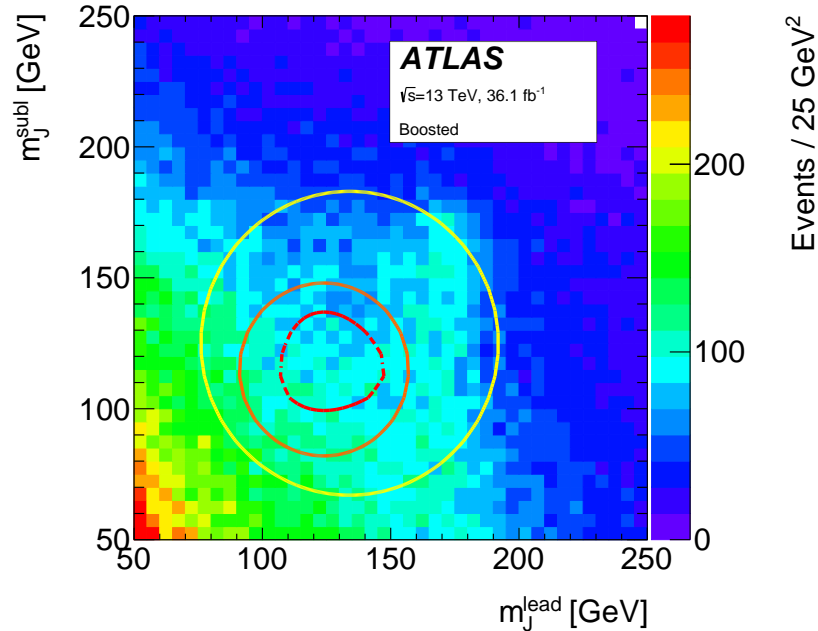


Figure 6.1: The m_J^{lead} vs m_J^{subl} distribution of data in $2bs$ region. The signal region is the area surrounded by the inner (red) dashed contour line, centered on $(m_J^{\text{lead}} = 124 \text{ GeV}, m_J^{\text{subl}} = 115 \text{ GeV})$. The control region is the area between the signal region and the intermediate (orange) contour line. The sideband region is the area between the control region and the outer (yellow) contour line.

The fraction between the expected events in different $m_J^{\text{lead}} - m_J^{\text{subl}}$ regions and the total number of events as a function of G_{KK}^* resonance mass is shown in Figure 6.2. For the $4b$, $3b$, and $2bs$ channels, there is no significant signal contamination in the control and sideband regions.

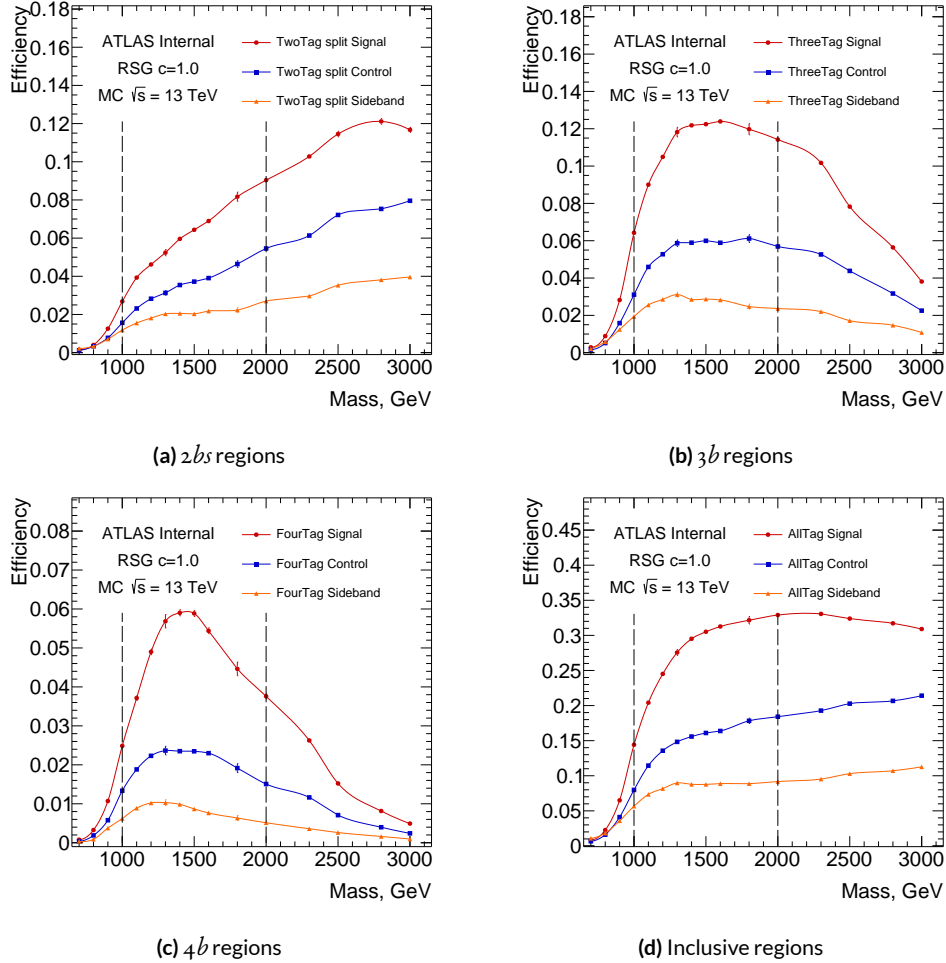


Figure 6.2: Detailed signal efficiency in different signal/control/sideband regions in n -tagged channels and the inclusive b -tagged channel, which includes $2b$, $1b$, and $0b$ as well, (bottom right) as a function of G_{KK}^* resonance mass for selection cuts. The efficiencies are relative to the total number of events in the preselection.

Table 6.2: Definitions of the QCD background estimation sample for $4b/3b/2bs$. $n_b^{lead/subJ}$ stands for the number of b -tagged track jets in the leading/subleading large- R jet.

Region ($n_b^{leadJ} - n_b^{subJ}$)	QCD background sample ($n_b^{leadJ} - n_b^{subJ}$)
$4b$ (2-2)	$2b$ data (2-0 or 0-2)
$3b$ (2-1 or 1-2)	$2b$ data (2-0 or 0-2)
$2bs$ (1-1)	$1b$ data (1-0 or 0-1)

6.3 QCD MULTI-JET

The QCD multi-jet background prediction relies on finding b -tagged channels that have events similar to signal channel event properties. These channels are defined to be identical to the signal channels except with a lower required number of b -tagged track jets associated with the large- R jets. They are orthogonal to the n -tagged channels with no overlapping events, as listed in Table 6.2. They are assumed to be all background, and the signal yield in these channels are negligible, as shown in Figure 5.11a. Detailed selection requirements and details are listed:

- For the $2bs$ category, $1b$ data events, where one large- R jet has one and only one b -tagged track jets, and the other large- R jet has no b -tagged track jet, is used for modeling.
- For the $3b$ and $4b$ categories, $2b$ data events, where one large- R jet has two b -tagged track jets, and the other large- R jet has no b -tagged track jet, is used for modeling. The $2b$ sample is further split into 80% – 20% parts, where each is used separately for $3b$ and $4b$ background estimations. This ensures the shape estimations of $3b$ and $4b$ QCD estimates are uncorrelated.

The $2b$ and $2bs$ channels are orthogonal channels without any overlapping events. The $1b$ -tagged channel also requires that both large- R jets are associated with at least one track jet. Similarly, the $2b$ -tagged channel requires that one large- R jet has at least one track jet and the other one has at least two track jets. Specifically for the $4b$ background modeling, each large- R jet must have at least two track jets. This prevents biases in the m_{2J} distribution from the number of associated track jets.

The MC predicted $t\bar{t}$ and $Z+jets$ events in the $1b/2b$ channels are subtracted from the data distributions to produce the QCD estimation. Therefore, the number of QCD events, N_{qcd} , is estimated in Equation 6.3.

$$N_{\text{qcd}} = N_{\text{data}} - N_{t\bar{t}} - N_{Z+jets} \quad (6.3)$$

The resolved veto imposed impacts the $4b$ background estimation. To account for this effect, the 20% $2b$ data events used for $4b$ background estimation are excluded. The excluded events must have at least two small- R jets that are b -tagged (passing the resolved 70% b -tagging working point), and in the case where the two other non b -tagged resolved jets can make a Higgs candidate, events must also pass the $X_{bh-\text{resolved}} < 1.6$ cut. This ensures that a similar sculpting effect from the resolved veto is reflected in the background estimation in the $4b$ signal region. This reduces the estimated number of events in the signal region by 10%.

Given the $1b/2b$ QCD background samples, the normalization estimation of the $4b/3b/2bs$ QCD background is determined in the sideband by fitting the m_j^{lead} distribution simultaneously with QCD and $t\bar{t}$ background templates, as described in section 6.5. There are kinematic differences between the $1b/2b$ channels and the $4b/3b/2bs$ channels. A kinematic reweighting is applied to correct for such differences, as described in Section 6.6.

6.4 $t\bar{t}$

The $t\bar{t}$ events in the signal region decay to $bW^+/\bar{b}W^-$ and the W further decays into two quarks. The leptonically decaying W s are rare due to the large- R jet p_T cut. The $t\bar{t}$ MC is first scaled by the total luminosity times the cross-section. The boosted event selections are then applied. The estimated $t\bar{t}$ kinematic distributions come from MC simulations. To account for possible mis-modeling

in the MC, a normalization scaling factor is derived from a fit to data in the sideband region, as described in section 6.5.

For $4b$ and $3b$ signal regions, there are not sufficient $t\bar{t}$ MC statistics for high m_{2J} . Instead, the $2bs t\bar{t}$ MC shapes are used. It is rescaled to the $4b$ and $3b$ $t\bar{t}$ MC yields. This reduces the statistical uncertainties for $4b$ and $3b$ $t\bar{t}$ at high m_{2J} . A comparison between the $4b/3b/2bs$ shapes for the m_{2J} distributions in the signal regions is shown in Figure 6.3. The shapes are compatible, with the $4b$ having much larger statistical uncertainties. Differences between these distributions will be used as a systematic, as described in chapter 7. Since the same $t\bar{t}$ distribution is used for the $4b/3b/2bs$ SR predictions, the $t\bar{t}$ shape systematics are considered correlated in the final results.

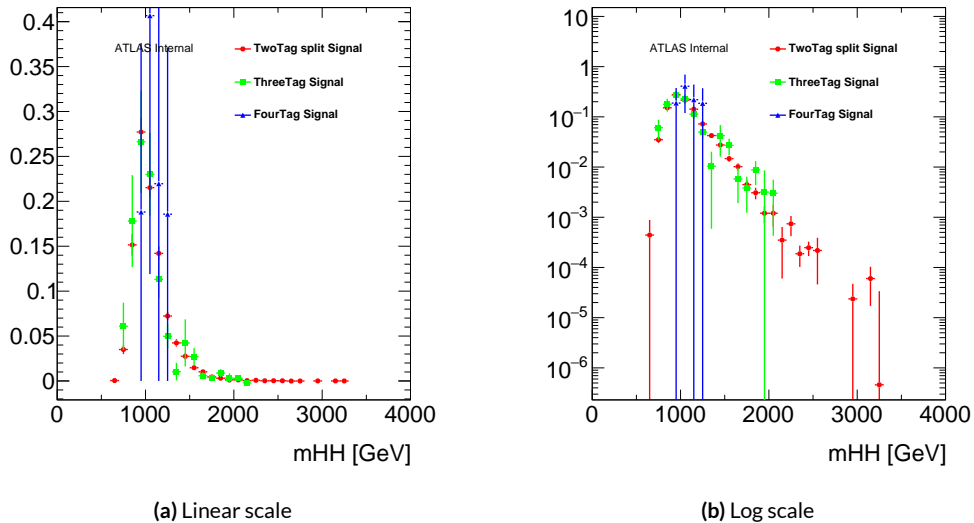


Figure 6.3: Normalized $2bs$, $3b$, and $4b$ $t\bar{t}$ MC m_{2J} (m_{HH}) distribution in the signal region. The uncertainties are statistical.

6.5 FITTING PROCEDURE FOR QCD AND $t\bar{t}$ NORMALIZATION

The number of $4b/3b/2bs$ background events in a given region R (SB / CR / SR) is shown in Equations 6.4, 6.5 and 6.6:

$$N_{\text{bkg}}^{4b-\text{R}} = \mu_{\text{qcd}}^{4b} N_{\text{qcd}}^{2b-\text{R}} + \alpha_{t\bar{t}}^{4b} N_{t\bar{t}}^{4b-\text{R}} + N_{Z+jets}^{4b-\text{R}}; \quad \mu_{\text{qcd}}^{4b} \sim \frac{N_{\text{qcd}}^{4b-\text{SB}}}{N_{\text{qcd}}^{2b-\text{SB}}} \quad (6.4)$$

$$N_{\text{bkg}}^{3b-\text{R}} = \mu_{\text{qcd}}^{3b-\text{R}} N_{\text{qcd}}^{2b-\text{R}} + \alpha_{t\bar{t}}^{3b} N_{t\bar{t}}^{3b-\text{R}} + N_{Z+jets}^{3b-\text{R}}; \quad \mu_{\text{qcd}}^{3b} \sim \frac{N_{\text{qcd}}^{3b-\text{SB}}}{N_{\text{qcd}}^{2b-\text{SB}}} \quad (6.5)$$

$$N_{\text{bkg}}^{2bs-\text{R}} = \mu_{\text{qcd}}^{2bs-\text{R}} N_{\text{qcd}}^{2b-\text{R}} + \alpha_{t\bar{t}}^{2bs} N_{t\bar{t}}^{2bs-\text{R}} + N_{Z+jets}^{2bs-\text{R}}; \quad \mu_{\text{qcd}}^{2bs} \sim \frac{N_{\text{qcd}}^{2bs-\text{SB}}}{N_{\text{qcd}}^{2b-\text{SB}}} \quad (6.6)$$

μ_{qcd} is essentially an extrapolation factor to account of the fewer number of events passing the higher number of b -tagged track jet selection. μ_{qcd} is roughly a constant over SB/CR/SR m_j^{lead} - m_j^{subl} regions. Validation of this assumption can be found in Appendix D. $\alpha_{t\bar{t}}$ is a scale factor, correcting the $t\bar{t}$ MC yield. μ_{qcd} and $\alpha_{t\bar{t}}$ are derived in the sideband region. They are used as multiplicative constants in other regions of the mass plane (i.e. the control region or the signal region).

A binned maximum likelihood fit is used to find the values of μ_{qcd} and $\alpha_{t\bar{t}}$, as well as the correlation between them. These scaling parameters are determined independently using the same procedure in the $4b/3b/2bs$ sideband regions. Due to the $p_T > 450$ GeV cut imposed on the leading large- R jet, the top quark decay products are fully contained inside the leading large- R jet in $t\bar{t}$ events. The m_j^{lead} from $t\bar{t}$ events has a clean peak around $m_{top} \sim 175$ GeV in the sideband region. It has the best separation between QCD and $t\bar{t}$ shapes. Therefore, the fit is performed on the m_j^{lead} spectrum in the sideband region.

Figure 6.4 shows the post-fit spectrum of m_j^{lead} in the n -tagged sideband regions. The m_j^{lead} shapes in data are well modeled by the predicted backgrounds. The sharp turn-on at $m_j^{\text{lead}} \sim 75$ GeV and

sharp fall around 180 GeV are due to the sideband region mass cut on m_J^{lead} . The dip in the m_J^{lead} distribution at ~ 125 GeV is because the sideband region doesn't contain events from the control and signal regions. The fitting errors on μ_{qcd} and $\alpha_{t\bar{t}}$ are applied as systematic uncertainties taking into account their correlation.

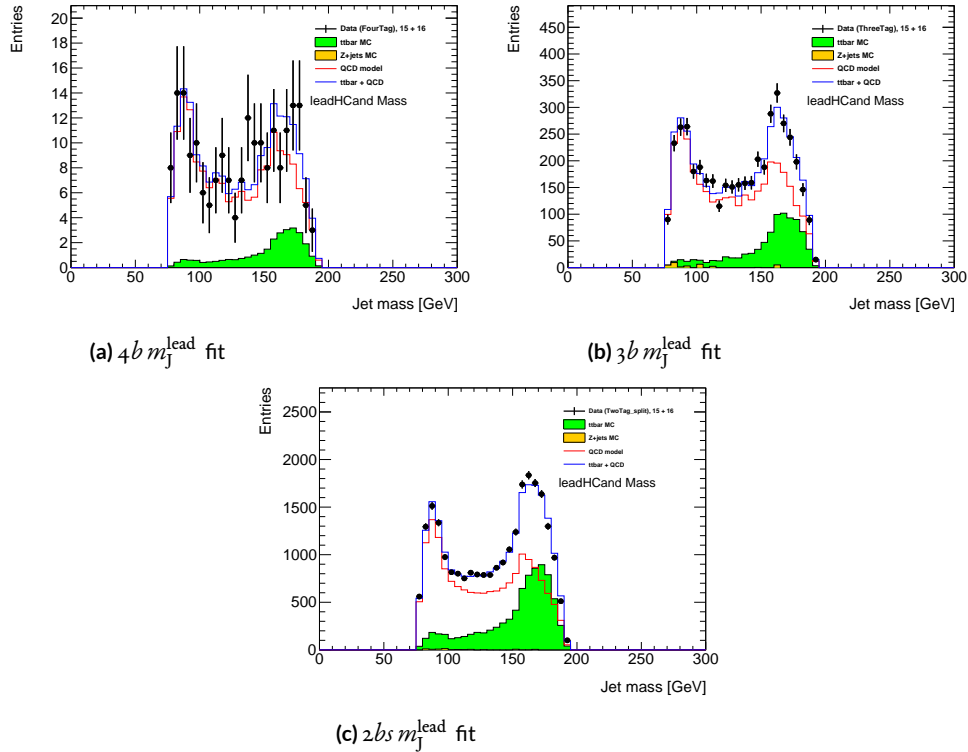


Figure 6.4: Simultaneous fit of μ_{qcd} and $\alpha_{t\bar{t}}$ in $4b$, $3b$ and $2bs$ sideband regions using the leading large- R jet mass.

The $t\bar{t}$ MC sample normalization is further corrected from the fitted $\alpha_{t\bar{t}}$. At first, $\alpha_{t\bar{t}}$ is assumed to be 1. Once the first fit is done, the QCD background is re-estimated using the updated $2bs$ $\alpha_{t\bar{t}}$ value, which has the smallest uncertainty. Then, the fit is repeated until the change in $\alpha_{t\bar{t}}$ is less than 0.01. This iterative procedure helps correct the $\alpha_{t\bar{t}}$ bias in the data-driven QCD template.

The values of μ_{qcd} and $\alpha_{t\bar{t}}$ estimated by the fits in the $4b/3b/2bs$ sideband regions can be found in Table 6.3, along with the correlation $\xi(\mu_{\text{qcd}}, \alpha_{t\bar{t}}) = \frac{\text{Cov}(\mu_{\text{qcd}}, \alpha_{t\bar{t}})}{\sigma_{\mu_{\text{qcd}}} \sigma_{\alpha_{t\bar{t}}}}$. μ_{qcd} and $\alpha_{t\bar{t}}$ are approximately 70% negatively correlated, due to the nature of the two components fit and the fixed normalization. This negative correlation leads to a smaller total normalization uncertainty.

Table 6.3: Background scaling parameters (μ_{qcd} and $\alpha_{t\bar{t}}$) estimated from fits to the m_j^{lead} distributions in $4b/3b/2bs$ sideband regions pre-reweighting. $\xi(\mu_{\text{qcd}}, \alpha_{t\bar{t}}) = \frac{\text{Cov}(\mu_{\text{qcd}}, \alpha_{t\bar{t}})}{\sigma_{\mu_{\text{qcd}}} \sigma_{\alpha_{t\bar{t}}}}$.

Sample	μ_{qcd}	$\alpha_{t\bar{t}}$	$\xi(\mu_{\text{qcd}}, \alpha_{t\bar{t}})$
FourTag	0.033987 ± 0.0043057	1.01697 ± 0.58642	-0.76397
ThreeTag	0.16247 ± 0.0041713	0.86508 ± 0.069019	-0.6778
TwoTag split	0.066713 ± 0.00091137	1.03747 ± 0.026199	-0.74785

6.6 QCD REWEIGHTING

Reweighting gives the QCD background sample events weights different from one. This results in a different distribution in all QCD kinematic distributions. The weights are derived from kinematic differences between a Higgs candidate that has b -tags and a Higgs candidate that doesn't have b -tags. The reweighting variables are the track jet p_{T} s and large- R jet p_{T} . More supporting plots are shown in Appendix E.

It is important to model the QCD background as well as possible in all regions of the phase space. Using the $1/2b$ channels to model the $2bs/3b/4b$ channels can introduce discrepancies in the modeling of the estimated QCD background versus the data. These discrepancies arise from the non-trivial effect that b -tagging requirements can have in sculpting the track jet p_{T} and η distributions.

The reweighting method is motivated by Figure 6.5. In the plots, ob , $1b$ and $2bs$ kinematic distributions in data are compared. Except $2bs$ data only contains the sideband region, ob and $1b$ are inclusive of sideband, control, and signal regions. The $1b$ sample is further split into four subcategories

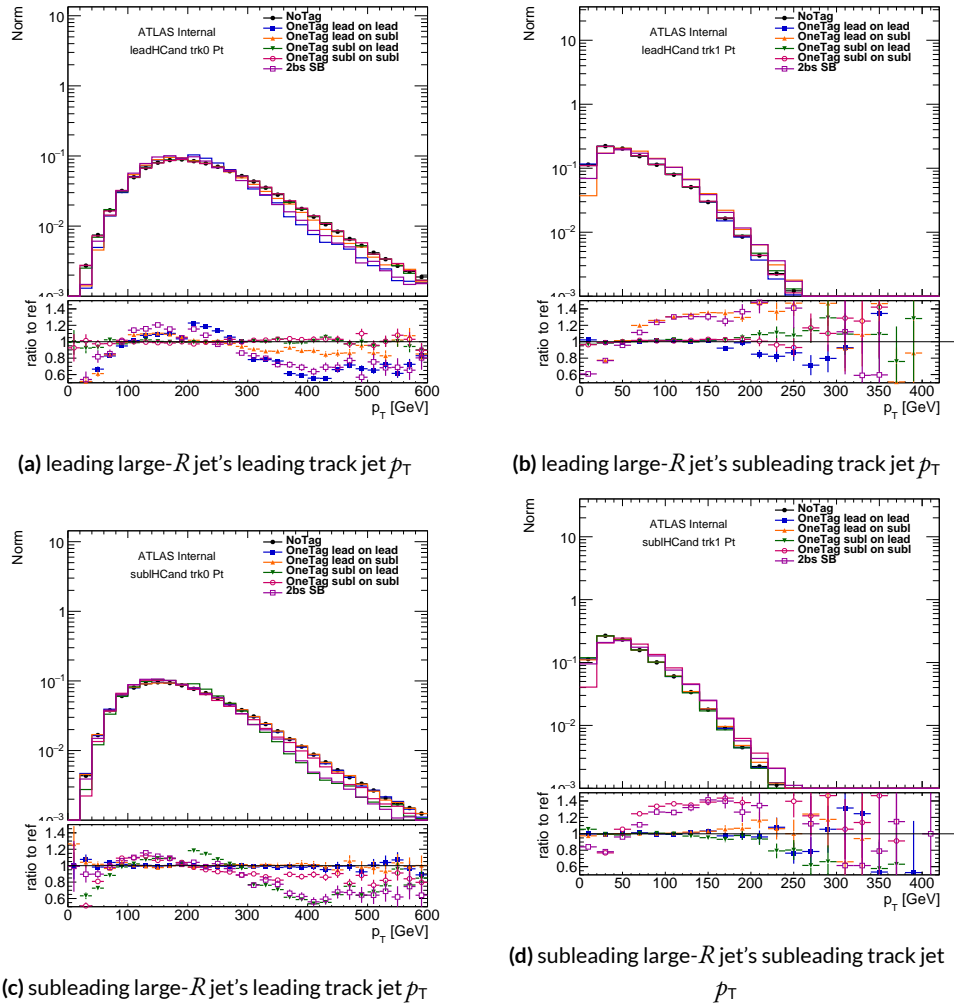


Figure 6.5: Comparison of track jet p_T distributions in different b -tag channels. Data are shown in the plots. They contain inclusive SB/CR/SR regions for $0b$ and $1b$, and only the SB region for $2bs$. At the bottom of the plots, all the ratios are taken with respect to the $0b$ tagged distribution.

listed in Table 6.4, depending on which track jet gets b tagged. The figure shows that $2bs$ channel has very similar track jet p_T distributions to the $1b$ channel with a b -tagged track jet. It also shows that in the $1b$ channel, the track jet p_T distribution in the non b -tagged Higgs candidate behaves like the $0b$ channel track jet p_T distribution.

Table 6.4: Definitions of the $1b$ subsamples.

Channel	$Nb_{leadtrkj}^{leadJ}$	$Nb_{subltrkj}^{leadJ}$	$Nb_{leadtrkj}^{sublJ}$	$Nb_{subltrkj}^{sublJ}$
“OneTag lead on lead”	I	O	O	O
“OneTag lead on subl”	O	I	O	O
“OneTag subl on lead”	O	O	I	O
“OneTag subl on subl”	O	O	O	I

This reweighting technique is applied to the $1/2b$ data only. The reweighting procedure is the same for the $4b$, $3b$, and $2bs$ channels. The $2b$ QCD sample is already split into orthogonal parts for $3b$ and $4b$ estimations, as described in section 6.3.

For $2bs$, the $1b$ non- b -tagged Higgs candidate is reweighted to be like a $1b$ -tagged Higgs candidate; for $3b$, the $2b$ non- b -tagged Higgs candidate is reweighted to be like a $1b$ -tagged Higgs candidate; for $4b$, the $2b$ non- b -tagged Higgs candidate is reweighted to be like a $2b$ -tagged Higgs candidate. For each category, the events are split into two orthogonal subgroups, based on whether leading/subleading Higgs candidate is b -tagged. Each event gets a weight, such that the reweighted untagged Higgs candidate’s distributions agree with the corresponding b -tagged Higgs candidate’s.

One natural choice of a reweighting variable is the p_T of the track jets in the event, since the b -tagging efficiency and the b -tagging fake rate have a strong track jet p_T dependence. Also, large- R jet p_T is reweighted to account for the difference from light/ c/b quarks composition in QCD events at different energy scales. The three reweighted variables are the leading large- R jet p_T , leading large- R jet leading track jet p_T , and subleading large- R jet leading track jet p_T .

The each reweighting iteration is described below:

- Subtract $1/2b t\bar{t}$ and $Z+jets$ samples in the SB + CR + SR regions from the $1/2b$ tag data in the SB + CR + SR regions to get the $1/2b$ QCD inclusive estimate. Weights from all previous iterations, if applicable, are all applied.

- Separate the $1/2b$ sample into two parts: (A) has the b -tagged Higgs as the leading p_T Higgs candidate, and (B) has the b -tagged Higgs as the subleading p_T Higgs candidate.
- For each variable, i.e. the large- R jet p_T : normalize sample A to sample B's total number of events, take the ratio of sample A's distribution over sample B's distribution, and fit the ratio with a smooth spline function (TSpline3). The binning of the distribution needs to be carefully chosen such that each bin has enough statistics to calculate a meaningful ratio.
- Use this spline function to extract reweighting values w_e for each variable that is considered. Then, the difference from one is scaled by 0.75 to get a new weight w . So $w = (w_e - 1) * 0.75$. This accounts for over correlation by the spline and accelerates convergence.
- For each event, all the three weights from three variables are multiplied together to get a data event weight. Another constraint is applied, such that each event's total reweighting value is constrained to be within a 0.05 to 10 range. This avoids over corrections.

Examples for the reweighting procedure are shown in Appendix E. The weights are almost converging to one after three iterations. To ensure all kinematics regions are covered, a total of ten iterations are used to stabilize the reweighting. The reweighting value for each variable is also constrained to be within a -30% to $+40\%$ range compared to one, to avoid over corrections.

Table 6.5: Background scaling parameters (μ_{qcd} and $\alpha_{t\bar{t}}$) estimated from fits to the m_J^{lead} distributions in $4b/3b/2b$ sideband regions post reweighting. $\xi(\mu_{qcd}, \alpha_{t\bar{t}}) = \frac{\text{Cov}(\mu_{qcd}, \alpha_{t\bar{t}})}{\sigma_{\mu_{qcd}} \sigma_{\alpha_{t\bar{t}}}}$.

Sample	μ_{qcd}	$\alpha_{t\bar{t}}$	$\xi(\mu_{qcd}, \alpha_{t\bar{t}})$
FourTag	0.033167 ± 0.0042799	0.89136 ± 0.59866	-0.7846
ThreeTag	0.16256 ± 0.0043405	0.79989 ± 0.073276	-0.72029
TwoTag split	0.062726 ± 0.00057307	0.98637 ± 0.018582	-0.4698

At the end of reweighting, the μ_{qcd} and $\alpha_{t\bar{t}}$ is re-evaluated. The estimated μ_{qcd} and $\alpha_{t\bar{t}}$ values before reweighting can be found in Table 6.5. The values are statistically consistent with the values in Table 6.3.

6.7 m_{2J} IN THE SIDEBAND REGION

Figure 6.6 shows comparisons of the predicted m_{2J} background distributions to those observed in data in the sideband regions. The predicted background and observed distributions are in agreement, with no significant excess. Other sideband region distributions are shown in Appendix A.

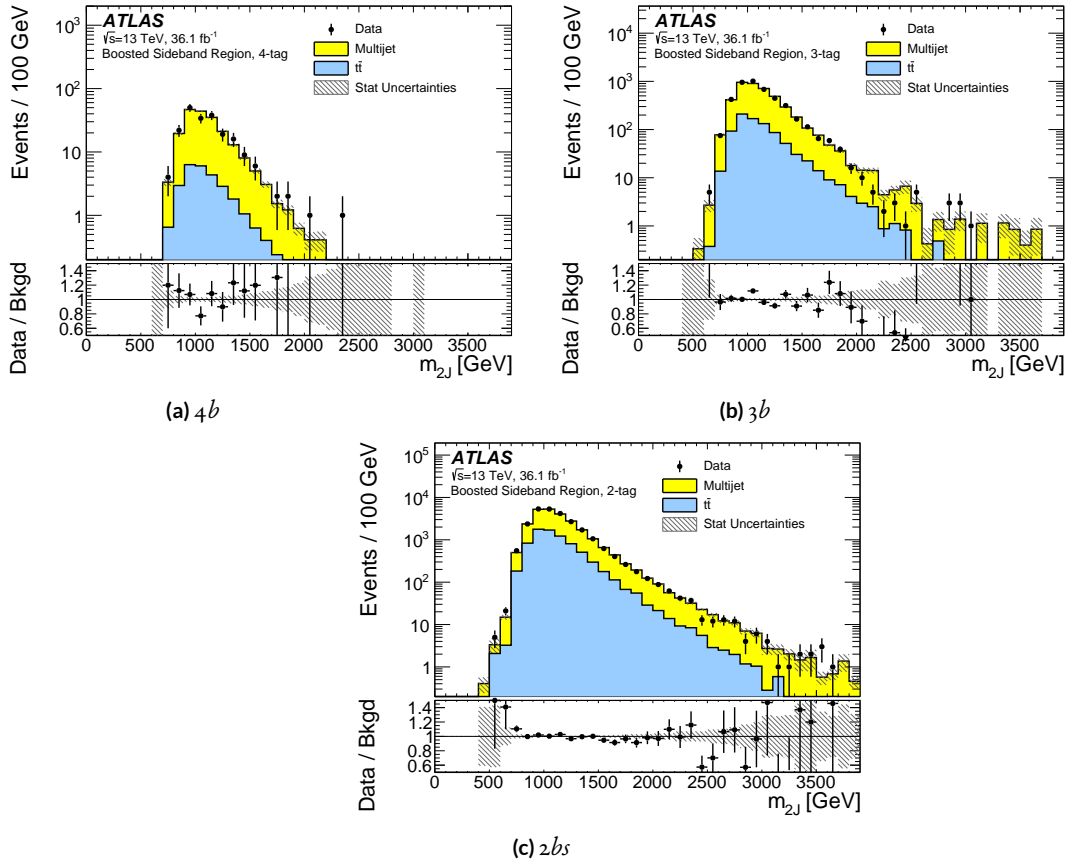


Figure 6.6: The m_{2J} distributions in the sideband region of the boosted analysis for the data and the predicted background for $4b$, $3b$, and $2bs$ channels. The data-to-background ratio (bottom panels) shows the statistical uncertainties as the gray hatched band.

6.8 m_{2J} IN THE CONTROL REGION

Figure 6.7 shows comparisons of the predicted m_{2J} background distributions to those observed in data in the control regions. The predicted background and observed distributions are in good agreement. Other control region distributions are shown in Appendix B.

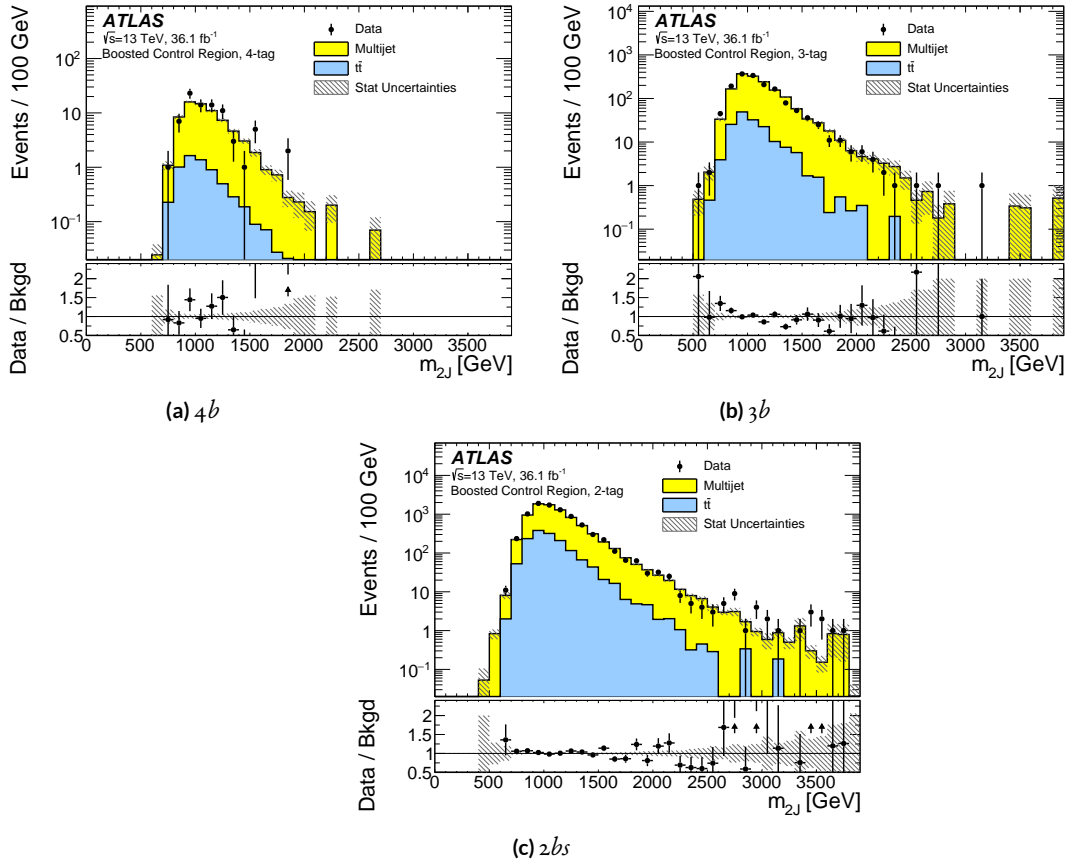


Figure 6.7: The m_{2J} distributions in the control region of the boosted analysis for the data and the predicted background for $4b$, $3b$, and $2bs$ channels. The data-to-background ratio (bottom panels) shows the statistical uncertainties as the gray hatched band.

6.9 m_{2J} RESCALE AND SMOOTHING IN THE SIGNAL REGION

The m_{2J} resolution is further improved by rescaling. In the signal region, the four-momentum of each large- R jet is multiplied by a factor m_H/m_J . From this, a scaled m_{2J} is calculated. This correction improves the jet mass and momentum resolution of each large- R jet for signal events. There is little impact on the background distribution. Using the scaled m_{2J} distribution, the expected exclusion limits are slightly better at low mass and slightly worse at high mass, with differences on the order of 10% from the nominal m_{2J} limits. The scaled m_{2J} distribution can be found in Figure 6.8.

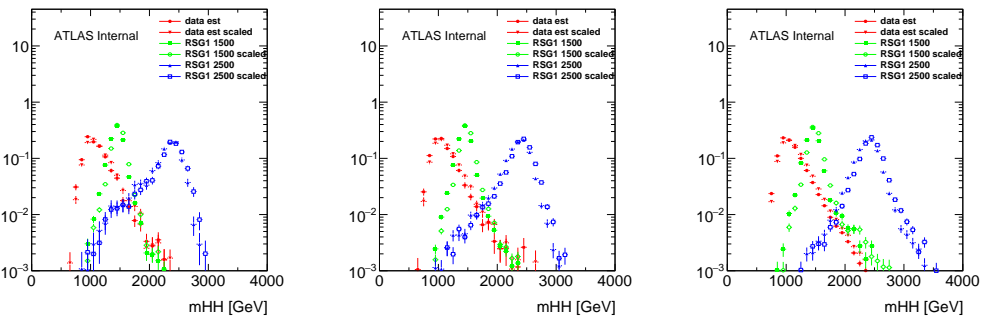


Figure 6.8: Normalized scaled m_{2J} distributions for the $4b$ (left), $3b$ (middle), and $2bs$ (right) signal regions. For comparison, the unscaled m_{2J} distributions are shown on the same plot.

Due to limited $1/2b$ statistics at high m_{2J} above 2500 GeV and the limited $t\bar{t}$ statistics above 1100 GeV, different fits are performed to smooth the m_{2J} mass distributions in the signal regions. The $4/3/2bs$ QCD and $t\bar{t}$ signal region scaled m_{2J} distributions are fitted with the following functional form:

$$y = \frac{a}{\left(\frac{m_{2J}}{\sqrt{s}}\right)^2} \left(1 - \frac{m_{2J}}{\sqrt{s}}\right)^{(b-c \log(\frac{m_{2J}}{\sqrt{s}}))} \quad (6.7)$$

where $\sqrt{s} = 13000$ GeV, the fit range is $1200 < m_{2J} < 3000$ GeV, and the three free parameters are a , b and c . The values of the estimated fit parameters in the $4b$, $3b$, and $2bs$ signal regions

can be found in Table 6.6. Figure 6.9, 6.10, and 6.11 show the smoothing fits for the QCD background and the $t\bar{t}$ background in the $4b$, $3b$, and $2bs$ signal regions. The smoothing fit statistical uncertainties are also shown on these two plots. Given that $1/2b$ channels are used for deriving the QCD shape for $4/3/2bs$ signal regions, the slope parameters (α) are similar for $4/3/2bs$ QCD backgrounds.

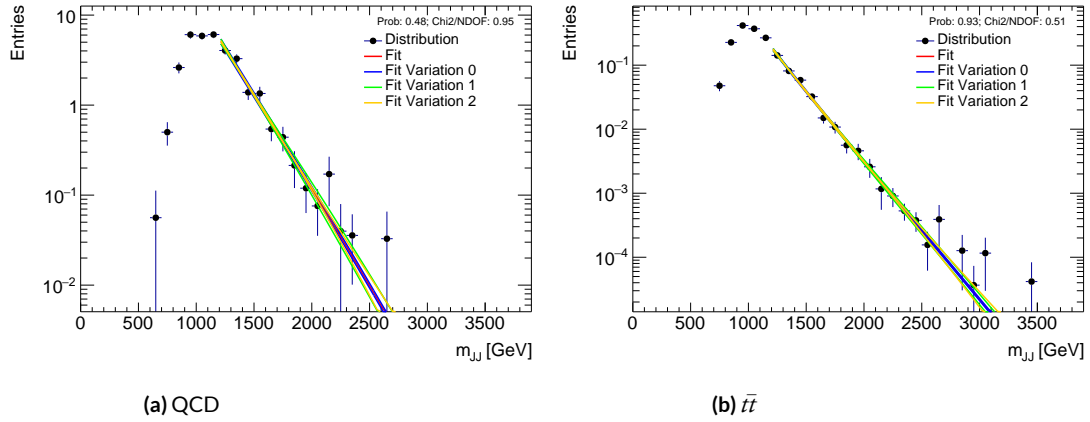


Figure 6.9: Fits for scaled background smoothing are shown for the $4b$ signal region. The figures show the distributions with the fit central value and the fit variations determined by varying the fit parameters within uncertainties and taking into account parameter correlations.

The final signal region predictions using scaled m_{2J} distributions, with only statistical uncertainties, are shown in Figures 6.12, 6.13, and 6.14. This includes smoothing statistical uncertainties only. Uncertainties on the fit parameters are propagated as systematic uncertainties, though they are essentially replacing the bin-by-bin statistical uncertainties of the background estimates (which are not used once smoothing is applied). More details on other systematics, including smoothing systematics, shape uncertainties, and other sources of uncertainties are discussed in section 7.9.

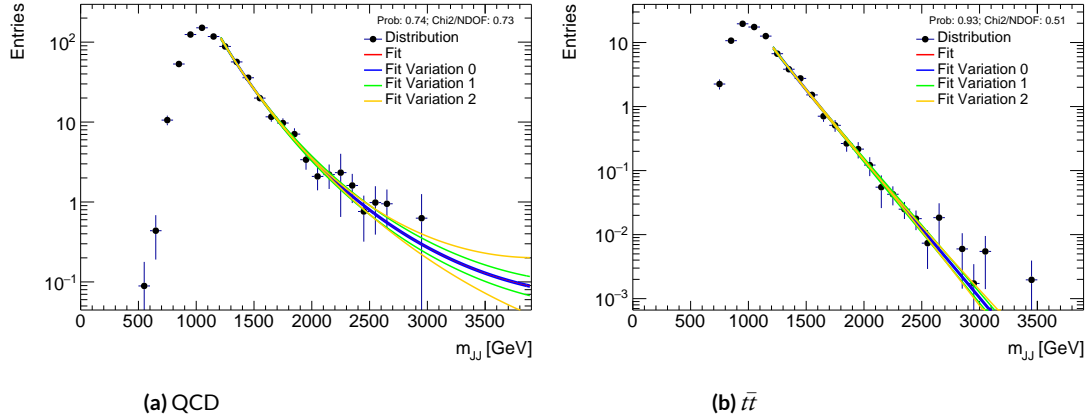


Figure 6.10: Fits for scaled background smoothing are shown for the $3b$ signal region. The figures show the distributions with the fit central value and the fit variations determined by varying the fit parameters within uncertainties and taking into account parameter correlations.

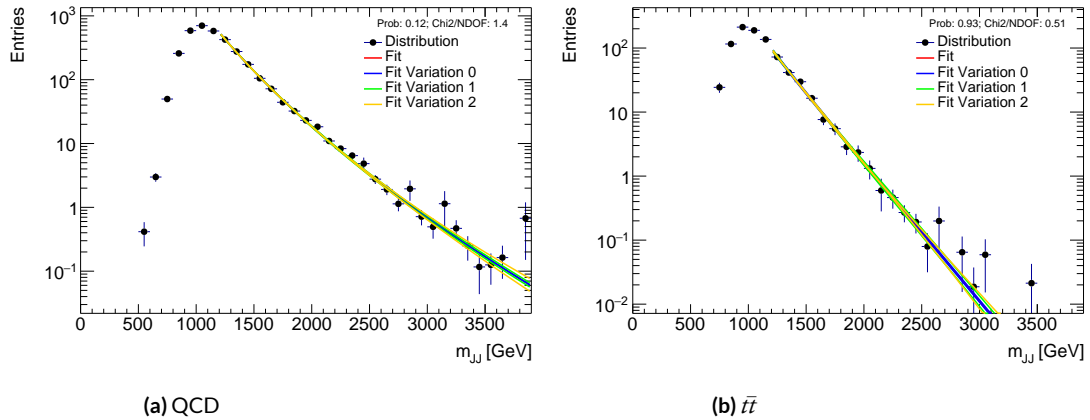


Figure 6.11: Fits for scaled background smoothing are shown for the $2bs$ signal region. The figures show the distributions with the fit central value and the fit variations determined by varying the fit parameters within uncertainties and taking into account parameter correlations.

6.10 YIELDS

The event yield results showing the estimated backgrounds, the signal predictions, and the observed data in the $4b$, $3b$, and $2bs$ signal regions, control regions, and sideband regions can be found in Table 6.7, 6.8, and 6.9, respectively. The total background statistical uncertainty is less than the

Table 6.6: Smoothing parameters in $4b$, $3b$, and $2bs$ signal regions for scaled mass distributions, the correlation between parameters is almost always 0.99.

Region	$a_{\bar{t}\bar{t}}$	$b_{\bar{t}\bar{t}}$	$c_{\bar{t}\bar{t}}$	a_{qcd}	b_{qcd}	c_{qcd}
FourTag	-2.02 ± 1.17	42.46 ± 9.87	1.31 ± 8.98	-0.49 ± 1.59	53.06 ± 15.2	-11.1 ± 12.8
ThreeTag	1.84 ± 1.17	42.45 ± 9.88	1.32 ± 8.98	8.51 ± 0.98	-13.8 ± 9.14	42.58 ± 7.87
TwoTag split	4.22 ± 1.17	42.45 ± 9.88	1.32 ± 8.98	7.06 ± 0.32	11.54 ± 2.77	19.05 ± 2.48

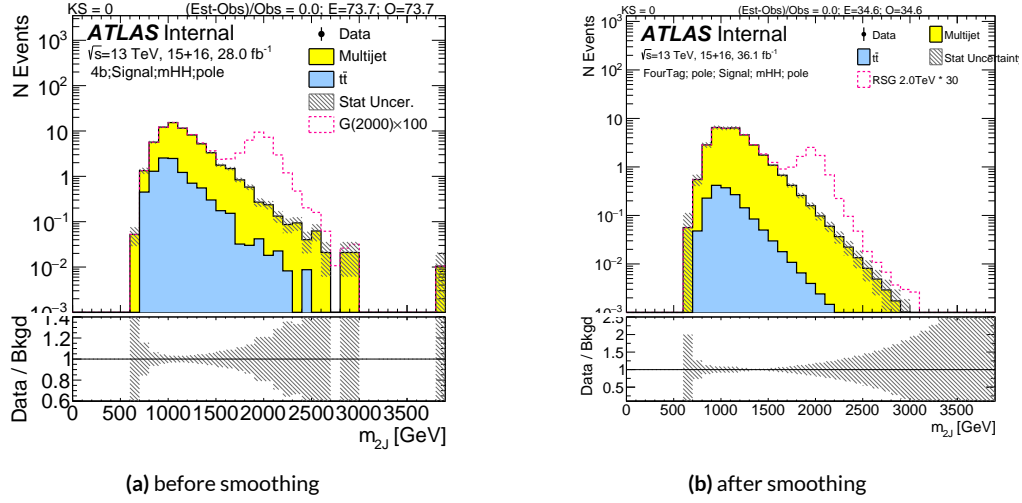


Figure 6.12: Background predictions for $4b$ signal region using scaled m_{2j} before and after smoothing. The uncertainty band includes only fit statistical uncertainties.

quadratic sum of $\bar{t}\bar{t}$ and QCD because of their anti-correlation. $Z+jets$ has a negligible yield in the signal regions; therefore, in the later chapters, it is not included in the figures and tables.

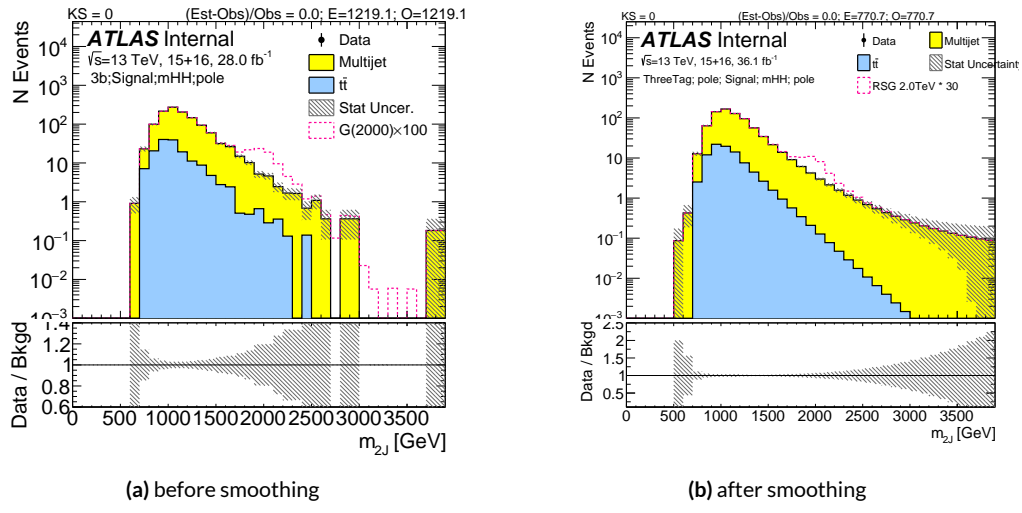


Figure 6.13: Background predictions for $3b$ signal region using scaled m_{jj} before and after smoothing. The uncertainty band includes only fit statistical uncertainties.

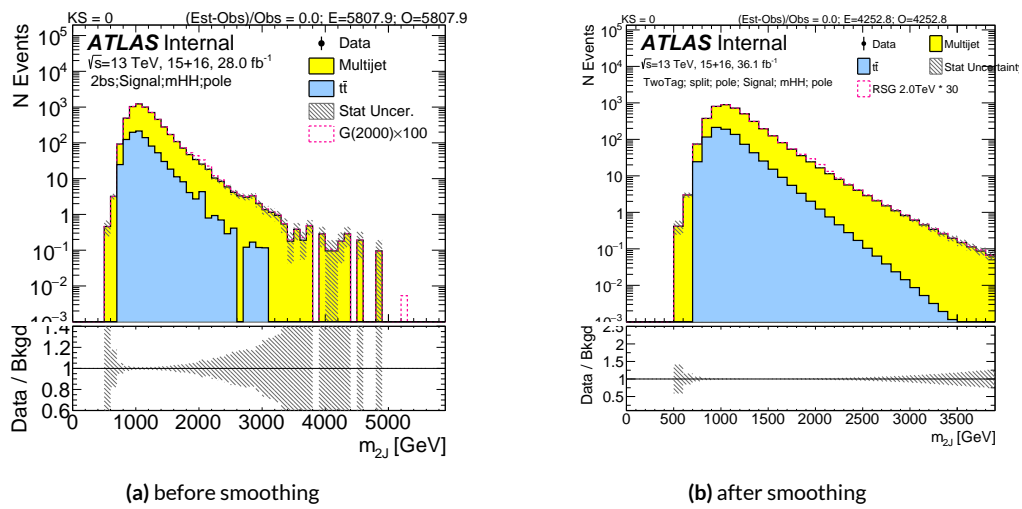


Figure 6.14: Background predictions for $2bs$ signal region using scaled m_{2J} before and after smoothing. The uncertainty band includes only fit statistical uncertainties.

Table 6.7: Expected yields for backgrounds in the $4b$ signal region, control region, and sideband region, along with the observed number of data events. The signal predictions for $G_{\text{KK}}^* m = 1.0, 1.5, 2.0 \text{ TeV}$ with $c = 1.0$. The uncertainty listed is statistical, without fit uncertainty.

FourTag	Sideband	Control	Signal
QCD Est	176.26 ± 2.96	64.21 ± 1.79	32.91 ± 1.25
$t\bar{t}$ Est.	27.86 ± 0.25	6.38 ± 0.13	1.68 ± 0.044
$Z + jets$	0 ± 0	6.18 ± 5.12	0 ± 0
Total Bkg Est	204.12 ± 2.97	76.77 ± 5.43	34.59 ± 1.25
Data	204.0 ± 14.28	81.0 ± 9.0	31 ± 5.57
$c = 1.0, m = 1.0 \text{ TeV}$	2.52 ± 0.1	5.4 ± 0.15	10.07 ± 0.2
$c = 1.0, m = 2.0 \text{ TeV}$	0.034 ± 0.0015	0.1 ± 0.0026	0.25 ± 0.0041
$c = 1.0, m = 3.0 \text{ TeV}$	$0.00032 \pm 3.7e-05$	$0.0008 \pm 5.6e-05$	$0.0016 \pm 8e-05$

Table 6.8: Expected yields for backgrounds in the $3b$ signal region, control region, and sideband region, along with the observed number of data events. The signal predictions for $G_{\text{KK}}^* m = 1.0, 1.5, 2.0 \text{ TeV}$ with $c = 1.0$. The uncertainty listed is statistical, without fit uncertainty.

ThreeTag	Sideband	Control	Signal
QCD Est	3518.01 ± 27.48	1413.52 ± 17.36	701.6 ± 11.95
$t\bar{t}$ Est.	852.88 ± 25.72	162.31 ± 11.15	79.34 ± 2.05
$Z + jets$	32.8 ± 11.34	11.21 ± 5.65	0.49 ± 0.49
Total Bkg Est	4403.69 ± 39.31	1587.04 ± 21.4	781.42 ± 12.14
Data	4403.0 ± 66.36	1553.0 ± 39.41	801.0 ± 28.3
$c = 1.0, m = 1.0 \text{ TeV}$	7.86 ± 0.18	12.58 ± 0.23	26.0 ± 0.33
$c = 1.0, m = 2.0 \text{ TeV}$	0.16 ± 0.0035	0.38 ± 0.0054	0.76 ± 0.0076
$c = 1.0, m = 3.0 \text{ TeV}$	0.0036 ± 0.00013	0.0075 ± 0.00018	0.013 ± 0.00023

Table 6.9: Expected yields for backgrounds in the $2bs$ signal region, control region, and sideband region, along with the observed number of data events. The signal predictions for $G_{\text{KK}}^* m = 1.0, 1.5, 2.0 \text{ TeV}$ with $c = 1.0$. The uncertainty listed is statistical, without fit uncertainty.

TwoTag split	Sideband	Control	Signal
QCD Est	17216.91 ± 38.33	6821.96 ± 23.49	3393.56 ± 16.64
$t\bar{t}$ Est.	7852.35 ± 70.3	1484.57 ± 29.24	858.27 ± 22.23
$Z + jets$	67.74 ± 16.82	26.44 ± 10.08	0.13 ± 0.091
Total Bkg Est	25137.01 ± 81.82	8332.97 ± 38.84	4251.96 ± 27.77
Data	25137.0 ± 158.55	8486.0 ± 92.12	4376.0 ± 66.15
$c = 1.0, m = 1.0 \text{ TeV}$	4.79 ± 0.14	6.33 ± 0.16	10.87 ± 0.22
$c = 1.0, m = 2.0 \text{ TeV}$	0.18 ± 0.0039	0.36 ± 0.0056	0.6 ± 0.0072
$c = 1.0, m = 3.0 \text{ TeV}$	0.013 ± 0.00025	0.027 ± 0.00034	0.039 ± 0.00041

Every question has a proper answer. Every soul has a proper place.

7

Systematics

7.1 OVERVIEW

Signal acceptance is affected by theoretical uncertainties. They result from renormalization and factorization scales uncertainties, PDF uncertainties, initial state radiation (ISR) and final state radiation (FSR) uncertainties. The total theoretical uncertainty is dominated by the ISR and FSR variations. The uncertainty on the expected signal yield is typically below 10% but can increase to 23%, depending on the signal mass.

Detector modeling uncertainties are propagated in the analysis. Those uncertainties include b -tagging efficiencies, jet energy scale (JES), jet energy resolution (JER) and jet mass resolution (JMR). These uncertainties can change both the shape and normalization of the signal and MC-based back-

grounds. In the data-driven background estimation, each uncertainty variation is evaluated.

A statistical uncertainty on the value of μ_{qcd} and $\alpha_{t\bar{t}}$ for the $4b$, $3b$ and $2bs$ signal regions is determined from the fitting procedure described in section 6.5. Two orthogonal eigenvariations are calculated from the covariance matrix of the normalization fit, which are then applied to the background predictions. Specifically, μ_{qcd} and $\alpha_{t\bar{t}}$ can be rewritten as a vector, $\alpha = (\alpha_1, \alpha_2)$, and the covariance matrix of α is C where $C_{ij} = \text{Cov}(\alpha_i, \alpha_j)$, then C can be decomposed as:

$$C = U\Lambda U^T \quad (7.1)$$

where U is a unitary matrix whose columns are the eigenvectors of C and $\Lambda = \text{Diag}(\Lambda_1, \Lambda_2)$ is a real diagonal matrix whose entries are the eigenvalues of C . The vector α can be projected along the direction of the eigenvectors, i.e. $\alpha \rightarrow \alpha' = U^T \alpha$, then the resulting eigenvalues are uncorrelated because $C \rightarrow C' = U^T C U = \Lambda$. Therefore, the values of α'_i can be varied independently by $\pm \Lambda_i$ to propagate the uncertainty. To return to the original space of α , the system is rotated back with the U matrix. Correlations between $\alpha_{t\bar{t}}$ and μ_{qcd} are fully retained this way.

Additional background modeling systematic uncertainties in the signal region are listed:

- Uncertainty on μ_{qcd} from the difference between data and prediction in the control region yield.
- Uncertainty on the QCD prediction from variations of the sideband and control region definitions.
- The shape uncertainty of the $t\bar{t}$ prediction in the $3/4b$ signal region.
- The shape uncertainty of the estimated QCD prediction, derived in the control region.
- Uncertainty from the smoothing function fit range and function choice.

These uncertainties will be discussed in the following sections. They are summarized in section 7.10.

7.2 THEORETICAL UNCERTAINTIES

The theoretical uncertainties on the acceptance times efficiency ($\mathcal{A} \times \varepsilon$) are evaluated by analysis of specially-generated, particle-level signal samples. The generation of these samples follows the configuration of the baseline samples, but with modifications to probe the following theoretical uncertainties: uncertainties in the parton density functions; uncertainties due to missing higher order terms in the matrix elements; and uncertainties in the modeling of the underlying event (including multi-parton interactions), of hadronic showers and of initial and final state radiation.

To evaluate the potential effect of missing higher order terms in the matrix element, the renormalization and factorization scales used in the signal generation are varied by $\times 0.5$ and $\times 2$ for the signals.

Uncertainties due to modeling of the parton shower and the underlying event are evaluated by varying the MC generator listed in section 4.2.1. For the Bulk RS graviton samples, PYTHIA8 are switched to Herwig++, while for the scalar and non-resonant it is Herwig++ to PYTHIA8.

PDF uncertainties are evaluated using the PDF4LHC15_nlo_mc set, which combines CT14, MMHT14 and NNPDF3.0 PDF sets⁷³. The uncertainty is evaluated by calculating the acceptance for each PDF set. The standard deviation of these acceptance values divided by the baseline acceptance is taken as the PDF uncertainty. The uncertainty in acceptance due to PDF is less than $\pm 1\%$ across the full mass range considered for the analysis.

These uncertainties are implemented in the final statistical analysis as normalization uncertainties on the signals, with the value taken from a polynomial fit of the cross section and the mass of the signal. This smooths out statistical fluctuations and allows interpolation between the generated mass points.

7.3 UNCERTAINTIES ON DETECTOR AND RECONSTRUCTION

7.3.1 LUMINOSITY UNCERTAINTY

The uncertainty in the integrated luminosity of the combined 2015 and 2016 datasets is $36.1\text{fb}^{-1} \pm 2.1\%$ ⁷⁴. This uncertainty is applicable to the backgrounds with normalizations determined from simulation, and further propagated to the QCD prediction through the data-driven background estimation procedure. This uncertainty is also applied to the signal normalization prediction. It has a small impact on this analysis.

7.3.2 LARGE- R JET RESOLUTION AND SCALE UNCERTAINTIES

There are uncertainties on the large- R jets energy scale (JES) and energy resolution (JER), as well as the mass scale (JMS) and mass resolution (JMR). The uncertainties on the JES and JMS are derived in situ from 13 TeV $p\bar{p}$ collisions, using techniques described in Ref.⁷⁵. Discrepancies in jet four-momenta observed between data and MC are assigned as uncertainties on the energy/mass scales of the jet. The uncertainties are only correlated between energy and mass.

The uncertainties on the jet mass resolutions are estimated by applying a Gaussian smearing. For each signal mass point, the large- R trimmed jet mass is smeared such that the intrinsic resolution is increased by 20%. For jet energy resolution, the momentum is smeared with an absolute 2% uncertainty. The nominal MC mass resolution (σ_M) for every signal mass point is determined by fitting the $M_{\text{JJ}}/M_{\text{truth}}$ distribution with a Gaussian. The σ_M is calculated before the final X_{hh} cut.

7.3.3 b -TAGGING UNCERTAINTIES

The uncertainties related to the b -tagging efficiency calibrations as measured in $t\bar{t}$ events for track jets are considered. The procedure to define these calibrations is similar to that described in Ref.⁵¹. The uncertainty in the b -tagging efficiency is evaluated by propagating the systematic uncertainty in the p_T -dependent, measured tagging efficiency for b -jets⁵. For b -jets with $p_T > 300$ GeV, systematic uncertainties in the tagging efficiencies are extrapolated with simulation and are consequently larger⁵¹. Uncertainties arising from mis-tagging jets that do not contain b -hadrons are negligible.

Calibrations, or correction factors in the form of scale factors per p_T bin, for the b -tagging efficiency of $R = 0.2$ track jets passing an MV2c10 weight cut corresponding to 77% efficiency have been derived in Ref.^{76,77}. These calibrations are applied to the RS graviton signal samples and $t\bar{t}$ simulation. The calibrations also include uncertainties which modify the b -tagging efficiency and thus modify the signal ($t\bar{t}$) acceptance, therefore these uncertainties are propagated through the analysis. The signal yield uncertainty due to b -tagging is less than 30% for the signal, and less than 12% for the $t\bar{t}$ yield.

A significant reduction of b -tagging systematic uncertainty for resonant signals in $3b$ signal region is observed. The reduced b -tagging uncertainty is due to the requirement that there must be one anti-tagged jet. For the signal, this is likely an anti-tagged b -jet. When a b -tagged jet is calibrated with a scale factor w_{sf} with uncertainties Δw_{sf} , any change in tagging efficiency must be corrected in the opposite direction for the anti-tagged jets in order to ensure that the total number of b -tagged plus anti-tagged jets does not change once the calibration is applied. Therefore, the anti-tagging calibration scale factor would be $w_{sf}^{anti} = (1 - w_{sf}\epsilon_b)/(1 - \epsilon_b)$, where ϵ_b is the tagging efficiency. Based on this equation, a shift in the scale factor for b -tagged jets causes an anti-correlated shift in the anti-tagging efficiency scale factor. This anti-correlation in turn reduces the overall impact of the

b -tagging uncertainty on the $3b$ SR. However, this anti-tagging efficiency scale factor is large, and in the $2bs$ SR, the total uncertainty is dominated by the square of this factor. Hence the b -tagging uncertainty on the $2bs$ SR can be larger than the b -tagging uncertainty on the $3b$ SR.

This behavior is shown in Figure 7.1. One eigenvariation of b -tagging scale factor is tested on a 2 TeV G_{KK}^* with $c = 1.0$. In the $4b$ plot, no inefficiency scale factor is applied. The variation on the signal yield is only due to w_{sf} . In the $3b$ plot, one inefficiency scale factor is applied. This w_{sf}^{anti} reduces the variation from w_{sf} . In the $2bs$ plot, two inefficiency scale factor are applied. This w_{sf}^{anti} further reduces the variation from w_{sf} , causing the signal yield difference increase compared with the $3b$ case.

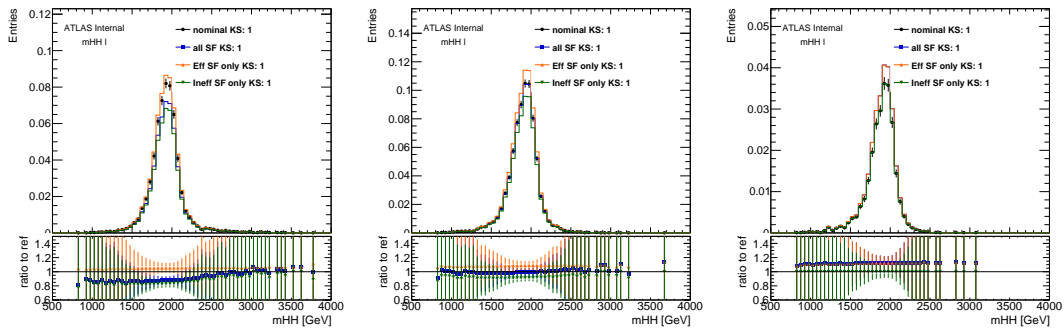


Figure 7.1: Impact of efficiency scale factor w_{sf} and inefficiency scale factor w_{sf}^{anti} on 2 TeV G_{KK}^* with $c = 1.0$. $4b$ signal region (left), $3b$ signal region (middle), and $2bs$ signal region are shown.

7.4 UNCERTAINTY ON $\bar{t}\bar{t}$ GENERATOR

In addition to the $\bar{t}\bar{t}$ fit uncertainties, additional $\bar{t}\bar{t}$ MC samples are considered with the following variations: hadronization, fragmentation, matrix element variation and additional radiation. The top quark mass variations are also considered.

These $t\bar{t}$ samples are used to replace the normal had and non-had MCs, stitched with $m_{t\bar{t}}$ slices samples, and the variation in the $t\bar{t}$ yield and background predictions are considered. The variation in total background, with different $t\bar{t}$ MC sample as input is tested. This is shown in Figure 7.2. This uncertainty is considered limited by the MC statistics and not included.

These $t\bar{t}$ samples are used to replace the normal had and non-had MCs, stitched with $m_{t\bar{t}}$ slices samples, and the variation in the $t\bar{t}$ yield and background predictions are considered. The variation in total background, with different $t\bar{t}$ MC sample as input is tested. This is shown in Figure 7.2. However, the predictions are consistent with MC statistical uncertainties and therefore no $t\bar{t}$ MC uncertainty is applied.

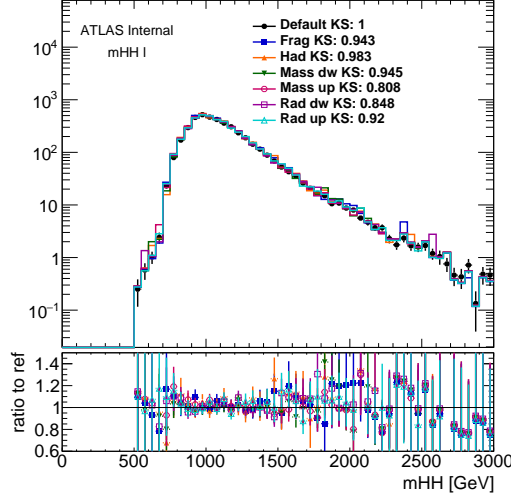


Figure 7.2: Total background estimation ($\text{QCD} + t\bar{t}$) with different $t\bar{t}\text{MC}$ variations. The different variations agree with the default within the statistical uncertainties.

7.5 UNCERTAINTY ON μ_{qcd} ESTIMATION

A further uncertainty is derived by comparing the value of μ_{qcd} to the overall difference between predicted to observed events in the control region, shown in section 6.10. The number events agrees

with the total data in the control region within statistical error, but the μ_{qcd} estimation is dependent on the SB and CR choice. An additional systematic on the background prediction in the signal region is assigned. It is the maximum between either the difference between the central value of the prediction to the observed number of events, or the statistical uncertainty of the observed data in the CR. For $4b$ it is 11.1%, for $3b$ it is 2.5%, and for $2b$ it is 1.1%.

Besides the nominal control region, additional sideband and control regions are designed and tested. They are further illustrated in Appendix F, and are listed below:

- Low-mass CR: the center position of the circle that defines nominal CR is moved down by 3 GeV, in both leading and sub-leading large-jet mass.
- High-mass CR: the center position of the circle that defines nominal CR is moved up by 3 GeV, in both leading and sub-leading large-R jet mass.
- Signal-depletion CR (Small CR): the X_{hh} cut that defines signal region is increased to 2.0 from 1.6. This variation only affect CR, while SR remains unchanged (i.e. signal region is still defined by $X_{hh} < 1.6$, while CR is defined as $X_{hh} > 2.0$ and $R_{hh} < 33$).
- High-mass SB: The signal region and control region remain unchanged, and the center position of the circle that defines nominal SB is moved up by 3 GeV in both leading and sub-leading large-R jet mass.
- Low-mass SB: The signal region and control region remain unchanged, and the center position of the circle that defines nominal SB is moved up by 3 GeV in both leading and sub-leading large-R jet mass.
- Large SB: The signal region and control region remain unchanged, and the sideband region is redefined as $33 < R_{hh}$ and $R_{hh}^{\text{high}} < 61$. μ_{QCD} will change.
- Small SB: The signal region and control region remain unchanged, and the sideband region is redefined as $33 < R_{hh}$ and $R_{hh}^{\text{high}} < 55$. μ_{QCD} will change.

To ensure that these values cover the QCD normalization uncertainty, further checks on the effect of adjusting the control and sideband definitions were done. All these tests are done on the control/sideband regions after the full reweighting procedure as described in 6.6, while applying the nominal reweighting values. The results are summarized in Table 7.1, 7.2 and 7.3. Based on all the variations, a final 2.8% normalization uncertainty is assigned to $2b$ s signal region, 4.2% to $3b$ signal region, and a 12.2% normalization uncertainty is assigned to $4b$ signal region.

CR Variations FourTag	Data	Prediction	(Predict - Data)/Data
Nominal	81.0 ± 9.0	76.77 ± 5.43	-5.22 % \pm 17.23 %
CR High	76.0 ± 8.72	71.12 ± 5.41	-6.43 % \pm 17.85 %
CR Low	91.0 ± 9.54	79.87 ± 5.45	-12.2 % \pm 15.19 %
CR Small	58.0 ± 7.62	55.96 ± 5.35	-3.52 % \pm 21.89 %
SB Large	81.0 ± 9.0	74.71 ± 5.4	-7.76 % \pm 16.91 %
SB Small	81.0 ± 9.0	74.15 ± 5.38	-8.45 % \pm 16.81 %
SB High	81.0 ± 9.0	78.72 ± 5.46	-2.82 % \pm 17.54 %
SB Low	81.0 ± 9.0	76.51 ± 5.38	-5.54 % \pm 17.14 %

Table 7.1: Agreement between data and prediction in $4b$ tag CR. Showing stat uncertainty only.

CR Variations ThreeTag	Data	Prediction	(Predict - Data)/Data
Nominal	1553.0 ± 39.41	1587.04 ± 21.4	2.19 % \pm 3.97 %
CR High	1461.0 ± 38.22	1473.89 ± 20.77	0.88 % \pm 4.06 %
CR Low	1628.0 ± 40.35	1697.38 ± 21.75	4.26 % \pm 3.92 %
CR Small	1134.0 ± 33.67	1127.34 ± 17.66	-0.59 % \pm 4.51 %
SB Large	1553.0 ± 39.41	1574.23 ± 21.47	1.37 % \pm 3.95 %
SB Small	1553.0 ± 39.41	1601.44 ± 21.64	3.12 % \pm 4.01 %
SB High	1553.0 ± 39.41	1602.74 ± 21.48	3.2 % \pm 4.0 %
SB Low	1553.0 ± 39.41	1576.56 ± 21.5	1.52 % \pm 3.96 %

Table 7.2: Agreement between data and prediction in $3b$ tag CR. Showing stat uncertainty only.

CR Variations TwoTag split	Data	Prediction	(Predict - Data)/Data
Nominal	8486.0 ± 92.12	8332.97 ± 38.84	$-1.8\% \pm 1.52\%$
CR High	8174.0 ± 90.41	7937.59 ± 39.61	$-2.89\% \pm 1.56\%$
CR Low	8907.0 ± 94.38	8800.86 ± 39.51	$-1.19\% \pm 1.49\%$
CR Small	5999.0 ± 77.45	5873.52 ± 32.31	$-2.09\% \pm 1.8\%$
SB Large	8486.0 ± 92.12	8341.7 ± 38.44	$-1.7\% \pm 1.52\%$
SB Small	8486.0 ± 92.12	8333.25 ± 39.12	$-1.8\% \pm 1.53\%$
SB High	8486.0 ± 92.12	8378.14 ± 38.45	$-1.27\% \pm 1.52\%$
SB Low	8486.0 ± 92.12	8356.86 ± 39.06	$-1.52\% \pm 1.53\%$

Table 7.3: Agreement between data and prediction in $2bs$ tag CR. Showing stat uncertainty only.

7.6 VALIDATION IN LOW MASS AND HIGH MASS SIGNAL REGION

Another check is the the so-called “low mass signal region” (or ZZ region) and “high mass signal region” (or TT region). Instead of the signal region around di-Higgs mass region on m_J^{lead} – m_J^{subl} large- R jet mass 2D plane, a separate lower mass (ZZ) and higher mass (TT) signal region are defined:

$$X_{ZZ} = \sqrt{\left(\frac{m_J^{\text{lead}} - 103 \text{ GeV}}{\text{o.I.}(m_J^{\text{lead}})}\right)^2 + \left(\frac{m_J^{\text{subl}} - 96 \text{ GeV}}{\text{o.I.}(m_J^{\text{subl}})}\right)^2} \quad (7.2)$$

$$X_{TT} = \sqrt{\left(\frac{m_J^{\text{lead}} - 164 \text{ GeV}}{\text{o.I.}(m_J^{\text{lead}})}\right)^2 + \left(\frac{m_J^{\text{subl}} - 155 \text{ GeV}}{\text{o.I.}(m_J^{\text{subl}})}\right)^2} \quad (7.3)$$

which is also illustrated in Figure 7.3. The analysis is repeated, using the same definition of sideband and control region as the nominal (but with events contained in the ZZ signal region excluded) for normalization fit. Then the low mass signal region is unblinded. This helps to validate the background estimation strategy, and the stability for other similar analysis.

The difference between data and prediction in the ZZ signal region is summarized in Table 7.4 for all the regions. The discrepancy between data and prediction is either covered by statistical uncertainty of data or comparable with data statistical uncertainty in $4b$, $3b$ and $2bs$ ZZ SR respectively.

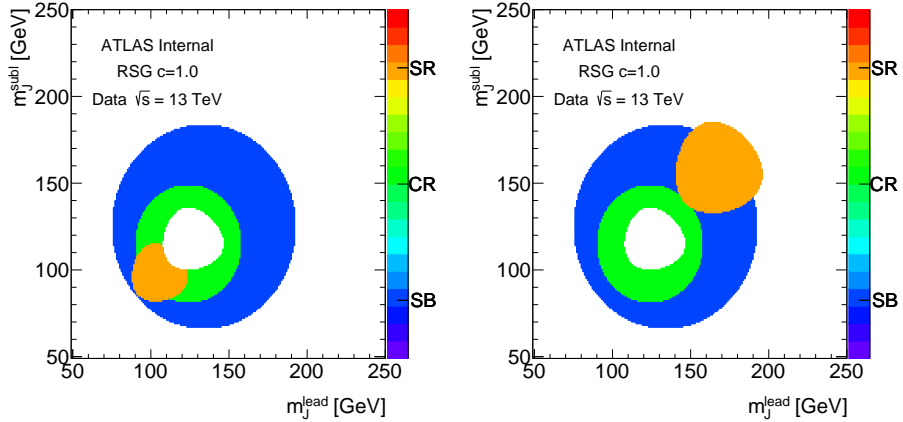


Figure 7.3: Illustration of ZZ (left) and TT (right) signal region as shown in the orange shaded region. Control region shown in green, and sideband region in blue. The white circle in the middle is the real signal region, and it is blinded.

The kinematic distribution between data and prediction in ZZ SR are shown in Figure 7.4. The data agrees with prediction well in general, though a few bins might not agree perfectly. The difference from $4b$ CR region test is 17%, which is smaller than the $4b$ ZZ region difference. But the statistical uncertainty in ZZ region (with yield 37) is much higher compared with the CR regions (with minimum yield 76), hence the CR region with more statistical power is still used for the non-closure uncertainty.

The difference between data and prediction in the TT signal region is summarized in Table ?? for all the regions. The discrepancy between data and prediction is either covered by statistical uncertainty of data or comparable with data statistical uncertainty in $4b$, $3b$ and $2bs$ TT SR respectively. The kinematic distribution between data and prediction in TT SR are shown in Figure 7.5. The data agrees with prediction well.

Based on all the variation tests, there is no need to introduce extra uncertainty on non-closure systematics. The disagreements in data/prediction are generally comparable to the statistical uncer-

tainty.

Table 7.4: Data and prediction in ZZ SR in $4b$, $3b$ and $2bs$ regions.

ZZ Signal Region	Data	Prediction	(Predict - Data)/Data
FourTag	37.0 ± 6.08	27.37 ± 1.16	$-26.0\% \pm 15.3\%$
ThreeTag	645.0 ± 25.4	671.15 ± 12.11	$4.05\% \pm 5.97\%$
TwoTag split	3258.0 ± 57.08	3395.59 ± 24.42	$4.22\% \pm 2.58\%$

Table 7.5: Data and prediction in TT SR in $4b$, $3b$ and $2bs$ regions.

TT Signal Region	Data	Prediction	(Predict - Data)/Data
FourTag	46.0 ± 6.78	43.62 ± 1.23	$-5.18\% \pm 16.66\%$
ThreeTag	1017.0 ± 31.89	976.88 ± 12.81	$-3.95\% \pm 4.27\%$
TwoTag split	6446.0 ± 80.29	6453.23 ± 51.41	$0.11\% \pm 2.04\%$

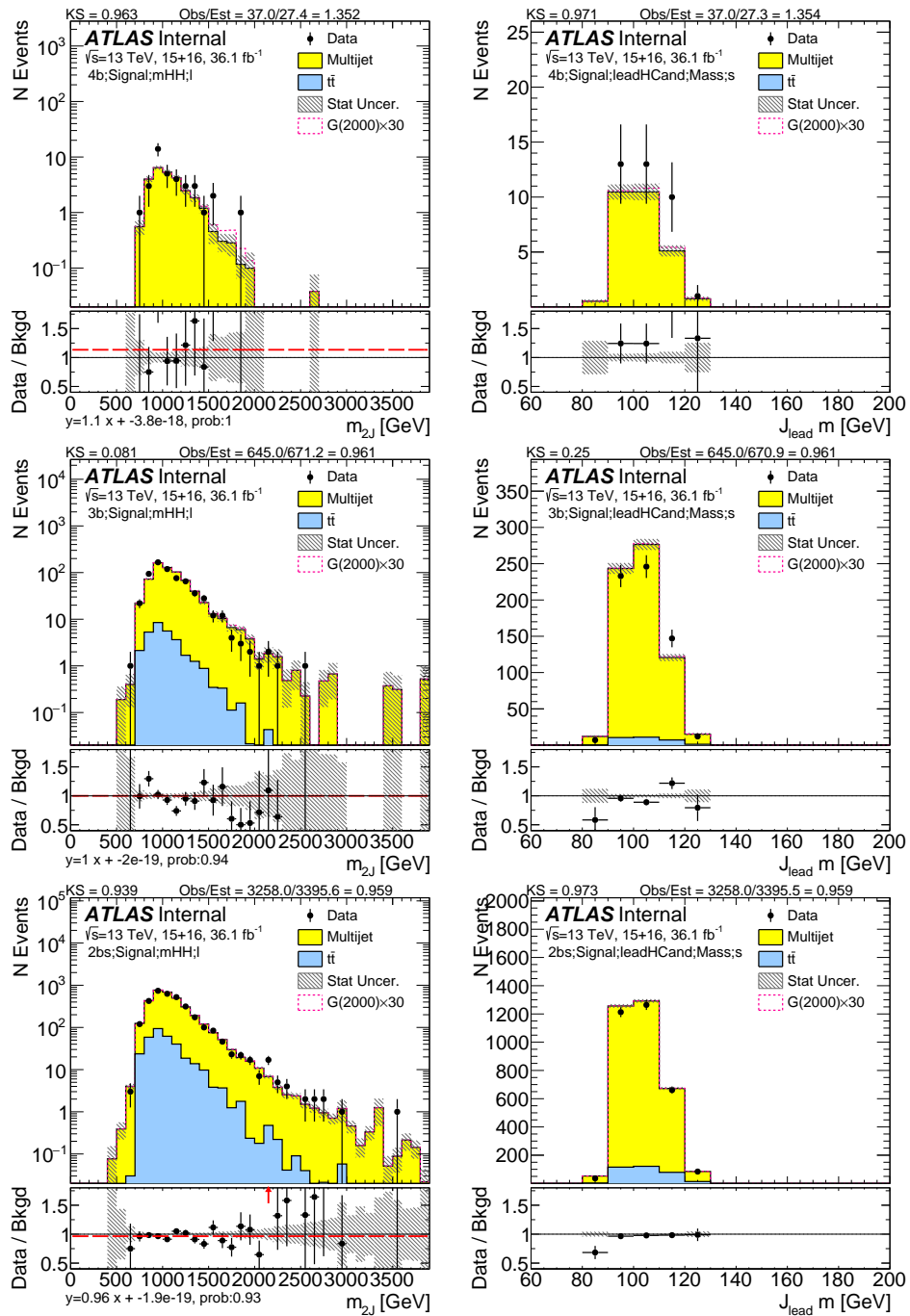


Figure 7.4: ZZ signal region distribution of m_{2J} (left column) and leading large-R jet mass (right column), for $4b$ (top row), $3b$ (middle row) and $2b$ split (bottom row). Only statistical uncertainties are shown.

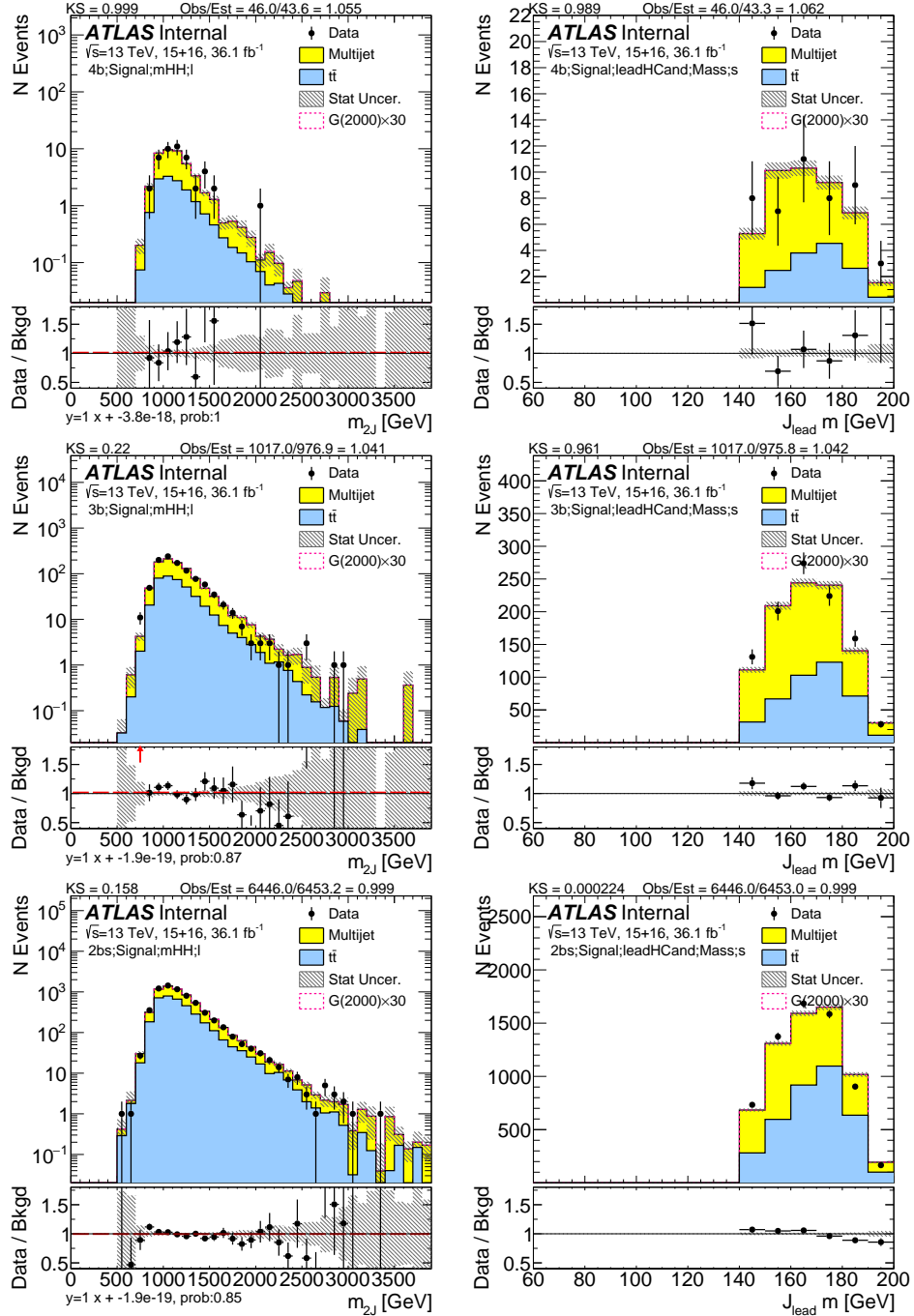


Figure 7.5: $T\bar{T}$ signal region distribution of m_{2J} (left column) and leading large-R jet mass (right column), for $4b$ (top row), $3b$ (middle row) and $2b$ split (bottom row). Only statistical uncertainties are shown.

7.7 UNCERTAINTY ON THE SHAPE OF $t\bar{t} m_{2J}$ IN THE $4/3b$ SIGNAL REGION

Because the $4/3b t\bar{t} m_{2J}$ distribution is statistically limited, the $2bs t\bar{t} m_{2J}$ shape is used to predict the final $t\bar{t}$ background shape in the $4/3b$ signal region. In order to estimate the possible shape uncertainty, the $2bs$ and $3b$ sideband shapes are normalized and compared in Figure 7.6. In order to avoid large statistical uncertainties, the distributions of the $3b$ and $2b$ are smoothed. The ratio of the two smoothed distributions is taken as the shape systematic. This ratio is used to apply a bin-by-bin scaling of the $t\bar{t}$ background prediction in the signal region, maintaining the same normalization given by nominal $t\bar{t}$ normalization prediction.

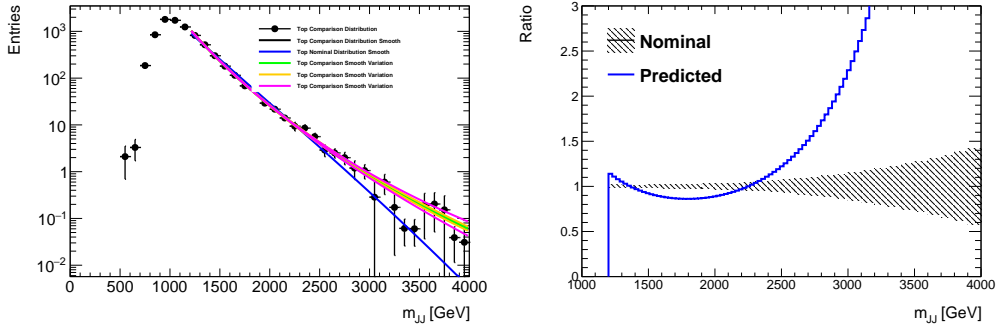


Figure 7.6: The shape of $t\bar{t} m_{2J}$ in the sideband region, comparing the $3b$ shape with that of the $2bs$, in order to assess the systematic effect of additional b -tags changing the dijet mass distribution. The m_{2J} distributions is shown on the left, and the ratio of $3b$ to $2bs$ distributions on the right.

7.8 UNCERTAINTY ON THE SHAPE OF THE QCD DISTRIBUTION IN THE SIGNAL REGION

As shown in Figure 6.7, the shape of the total predicted background distribution is found to be in good agreement with the $4b$, $3b$, and $2bs$ data in the control region. However due to the low statistics in the high m_{2J} mass bins, there are statistical fluctuations that cannot be ignored. A comparison is performed by first smoothing the prediction and the data distribution in the control region. The ratio of the smoothed QCD distributions to that of the smoothed $4/3/2bs$ data distributions

is taken as the shape systematic. This ratio is then used to apply a bin-by-bin scaling of the QCD background prediction in the signal region, maintaining the same normalization given by μ_{qcd} . The smoothing fit and the ratios can be found in Figure 7.7. This systematics is further split into two parts: one below 2000 GeV and the other above 2000 GeV, to ensure the low and high mass shape variation post-fit pulls can vary independently. This uncertainty is applied for both the m_{2J} , and the scaled m_{2J} distribution, since the scaling correction has small impacts on m_{2J} .

7.9 UNCERTAINTY ON SMOOTHING FUNCTION IN THE SIGNAL REGION

A specific function has been used to fit the QCD background prediction in order to smooth the distribution and provide non-zero background estimates up to dijet masses. While this distribution is observed to fit the predicted signal region m_{2J} well, it does not have a concrete physical motivation, and in principle the high mass tail of the distribution could be larger than predicted. Two checks are performed, changing the boundaries where the fit is performed, and changing the fit function. The checks shows the smoothing function range and form variations are almost always smaller than the statistical uncertainties of the distributions. This gives this systematic uncertainty strong correlations with the shape uncertainties discussed in the previous section. As a result, this systematic uncertainty is excluded. Nevertheless, the tests are discussed below.

To test the impact of the region in which the fit is performed, the upper bound on the dijet fit region are varied to be $\{2800, 3000, 3200\}$ GeV and the lower bound are varied to be $\{1200, 1300, 1400\}$ GeV. The ratio of the fits for each upper bound, to that of the nominal (1200–3000 GeV) are shown in Figure 7.8, along with a hash band showing the statistical uncertainty of the nominal fit. This is estimated separately for $2b$, $3b$, and $4b$ samples.

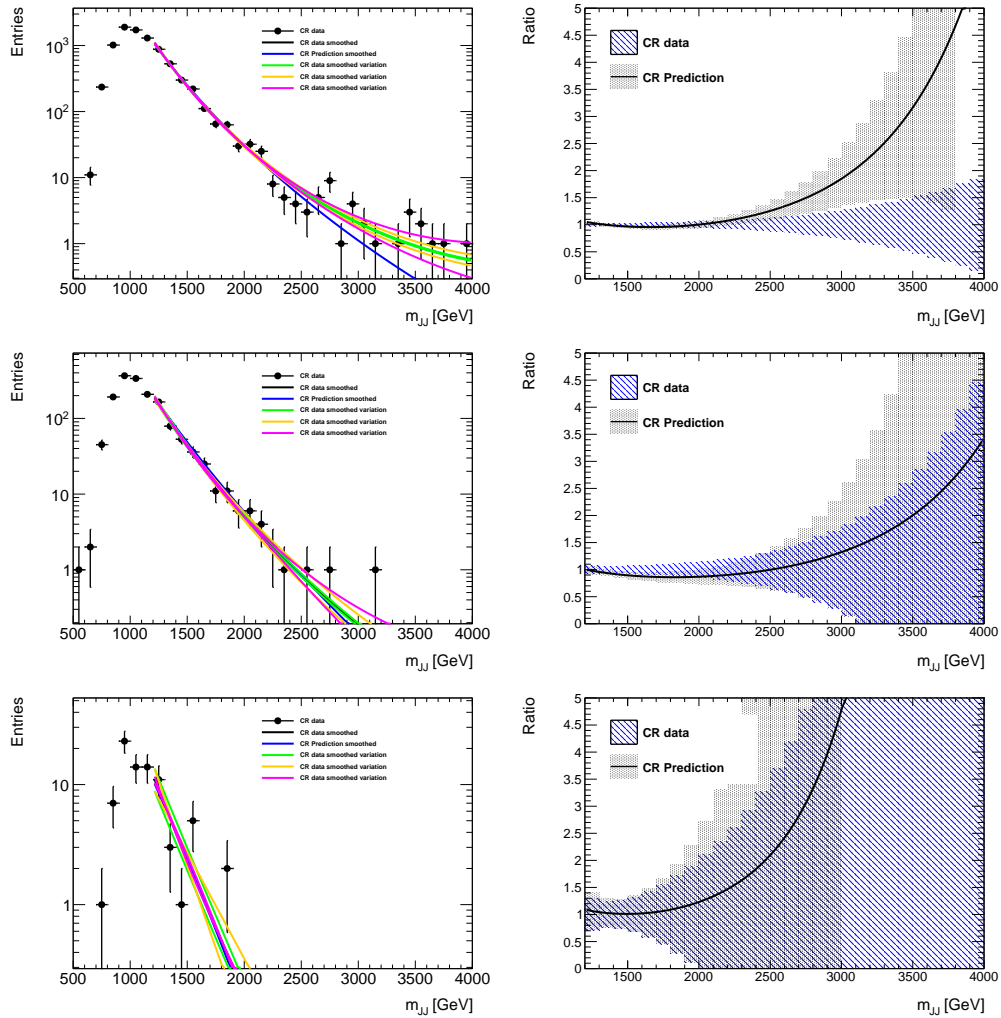


Figure 7.7: Dijet mass distribution in the CR along with the prediction (left) and the ratio of the prediction to the CR distribution (right) for the $2bs$ (top), $3b$ (middle) and $4b$ (bottom) samples. Ratios are from the smoothed distributions, the data uncertainty band contains the smoothing parameter variations, and the prediction uncertainty band also contains smoothing parameter variations.

Fits in which the fit χ^2 probability was less than 0.001%, or in which the fit integrals between 1500-2000 GeV, 2000-2500 GeV, or > 2500 GeV were not in agreement with the original distribution within a factor of 2 or 0.5, are not used to estimate the uncertainty. This ensures that poor fits

are not used to estimate the uncertainty.

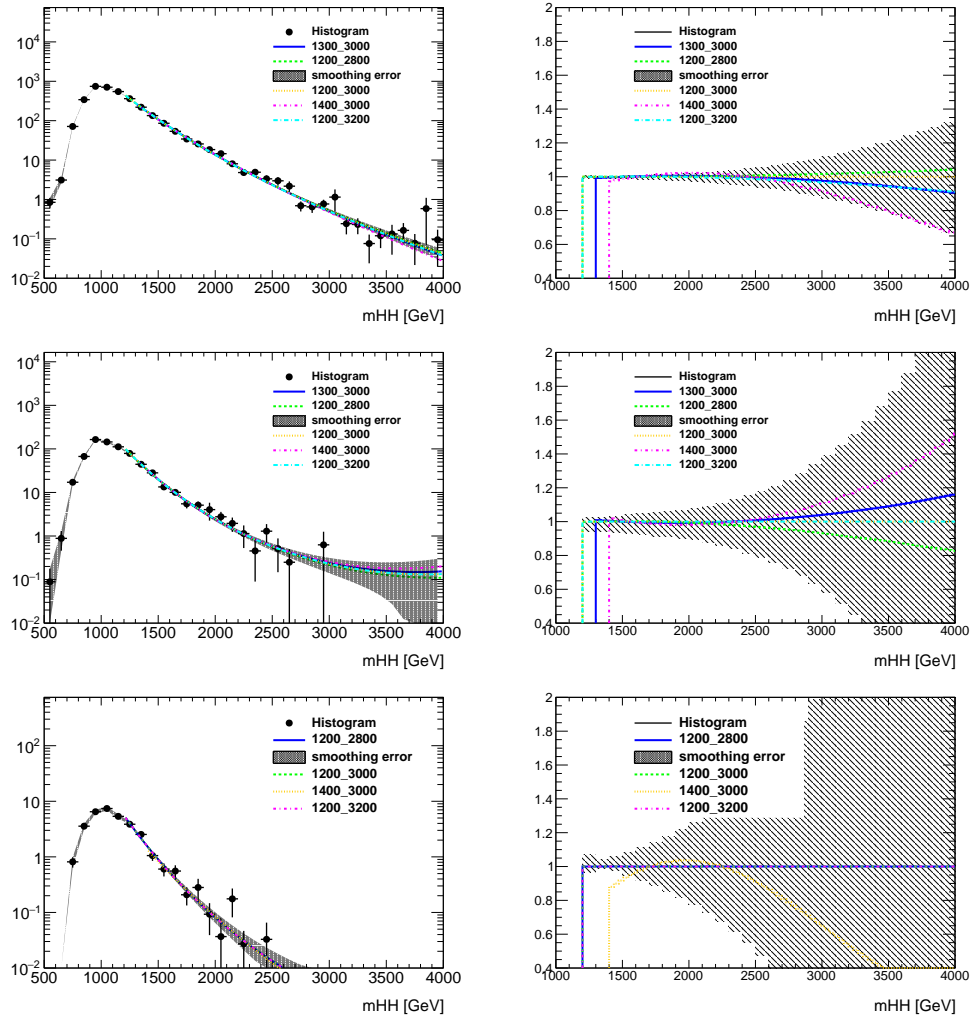


Figure 7.8: Dijet mass distribution SR prediction fit with several fit ranges (left) and the ratio of nominal to fits with different fit ranges (right) for the $2b$ (top) $3b$ (middle) and $4b$ (bottom) samples.

The signal region QCD prediction is also fit with a variety of other distributions which have power law behavior in the bulk of the distribution. The set of additional functions examined (labeled MJ1-MJ7) can be found in Table 7.6, where $x = m_{JJ}/\sqrt{s}$.

Name	Functional Form
MJ1 (Dijet)	$f_1(x) = p_o(1-x)^{p_1}x^{p_2}$
MJ2	$f_2(x) = p_o(1-x)^{p_1}e^{p_2 x^2}$
MJ3	$f_3(x) = p_o(1-x)^{p_1}x^{p_2 x}$
MJ4	$f_4(x) = p_o(1-x)^{p_1}x^{p_2 \ln x}$
MJ5	$f_5(x) = p_o(1-x)^{p_1}(1+x)^{p_2 x}$
MJ6	$f_6(x) = p_o(1-x)^{p_1}(1+x)^{p_2 \ln x}$
MJ7	$f_7(x) = \frac{p_o}{x}(1-x)^{p_1-p_2 \ln x}$
MJ8	$f_8(x) = \frac{p_o}{x^2}(1-x)^{p_1-p_2 \ln x}$

Table 7.6: Functions used to fit the QCD dijet mass distributions, where $x = m_{JJ}/\sqrt{s}$.

Figure 7.9 shows the fits to the QCD prediction in the $4/3/2bs$ signal regions, and the nominal dijet fit, as well as the ratios of the nominal fit to that of the additional functions. As before, poor fits are not used to estimate the uncertainty.

7.10 SUMMARY OF SYSTEMATICS

Table 7.7 shows the percent impact of systematics used in the boosted analysis on the predicted signal and background yields in the $4b$ signal region. The corresponding values are shown for the $3b$ signal region in Table 7.8, and are shown for the $2bs$ signal region in Table 7.9. The systematics that have no impact the yield are not listed. These are uncertainties on the shape of the QCD and $t\bar{t}$ backgrounds in the signal region.

The background normalization fit’ uncertainty comes from summing in quadrature the independent uncertainty components calculated from the correlated statistical errors of μ_{qcd} and $\alpha_{t\bar{t}}$. The QCD non-closure uncertainty is derived as the maximum of the difference between the predicted and observed $4b/3b/2bs$ QCD yields in the control region, or the fractional change in SR predictions from varying the CR and SB definitions. Both options gave similar sized uncertainties. All these uncertainties are summed in quadrature and shown in the “Bkg Est” row in the table.

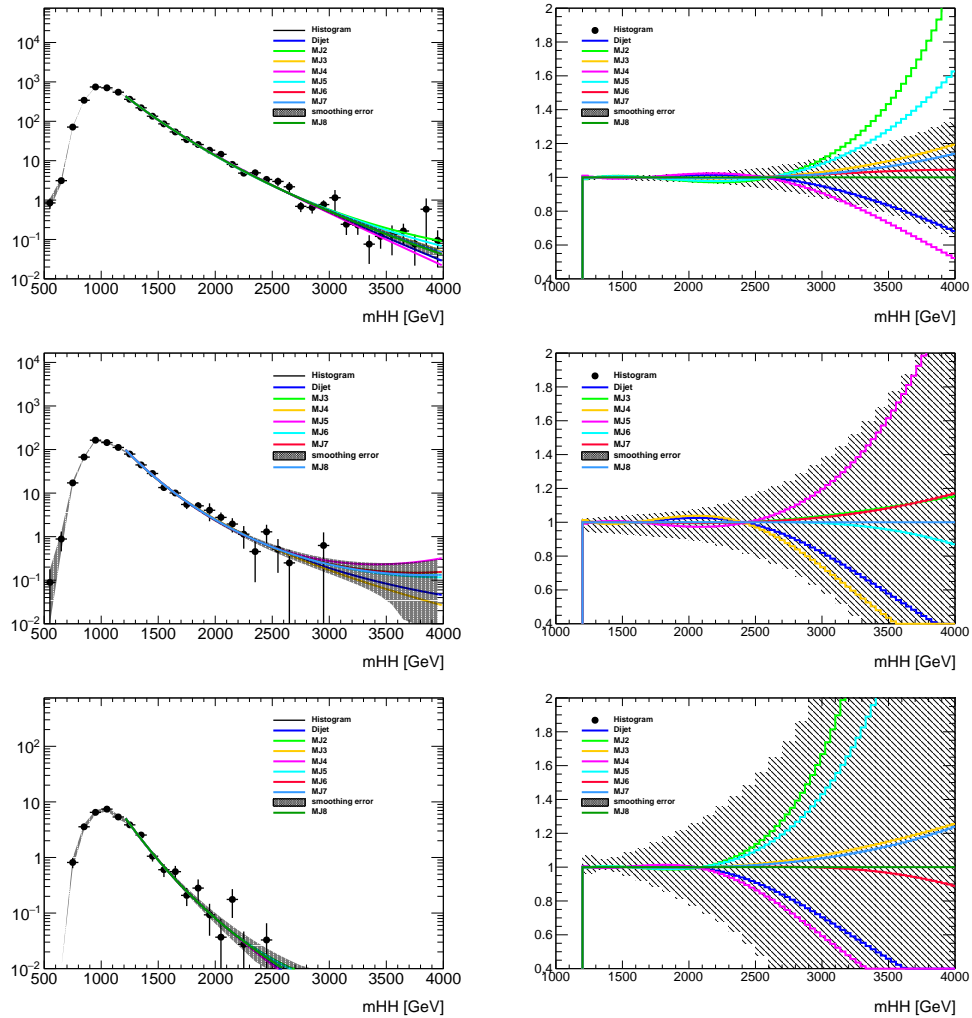


Figure 7.9: Dijet mass distribution SR prediction fit with several fit functions (left) and the ratio of nominal to fits with different fit functions (right) for the $2bs$ (top) $3b$ (middle) and $4b$ (bottom) samples. The additional fit functions are from Table 7.6.

The size of the Monte Carlo modeling systematics on the G_{KK}^* with $c = 1.0$ yield as a function of the signal mass can be found in Figure 7.10. These uncertainties have a similar impact on the other signals. The largest uncertainty in the $4b$ and $2b$ signal region is from b -tagging, followed by the JMR uncertainty. In the $3b$ signal region, although b -tagging systematics is still one of the largest

uncertainties, it is much reduced compared to $4b$ region, as discussed in Section 7.3.3.

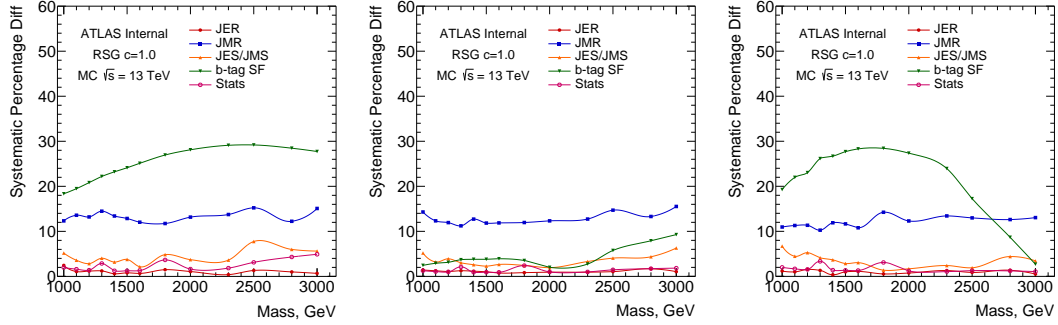


Figure 7.10: Impact of each systematic on the signal prediction as a function of the signal mass, in the $4b$ (left) and $3b$ (middle) and $2bs$ (right) signal regions.

Table 7.7: Percent impact of the dominant systematics on the background acceptance and on the signal acceptance of G_{KK}^* with $c = 1.0$ in the $4b$ signal region.

Four Tag	totalbkg	qcd	ttbar	RSG ₁ 1000	RSG ₁ 2000	RSG ₁ 3000
JER	0.45	0.27	3.98	2.44	1.07	0.67
JMR	7.9	10.35	39.95	12.33	13.16	15.08
Top	-	-	-	-	-	-
JES/JMS	1.32	1.49	24.36	5.18	3.72	5.62
Bkg Est	15.67	18.19	67.82	-	-	-
b-tag SF	1.11	0.79	18.85	18.34	28.11	27.73
Total Sys	17.64	21.0	84.62	22.83	31.28	32.07
Stat	3.13	3.29	2.47	1.97	1.63	4.9
Estimated Events	34.59	32.91	1.68	10.07	0.25	0.0016

Table 7.8: Percent impact of the dominant systematics on the background acceptance and on the signal acceptance of G_{KK}^* with $c = 1.0$ in the $3b$ signal region.

ThreeTag	totalbkg	qcd	ttbar	RSG ₁ 1000	RSG ₁ 2000	RSG ₁ 3000
JER	1.38	3.52	17.5	1.41	0.93	1.08
JMR	1.35	4.26	24.38	14.3	12.33	15.53
Top	-	-	-	-	-	-
JES/JMS	2.03	1.26	26.22	5.19	1.94	6.35
Bkg Est	4.84	5.62	9.45	-	-	-
b-tag SF	0.47	0.53	8.45	2.45	2.01	9.27
Total Sys	5.61	8.0	41.82	15.47	12.68	19.2
Stat	1.32	1.44	2.47	1.26	1.0	1.83
Estimated Events	780.89	701.52	79.38	26.0	0.76	0.013

Table 7.9: Percent impact of the dominant systematics on the background acceptance and on the signal acceptance of G_{KK}^* with $c = 1.0$ in the $2bs$ signal region.

TwoTag split	totalbkg	qcd	ttbar	RSG ₁ 1000	RSG ₁ 2000	RSG ₁ 3000
JER	0.25	0.48	3.14	1.18	0.74	0.5
JMR	0.52	1.73	9.43	10.96	12.3	13.03
Top	-	-	-	-	-	-
JES/JMS	0.43	1.67	7.17	6.72	1.7	3.55
Bkg Est	2.7	3.32	2.4	-	-	-
b-tag SF	0.83	1.43	1.82	19.28	27.36	2.72
Total Sys	2.92	4.37	12.62	23.2	30.05	13.79
Stat	0.6	0.41	2.47	2.0	1.2	1.07
Estimated Events	4251.49	3392.79	858.7	10.87	0.6	0.039

*Madness and genius are separated only by degrees of
success.*

8

Result

The signal regions in data were blinded to reduce the bias in selection optimization. After approval within the ATLAS analysis group, the signal regions were unblinded in July 2017. The unblinded boosted signal region results are shown in section 8.1. The resolved signal region results are shown in section 8.2. The boosted analysis observed limits for G_{KK}^* and scalar H are shown in section 8.3. The combined boosted and resolved limits are shown in section 8.4.

8.1 BOOSTED SIGNAL REGION

The unblinded signal region yields are summarized in Table 8.1. The $4b/3b/2bs$ channel unscaled m_{2J} distributions are shown in Figures 8.1, 8.2, and 8.3. No significant excess in the number of ob-

served events or in the dijet mass distributions is observed. The $4b/3b/2bs$ channel scaled m_{2J} distributions are shown in Figures 8.4, 8.5, and 8.6. Again, no significant excess in the scaled m_{2J} distributions is observed. No events are observed with m_{2J} or scaled m_{2J} above 4 TeV. The other kinematic distributions in the signal region are shown in Appendix C.

Table 8.1: Unblinded signal region predictions and results. All systematic uncertainties are included for backgrounds. The Poisson uncertainty in data is shown for comparison.

Sample	FourTag	ThreeTag	TwoTag split
qcd	32.92 ± 7.07	702.16 ± 63.12	3393.81 ± 148.78
ttbar	1.68 ± 1.43	79.41 ± 33.12	859.03 ± 107.86
totalbkg	34.6 ± 6.28	781.56 ± 52.42	4252.83 ± 125.73
Data	31.0 ± 5.57	801.0 ± 28.3	4376.0 ± 66.15

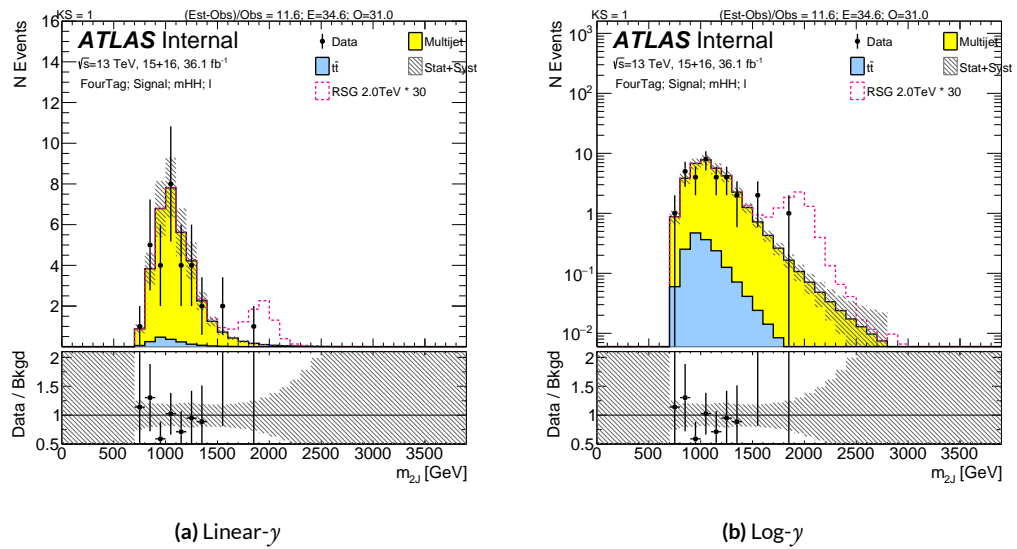


Figure 8.1: Unscaled m_{2J} distributions in the $4b$ signal region after unblinding.

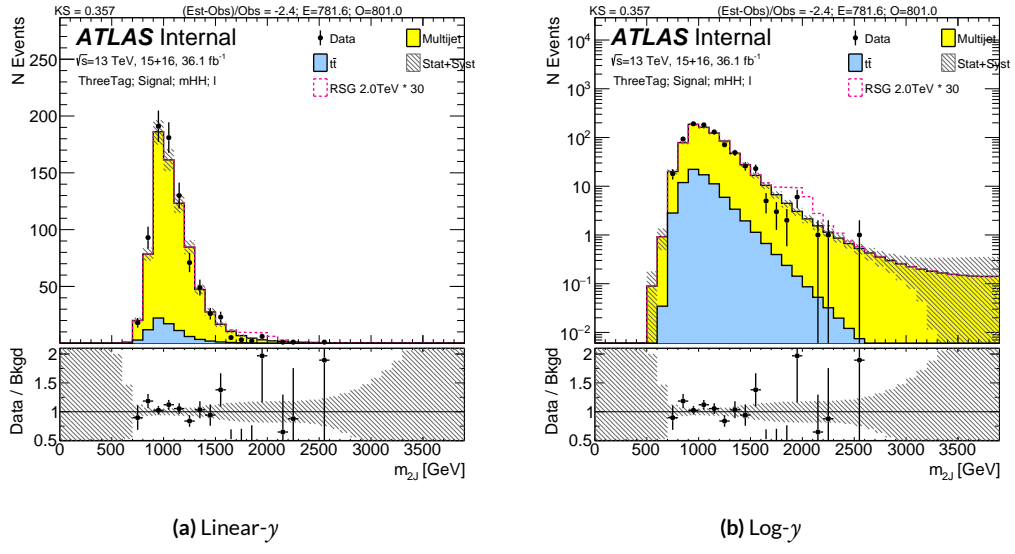


Figure 8.2: Unscaled m_{2J} distributions in the $3b$ signal region after unblinding.

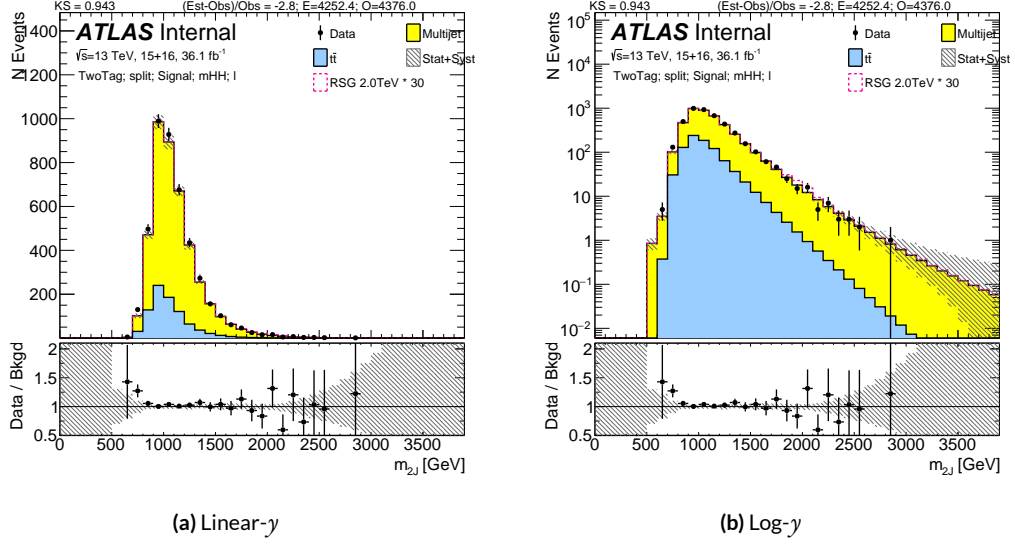
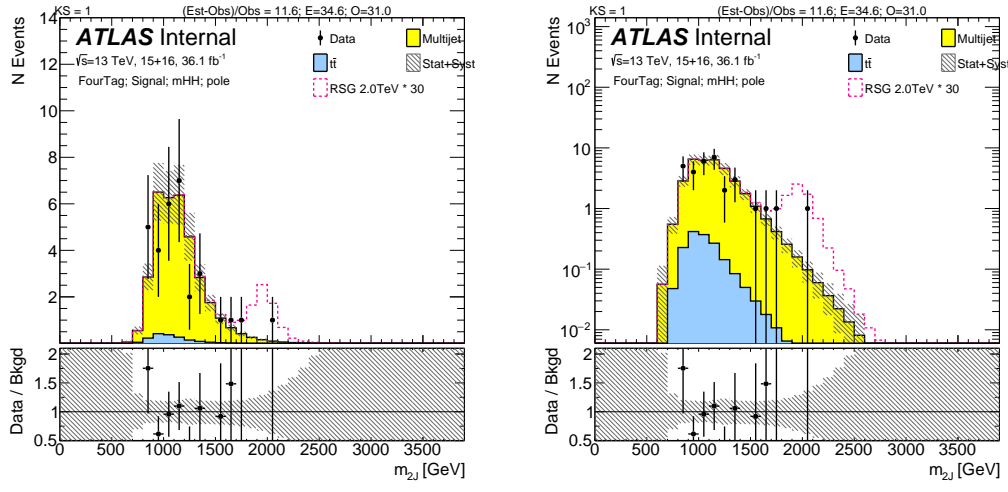
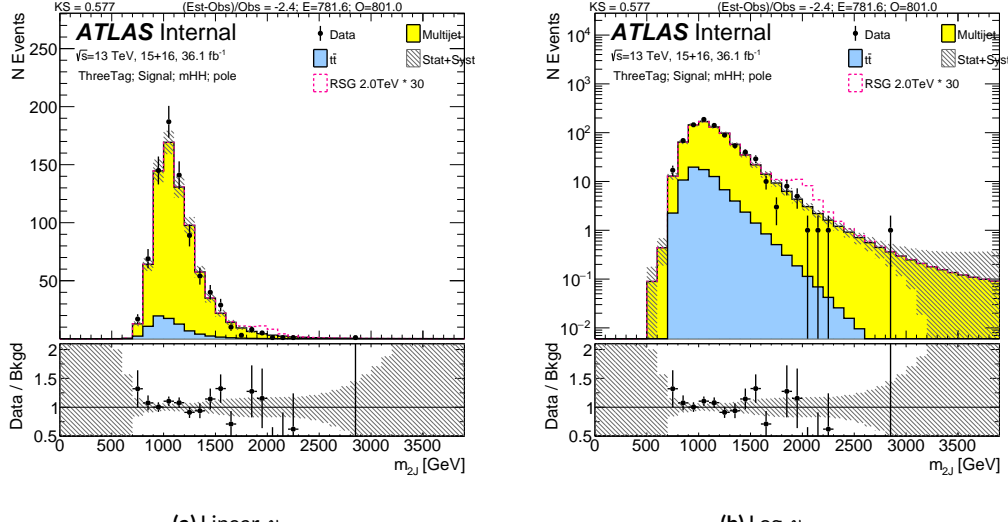


Figure 8.3: Unscaled m_{2J} distributions in the $2bs$ signal region after unblinding.

8.2 RESOLVED SIGNAL REGION

The number of events observed in the data, the predicted number of background events in the signal region, and the predicted yield for three potential signals are presented in Table 8.2 for both

(a) Linear- y (b) Log- y Figure 8.4: Scaled m_{2J} distributions in the $4b$ signal region after unblinding.(a) Linear- y (b) Log- y Figure 8.5: Scaled m_{2J} distributions in the $3b$ signal region after unblinding.

the 2015 and 2016 datasets. The numbers of observed and predicted events in the control region are also shown. A discrepancy between data and the total prediction is seen in the 2016 dataset; about

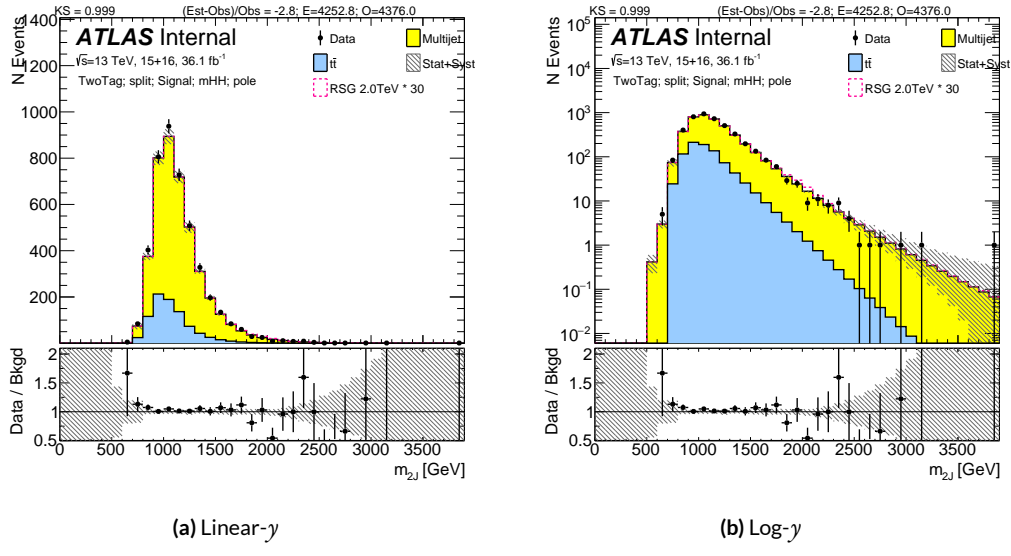


Figure 8.6: Scaled m_{2J} distributions in the $2b$ signal region after unblinding.

half of this excess can be attributed to one bin at $m_{4j} = 280$ GeV. This could be a trigger turn-on effect.

Table 8.2: The number of predicted background events in the signal region for the resolved analysis compared to the data, for the 2015 and 2016 datasets. The yields for three potential signals, an 800 GeV G_{KK}^* resonance with $c = 1$, a scalar with a mass of 280 GeV, and SM non-resonant Higgs boson pair production, are also shown. The scalar sample is normalized to a cross section times branching ratio of 2.7 pb. The quoted uncertainties include both the statistical and systematic uncertainties, and the total uncertainty considers correlations. The numbers of observed and predicted events are also given in the control region.

Sample	2015 SR	2016 SR	2015 CR	2016 CR
Multijet	866 ± 70	6750 ± 170	880 ± 71	7110 ± 180
$t\bar{t}$, hadronic	52 ± 35	259 ± 57	56 ± 37	276 ± 61
$t\bar{t}$, leptonic	13.9 ± 6.5	123 ± 30	20 ± 9	168 ± 40
Total	930 ± 70	7130 ± 130	956 ± 50	7550 ± 130
Data	928	7430	969	7656
$G_{KK}^*(800 \text{ GeV})$	12.5	1.9	89	14
Scalar (280 GeV)	24	7.5	180	57
SM di-Higgs	0.607	0.091	4.43	0.66

Figure 8.7 shows comparisons of the predicted m_{4j} background distributions to those observed in the 2015 and 2016 datasets. A few signal models are also displayed. The scalar sample shown is normalized to a cross section times $b \rightarrow b\bar{b}$ branching ratio of 2.7 pb, which is the best-fit value. The predicted background and observed distributions are mostly in agreement, with an excess above the predicted background in one bin around 280 GeV.

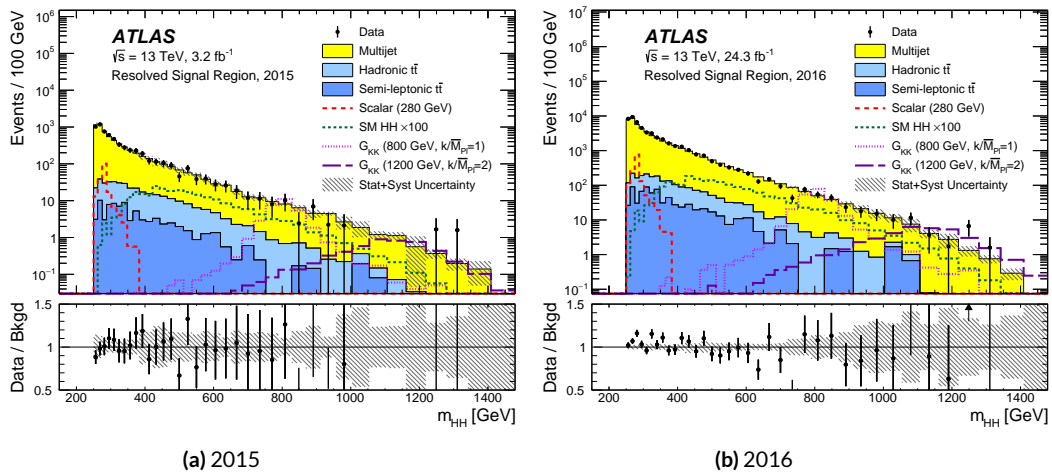


Figure 8.7: Distributions of m_{4j} in the signal region of the resolved analysis for (a) 2015 data and (b) 2016 data, compared to the predicted backgrounds. The hatched bands shown in the bottom panels represent the combined statistical and systematic uncertainties in the total background estimates. The expected signal distributions of G_{KK}^* resonances with masses of 800 and 1200 GeV, the 280 GeV scalar sample and SM non-resonant di-Higgs production ($\times 100$) are also shown. The scalar sample is normalized to a cross section times branching ratio of 2.7 pb.

8.3 STATISTICAL ANALYSIS

Following the statistical procedures outlined in Ref.⁷⁸, a test statistic based on the profile likelihood ratio⁷⁹ is used to test hypothesized values of $\mu = \sigma/\sigma_{\text{model}}$, the global signal strength factor, separately for each signal model. The exclusion limits are computed using asymptotic formula⁷⁹ and are based on the CL_s method⁸⁰, where a value of μ is regarded as excluded at the 95% confidence level (CL) when CL_s is less than 5%.

The test statistic used is a one sided profile likelihood ratio:

$$q_o = -2 \ln \frac{L(o, \hat{\vartheta}(o))}{L(\hat{\mu}, \hat{\vartheta})}; \hat{\mu} > o \quad (8.1)$$

$$q_o = o; \hat{\mu} < o \quad (8.2)$$

where μ is the value of the signal normalization considered, and $\hat{\mu}$ is the maximum likelihood (ML) value of μ . ϑ is the set of nuisance parameters (NP): $\hat{\vartheta}$ is the ML value of ϑ and $\hat{\vartheta}$ is the ML value of ϑ when μ is fixed at a particular value. L denotes the profile likelihood: $L(\hat{\mu}, \hat{\vartheta})$ is the likelihood where μ is allowed to take any value, the unconstrained likelihood. $L(o, \hat{\vartheta}(o))$ is the likelihood for the value of $\mu = o$, the constrained likelihood.

This tests the compatibility of the data with the background-only hypothesis, $\mu = o$. The local p-value of a set of data, p_o , is defined as the probability for the background-only hypothesis to have a value of q_o that is higher than the value of q_o in that data. In order to obtain p_o , pseudo-experiments are generated with the background only model, and the distribution of the test statistic, q_o , is built up from the values of the pseudo-experiments.

The background model is found to describe the data, and no significant excess is observed. The smallest local $p_o = 0.175$ (1σ) is found at 1100 GeV when fitting with the narrow scalar model. The local p_o values for the three signal models as a function of the resonance mass are shown in Fig. 8.8.

Figure 8.9 shows the pulls of the systematic uncertainty nuisance parameters and their correlations for the 2000 GeV mass point. The parameters are ranked by their post-fit impact on $\hat{\mu}$. Only the leading 30 nuisance parameters are displayed. One nuisance parameter (QCD_ShapeCRHigh) in both the $2b$ and $3b$ samples shows a significant constraint coming from the signal region data. This nuisance parameter corresponds to the shape uncertainty on the QCD background derived

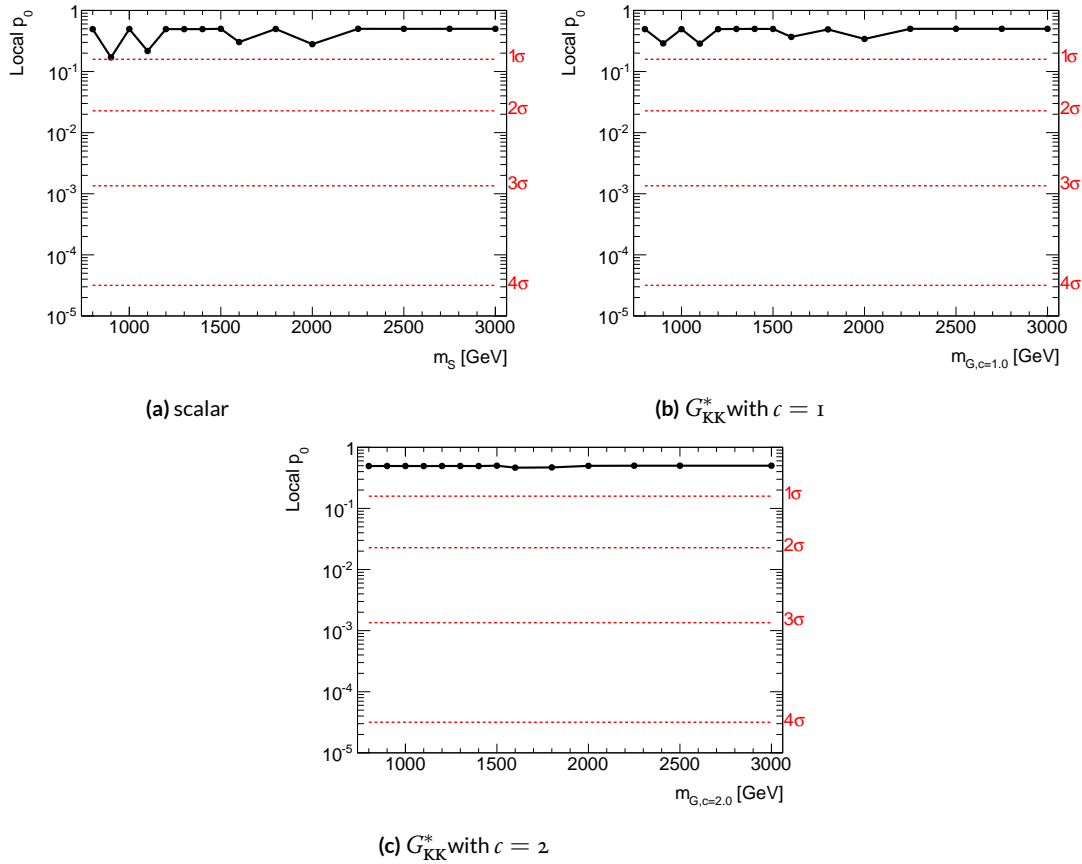


Figure 8.8: Local p_o of the (a) scalar, (b) G_{KK}^* with $c = 1$, and (c) G_{KK}^* with $c = 2$.

from the $2b$ and $3b$ control regions, as explained in section 7.8. The prior probability distributions for this nuisance parameter are very broad. The relative uncertainty on the background prediction is extremely high at high m_{2J} . This is because there is very little data in the control region at high mass to constrain this uncertainty.

Examples of the fit used to set these limits are shown in Figure 8.10, where a narrow-width scalar H is used for the signal model. In cases where the best-fit is negative, the fit is repeated with μ bounded to zero. At 2 TeV, the fitted signal is positive ($\mu = 0.1 \pm 0.25$) though consistent with the background-only hypothesis. In all fits, good agreement is seen between data and the background only model.

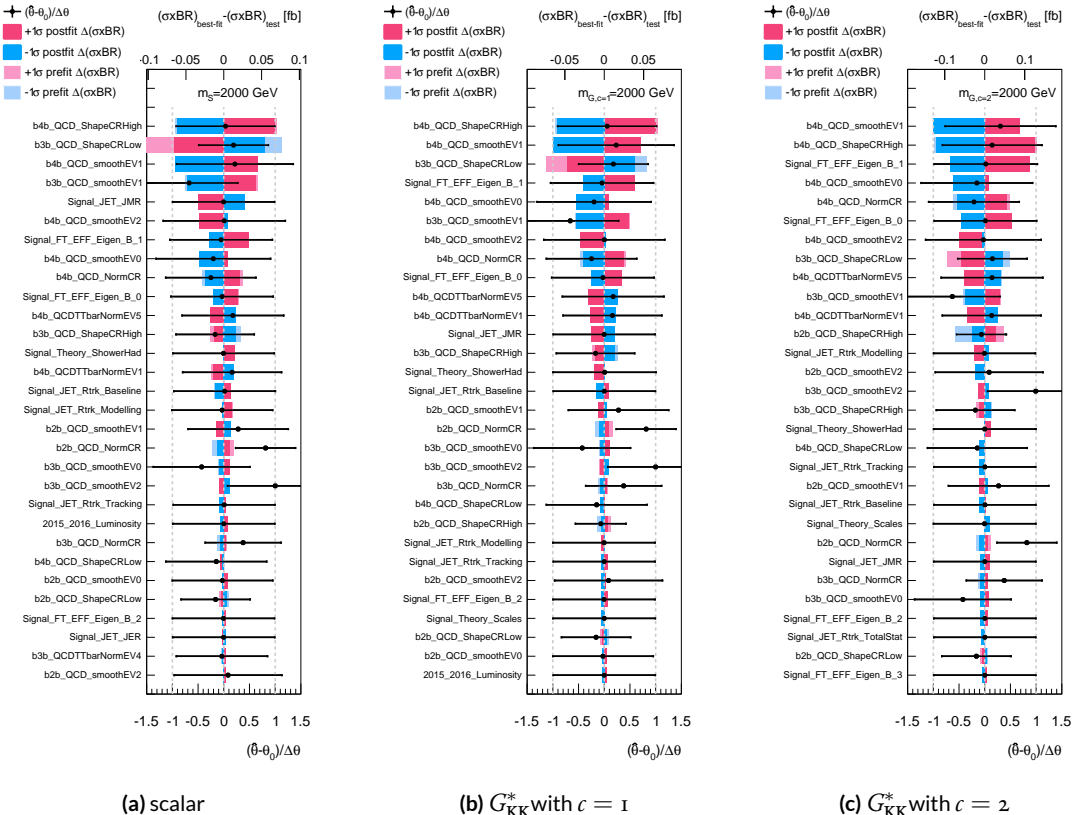


Figure 8.9: The impact of nuisance parameters on the fitted cross section, ranked by their post-fit impact. The signal mass used in these fits is 2000 GeV, and the signal model is (a) narrow scalar, (b) G_{KK}^* with $c = 1$, and (c) G_{KK}^* with $c = 2$.

The observed limit for the narrow scalar and G_{KK}^* are shown in Figures 8.11, 8.12, and 8.13. The stat-only limit is also shown. The impact of systematic uncertainties is small. These limits do not contain any input from the resolved analysis.

8.4 BOOSTED AND RESOLVED COMBINED LIMITS

The observed limits for the Graviton models is shown in Figure 8.14 for $c = 1$ and in Figure 8.15 for $c = 2$. The observed limit for the narrow scalar is shown in Figure 8.16. The bulk RS model with $c = 1$ is excluded for masses between 313 and 1362 GeV, and the bulk RS model with $c = 2$ is

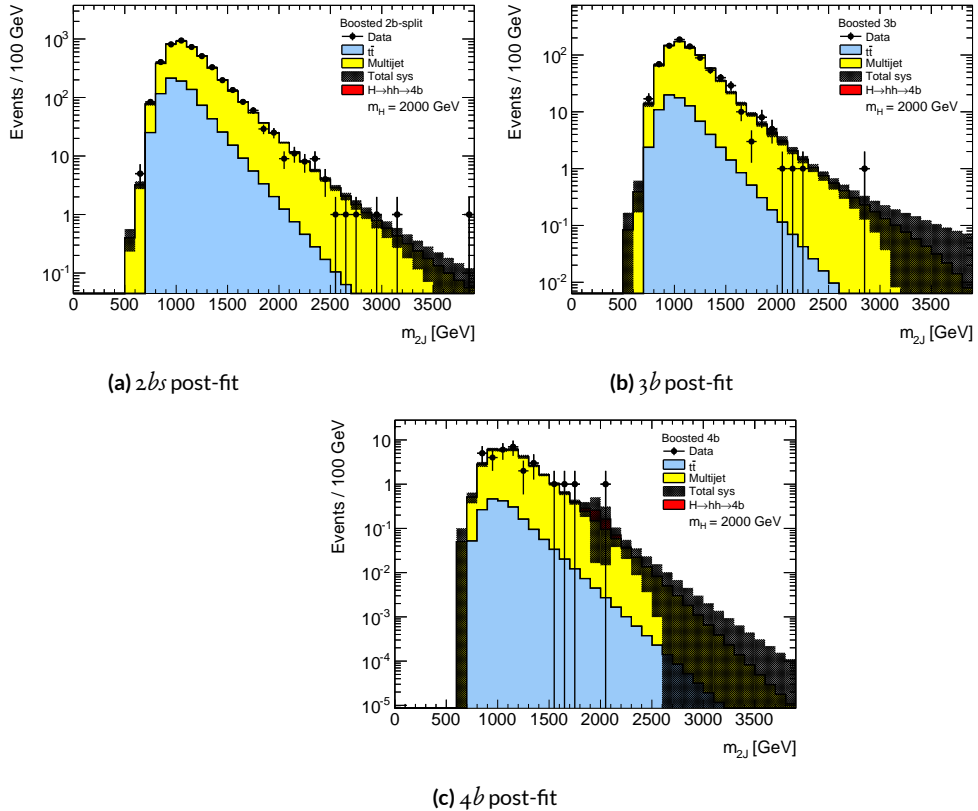


Figure 8.10: Post-fit signal region scaled m_{2J} distributions after fitting the data with the 2 TeV G_{KK}^* with $c = 1.0$ hypothesis. The signal strength is slightly positive.

excluded for masses below 1744 GeV. In the heavy Higgs model, the cross section upper limits for $\sigma(pp \rightarrow H \rightarrow hh \rightarrow b\bar{b}b\bar{b})$ range from 1 to 10 fb in the 1000 to 3000 GeV mass range.

Different expected exclusion limits from the analysis can be compared in Figure 8.16. The resolved analysis is only sensitive to resonance searches up to 900 GeV. The boosted 4 b is most sensitive for resonances between 1200 and 1800 GeV. The boosted 3 b is most sensitive for resonances between 2000 and 2500 GeV. The boosted 2 b s is most sensitive for resonances between 2500 and 3000 GeV. The combination significantly improves the sensitivity between 1 and 1.5 TeV for resonant signals. The result is limited by systematic uncertainties in the background normalization and shape. Since

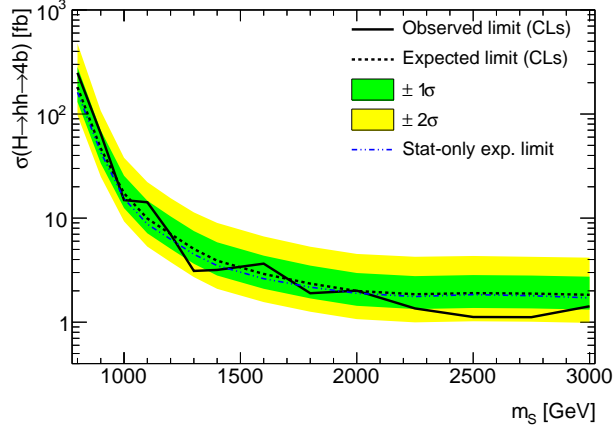


Figure 8.11: The expected and observed 95% CL upper exclusion limits for the boosted analysis calculated including all systematic uncertainties for the narrow scalar model. The dot-dashed line shows the expected limit when only statistical uncertainties are included. The limits are derived with the asymptotic approximation.

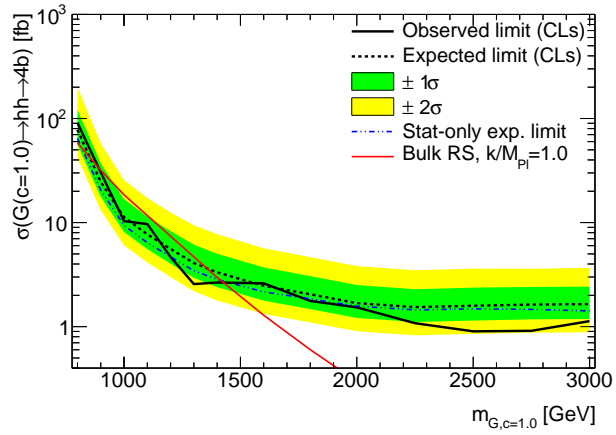


Figure 8.12: The expected and observed 95% CL upper exclusion limits for the boosted analysis calculated including all systematic uncertainties for the $c = 1.0$ Graviton. The dot-dashed line shows the expected limit when only statistical uncertainties are included. The limits are derived with the asymptotic approximation.

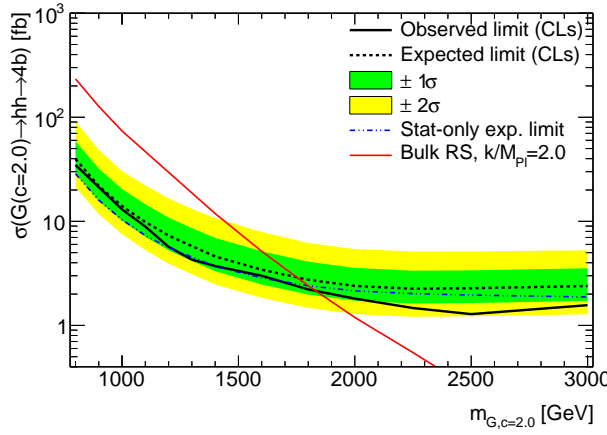


Figure 8.13: The expected and observed 95% CL upper exclusion limits for the boosted analysis calculated including all systematic uncertainties for the $c = 2.0$ Graviton. The dot-dashed line shows the expected limit when only statistical uncertainties are included. The limits are derived with the asymptotic approximation.

these are data-driven, an increase of the integrated luminosity will improve the sensitivity.

The non-resonant search is performed using the resolved analysis only, since it has much better sensitivity to non-resonant signals than the boosted analysis. Using SM di-Higgs non-resonant production via gluon–gluon fusion as the signal model and applying the NNLO and finite top-quark mass correction, the observed 95% CL upper limit is $\sigma(pp \rightarrow hh \rightarrow b\bar{b}b\bar{b}) < 147$ fb. The expected and observed limit values and the associated uncertainties are given in Table 8.3. The observed limit is stronger than the expected due to the slight deficit of events in m_{4j} around 500 – 600 GeV.

Table 8.3: 95% CL exclusion limits for SM non-resonant di-Higgs production, in units of the SM predicted value for $\sigma(pp \rightarrow hh \rightarrow b\bar{b}b\bar{b})$.

Observed	-2σ	-1σ	Expected	$+1\sigma$	$+2\sigma$
13.0	11.1	14.9	20.7	30.0	43.5

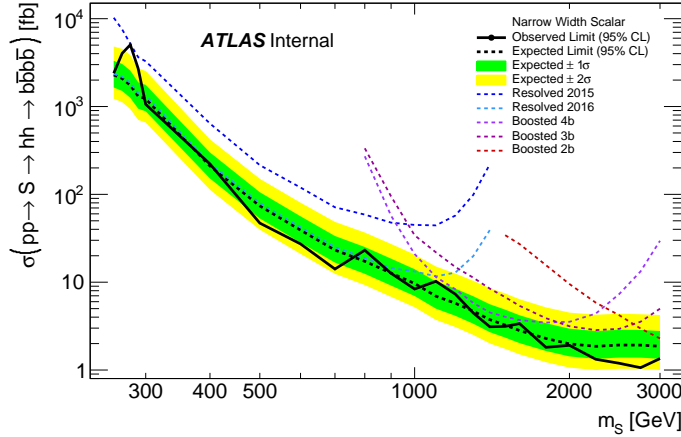


Figure 8.14: The expected and observed 95% CL upper exclusion limits for the combined analysis calculated including all systematic uncertainties for the narrow scalar model. The dot-dashed line shows the expected limit when only statistical uncertainties are included. The limits are derived with the asymptotic approximation.

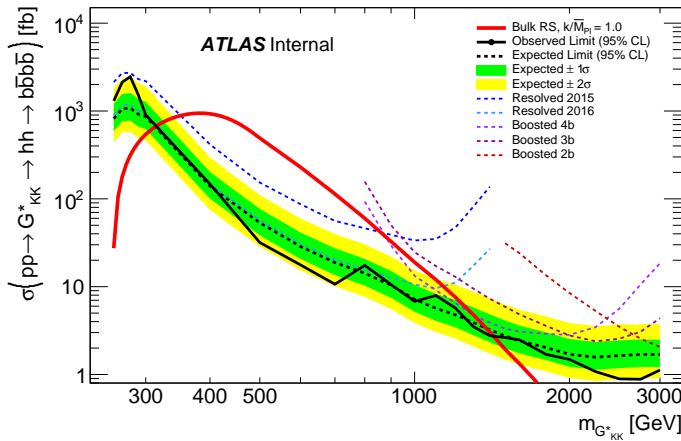


Figure 8.15: The expected and observed 95% CL upper exclusion limits for the combined analysis calculated including all systematic uncertainties for the $c = 1.0$ G_{KK}^* . The dot-dashed line shows the expected limit when only statistical uncertainties are included. The limits are derived with the asymptotic approximation.

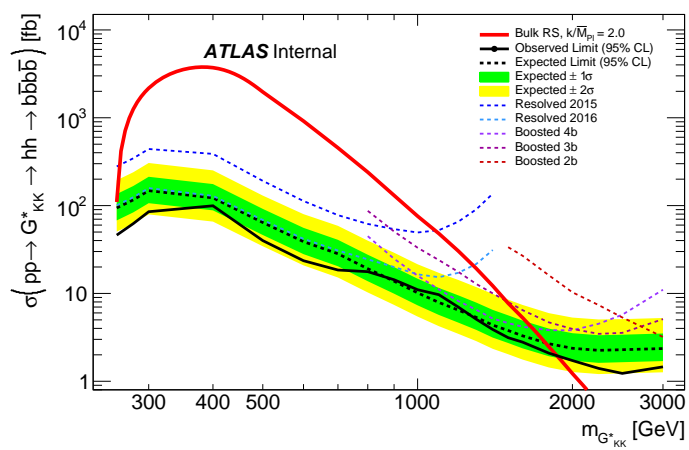


Figure 8.16: The expected and observed 95% CL upper exclusion limits for the combined analysis calculated including all systematic uncertainties for the $c = 2.0$ G^*_{KK} . The dot-dashed line shows the expected limit when only statistical uncertainties are included. The limits are derived with the asymptotic approximation.

*It is a far, far better thing that I do, than I have ever
done; it is a far, far better rest that I go to than I have
ever known.*

Charles Dickens

9

Conclusion

The searches for di-Higgs production have a short history, but they will have a long future. This thesis presents a search for both resonant and non-resonant production of pairs of Standard Model Higgs bosons in the dominant $b\bar{b}b\bar{b}$ channel, using 36.1 fb^{-1} of LHC pp collision data at $\sqrt{s} = 13 \text{ TeV}$ collected by ATLAS in 2015 and 2016. The search sensitivity of this analysis exceeds that of the previous analysis of the $\sqrt{s} = 13 \text{ TeV}$ 2015 dataset⁸¹ for non-resonant signal and also across the entire mass range of 260 to 3000 GeV for the resonance search, with significant improvement in the high mass resonance region. The resolved analysis reconstructs each $h \rightarrow b\bar{b}$ decay as two separate b -tagged jets, while the boosted analysis reconstructs each $h \rightarrow b\bar{b}$ decay as a single large-radius jet associated with at least one small-radius b -tagged track jet. The estimated background consists mainly of multi-jet and $t\bar{t}$ events.

No significant excess is observed in the data. Upper limits at 95% confidence level on the production cross-section times branching ratio to the $b\bar{b}b\bar{b}$ final state are set for a narrow-width spin-0 scalar and for wider spin-2 resonances. The bulk RS model with $c = 1$ is excluded for masses between 313 and 1362 GeV, and the bulk RS model with $c = 2$ is excluded for masses below 1744 GeV. The upper limit on the non-resonant production is 147 fb, which corresponds to 13.0 times the SM expectation. This result confirms the great success of the Standard Model. In light of these results, the Higgs potential shape at the TeV energy scale is currently consistent with the SM prediction. Without any significant excess, the phase space for beyond the Standard Model physics is further constrained.

Increased sensitivity with future Run 2 and beyond datasets could come through efficiency improvements in b -tagging for the high p_T jets. Other improvements involve advanced trigger technologies, which would increase the number of signal events recorded, as well as improvements in jet energy and mass resolution, which would increase the purity of the signal selection. These improvements, combined with a larger dataset, may double the current resonance search sensitivity. For the non-resonance search, a combined sensitivity of $|\frac{\lambda}{\lambda_{SM}}| \sim 10$ is possible at the end of Run 2 in 2020.

Di-Higgs searches and measurements will continue to be some of the most important analyses. These measurements can show hints of the physics beyond the Standard Model. After the 2030 to 2040 run, the High Luminosity LHC will be able to constrain $|\frac{\lambda}{\lambda_{SM}}| \sim 1$ with all the different channels from both ATLAS and CMS combined. Future electron-electron colliders can produce di-Higgs events from ZH channel and could further constrain $|\frac{\lambda}{\lambda_{SM}}| \sim 0.3$. This requires combined advances in accelerator and detector technology, computation, and theoretical precision^{82,83}.

Life is short, and the understanding of the universe is an endless journey. I am deeply honored to have been a small part of this odyssey by working on the boosted $pp \rightarrow hh \rightarrow b\bar{b}b\bar{b}$ analysis.

A

Boosted sideband region kinematic distributions

This appendix shows comparisons of data with the prediction of QCD multi-jets and $t\bar{t}$ backgrounds in the control region. The definition of the sideband region is discussed in Section 6.2. Because of the fit method in Section 6.5, the predicted normalization agrees perfectly with data. The

agreement of the data and predictions is generally very good, without significant deviations.

Figures A.1, A.2, A.3, and A.4 show predictions of various kinematics of the large- R jets and their associated track jets in the $4b$ selection. Figures A.5, A.6, A.7, and A.8 show predictions of various kinematics of the large- R jets and their associated track jets in the $3b$ selection. Figures A.9, A.10, A.11, and A.12 show predictions of various kinematics of the large- R jets and their associated track jets in the $2bs$ selection.

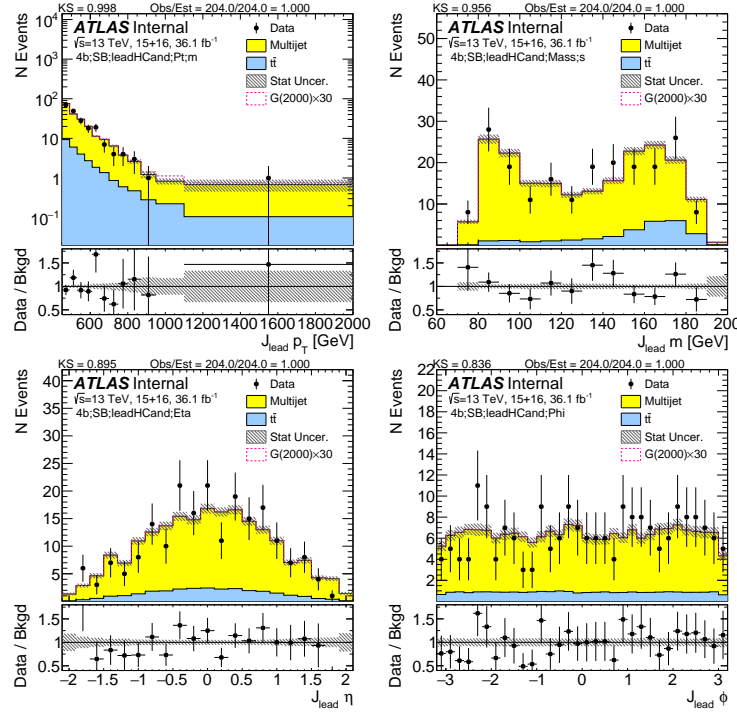


Figure A.1: Kinematics (p_T , mass, η , ϕ) of the lead large- R jet in data and prediction in the sideband region after requiring $4 b$ -tags.

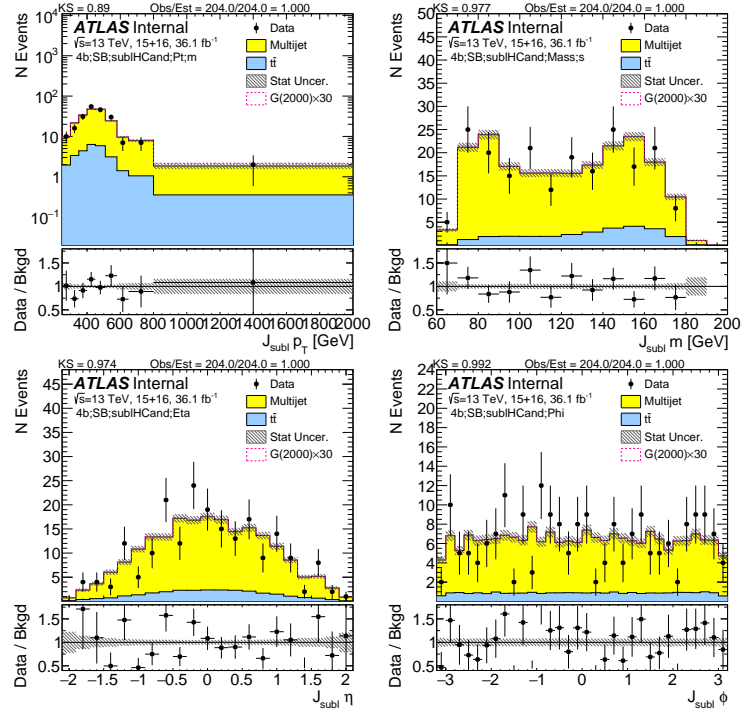


Figure A.2: Kinematics (p_T , mass, η , ϕ) of the subleading large- R jet in data and prediction in the sideband region after requiring 4 b -tags.

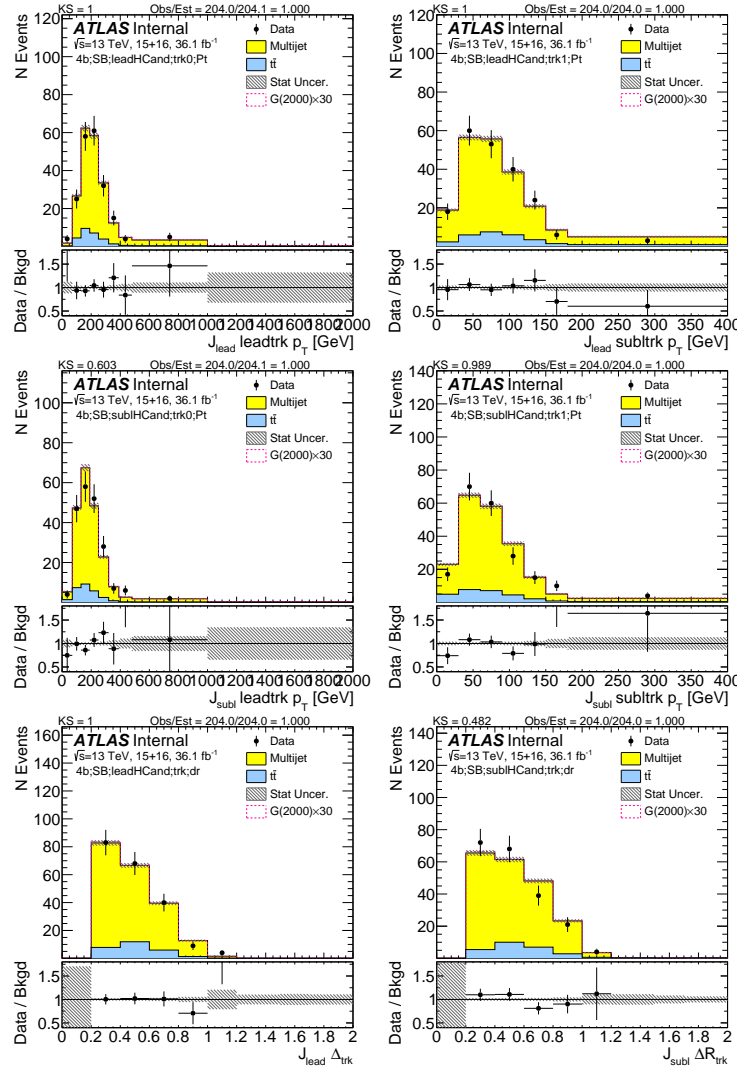


Figure A.3: First two rows show the p_T of the lead (left) and sub-lead (right) small- R track jets associated to the lead (first-row) and sub-lead (second-row) large- R jet in data and prediction in the sideband region after requiring 4 b -tags. Third row shows the ΔR between two leading small- R track-jets associated to the leading (left) and sub-leading (right) large- R jet.

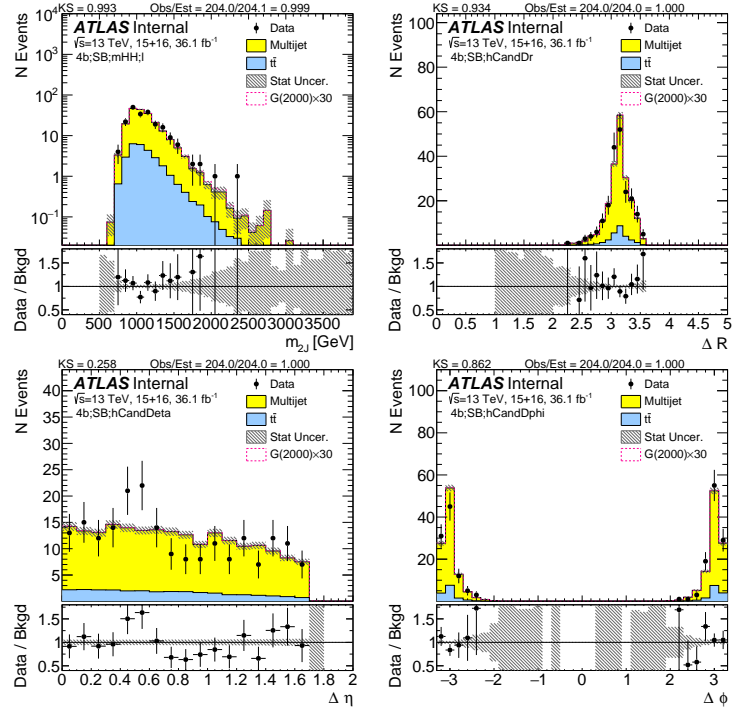


Figure A.4: Kinematics (invariant mass, ΔR , $\Delta\eta$ and $\Delta\phi$) of two large- R jets in data and prediction in the sideband region after requiring 4 b -tags.

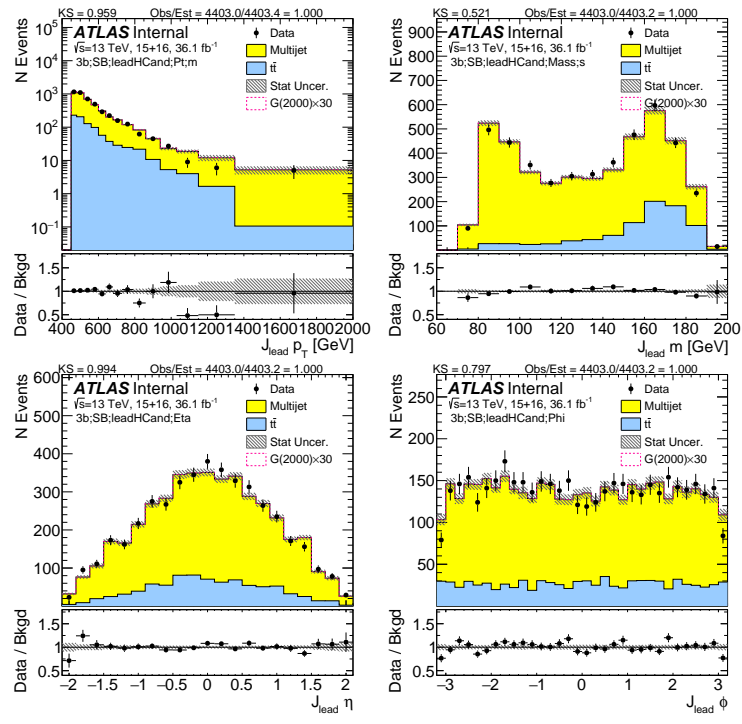


Figure A.5: Kinematics (p_T , mass, η , ϕ) of the lead large- R jet in data and prediction in the sideband region after requiring 3 b -tags.

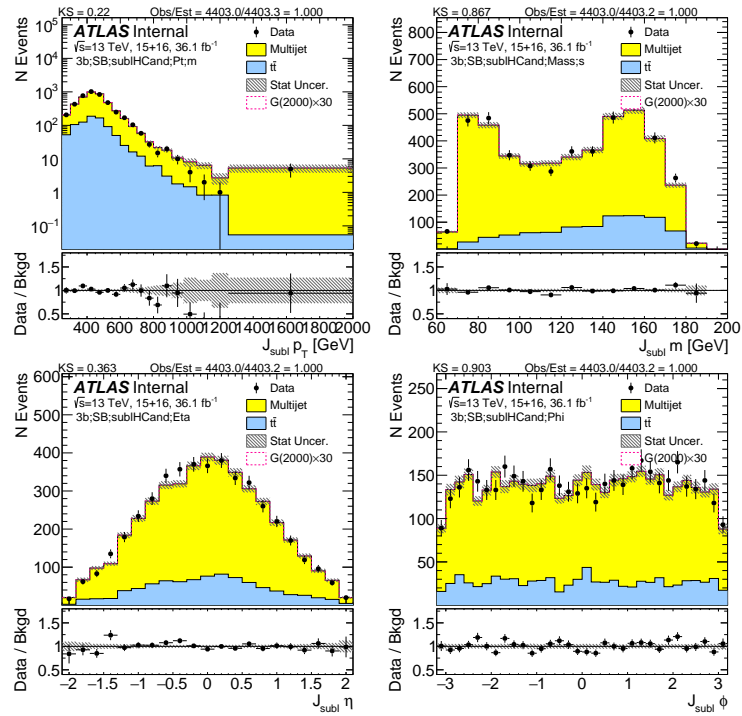


Figure A.6: Kinematics (p_T , mass, η , ϕ) of the subleading large- R jet in data and prediction in the sideband region after requiring 3 b -tags.

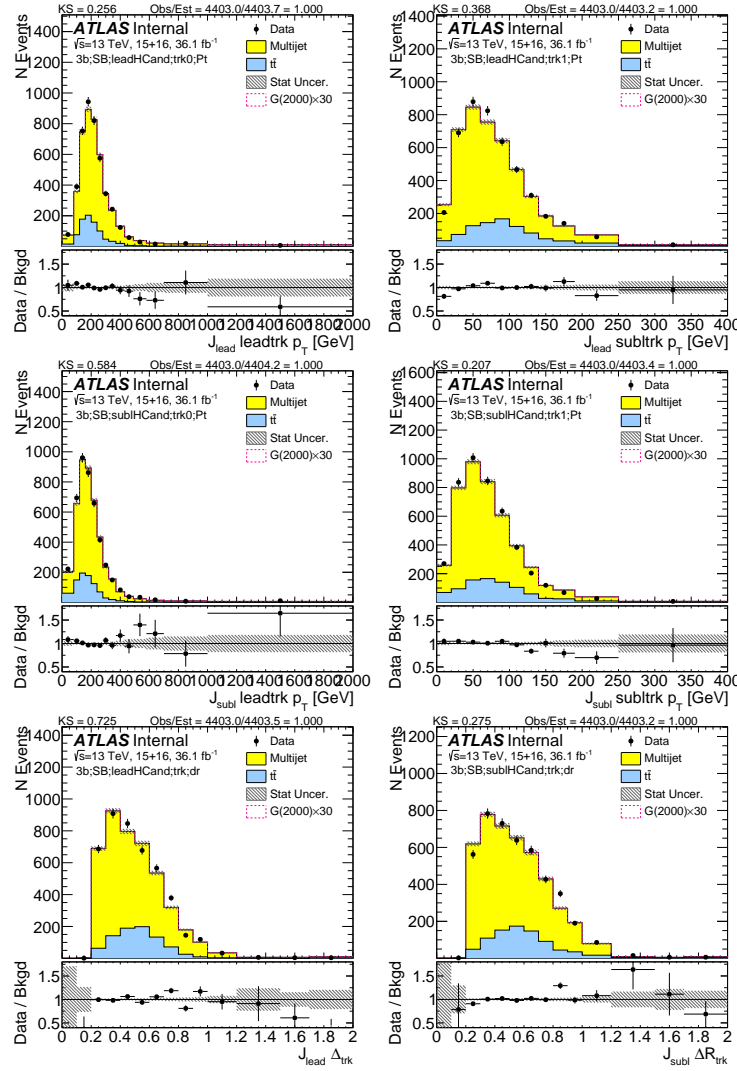


Figure A.7: First two rows show the p_T of the lead (left) and sub-lead (right) small- R track jets associated to the lead (first-row) and sub-lead (second-row) large- R jet in data and prediction in the sideband region after requiring 3 b -tags. Third row shows the ΔR between two leading small- R track-jets associated to the leading (left) and sub-leading (right) large- R jet.

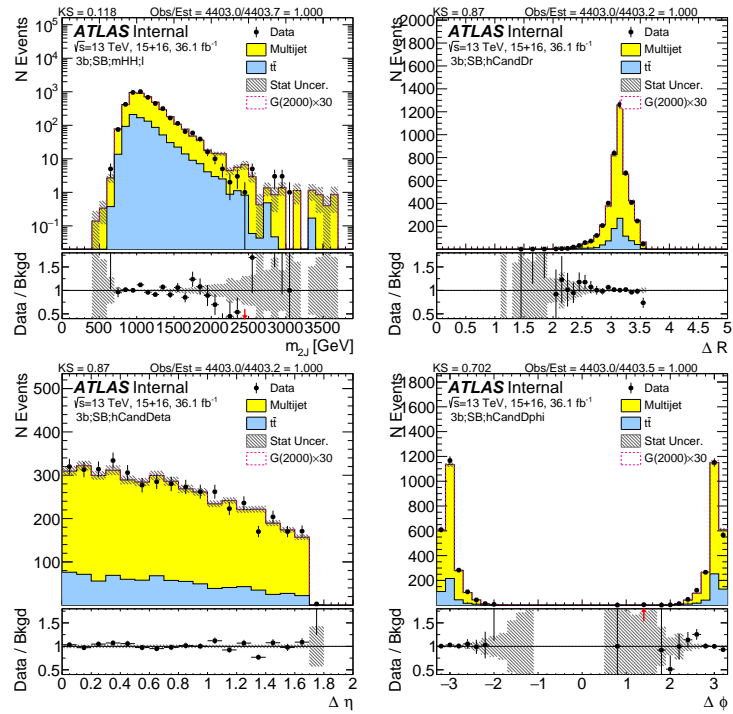


Figure A.8: Kinematics (invariant mass, ΔR , $\Delta\eta$ and $\Delta\phi$) of two large- R jets in data and prediction in the sideband region after requiring 3 b -tags.

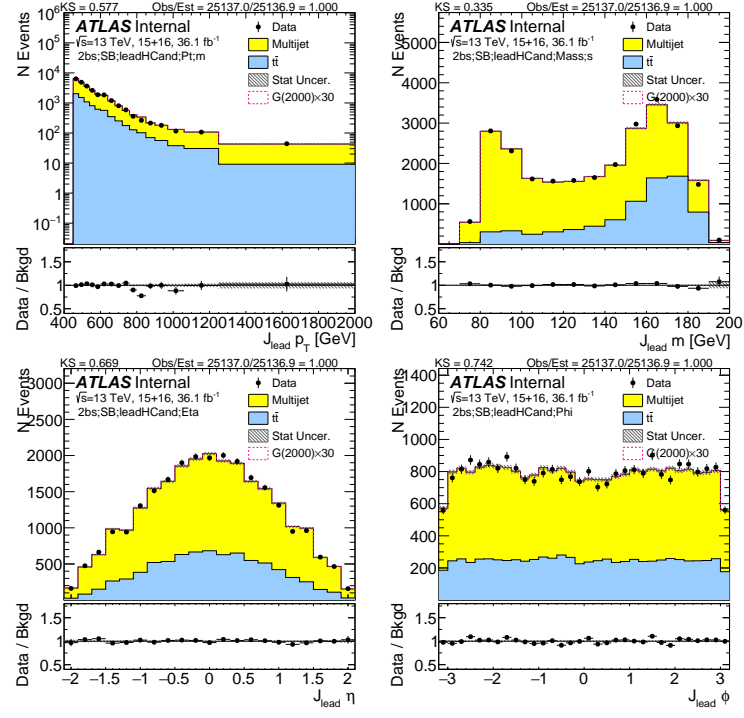


Figure A.9: Kinematics (p_T , mass, η , ϕ) of the lead large- R jet in data and prediction in the sideband region after requiring 2 b -tags split.

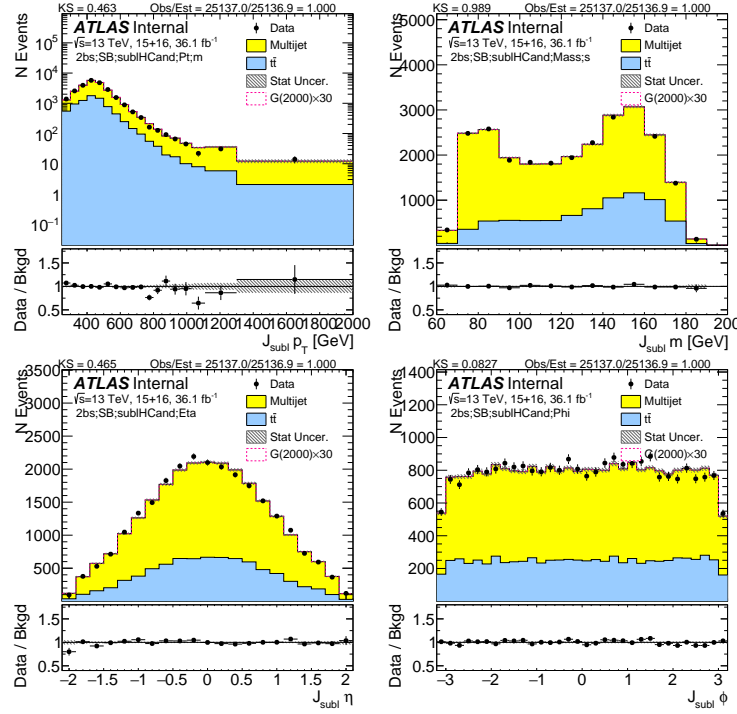


Figure A.10: Kinematics (p_T , mass, η , ϕ) of the subleading large- R jet in data and prediction in the sideband region after requiring 2 b -tags split.

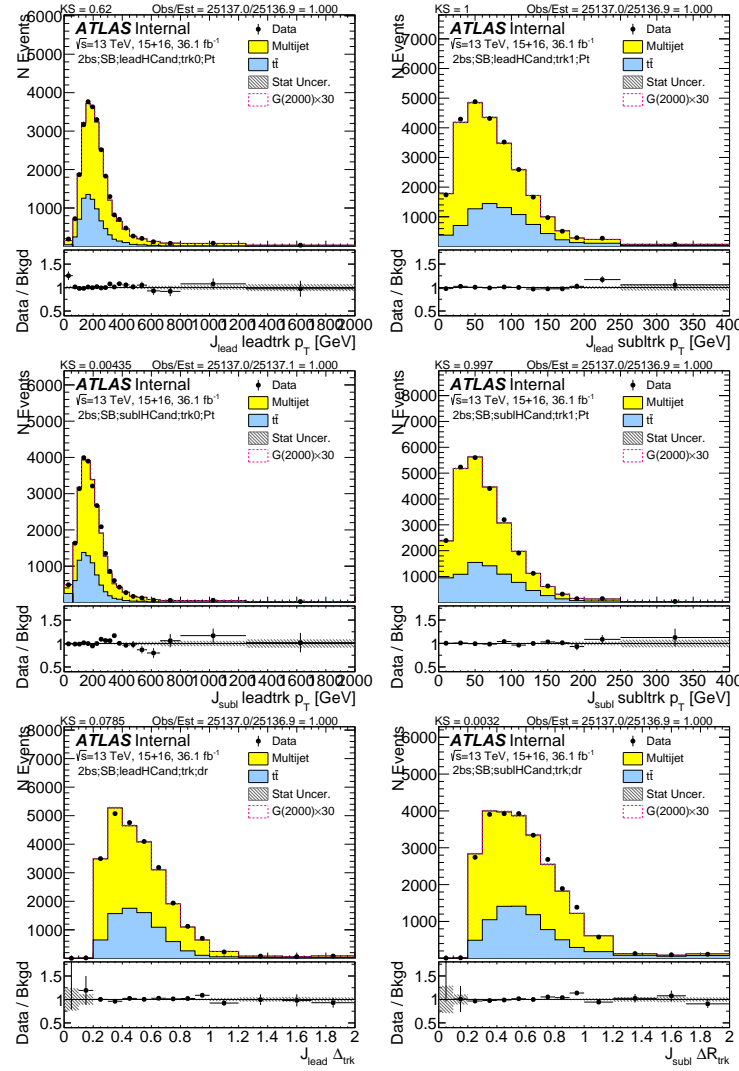


Figure A.11: First two rows show the p_T of the lead (left) and sub-lead (right) small- R track jets associated to the lead (first-row) and sub-lead (second-row) large- R jet in data and prediction in the sideband region after requiring 2 b -tags split. Third row shows the ΔR between two leading small- R track-jets associated to the leading (left) and sub-leading (right) large- R jet.

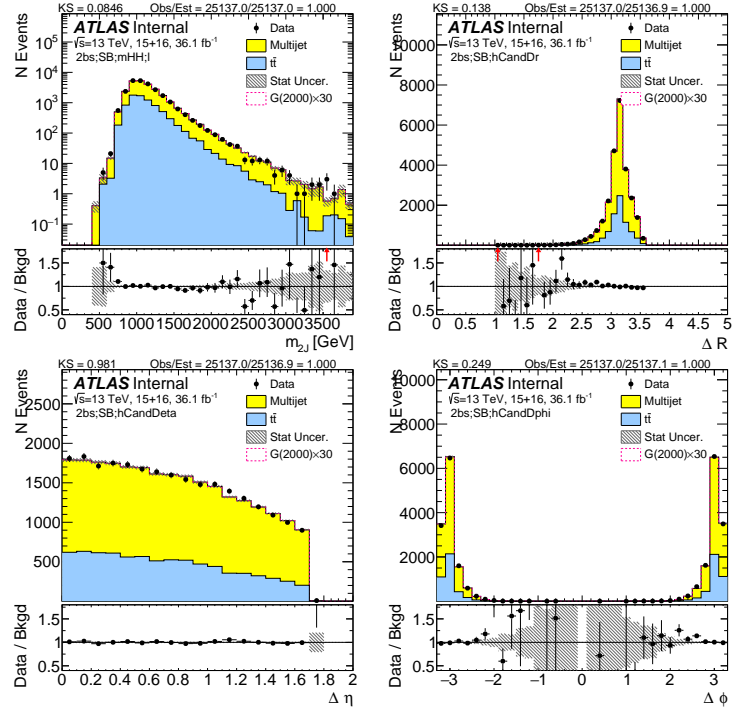


Figure A.12: Kinematics (invariant mass, ΔR , $\Delta\eta$ and $\Delta\phi$) of two large- R jets in data and prediction in the sideband region after requiring 2 b -tags split.

B

Boosted control region kinematic distributions

This section shows comparisons of data with the prediction of QCD multi-jets and $t\bar{t}$ backgrounds in the control region. The definition of the control region is discussed in Section 6.2. The agreement between data and background prediction is generally good, without any systematic biases

observed.

Figures B.1, B.2, B.3, and B.4 show predictions of various kinematics of the large- R jets and their associated track jets in the $4b$ selection. Figures B.5, B.6, B.7, and B.8 show predictions of various kinematics of the large- R jets and their associated track jets in the $3b$ selection. Figures B.9, B.10, B.11, and B.12 show predictions of various kinematics of the large- R jets and their associated track jets in the $2bs$ selection.

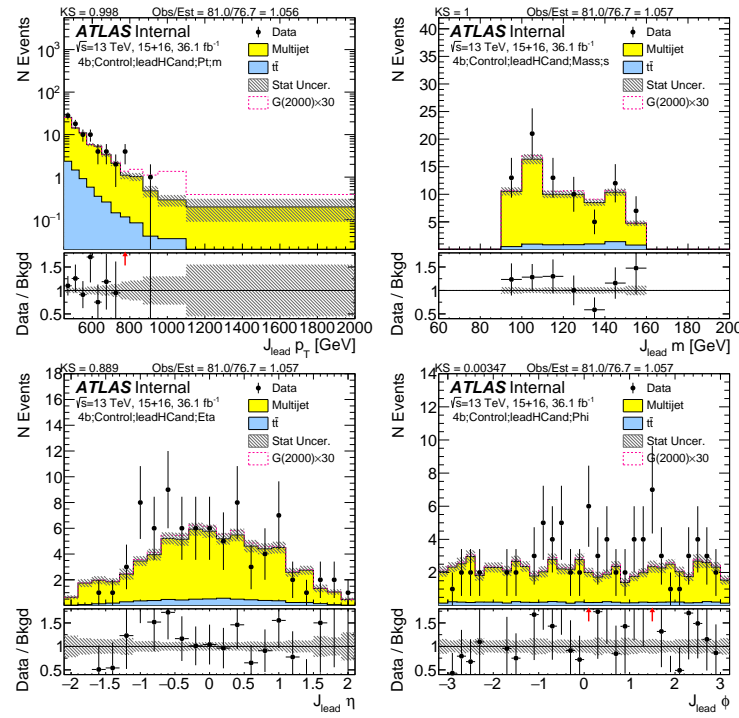


Figure B.1: Kinematics (p_T , mass, η , ϕ) of the lead large- R jet in data and prediction in the control region after requiring $4 b$ -tags.

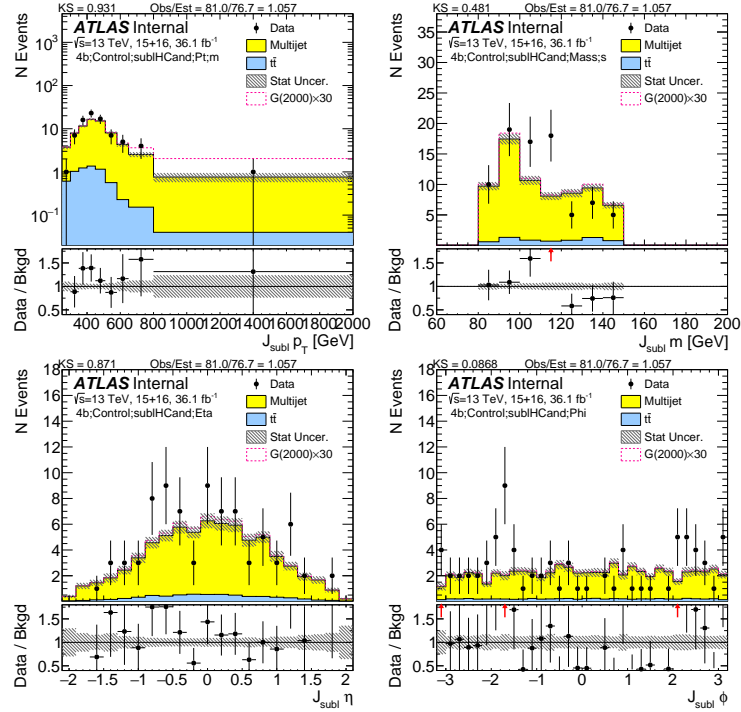


Figure B.2: Kinematics (p_T , mass, η , ϕ) of the subleading large- R jet in data and prediction in the control region after requiring 4 b -tags.

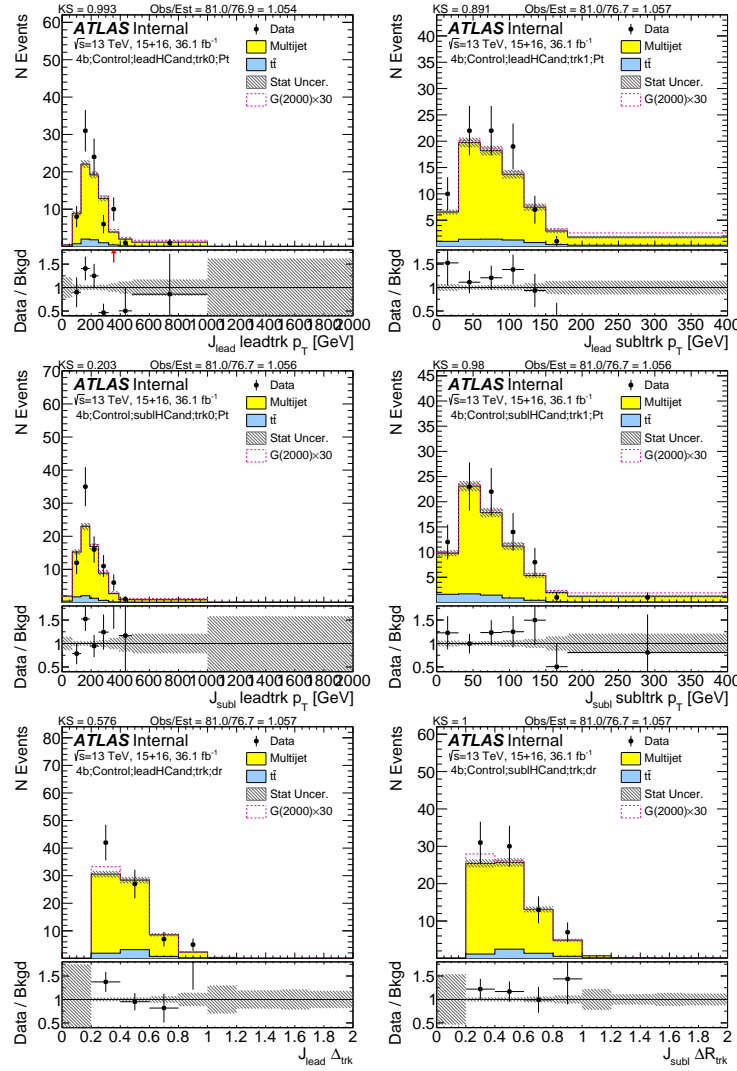


Figure B.3: First two rows show the p_T of the lead (left) and sub-lead (right) small- R track jets associated to the lead (first-row) and sub-lead (second-row) large- R jet in data and prediction in the control region after requiring 4 b -tags. Third row shows the ΔR between two leading small- R track-jets associated to the leading (left) and sub-leading (right) large- R jet.

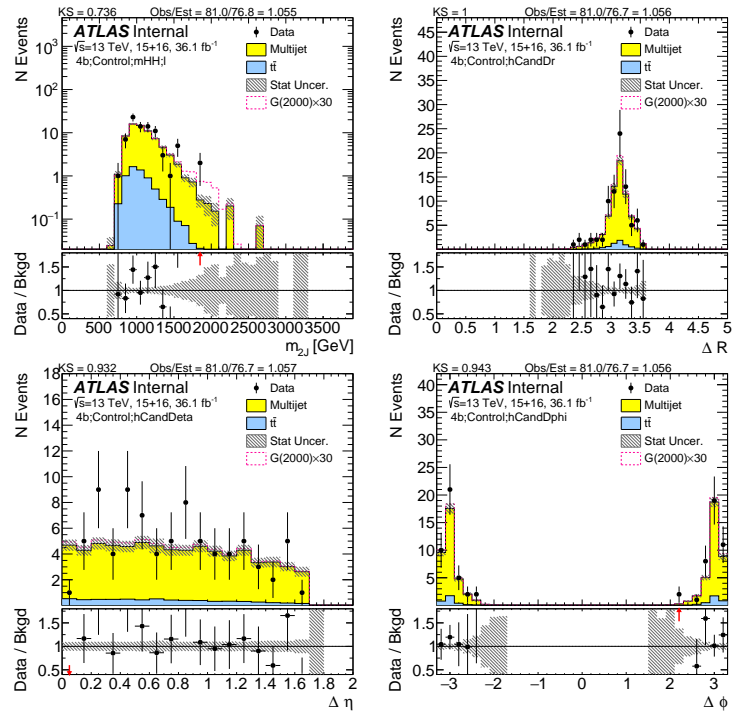


Figure B.4: Kinematics (invariant mass, ΔR , $\Delta \eta$ and $\Delta \phi$) of two large- R jets in data and prediction in the control region after requiring 4 b -tags.

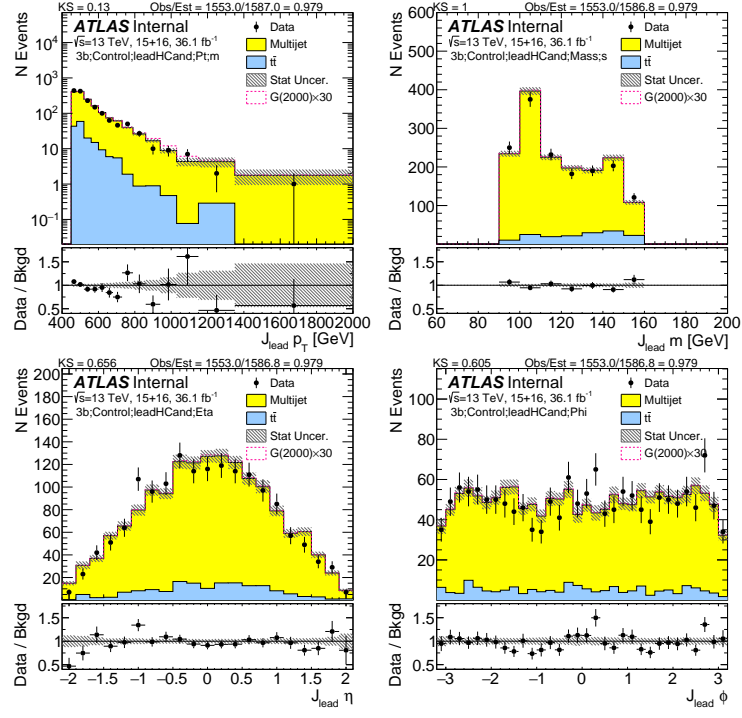


Figure B.5: Kinematics (p_T , mass, η , ϕ) of the lead large- R jet in data and prediction in the control region after requiring 3 b -tags.

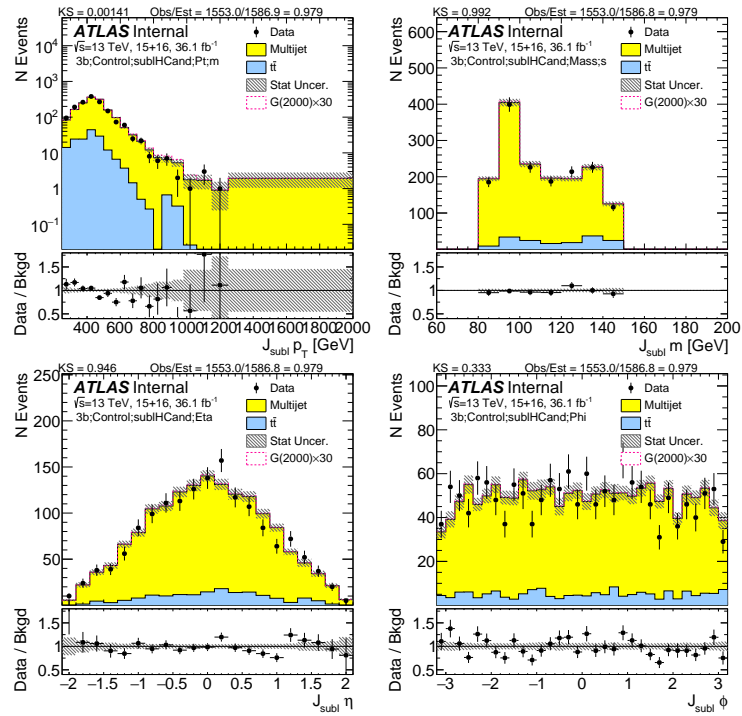


Figure B.6: Kinematics (p_T , mass, η , ϕ) of the subleading large- R jet in data and prediction in the control region after requiring 3 b -tags.

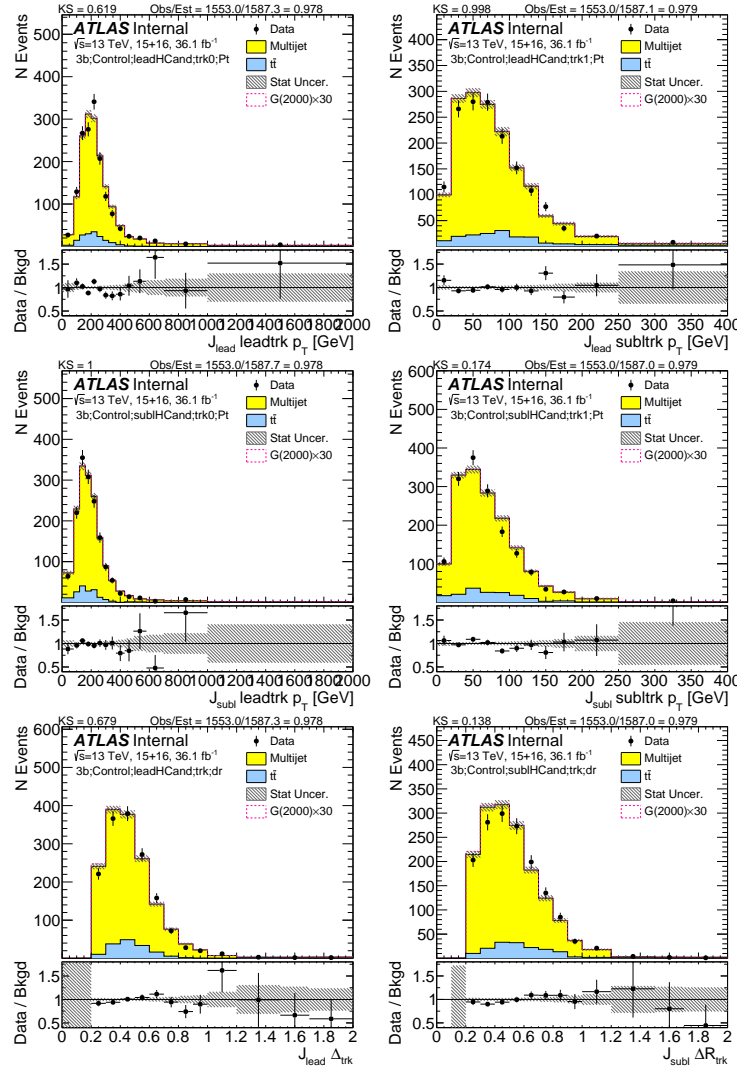


Figure B.7: First two rows show the p_T of the lead (left) and sub-lead (right) small- R track jets associated to the lead (first-row) and sub-lead (second-row) large- R jet in data and prediction in the control region after requiring 3 b -tags. Third row shows the ΔR between two leading small- R track-jets associated to the leading (left) and sub-leading (right) large- R jet.

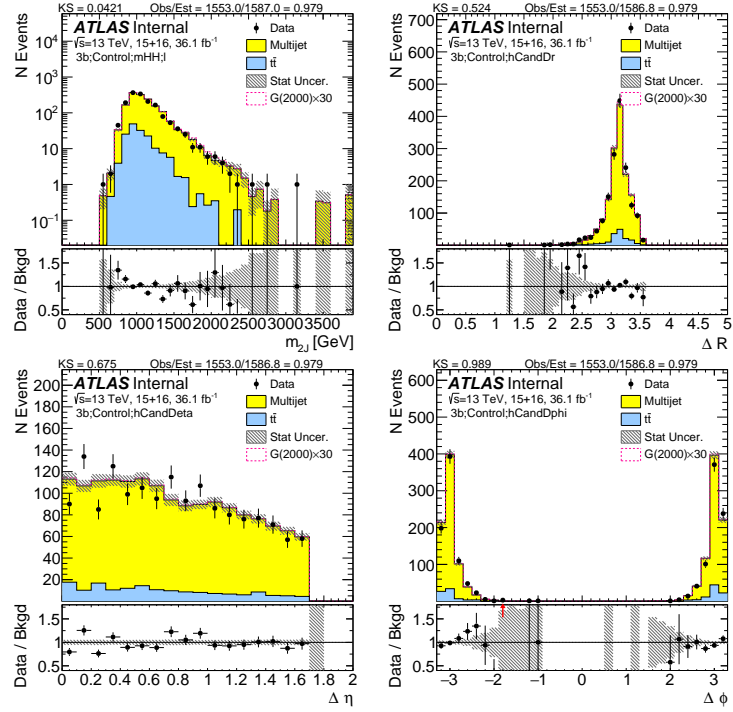


Figure B.8: Kinematics (invariant mass, ΔR , $\Delta\eta$ and $\Delta\phi$) of two large- R jets in data and prediction in the control region after requiring 3 b -tags.

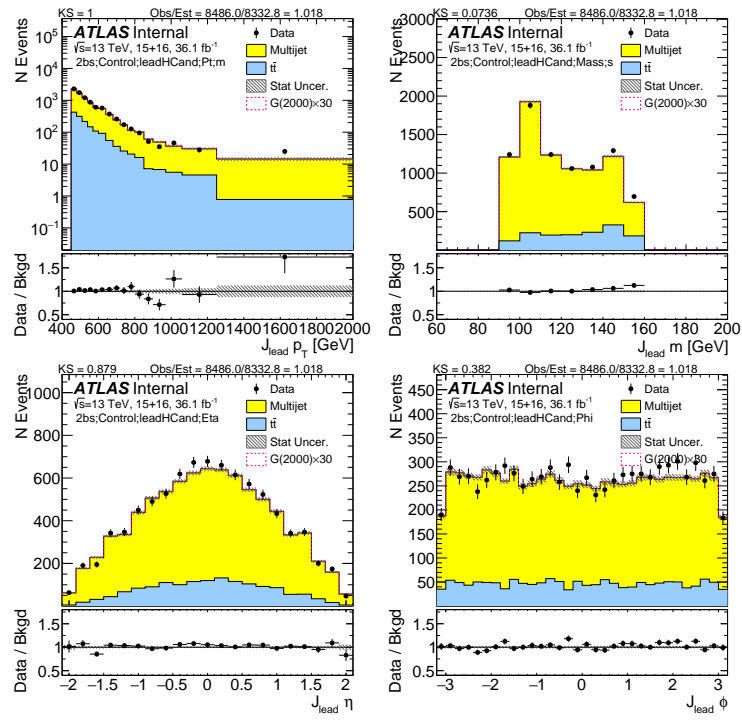


Figure B.9: Kinematics (p_T , mass, η , ϕ) of the lead large- R jet in data and prediction in the control region after requiring 2 b -tags split.

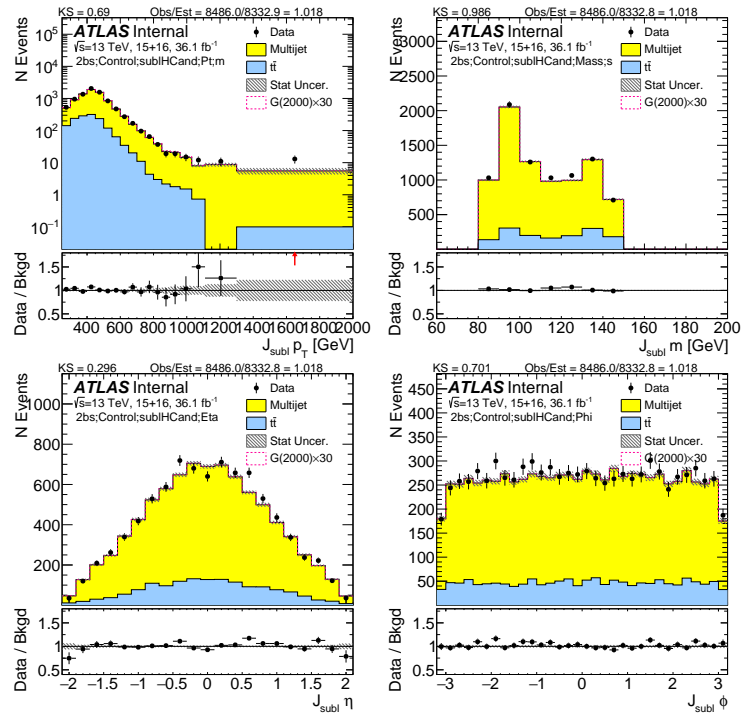


Figure B.10: Kinematics (p_T , mass, η , ϕ) of the subleading large- R jet in data and prediction in the control region after requiring 2 b -tags split.

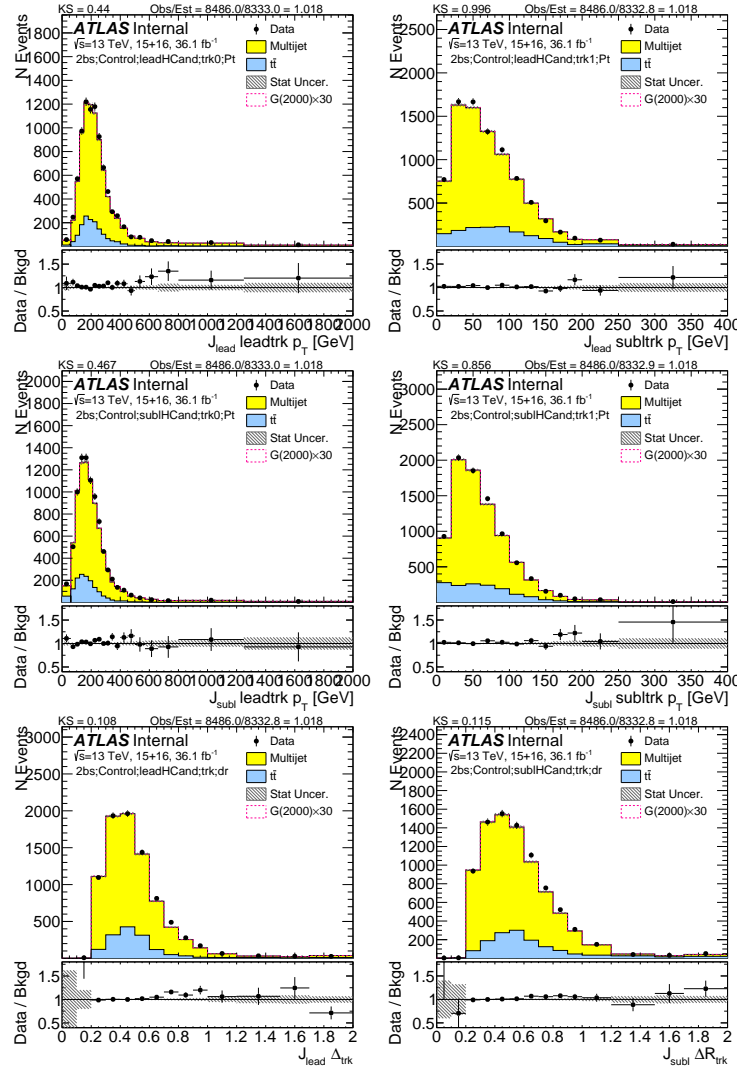


Figure B.11: First two rows show the p_T of the lead (left) and sub-lead (right) small- R track jets associated to the lead (first-row) and sub-lead (second-row) large- R jet in data and prediction in the control region after requiring 2 b -tags split. Third row shows the ΔR between two leading small- R track-jets associated to the leading (left) and sub-leading (right) large- R jet.

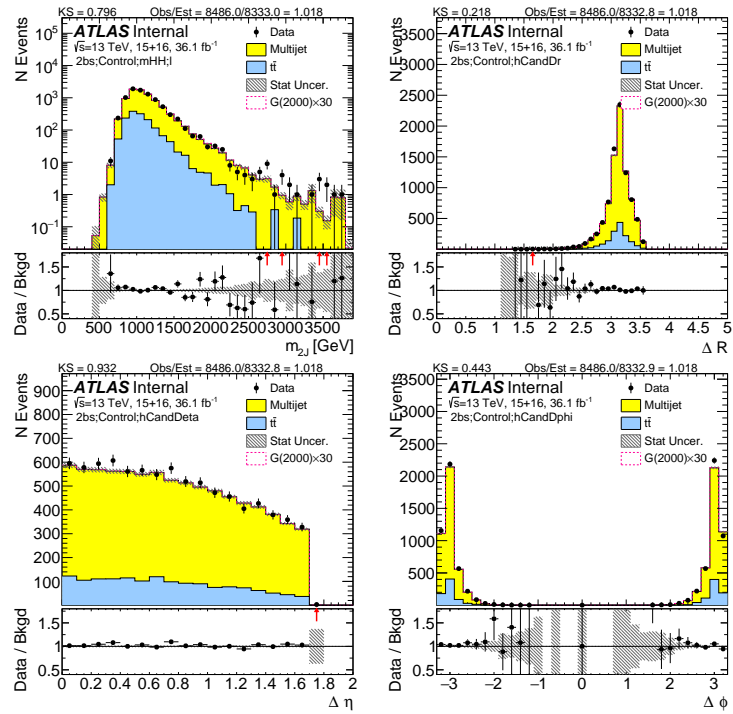


Figure B.12: Kinematics (invariant mass, ΔR , $\Delta\gamma$ and $\Delta\phi$) of two large- R jets in data and prediction in the control region after requiring 2 b -tags split.

C

Boosted signal region kinematic distributions

This appendix shows unblinded data with the prediction of QCD multi-jets and $t\bar{t}$ backgrounds in the signal region. Plots shown are with stat uncertainty only.

Tables C.1, C.2, C.3, C.4, C.5, C.6 shows the integrated SR predictions and yields, in different m_{2J} or scaled m_{2J} ranges. The predictions agree with the data fairly well, with the exception of the $3b$ deficient in m_{2J} above 2 TeV.

Mass Range	>1000	>1500	>2000	>2500	>3000
totalbkg	23.09 ± 1.59	1.94 ± 0.15	0.26 ± 0.072	0.061 ± 0.058	0.021 ± 0.047
data	21.0 ± 4.58	3.0 ± 1.73	-	-	-

Table C.1: $4b$ unblinded signal region predictions and results. All systematic uncertainties included for backgrounds. For Data, the statistical uncertainty is shown. Mass range is broken into greater than 1 TeV, 1.5 TeV, 2 TeV, 2.5 TeV, and 3 TeV intervals.

Mass Range	>1000	>1500	>2000	>2500	>3000
totalbkg	495.92 ± 12.34	51.72 ± 2.46	10.42 ± 0.95	4.07 ± 0.85	2.21 ± 0.79
data	499.0 ± 22.34	42.0 ± 6.48	3.0 ± 1.73	1.0 ± 1.0	-

Table C.2: $3b$ unblinded signal region predictions and results. All systematic uncertainties included for backgrounds. For Data, the statistical uncertainty is shown. Mass range is broken into greater than 1 TeV, 1.5 TeV, 2 TeV, 2.5 TeV, and 3 TeV intervals.

Mass Range	>1000	>1500	>2000	>2500	>3000
totalbkg	2688.71 ± 34.09	288.51 ± 4.96	42.19 ± 2.13	8.85 ± 1.55	2.72 ± 1.09
data	2755.0 ± 52.49	287.0 ± 16.94	38.0 ± 6.16	4.0 ± 2.0	1.0 ± 1.0

Table C.3: $2bs$ unblinded signal region predictions and results. All systematic uncertainties included for backgrounds. For Data, the statistical uncertainty is shown. Mass range is broken into greater than 1 TeV, 1.5 TeV, 2 TeV, 2.5 TeV, and 3 TeV intervals.

Figures C.1, C.2, C.3, and C.4 show predictions of various kinematics of the large- R jets and their associated track jets in the $4b$ selection. Figures C.5, C.6, C.7, and C.8 show predictions of various kinematics of the large- R jets and their associated track jets in the $3b$ selection. Figures C.9, C.10, C.11,

Mass Range	>1000	>1500	>2000	>2500	>3000
totalbkg	24.64 ± 1.84	2.84 ± 0.22	0.25 ± 0.044	0.02 ± 0.011	0.0014 ± 0.0026
data	22.0 ± 4.69	4.0 ± 2.0	1.0 ± 1.0	-	-

Table C.4: $4b$ unblinded scaled dijet mass signal region predictions and results. All systematic uncertainties included for backgrounds. For Data, the statistical uncertainty is shown. Mass range is broken into greater than 1 TeV, 1.5 TeV, 2 TeV, 2.5 TeV, and 3 TeV intervals.

Mass Range	>1000	>1500	>2000	>2500	>3000
totalbkg	559.38 ± 14.06	69.27 ± 3.22	13.35 ± 1.14	4.37 ± 0.96	2.0 ± 0.87
data	570.0 ± 23.87	59.0 ± 7.68	4.0 ± 2.0	1.0 ± 1.0	-

Table C.5: $3b$ unblinded scaled dijet mass signal region predictions and results. All systematic uncertainties included for backgrounds. For Data, the statistical uncertainty is shown. Mass range is broken into greater than 1 TeV, 1.5 TeV, 2 TeV, 2.5 TeV, and 3 TeV intervals.

Mass Range	>1000	>1500	>2000	>2500	>3000
totalbkg	2998.69 ± 40.31	377.8 ± 6.39	57.47 ± 2.88	11.78 ± 1.95	3.39 ± 1.27
data	3078.0 ± 55.48	379.0 ± 19.47	47.0 ± 6.86	6.0 ± 2.45	2.0 ± 1.41

Table C.6: $2bs$ unblinded scaled dijet mass signal region predictions and results. All systematic uncertainties included for backgrounds. For Data, the statistical uncertainty is shown. Mass range is broken into greater than 1 TeV, 1.5 TeV, 2 TeV, 2.5 TeV, and 3 TeV intervals.

and C.12 show predictions of various kinematics of the large- R jets and their associated track jets in the $2b$ selection.

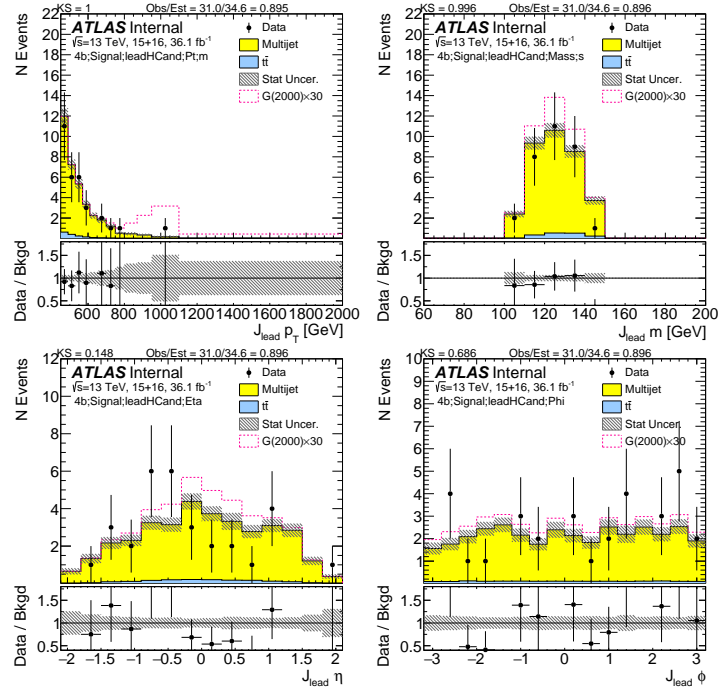


Figure C.1: Kinematics (p_T , mass, η , ϕ) of the lead large- R jet in data and prediction in the signal region after requiring 4 b -tags.

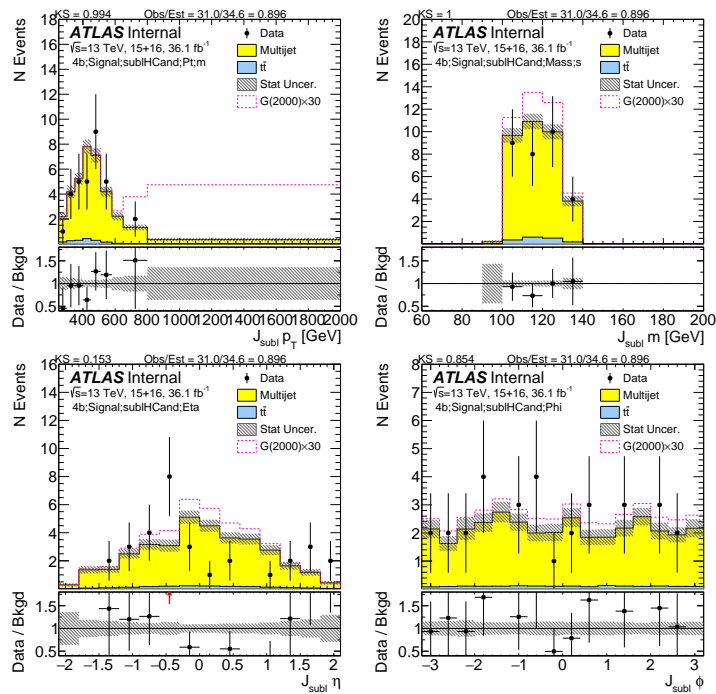


Figure C.2: Kinematics (p_T , mass, η , ϕ) of the subleading large- R jet in data and prediction in the signal region after requiring 4 b -tags.

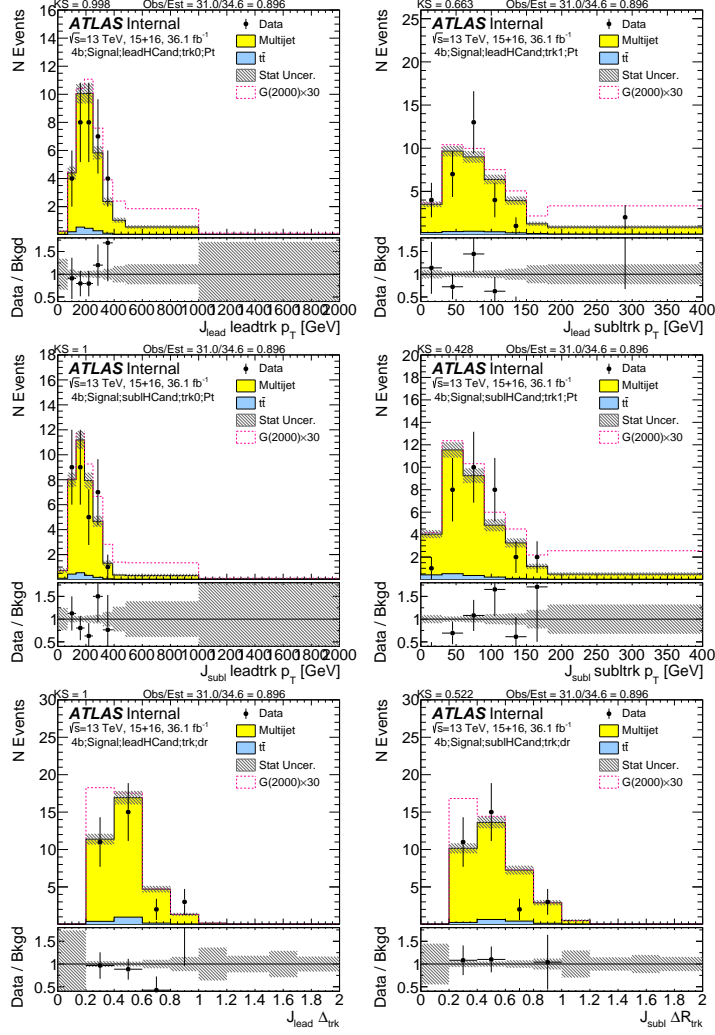


Figure C.3: First two rows show the p_T of the lead (left) and sub-lead (right) small- R track jets associated to the lead (first-row) and sub-lead (second-row) large- R jet in data and prediction in the signal region after requiring 4 b -tags. Third row shows the ΔR between two leading small- R track-jets associated to the leading (left) and sub-leading (right) large- R jet.

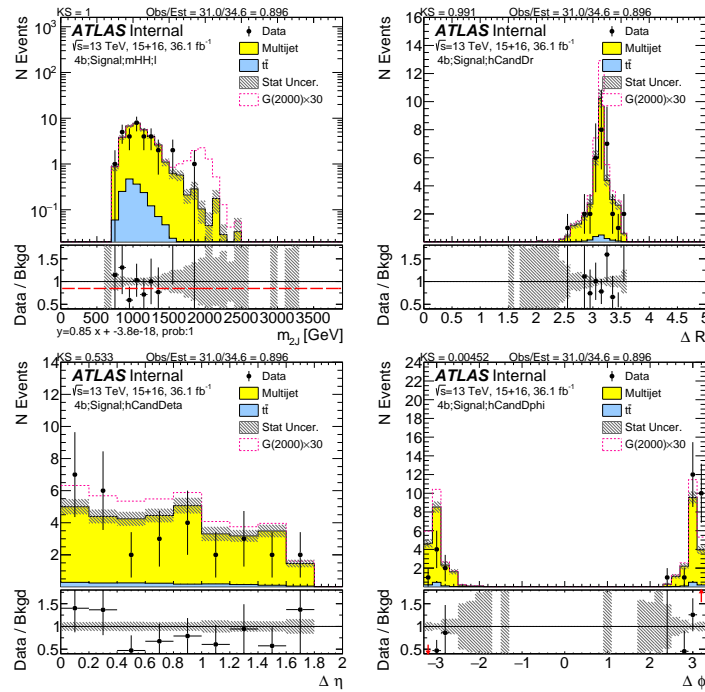


Figure C.4: Kinematics (invariant mass, ΔR , $\Delta\eta$ and $\Delta\phi$) of two large- R jets in data and prediction in the signal region after requiring 4 b -tags.

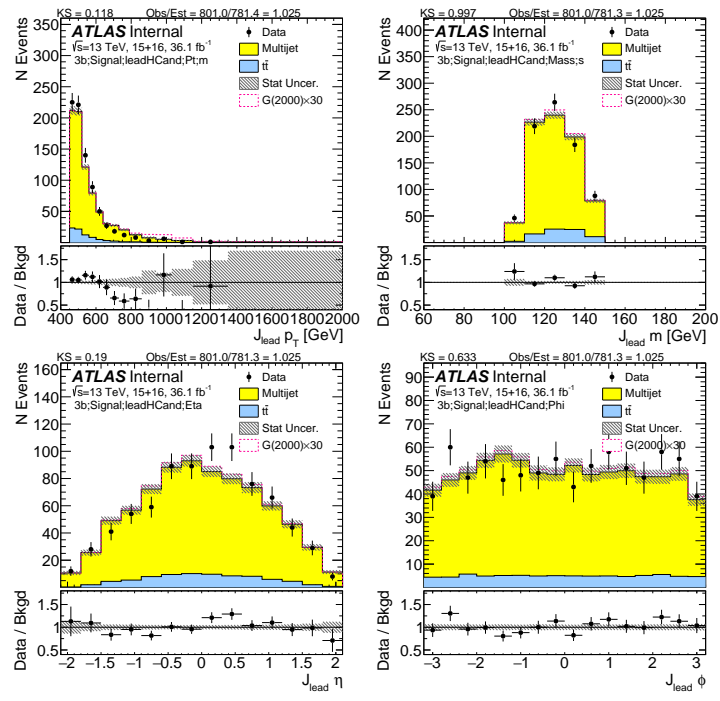


Figure C.5: Kinematics (p_T , mass, η , ϕ) of the lead large- R jet in data and prediction in the signal region after requiring 3 b -tags.

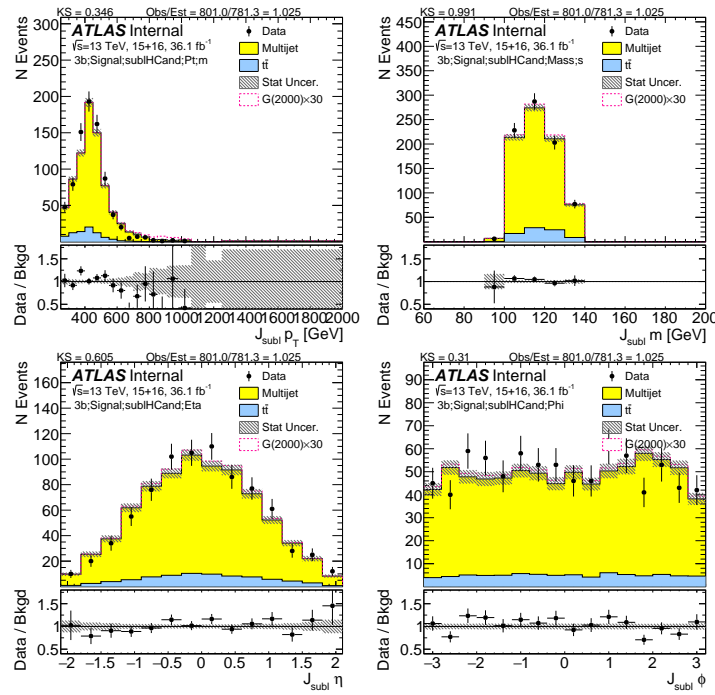


Figure C.6: Kinematics (p_T , mass, η , ϕ) of the subleading large- R jet in data and prediction in the signal region after requiring 3 b -tags.

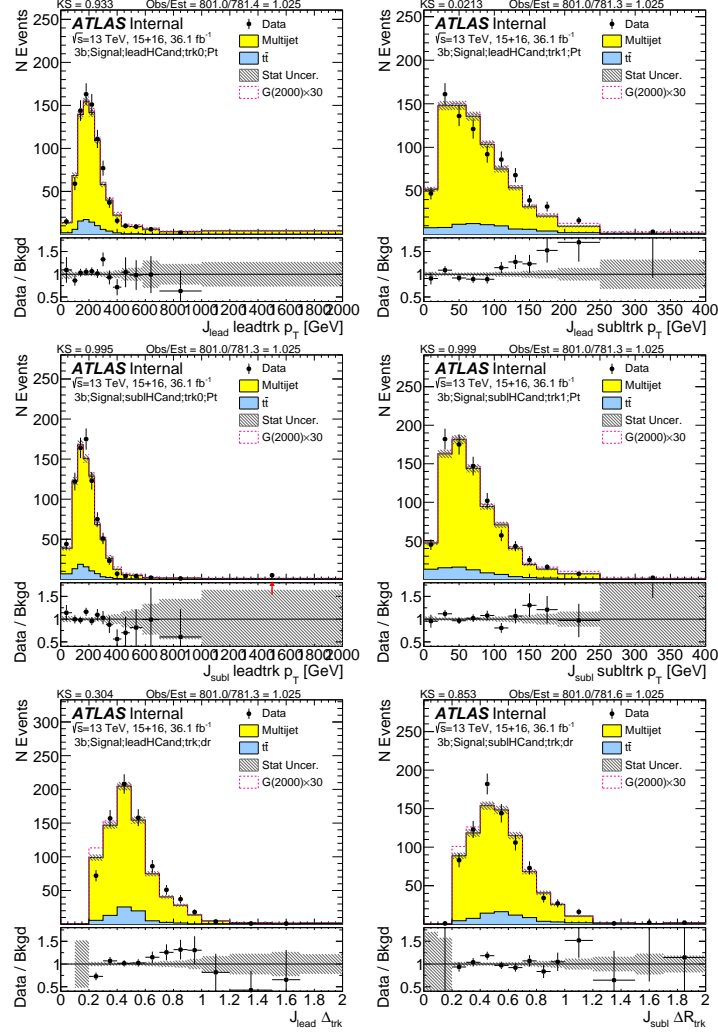


Figure C.7: First two rows show the p_T of the lead (left) and sub-lead (right) small- R track jets associated to the lead (first-row) and sub-lead (second-row) large- R jet in data and prediction in the signal region after requiring 3 b -tags. Third row shows the ΔR between two leading small- R track-jets associated to the leading (left) and sub-leading (right) large- R jet.

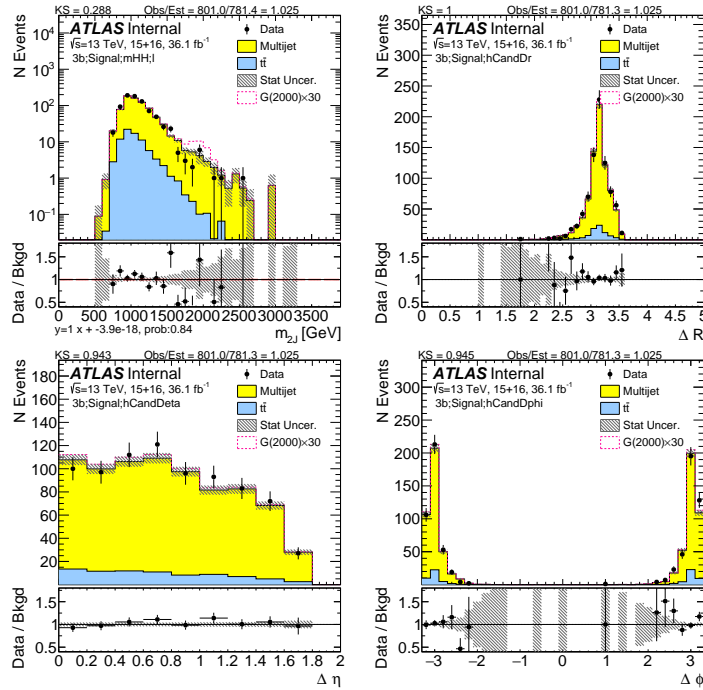


Figure C.8: Kinematics (invariant mass, ΔR , $\Delta\eta$ and $\Delta\phi$) of two large- R jets in data and prediction in the signal region after requiring 3 b -tags.

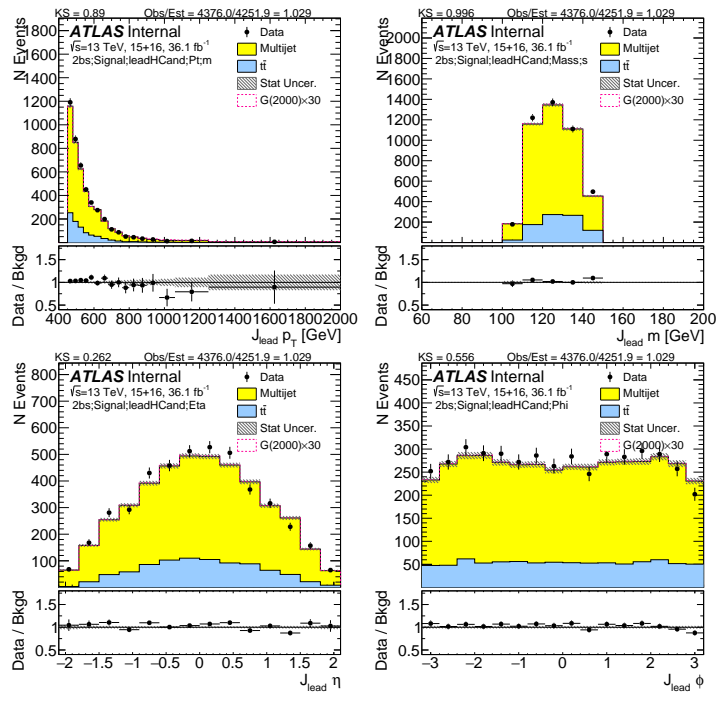


Figure C.9: Kinematics (p_{T} , mass, η , ϕ) of the lead large- R jet in data and prediction in the signal region after requiring 2 b -tags split.

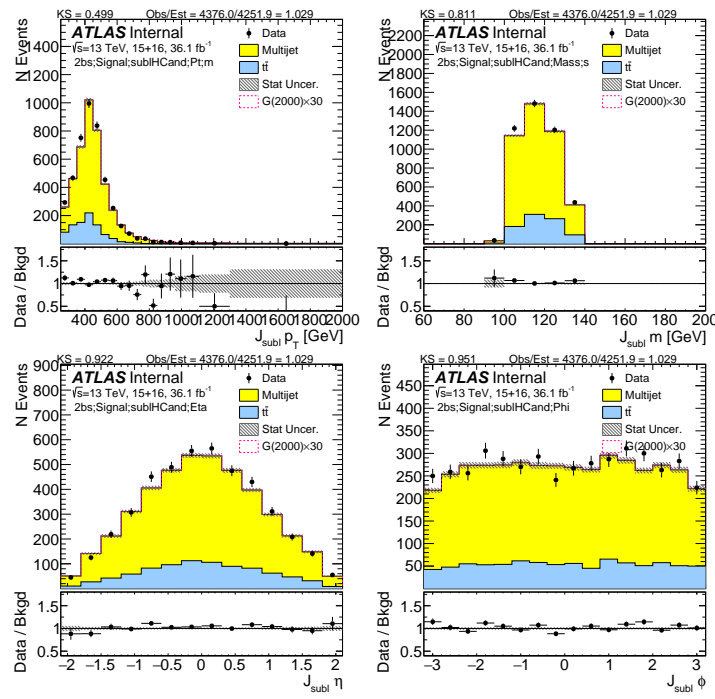


Figure C.10: Kinematics (p_T , mass, η , ϕ) of the subleading large- R jet in data and prediction in the signal region after requiring 2 b -tags split.

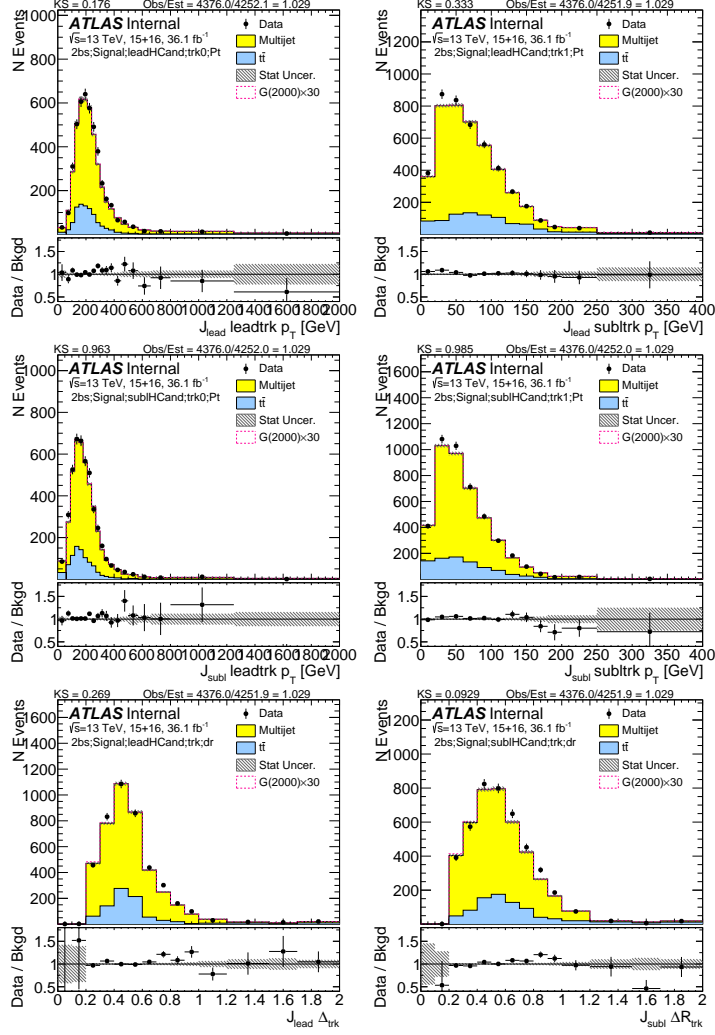


Figure C.11: First two rows show the p_T of the lead (left) and sub-lead (right) small- R track jets associated to the lead (first-row) and sub-lead (second-row) large- R jet in data and prediction in the signal region after requiring 2 b -tags split. Third row shows the ΔR between two leading small- R track-jets associated to the leading (left) and sub-leading (right) large- R jet.

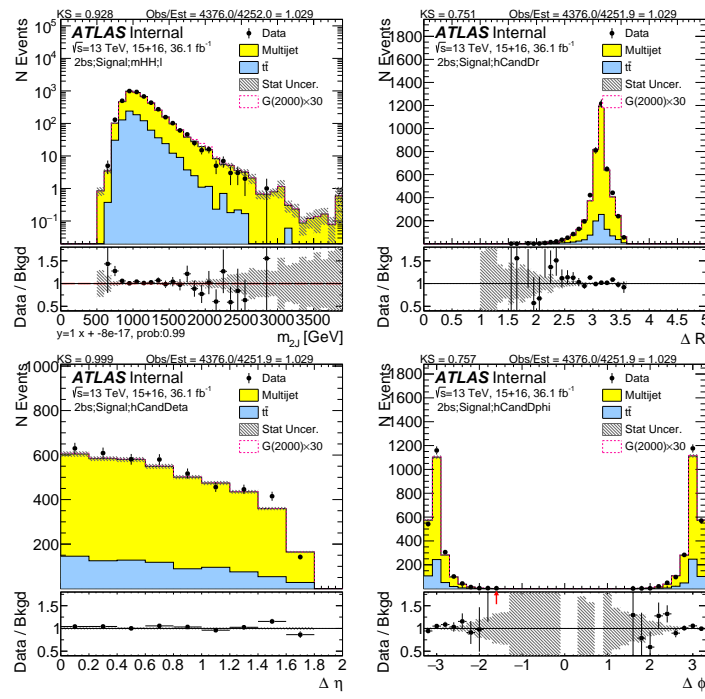


Figure C.12: Kinematics (invariant mass, ΔR , $\Delta \eta$ and $\Delta \phi$) of two large- R jets in data and prediction in the signal region after requiring 2 b -tags split.

D

Constant μ_{qcd} Validation

One important assumption is the constant μ_{qcd} for different regions on the 2D $m_J^{\text{lead}} - m_J^{\text{subl}}$ plane.

This can be validated in data, excluding signal regions which were blinded during this check. The $t\bar{t}$ contribution is estimated directly from MC and subtracted in the data distributions. The ratio of the number of n- b tagged events versus the number of less- b tagged events in each $m_J^{\text{lead}} - m_J^{\text{subl}}$ bin is calculated. The pull of the ratios in SB/CR/SR is also calculated. These two distributions shows the

consistency of μ_{qcd} in SB/CR/SR, as seen in Figure D.1 (1b over ob), D.2 (2b over 1b), D.3 (2bs over 1b), D.4 (3b over 2b), D.5 (4b over 2b). For 4/3/2bs, the μ_{qcd} value can be compared with Table 6.5. This validates the choice of SB region and the constant μ_{qcd} assumption in the analysis.

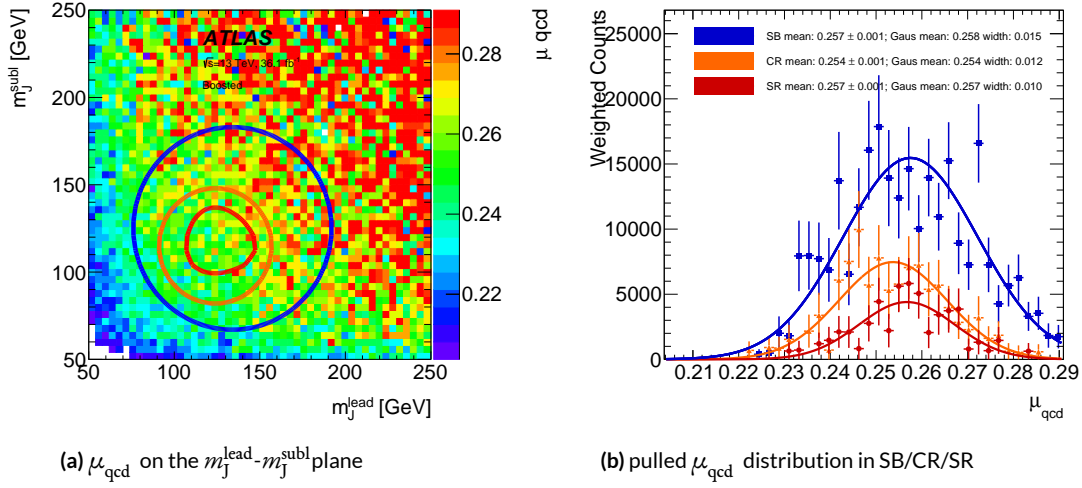


Figure D.1: 1b over ob μ_{qcd} values evaluated in data, with the N_{event} weighted mean and the Gaussian fit mean listed.

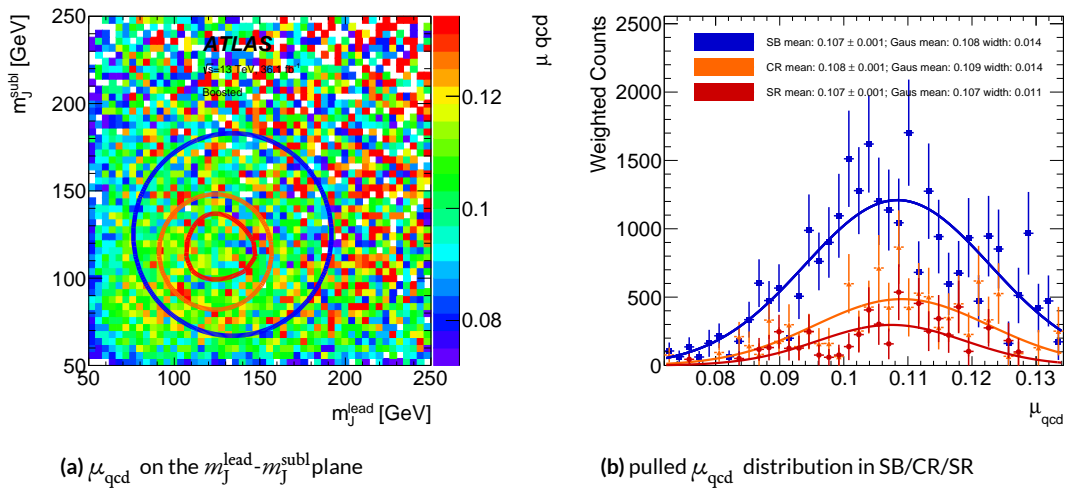


Figure D.2: 2b over 1b μ_{qcd} values evaluated in data, with the N_{event} weighted mean and the Gaussian fit mean listed.

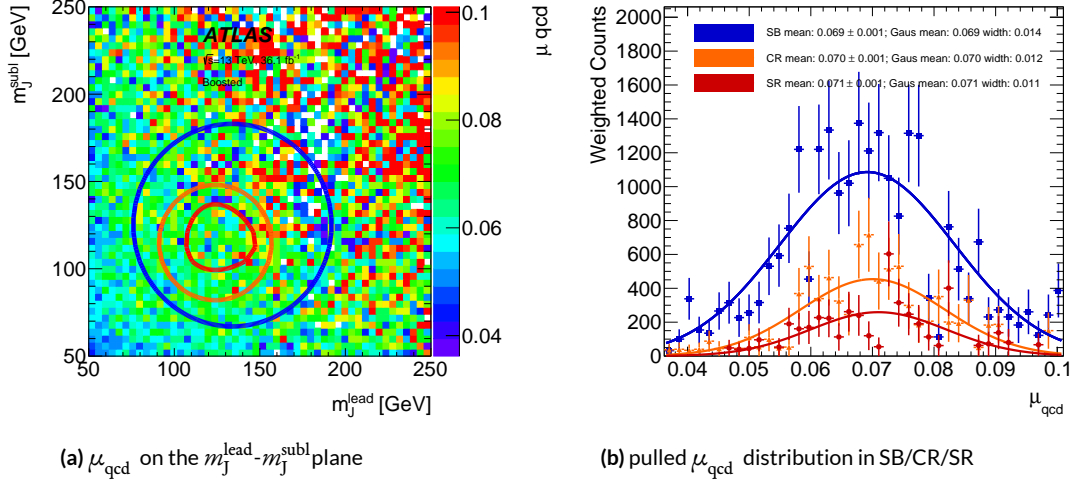


Figure D.3: $2b$ over $1b$ μ_{qcd} values evaluated in data, with the N_{event} weighted mean and the Gaussian fit mean listed.

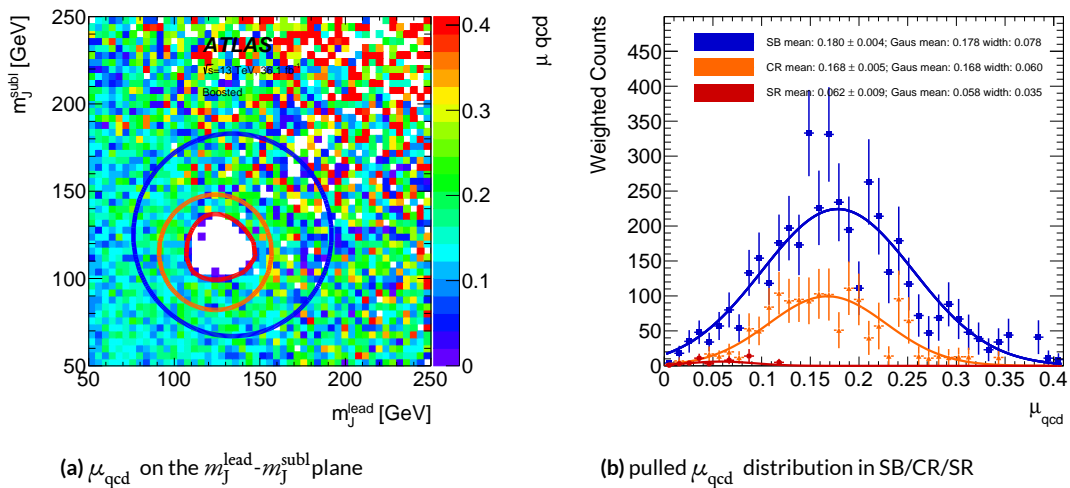


Figure D.4: $3b$ over $2b$ μ_{qcd} values evaluated in data, with the N_{event} weighted mean and the Gaussian fit mean listed.
SR is blinded.

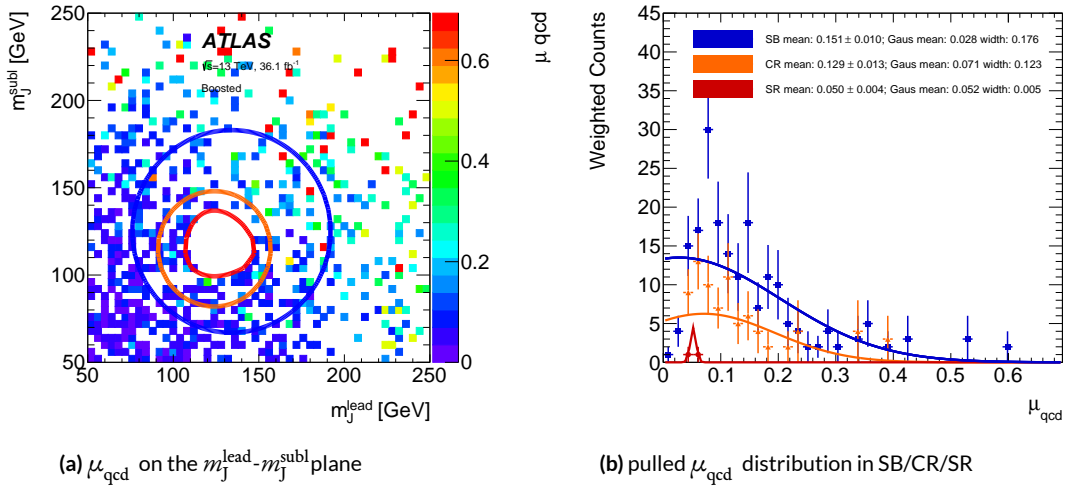


Figure D.5: $4b$ over $2b$ μ_{qcd} values evaluated in data, with the N_{event} weighted mean and the Gaussian fit mean listed. SR is blinded.

Also, the Dijet MC can be used for constant μ_{qcd} validation. The same distributions evaluated in dijet MC are shown in Figure D.6 ($1b$ over ob), D.7 ($2b$ over $1b$), D.8 ($2bs$ over $1b$), D.9 ($3b$ over $2b$), D.10 ($4b$ over $2b$). Poor statistics of the dijet MC affects the pull distributions, especially in $3b$ and $4b$, yet the consistency of μ_{qcd} in SB/CR/SR is still validated. The large difference in μ_{qcd} between data and MC also shows that the dijet MC could not be used directly for background estimation.

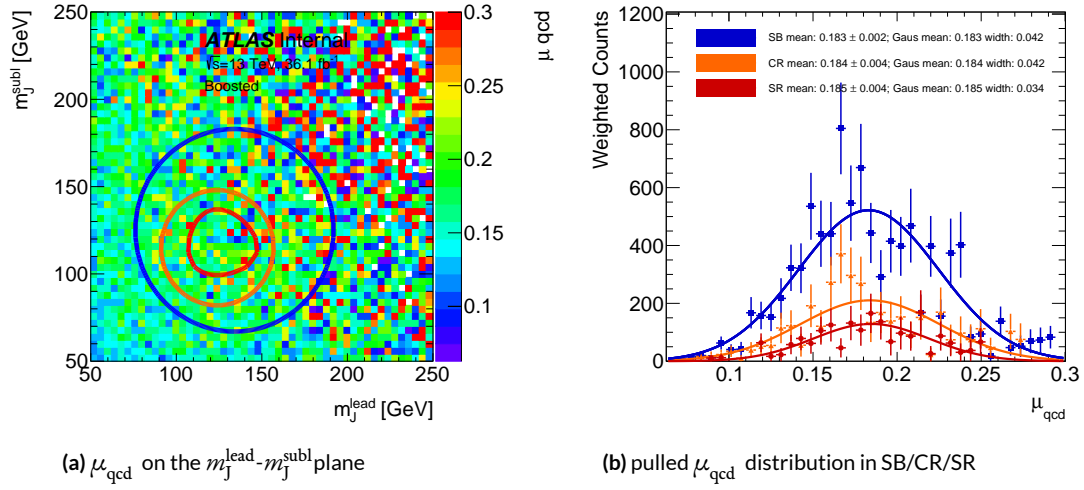


Figure D.6: $1b$ over ob μ_{qcd} values evaluated in dijet MC, with the N_{event} weighted mean and the Gaussian fit mean listed.

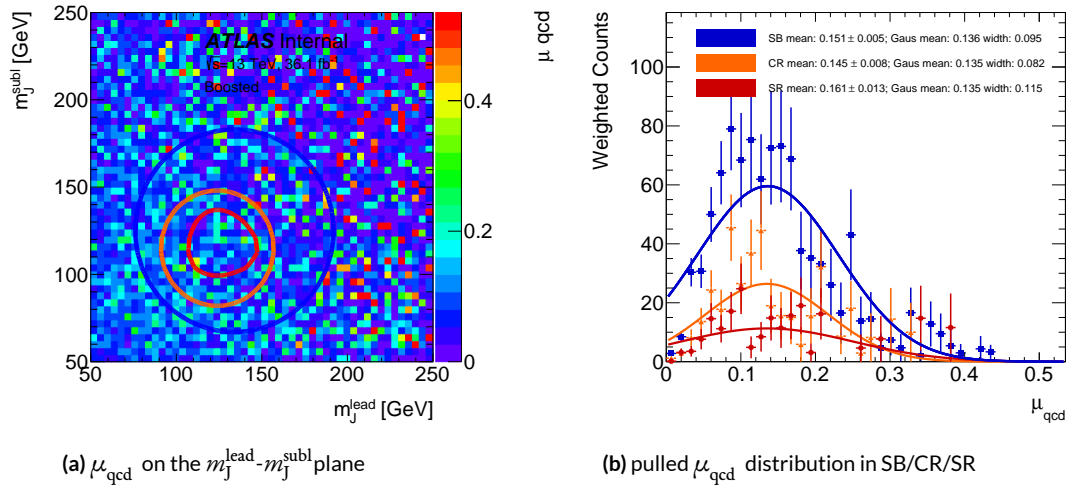


Figure D.7: zb over $1b$ μ_{qcd} values evaluated in dijet MC, with the N_{event} weighted mean and the Gaussian fit mean listed.

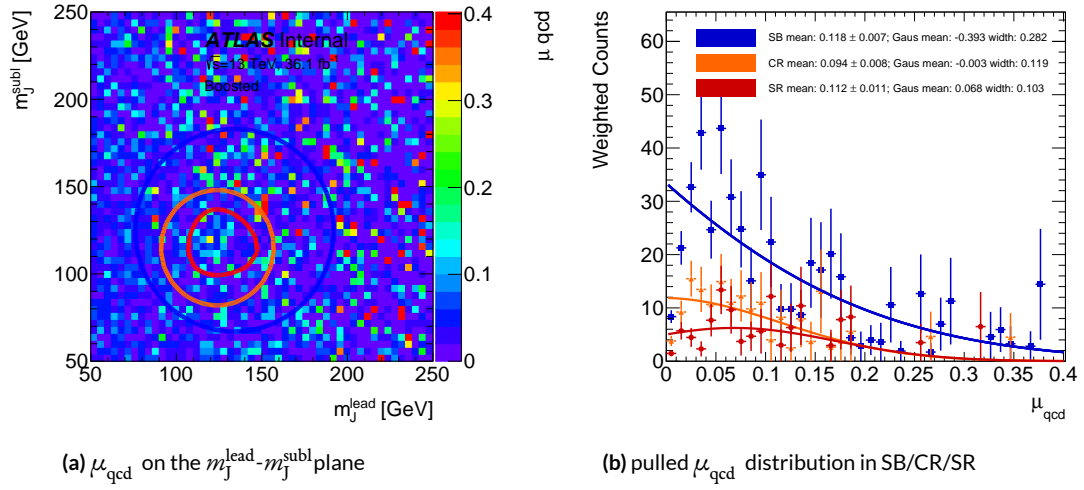


Figure D.8: $2bs$ over $1b$ μ_{qcd} values evaluated in dijet MC, with the N_{event} weighted mean and the Gaussian fit mean listed.

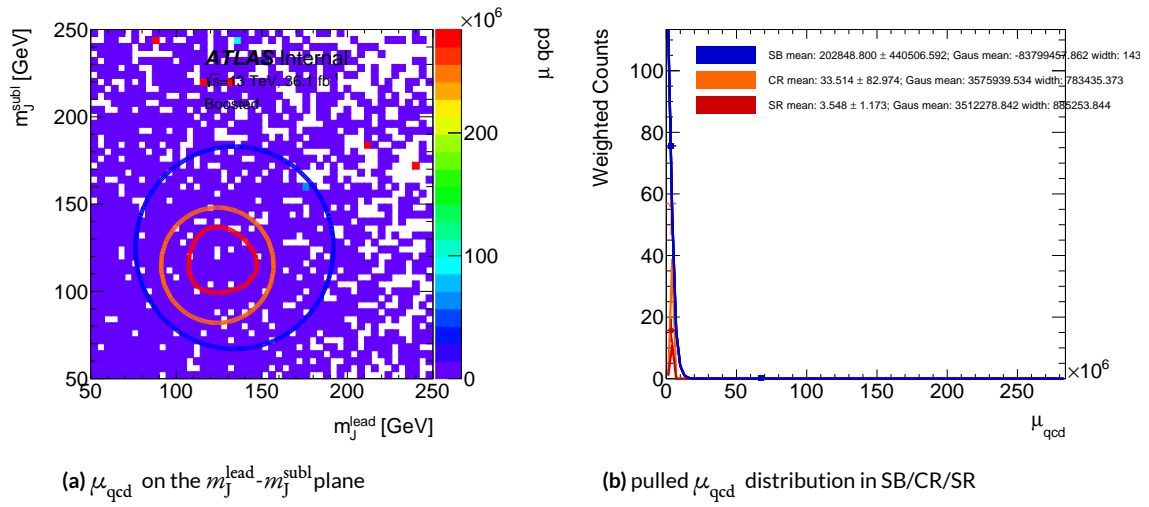


Figure D.9: $3b$ over $2b$ μ_{qcd} values evaluated in dijet MC, with the N_{event} weighted mean and the Gaussian fit mean listed.

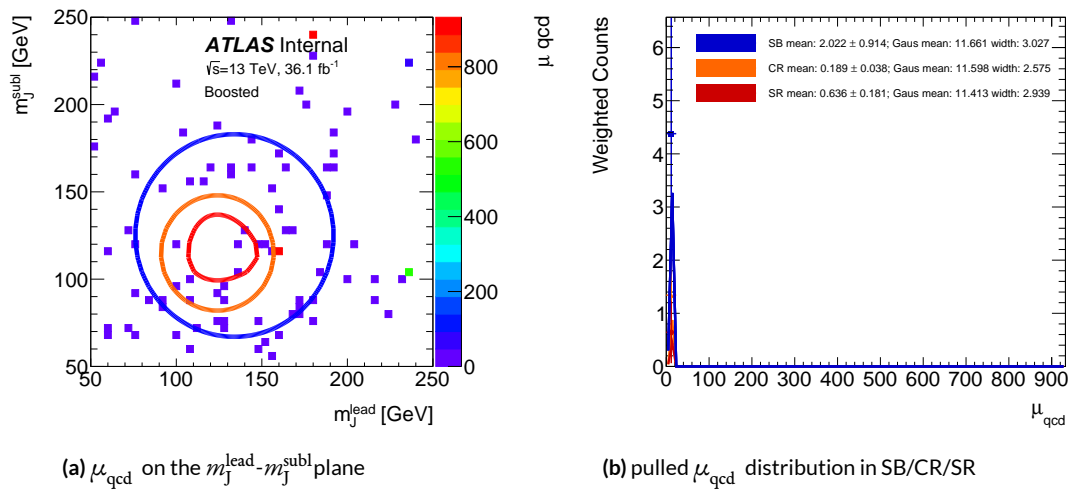


Figure D.10: $4b$ over $2b$ μ_{qcd} values evaluated in dijet MC, with the N_{event} weighted mean and the Gaussian fit mean listed.

E

Reweighting Details

The first iteration, second iteration, and last iteration of fits for $2b$ s, where in $1b$ data, the non- b tagged Higgs candidate are reweighed to be like a $1b$ tagged Higgs candidate, can be seen in Figure E.1 and E.2. Similar distributions for $3b$, where in $2b$ data, the non- b tagged Higgs candidate are reweighed to be like a $1b$ tagged Higgs candidate, are shown in Figure E.3 and E.4. Similar distributions for $4b$, where in $2b$ data, the non- b tagged Higgs candidate are reweighed to be like a $2b$ tagged

Higgs candidate, are shown in Figure E.5 and E.6. The before reweighting distribution (first row), the reweighting result after the first iteration (second row), and the final distribution after reweighting (last row) are presented.

In some plots, like Figure E.5 and E.6, the last ratio bin sometimes still doesn't converge to unity. This is a feature from the limited statistics from the last bin, especially in the $4b$ case, where only 20% number of events in $2b$ is used for background prediction and therefore reweighed. To make this fully converge, a different binning or more iterations could be used. Yet the last bin's few event will also likely to end up with a large unphysical weight and therefore harm the background prediction later.

A comparison of the SB shapes before and after reweighting for $2bs$, $3b$ and $4b$ are shown in Figures E.7, E.8, and E.9. Also, a comparison of the CR shapes before and after reweighting for $2bs$, $3b$ and $4b$ can be seen in Figures E.10, E.11, and E.12. In almost all cases, both the reweighted/non-reweighted prediction agrees fairly well with the data, and the reweighted plots' KS scores are greater than those from non-reweighted distributions.

More reweighting methods are tested to further validate our current reweighting method. The original method tries to reweight the non-Tagged Higgs candidate in the lower b -tagged region to be like a b -tagged Higgs candidate. This AddTag reweighting is done on three variables: large- R jet p_T and the two track jet $p_{T\gamma}$ s, which is counted as one iteration of reweighting.

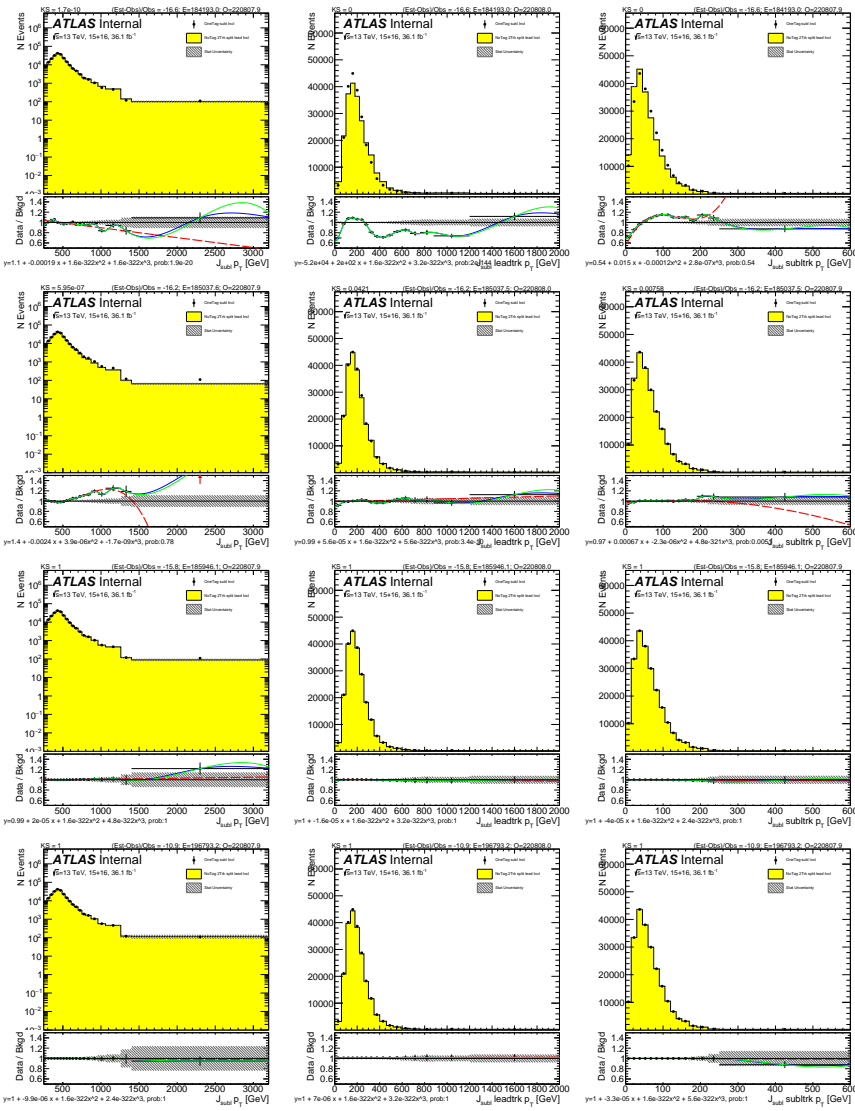


Figure E.1: For $2bs$ background estimate: the fits to the ratio of the data in the $1b$ category, of the subleading Higgs candidate $1b$ -tagged events' subleading Higgs candidate distributions (black point), over the leading Higgs candidate $1b$ -tagged events' subleading Higgs candidate distributions (yellow). Distributions and fits to the estimated QCD background for large- R jet p_T (left), the large- R jet's leading track jet p_T (middle), and large- R jet's subleading track jet p_T (right) are shown. Figures are before reweighting (top row), after the first iteration (second row), after the fourth iteration (third row), and after the last iteration (bottom row). The green line is the spline fit; the red line is a polynomial fit; the blue line is the spline interpolation.

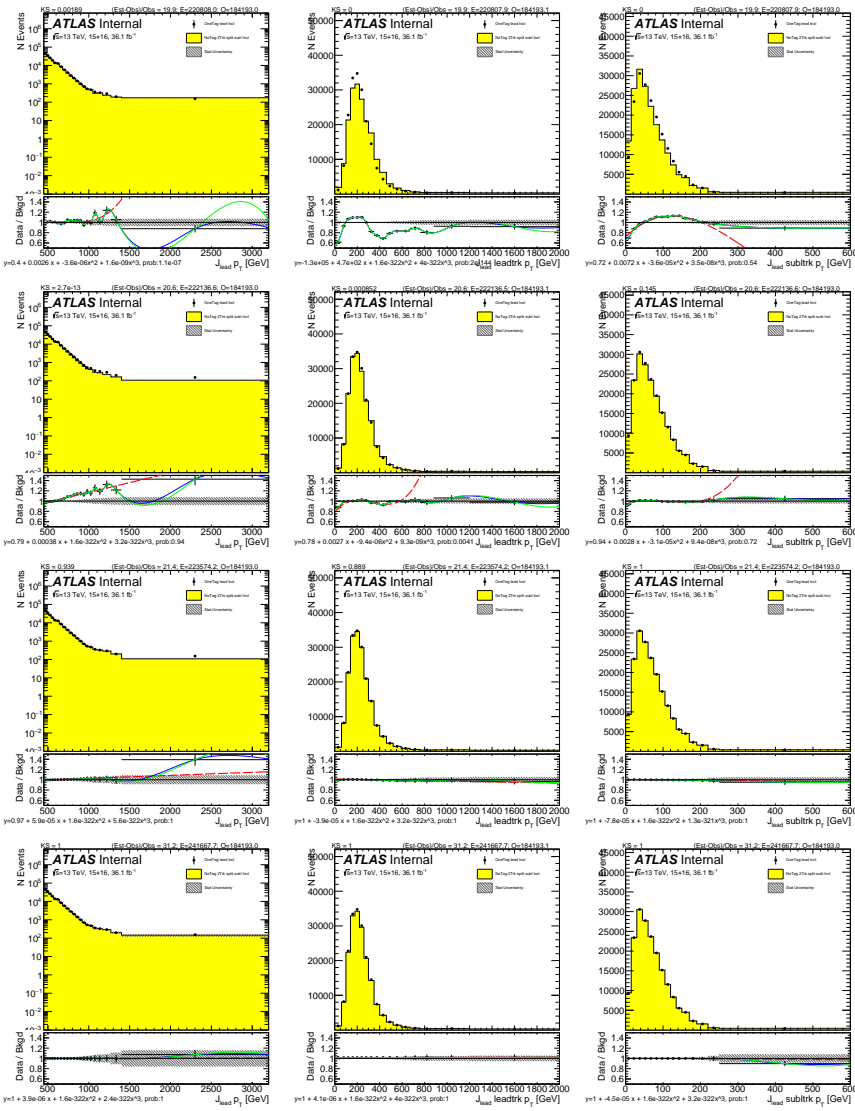


Figure E.2: For zbs background estimate: the fits to the ratio of the data in the $1b$ category, of the leading Higgs candidate $1b$ -tagged events' leading Higgs candidate distributions (black point), over the subleading Higgs candidate $1b$ -tagged events' leading Higgs candidate distributions (yellow). Distributions and fits to the estimated QCD background for large- R jet p_T (left), the large- R jet's leading track jet p_T (middle), and large- R jet's subleading track jet p_T (right) are shown. Figures are before reweighting (top row), after the first iteration (second row), after the fourth iteration (third row), and after the last iteration (bottom row). The green line is the spline fit; the red line is a polynomial fit; the blue line is the spline interpolation.

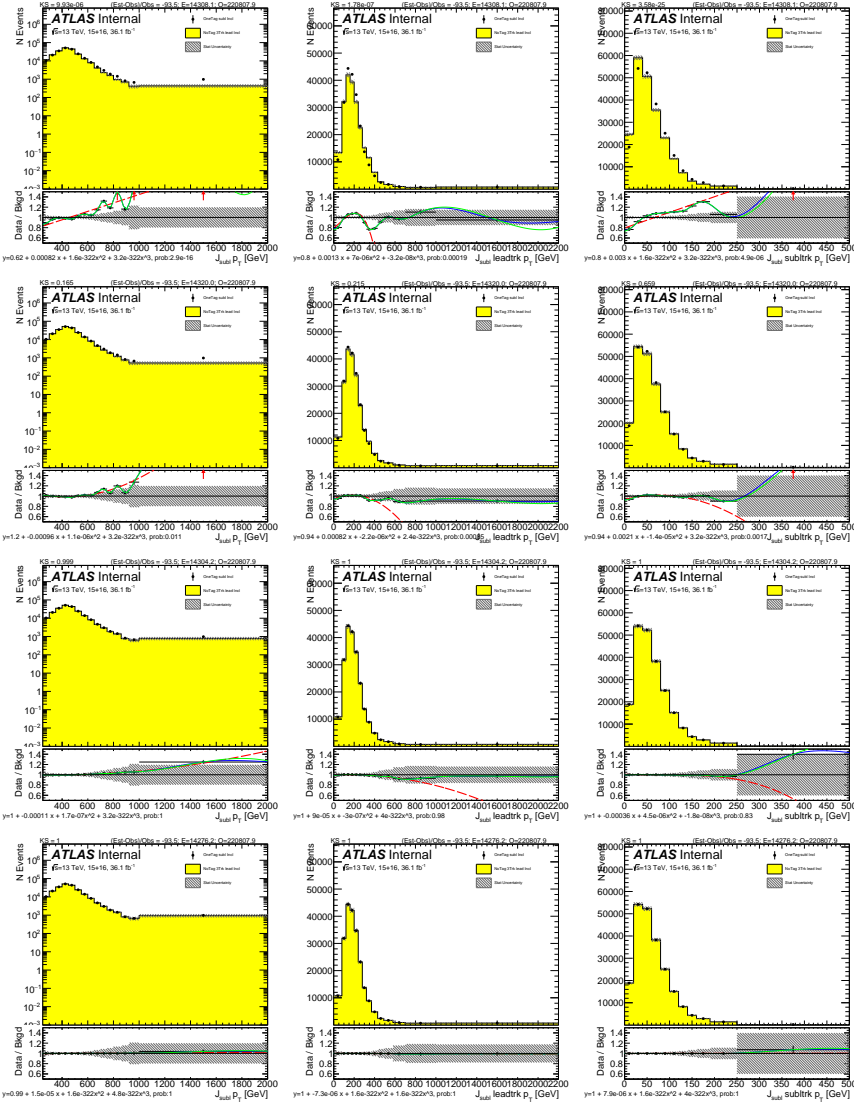


Figure E.3: For $3b$ background estimate: the fits to the ratio of the data in the $2b$ category, of the subleading Higgs candidate $2b$ -tagged events' subleading Higgs candidate distributions (black point), over the leading Higgs candidate $1b$ -tagged events' subleading Higgs candidate distributions (yellow). Distributions and fits to the estimated QCD background for large- R jet p_T (left), the large- R jet's leading track jet p_T (middle), and large- R jet's subleading track jet p_T (right) are shown. Figures are before reweighting (top row), after the first iteration (second row), after the fourth iteration (third row), and after the last iteration (bottom row). The green line is the spline fit; the red line is a polynomial fit; the blue line is the spline interpolation.

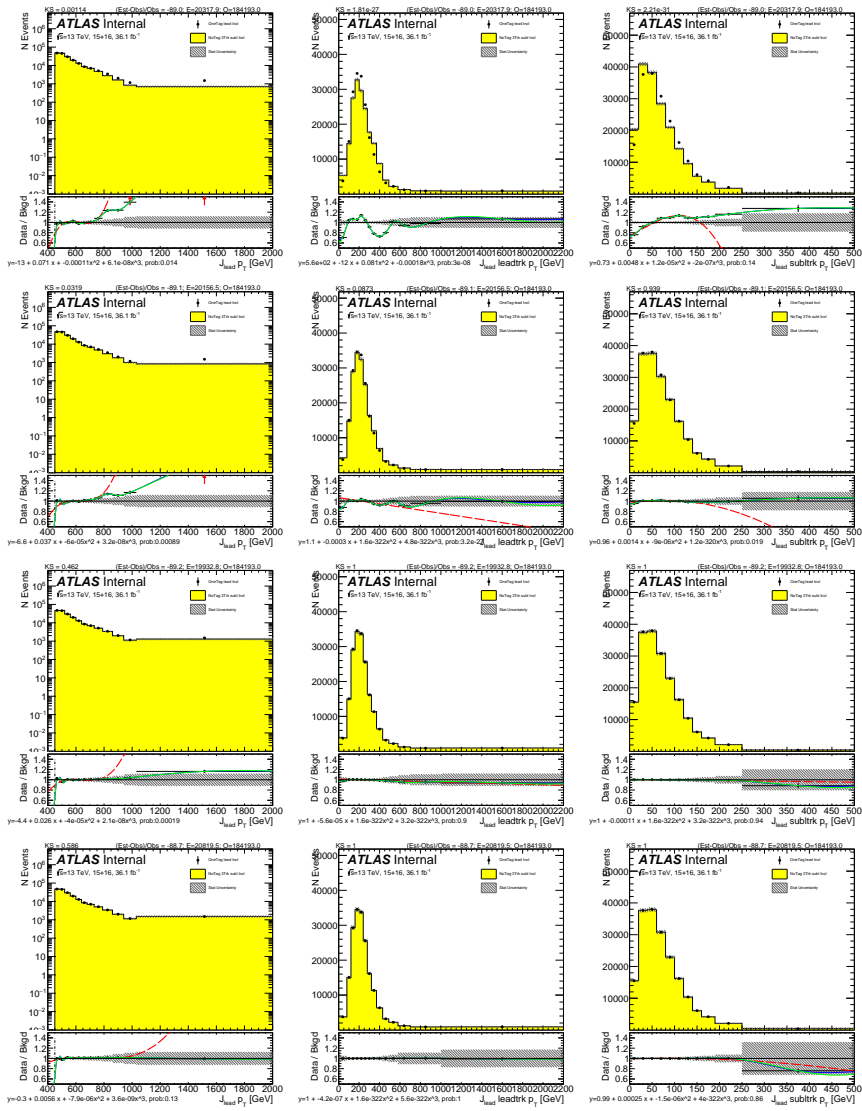


Figure E.4: For $3b$ background estimate: the fits to the ratio of the data in the $2b$ category, of the leading Higgs candidate $2b$ -tagged events' leading Higgs candidate distributions(black point), over the subleading Higgs candidate $1b$ -tagged events' leading Higgs candidate distributions(yellow). Distributions and fits to the estimated QCD background for large- R jet p_T (left), the large- R jet's leading track jet p_T (middle), and large- R jet's subleading track jet p_T (right) are shown. Figures are before reweighting (top row), after the first iteration(second row), after the fourth iteration(third row), and after the last iteration (bottom row). The green line is the spline fit; the red line is a polynomial fit; the blue line is the spline interpolation.

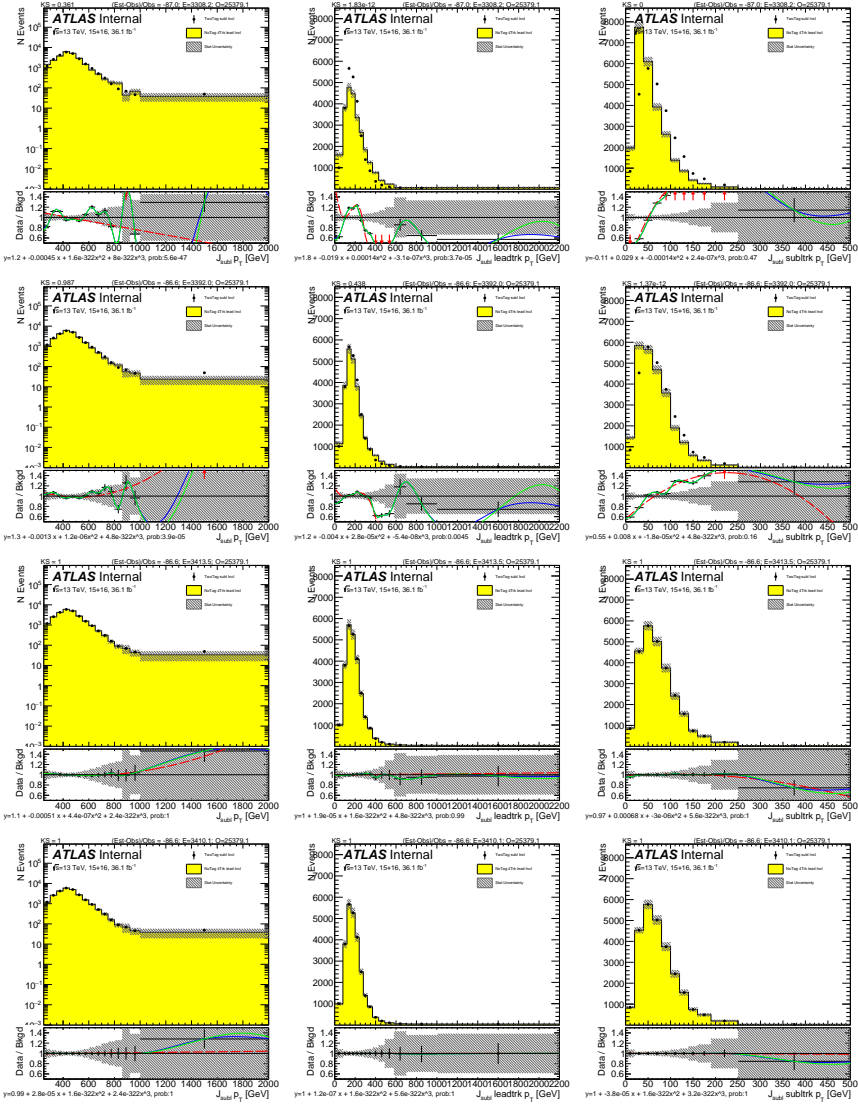


Figure E.5: For $4b$ background estimate: the fits to the ratio of the data in the $2b$ category, of the subleading Higgs candidate $2b$ -tagged events' subleading Higgs candidate distributions (black point), over the leading Higgs candidate $2b$ -tagged events' subleading Higgs candidate distributions (yellow). Distributions and fits to the estimated QCD background for large- R jet p_T (left), the large- R jet's leading track jet p_T (middle), and large- R jet's subleading track jet p_T (right) are shown. Figures are before reweighting (top row), after the first iteration (second row), after the fourth iteration (third row), and after the last iteration (bottom row). The green line is the spline fit; the red line is a polynomial fit; the blue line is the spline interpolation.

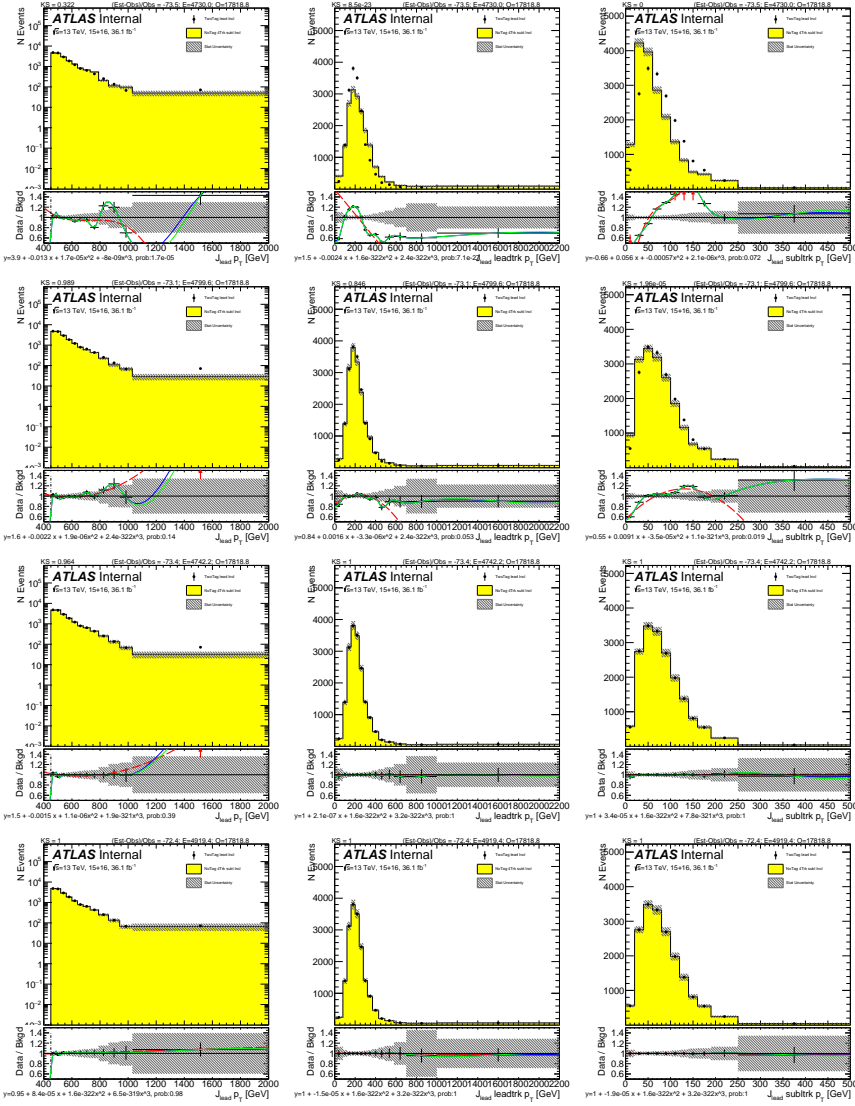


Figure E.6: For $4b$ background estimate: the fits to the ratio of the data in the $2b$ category, of the leading Higgs candidate $2b$ -tagged events' leading Higgs candidate distributions (black point), over the subleading Higgs candidate $2b$ -tagged events' leading Higgs candidate distributions (yellow). Distributions and fits to the estimated QCD background for large- R jet p_T (left), the large- R jet's leading track jet p_T (middle), and large- R jet's subleading track jet p_T (right) are shown. Figures are before reweighting (top row), after the first iteration (second row), after the fourth iteration (third row), and after the last iteration (bottom row). The green line is the spline fit; the red line is a polynomial fit; the blue line is the spline interpolation.

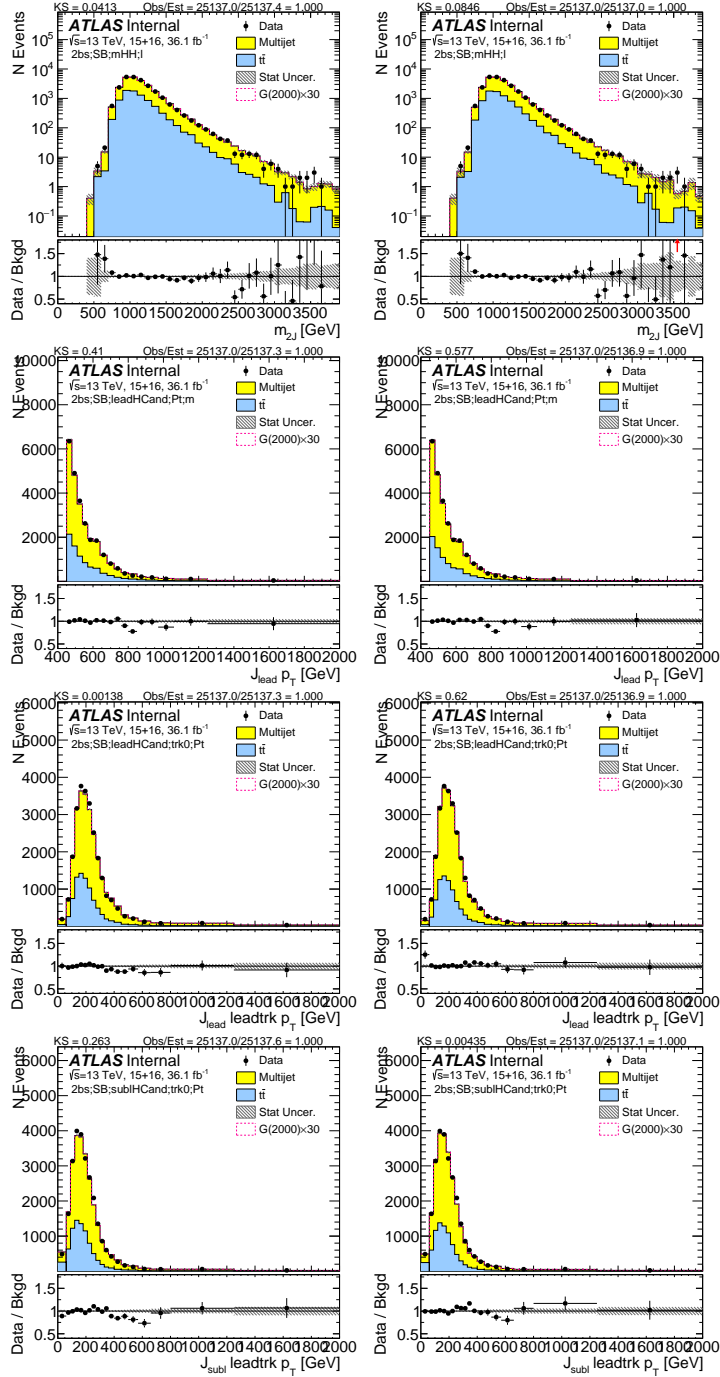


Figure E.7: Reweighted $2bs$ sideband region predictions comparison. Top row is the dijet Mass, second row is leading large- R jet p_T , third row is the leading large- R jet's leading track jet p_T and the last row subleading large- R jet's leading track jet p_T . On the left are the distributions before reweighting, and on the right are the distributions after reweighting.

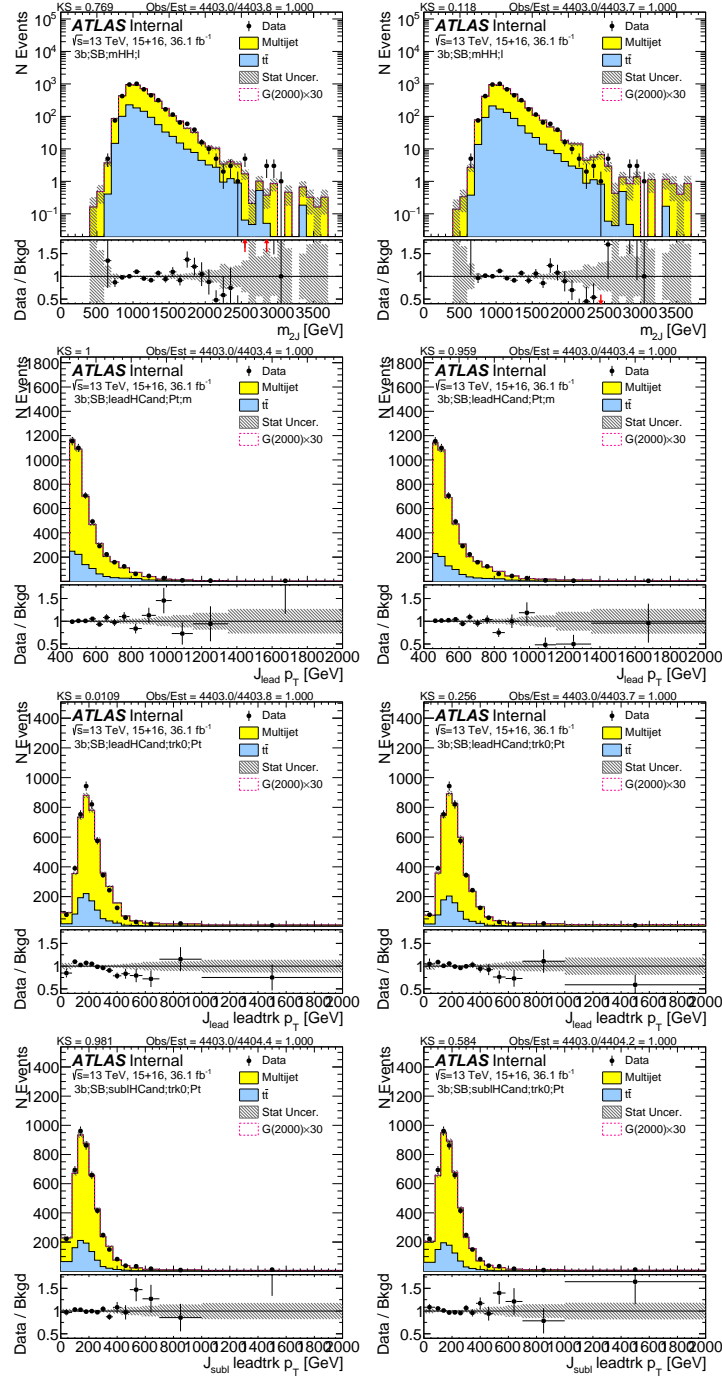


Figure E.8: Reweighted $3b$ sideband region predictions comparison. Top row is the dijet Mass, second row is leading large- R jet p_T , third row is the leading large- R jet's leading track jet p_T and the last row subleading large- R jet's leading track jet p_T . On the left are the distributions before reweighting, and on the right are the distributions after reweighting.

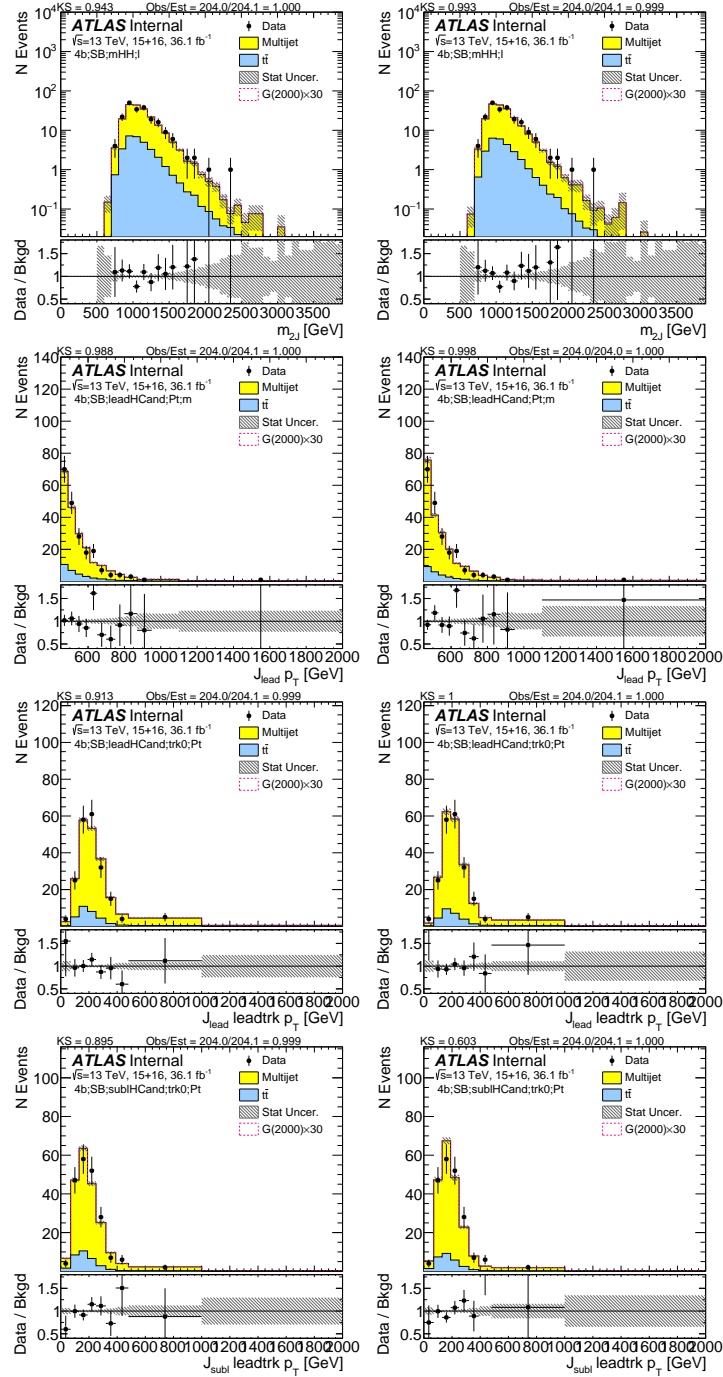


Figure E.9: Reweighted $4b$ sideband region predictions comparison. Top row is the dijet Mass, second row is leading large- R jet p_T , third row is the leading large- R jet's leading track jet p_T and the last row subleading large- R jet's leading track jet p_T . On the left are the distributions before reweighting, and on the right are the distributions after reweighting.

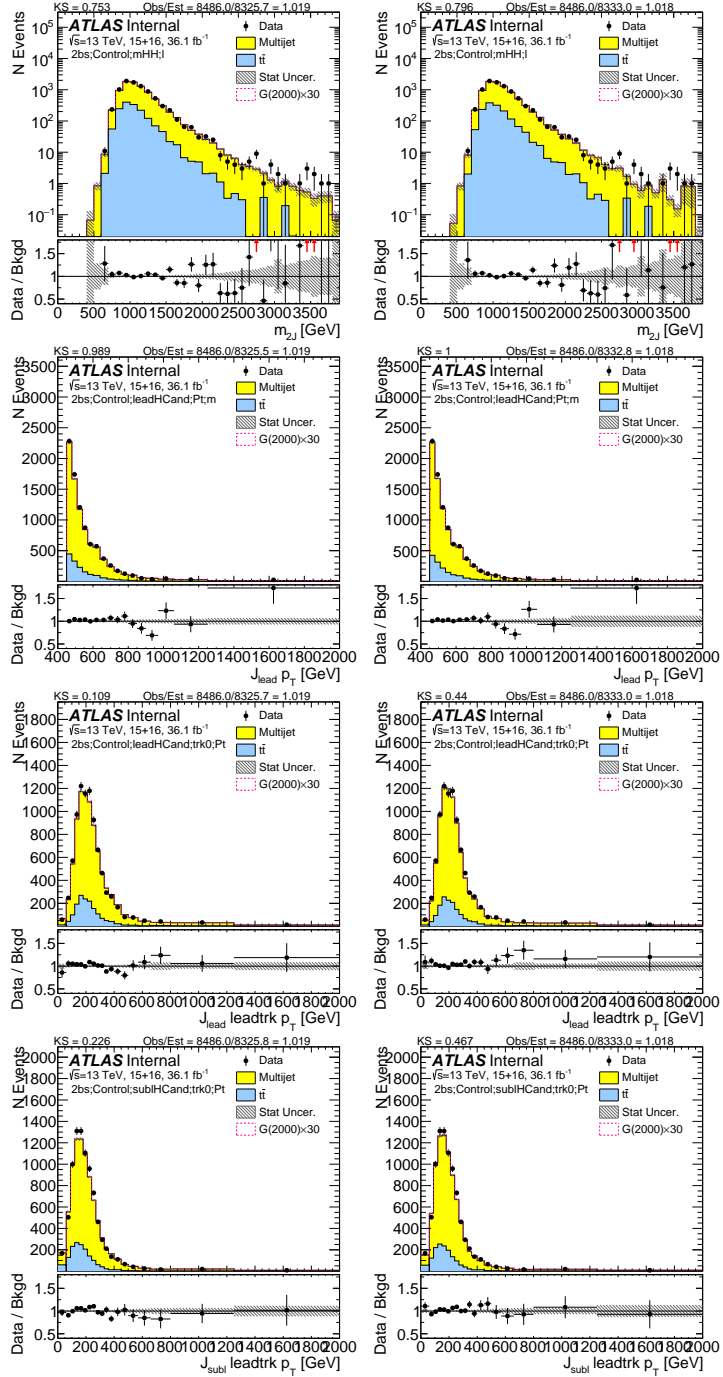


Figure E.10: Reweighted $2bs$ control region predictions comparison. Top row is the dijet Mass, second row is leading large- R jet p_T , third row is the leading large- R jet's leading track jet p_T and the last row subleading large- R jet's leading track jet p_T . On the left are the distributions before reweighting, and on the right are the distributions after reweighting.

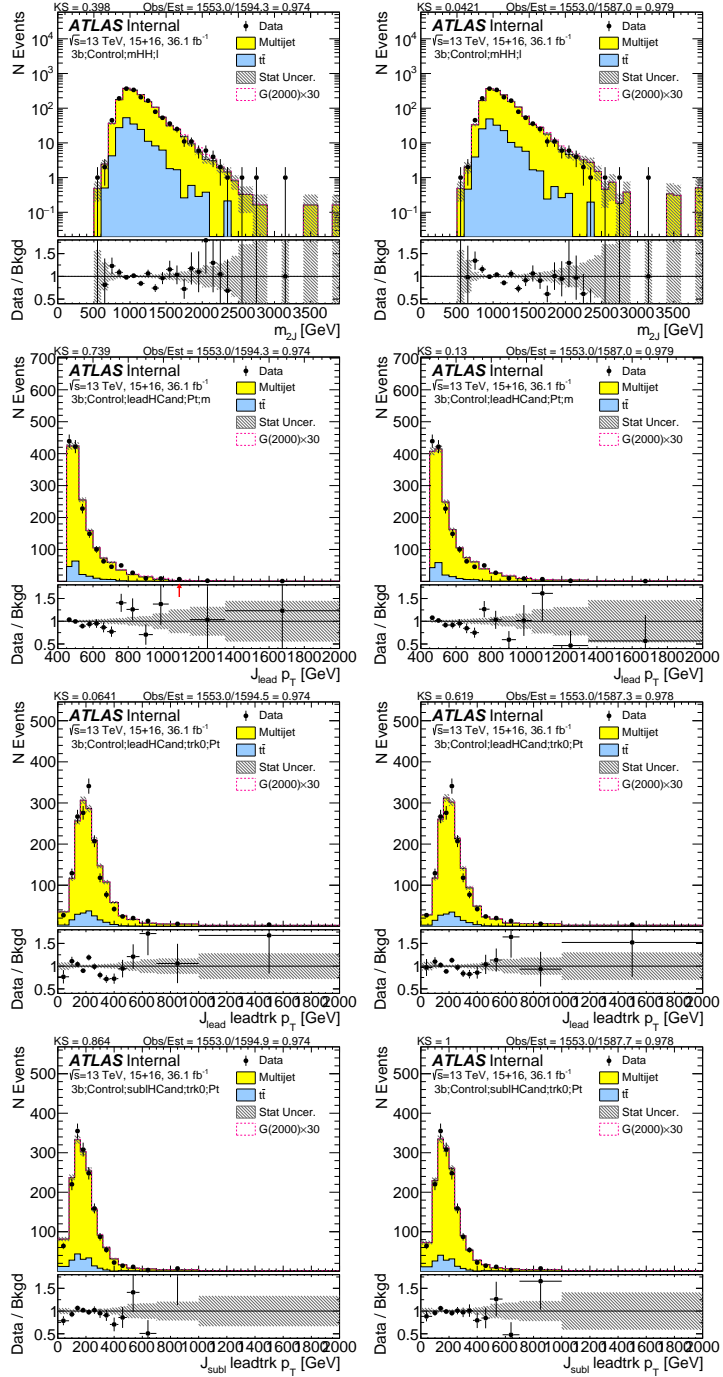


Figure E.11: Reweighted $3b$ control region predictions comparison. Top row is the dijet Mass, second row is leading large- R jet p_T , third row is the leading large- R jet's leading track jet p_T and the last row subleading large- R jet's leading track jet p_T . On the left are the distributions before reweighting, and on the right are the distributions after reweighting.

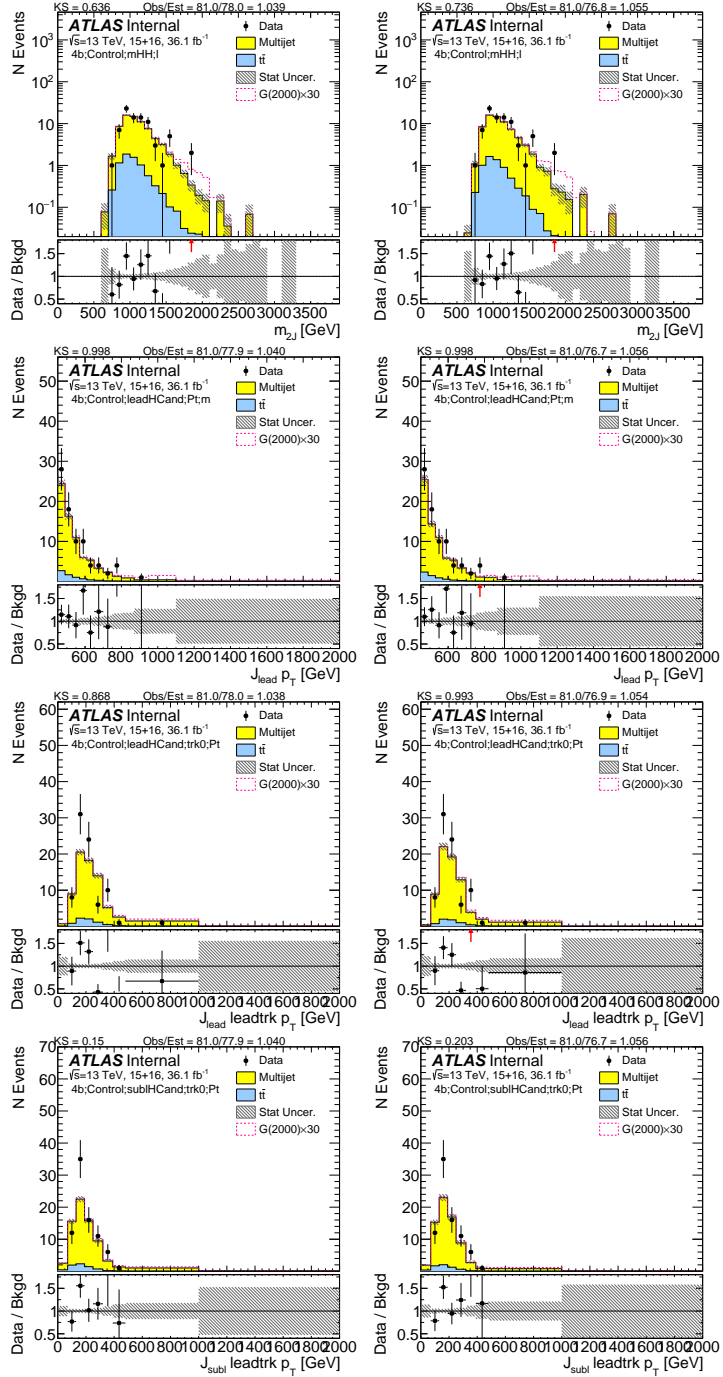


Figure E.12: Reweighted 4b control region predictions comparison. Top row is the dijet Mass, second row is leading large- R jet p_T , third row is the leading large- R jet's leading track jet p_T and the last row subleading large- R jet's leading track jet p_T . On the left are the distributions before reweighting, and on the right are the distributions after reweighting.

Other reweighting methods, that share similar idea with the AddTag method, where $1/2b$ samples are inclusively reweighted, have been tested:

- bkgeta: AddTag reweighting, but on four variables: large- R jet p_T , the two track jet $p_{T\text{s}}$, and large- R jet η .
- bkgdr: AddTag reweighting, but on four variables: large- R jet p_T , the two track jet $p_{T\text{s}}$, and two track jet ΔR .
- bkgtrk: AddTag reweighting, but on two variables: only the two track jet $p_{T\text{s}}$.
- bkgsb: AddTag reweighting, using the same three variables but instead of reweighting the $1b$ non-tagged Higgs candidate to be like the $1b$ tagged Higgs candidate, reweight $1b$ non-tagged Higgs candidate's distributions to be like the $2bs$ Higgs candidate in the sideband. Similarly, for $3b$, reweight $2b$ non-tagged Higgs candidate's distributions to be like the $3b$ Higgs candidate in the sideband, and for $4b$, reweight $2b$ non-tagged Higgs candidate's distributions to be like the $4b$ Higgs candidate in the sideband.

Also, reweighting the $1b$ Sideband directly to be like $2bs$ Sideband, and propagate the weight to control and signal regions, as the method used for previous analysis, has been tested:

- leadtrk: on three variables: leading Higgs candidate large- R jet p_T , the two lead-track jet $p_{T\text{s}}$.
- subltrk: on three variables: leading Higgs candidate large- R jet p_T , the two sublead-track jet $p_{T\text{s}}$.
- alltrk: on five variables: leading Higgs candidate large- R jet p_T , the two lead-track jet $p_{T\text{s}}$, and the two sublead-track jet $p_{T\text{s}}$.

For m_{2J} , the dijet mass distribution, the distribution comparisons are shown in Figure E.13. Signal regions are blinded, and the data distribution is replaced with the non-reweighted background estimate. For track jet p_T distributions, the comparisons are shown in Figure E.14, E.15, E.16. In most cases, the χ^2 per degree of freedom is improved for the background estimations, and very similar distributions in signal region is observed. Hence no extra systematics is assigned for the reweighting method.

The reweighting method can be further validated using Dijet MC. Due to the limited statistics, only $2bs$ dijet MC has enough event for testing. The weights derived in data are applied in the MC $1b$ using the AddTag method, and compared with the $1b$ un-reweighted distribution and the $2bs$ distribution. The inclusive region (sideband + control + signal) track jet p_T distributions are shown in Figure E.17. As can be seen, reweighting helps to model different b tagging sculpting effect. The m_{2J} distributions can be seen in Figure E.18. Reweighting differs from the non-reweighted distribution only by a small amount, yet improves the overall χ^2 per degree of freedom.

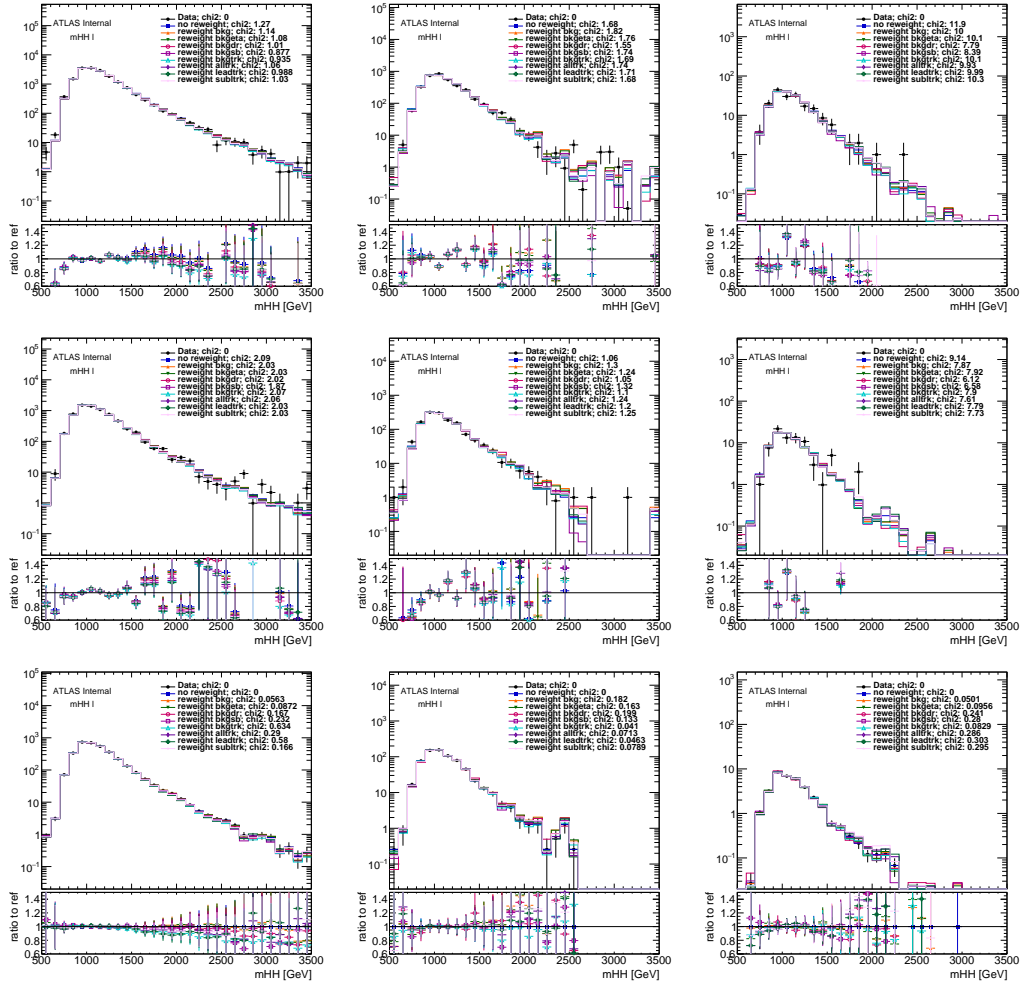


Figure E.13: Reweighted $2b$ s (left column), $3b$ (middle column), and $4b$ (right column) sideband (top row), control (middle row) and signal (bottom row) region predictions comparison, for MJJ. The Signal region is blinded, and the data distribution is replaced with the non-reweighted background predictions.

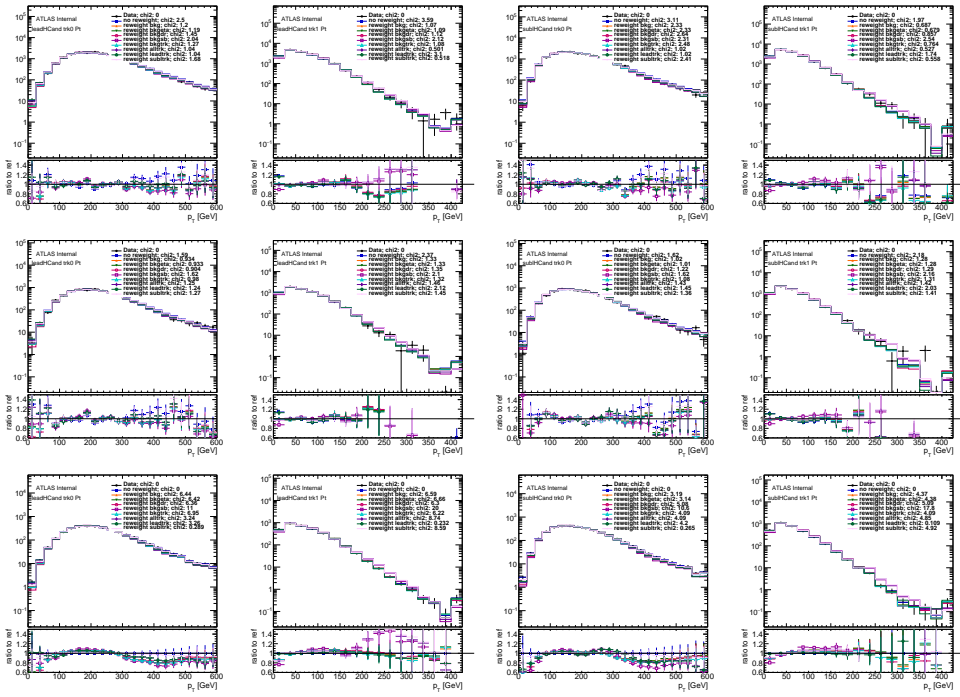


Figure E.14: Reweighted $2bs$ sideband (top row), control (middle row) and signal (bottom row) region predictions comparison, for leading Higgs Candidate leading track jet p_T (first column), leading Higgs Candidate subleading track jet p_T (second column), subleading Higgs Candidate leading track jet p_T (third column), subleading Higgs Candidate subleading track jet p_T (fourth column). The signal region is blinded, where the distribution is replaced with the non-reweighted predictions.

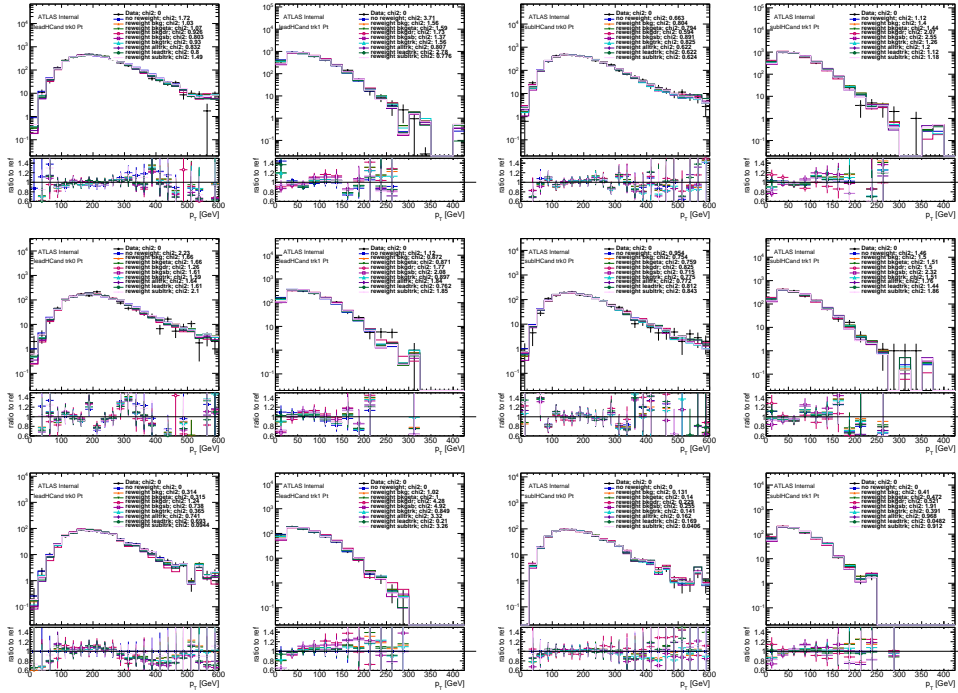


Figure E.15: Reweighted $3b$ sideband (top row), control (middle row) and signal (bottom row) predictions comparison, for leading Higgs Candidate leading track jet p_T (first column), leading Higgs Candidate subleading track jet p_T (second column), subleading Higgs Candidate leading track jet p_T (third column), subleading Higgs Candidate subleading track jet p_T (fourth column). The signal region is blinded, where the distribution is replaced with the non-reweighted predictions.

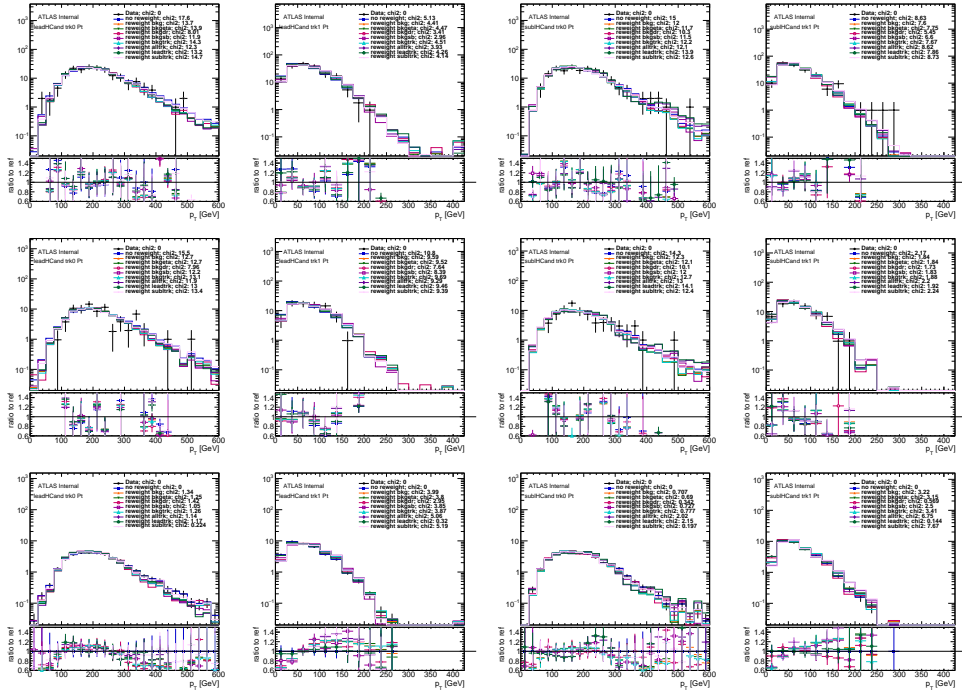


Figure E.16: Reweighted $4b$ sideband (top row), control (middle row) and signal (bottom row) region predictions comparison, for leading Higgs Candidate leading track jet p_T (first column), leading Higgs Candidate subleading track jet p_T (second column), subleading Higgs Candidate leading track jet p_T (third column), subleading Higgs Candidate subleading track jet p_T (fourth column). The signal region is blinded, where the distribution is replaced with the non-reweighted predictions.

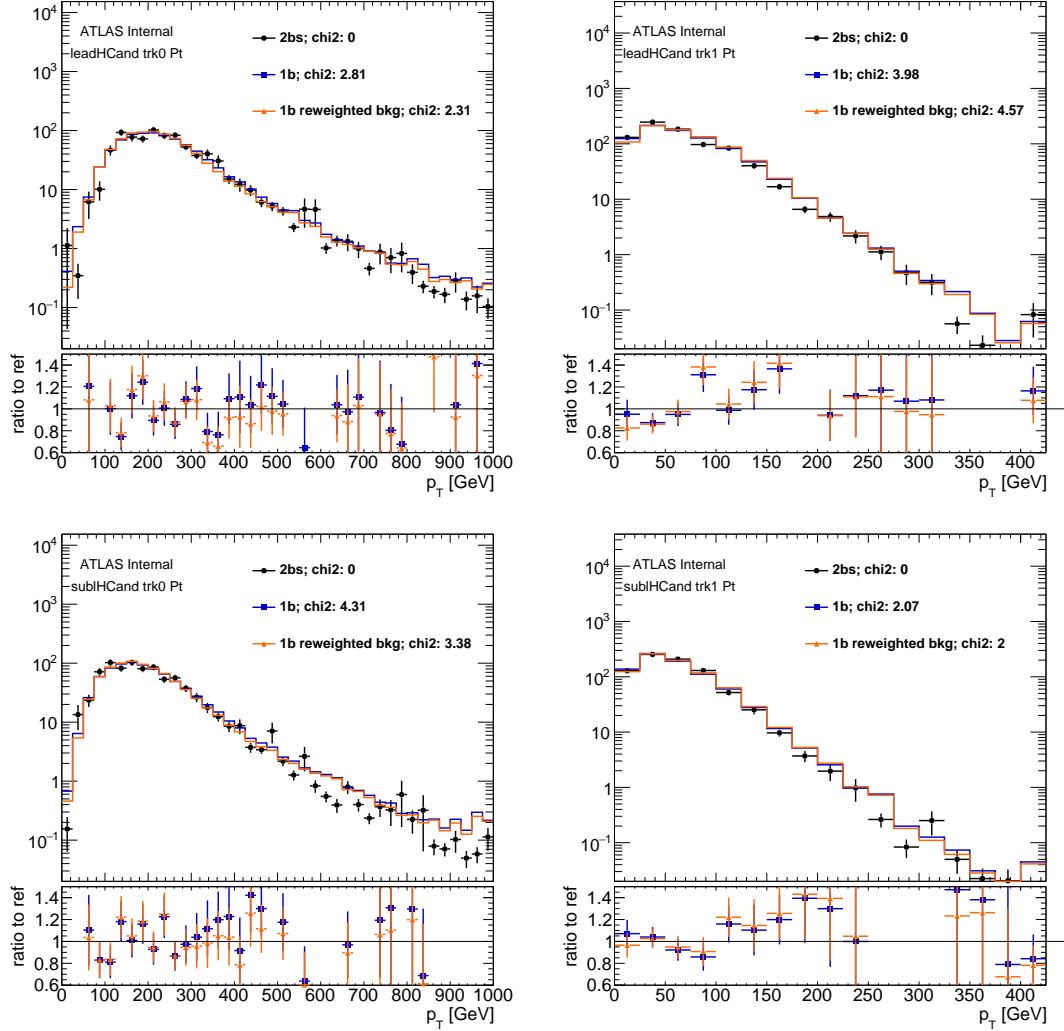


Figure E.17: Reweighted $2bs$ inclusive region predictions comparison in dijet MC, for leading Higgs Candidate leading track jet p_T (top left), leading Higgs Candidate subleading track jet p_T (top right), subleading Higgs Candidate leading track jet p_T (bottom left), subleading Higgs Candidate subleading track jet p_T (bottom right). $1b$ and reweighted $1b$ distributions are normalized to $2bs$.

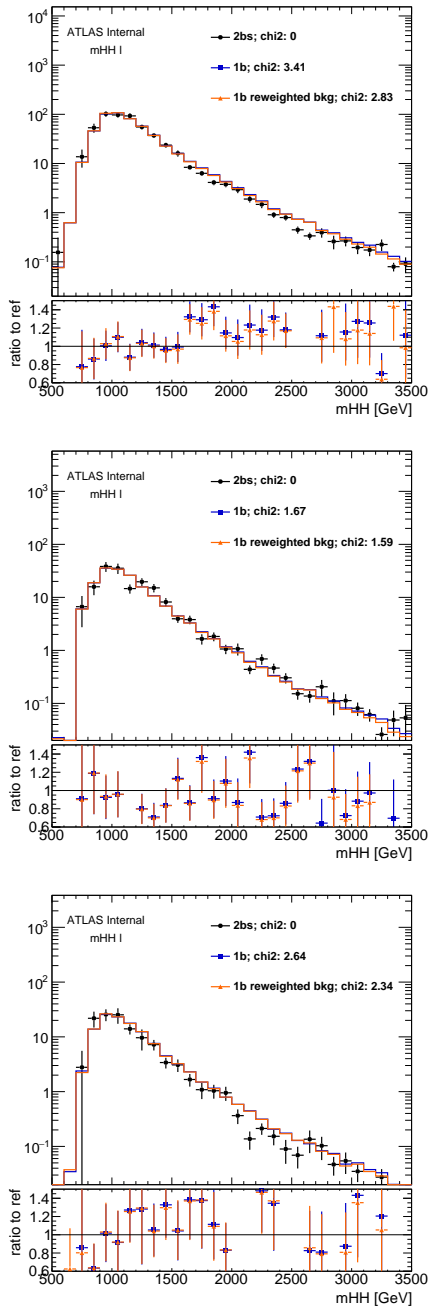


Figure E.18: Reweighted 2bs sideband (top) / control (middle) / signal (bottom) region predictions comparison, for MJJ. The signal region is not blinded, since it is dijet MC distribution. 1b and reweighted 1b distributions are normalized to 2bs .

F

Effects on yield prediction from variations of the sideband and control regions

This Appendix is the supporting material for section 7.5. The effect on signal region yield from different control region and sideband region is tested. All these tests are done on the control/sideband regions after the full reweighting procedure as described in 6.6, while applying the nominal reweight-

ing values.

Besides the nominal control region and sideband region definitions, seven additional variations, as illustrated in Figure F.2, F.1, F.3, F.5, F.4, F.7, F.6, are tested. They are:

- Low-mass control region: the center position of the circle that defines nominal CR is moved down by 3 GeV, in both leading and sub-leading large-jet mass.
- High-mass control region: the center position of the circle that defines nominal CR is moved up by 3 GeV, in both leading and sub-leading large-R jet mass.
- Signal-depletion (Small) control region: the X_{hh} cut that defines signal region is increased to 2.0 from 1.6. This variation only affect CR, while SR remains unchanged (i.e. signal region is still defined by $X_{hh} < 1.6$, while CR is defined as $X_{hh} > 2.0$ and $R_{hh} < 33$).
- High-mass sideband region: The signal region and control region remain unchanged, the center position of the circle that defines nominal SB is moved up by 3 GeV in both leading and sub-leading large-R jet mass.
- Low-mass sideband region: The signal region and control region remain unchanged, the center position of the circle that defines nominal SB is moved up by 3 GeV in both leading and sub-leading large-R jet mass.
- Large sideband region: The signal region and control region remain unchanged, while the SB is $33 < R_{hh}$ and $R_{hh}^{\text{high}} < 61$. μ_{QCD} will change.
- Small sideband region: The signal region and control region remain unchanged, while the SB is $33 < R_{hh}$ and $R_{hh}^{\text{high}} < 55$. μ_{QCD} will change.

The high mass and low mass CR tests how background modeling is sensitive to the exact position of CR. The signal-depletion CR is designed to test whether there is significant signal contamination in the CR. The agreement between data and prediction in the CR would be significantly different

from the number calculated with nominal CR, if there is a large amount of signal contamination in CR. The sideband variations are designed to test how sensitive the normalization fit is to the sideband definition.

The agreement between data and prediction in CR are summarized in Table 7.1, 7.2 and 7.3. For most CR variations, the discrepancy between data and prediction is smaller than statistical uncertainty of data. The only exception is $2bs$ high CR variation, where the prediction is $\sim 1.5\sigma$ away from the data. The variation in signal-depletion CR definition is not significantly deviated from the number derived from nominal CR definition, and the discrepancy is also within the statistical uncertainty of data as well. This shows no significant signal contamination in CR is found.

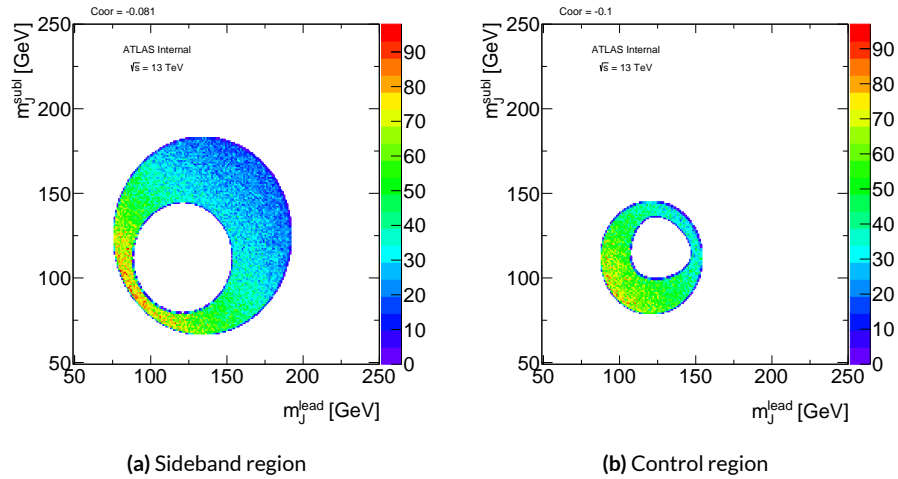


Figure F.1: In $1b$ data, with low-mass CR variation, new SB and CR $m_j^{\text{lead}} - m_j^{\text{subl}}$ distribution.

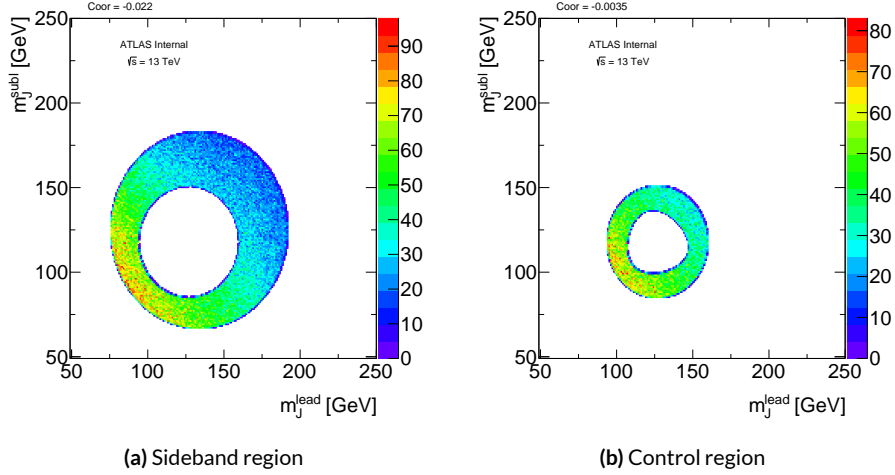


Figure F.2: In $1b$ data, with high-mass CR variation, new SB and CR $m_j^{\text{lead}} - m_j^{\text{subl}}$ distribution.

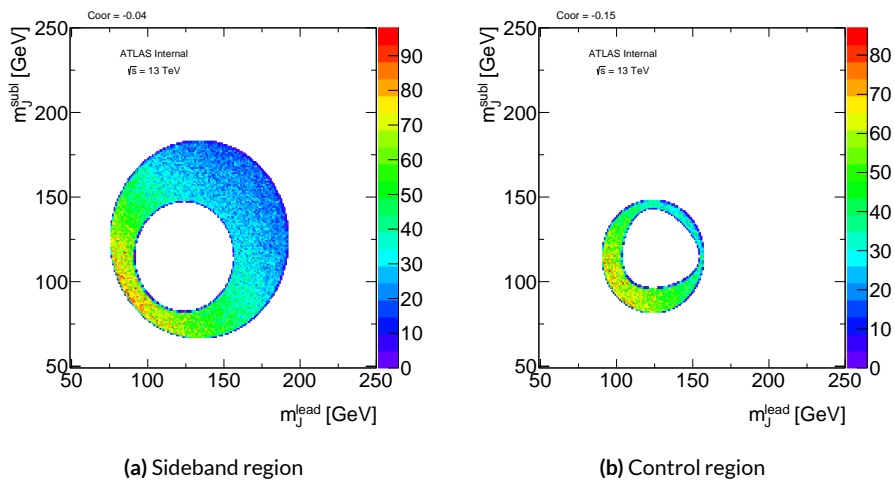


Figure F.3: In $1b$ data, with signal-depletion (small) CR variation, new SB and CR $m_j^{\text{lead}} - m_j^{\text{subl}}$ distribution.

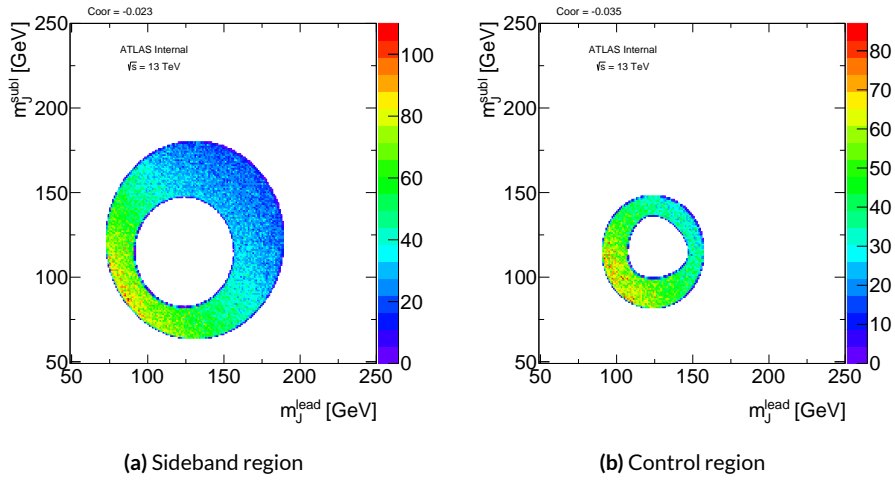


Figure F.4: In $1b$ data, with low-mass SB variation, new SB and CR $m_J^{\text{lead}} - m_J^{\text{subl}}$ distribution.

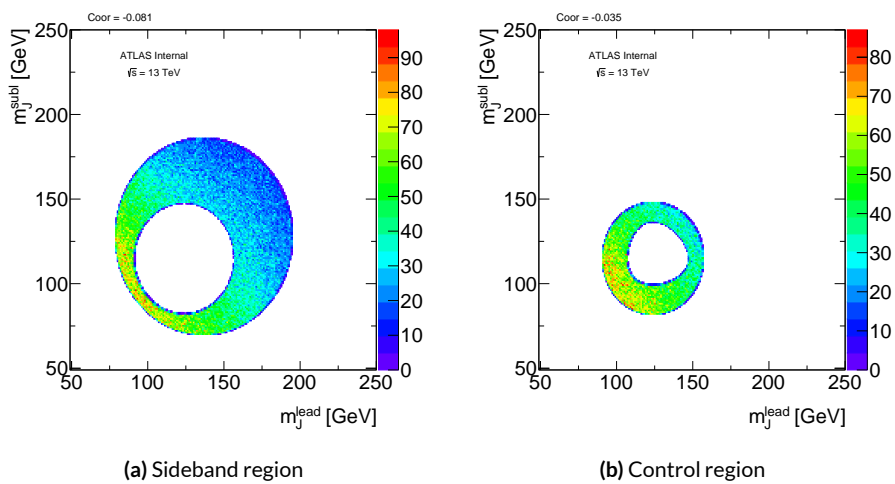


Figure F.5: In $1b$ data, with high-mass SB variation, new SB and CR $m_J^{\text{lead}} - m_J^{\text{subl}}$ distribution.

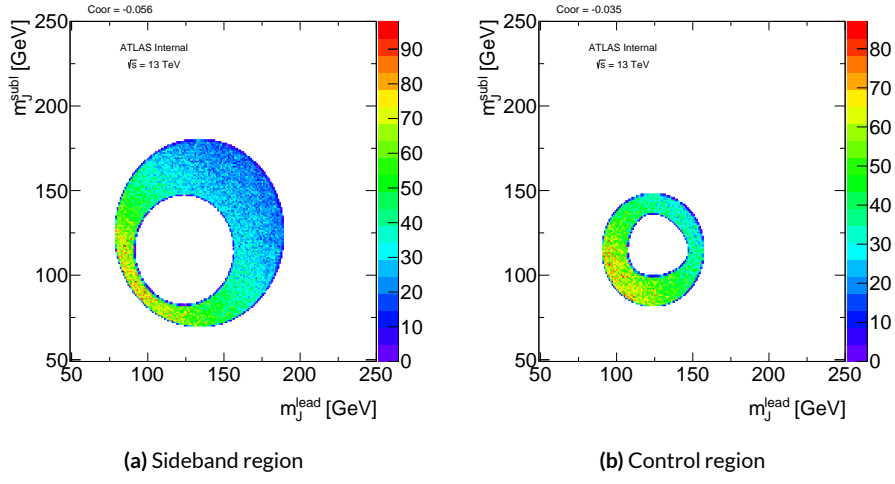


Figure F.6: In $1b$ data, with small SB variation, new SB and CR $m_J^{\text{lead}} - m_J^{\text{subl}}$ distribution.

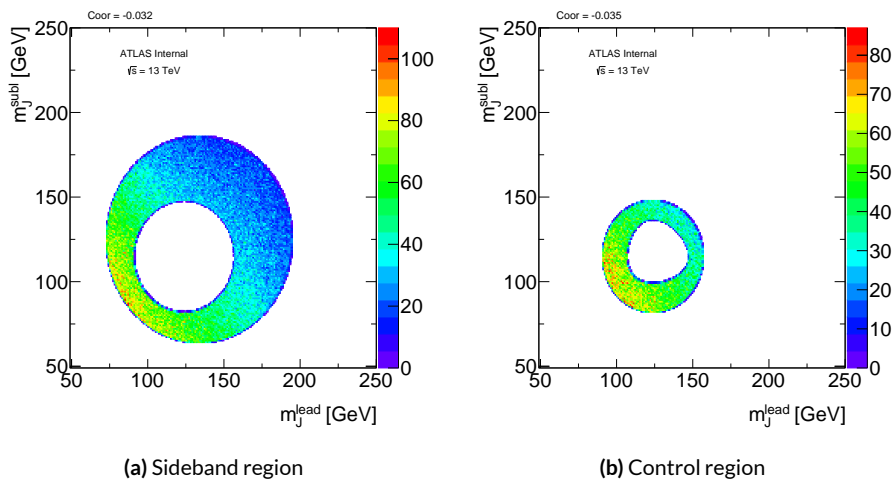


Figure F.7: In $1b$ data, with large SB variation, new SB and CR $m_J^{\text{lead}} - m_J^{\text{subl}}$ distribution.

The whole background estimation procedure is repeated after the variation. The summary of background estimated yields for $4b$ region can be found in Table ??, ??, F.3, F.4, F.5, F.6, F.7, for each variation.

Table F.1: Background prediction in SR/CR/SB for High CR in $4b$ region.

Four Tag	Sideband	Control	Signal
QCD Est	183.14 ± 3.02	58.01 ± 1.72	33.01 ± 1.25
$t\bar{t}$ Est.	25.97 ± 0.23	6.92 ± 0.13	1.62 ± 0.042
$Z + jets$	0 ± 0	6.18 ± 5.12	0 ± 0
Total Bkg Est	209.12 ± 3.03	71.12 ± 5.41	34.63 ± 1.25
Data	209.0 ± 14.46	76.0 ± 8.72	31.0 ± 5.57
$c = 1.0, m = 1.0 TeV$	2.68 ± 0.1	5.23 ± 0.14	10.07 ± 0.2
$c = 1.0, m = 2.0 TeV$	0.04 ± 0.0017	0.095 ± 0.0025	0.25 ± 0.0041
$c = 1.0, m = 3.0 TeV$	$0.00032 \pm 3.7e-05$	$0.0008 \pm 5.6e-05$	$0.0016 \pm 8e-05$

Table F.2: Background prediction in SR/CR/SB for Low CR in $4b$ region.

Four Tag	Sideband	Control	Signal
QCD Est	165.7 ± 2.84	69.9 ± 1.87	32.26 ± 1.22
$t\bar{t}$ Est.	28.47 ± 0.25	3.79 ± 0.078	1.59 ± 0.041
$Z + jets$	0 ± 0	6.18 ± 5.12	0 ± 0
Total Bkg Est	194.17 ± 2.85	79.87 ± 5.45	33.84 ± 1.23
Data	194.0 ± 13.93	91.0 ± 9.54	31.0 ± 5.57
$c = 1.0, m = 1.0 TeV$	2.66 ± 0.1	5.26 ± 0.14	10.07 ± 0.2
$c = 1.0, m = 2.0 TeV$	0.034 ± 0.0015	0.1 ± 0.0026	0.25 ± 0.0041
$c = 1.0, m = 3.0 TeV$	$0.0003 \pm 3.6e-05$	$0.00082 \pm 5.6e-05$	$0.0016 \pm 8e-05$

Table F.3: Background prediction in SR/CR/SB for Small CR in $4b$ region.

FourTag	Sideband	Control	Signal
QCD Est	176.26 ± 2.96	46.97 ± 1.54	32.91 ± 1.25
$t\bar{t}$ Est.	27.86 ± 0.25	2.81 ± 0.07	1.68 ± 0.044
$Z + jets$	0 ± 0	6.18 ± 5.12	0 ± 0
Total Bkg Est	204.12 ± 2.97	55.96 ± 5.35	34.59 ± 1.25
Data	204.0 ± 14.28	58.0 ± 7.62	31.0 ± 5.57
$c = 1.0, m = 1.0 TeV$	2.52 ± 0.1	2.82 ± 0.11	10.07 ± 0.2
$c = 1.0, m = 2.0 TeV$	0.034 ± 0.0015	0.054 ± 0.0019	0.25 ± 0.0041
$c = 1.0, m = 3.0 TeV$	$0.00032 \pm 3.7e-05$	$0.00048 \pm 4.3e-05$	$0.0016 \pm 8e-05$

Table F.4: Background prediction in SR/CR/SB for High SB in $4b$ region.

FourTag	Sideband	Control	Signal
QCD Est	168.37 ± 2.98	67.36 ± 1.88	34.53 ± 1.31
$t\bar{t}$ Est.	23.75 ± 0.21	5.18 ± 0.1	1.37 ± 0.035
$Z + jets$	0 ± 0	6.18 ± 5.12	0 ± 0
Total Bkg Est	192.12 ± 2.99	78.72 ± 5.46	35.89 ± 1.31
Data	192.0 ± 13.86	81.0 ± 9.0	31.0 ± 5.57
$c = 1.0, m = 1.0 TeV$	2.46 ± 0.098	5.4 ± 0.15	10.07 ± 0.2
$c = 1.0, m = 2.0 TeV$	0.031 ± 0.0015	0.1 ± 0.0026	0.25 ± 0.0041
$c = 1.0, m = 3.0 TeV$	$0.0003 \pm 3.5e-05$	$0.0008 \pm 5.6e-05$	$0.0016 \pm 8e-05$

Table F.5: Background prediction in SR/CR/SB for Low SB in $4b$ region.

FourTag	Sideband	Control	Signal
QCD Est	176.2 ± 2.81	58.42 ± 1.63	29.95 ± 1.14
$t\bar{t}$ Est.	40.93 ± 0.38	11.91 ± 0.23	3.14 ± 0.081
$Z + jets$	0 ± 0	6.18 ± 5.12	0 ± 0
Total Bkg Est	217.12 ± 2.84	76.51 ± 5.38	33.09 ± 1.14
Data	217.0 ± 14.73	81.0 ± 9.0	31.0 ± 5.57
$c = 1.0, m = 1.0 TeV$	2.52 ± 0.1	5.4 ± 0.15	10.07 ± 0.2
$c = 1.0, m = 2.0 TeV$	0.035 ± 0.0015	0.1 ± 0.0026	0.25 ± 0.0041
$c = 1.0, m = 3.0 TeV$	$0.00033 \pm 3.7e-05$	$0.0008 \pm 5.6e-05$	$0.0016 \pm 8e-05$

Table F.6: Background prediction in SR/CR/SB for Large SB in $4b$ region.

FourTag	Sideband	Control	Signal
QCD Est	198.09 ± 3.04	60.63 ± 1.69	31.08 ± 1.18
$t\bar{t}$ Est.	37.04 ± 0.31	7.9 ± 0.16	2.08 ± 0.054
$Z + jets$	0 ± 0	6.18 ± 5.12	0 ± 0
Total Bkg Est	235.12 ± 3.06	74.71 ± 5.4	33.16 ± 1.18
Data	235.0 ± 15.33	81.0 ± 9.0	31.0 ± 5.57
$c = 1.0, m = 1.0 TeV$	2.75 ± 0.1	5.4 ± 0.15	10.07 ± 0.2
$c = 1.0, m = 2.0 TeV$	0.037 ± 0.0016	0.1 ± 0.0026	0.25 ± 0.0041
$c = 1.0, m = 3.0 TeV$	$0.00034 \pm 3.8e-05$	$0.0008 \pm 5.6e-05$	$0.0016 \pm 8e-05$

Table F.7: Background prediction in SR/CR/SB for Small SB in $4b$ region.

FourTag	Sideband	Control	Signal
QCD Est	133.42 ± 2.47	58.2 ± 1.63	29.83 ± 1.13
$t\bar{t}$ Est.	34.72 ± 0.33	9.77 ± 0.19	2.58 ± 0.067
$Z + jets$	0 ± 0	6.18 ± 5.12	0 ± 0
Total Bkg Est	168.13 ± 2.49	74.15 ± 5.38	32.41 ± 1.13
Data	168.0 ± 12.96	81.0 ± 9.0	31.0 ± 5.57
$c = 1.0, m = 1.0 TeV$	2.29 ± 0.095	5.4 ± 0.15	10.07 ± 0.2
$c = 1.0, m = 2.0 TeV$	0.03 ± 0.0014	0.1 ± 0.0026	0.25 ± 0.0041
$c = 1.0, m = 3.0 TeV$	$0.00029 \pm 3.5e-05$	$0.0008 \pm 5.6e-05$	$0.0016 \pm 8e-05$

The summary of background estimated yields for $3b$ region can be found in Table F.8, F.9, F.10, F.11, F.12, F.13, F.14, for each variation.

Table F.8: Background prediction in SR/CR/SB for High CR in $3b$ region.

ThreeTag	Sideband	Control	Signal
QCD Est	3632.79 ± 28.07	1288.95 ± 16.26	700.18 ± 11.93
$t\bar{t}$ Est.	829.13 ± 25.15	174.53 ± 11.64	78.43 ± 2.03
$Z + jets$	33.59 ± 11.36	10.42 ± 5.62	0.49 ± 0.49
Total Bkg Est	4495.51 ± 39.36	1473.89 ± 20.77	779.1 ± 12.11
Data	4495.0 ± 67.04	1461.0 ± 38.22	801.0 ± 28.3
$c = 1.0, m = 1.0 TeV$	8.46 ± 0.19	11.99 ± 0.22	26.0 ± 0.33
$c = 1.0, m = 2.0 TeV$	0.18 ± 0.0037	0.36 ± 0.0052	0.76 ± 0.0076
$c = 1.0, m = 3.0 TeV$	0.0039 ± 0.00013	0.0072 ± 0.00018	0.013 ± 0.00023

Table F.9: Background prediction in SR/CR/SB for Low CR in $3b$ region.

ThreeTag	Sideband	Control	Signal
QCD Est	3412.05 ± 27.11	1542.75 ± 18.27	705.03 ± 12.02
$t\bar{t}$ Est.	887.39 ± 26.48	140.33 ± 10.2	80.32 ± 2.08
$Z + jets$	29.7 ± 11.19	14.3 ± 5.94	0.49 ± 0.49
Total Bkg Est	4329.15 ± 39.51	1697.38 ± 21.75	785.83 ± 12.2
Data	4328.0 ± 65.79	1628.0 ± 40.35	801.0 ± 28.3
$c = 1.0, m = 1.0 TeV$	7.87 ± 0.18	12.58 ± 0.23	26.0 ± 0.33
$c = 1.0, m = 2.0 TeV$	0.15 ± 0.0034	0.39 ± 0.0054	0.76 ± 0.0076
$c = 1.0, m = 3.0 TeV$	0.0036 ± 0.00013	0.0075 ± 0.00018	0.013 ± 0.00023

Table F.10: Background prediction in SR/CR/SB for Small CR in $3b$ region.

ThreeTag	Sideband	Control	Signal
QCD Est	3518.01 ± 27.48	1020.18 ± 14.79	701.6 ± 11.95
$t\bar{t}$ Est.	852.88 ± 25.72	98.31 ± 8.12	79.34 ± 2.05
$Z + jets$	32.8 ± 11.34	8.84 ± 5.19	0.49 ± 0.49
Total Bkg Est	4403.69 ± 39.31	1127.34 ± 17.66	781.42 ± 12.14
Data	4403.0 ± 66.36	1134.0 ± 33.67	801.0 ± 28.3
$c = 1.0, m = 1.0 TeV$	7.86 ± 0.18	7.5 ± 0.18	26.0 ± 0.33
$c = 1.0, m = 2.0 TeV$	0.16 ± 0.0035	0.22 ± 0.0041	0.76 ± 0.0076
$c = 1.0, m = 3.0 TeV$	0.0036 ± 0.00013	0.0043 ± 0.00014	0.013 ± 0.00023

Table F.11: Background prediction in SR/CR/SB for High SB in $3b$ region.

ThreeTag	Sideband	Control	Signal
QCD Est	3244.66 ± 26.66	1431.35 ± 17.56	710.47 ± 12.09
$t\bar{t}$ Est.	889.75 ± 26.15	160.18 ± 11.01	78.3 ± 2.03
$Z + jets$	28.07 ± 10.31	11.21 ± 5.65	0.49 ± 0.49
Total Bkg Est	4162.48 ± 38.74	1602.74 ± 21.48	789.26 ± 12.27
Data	4162.0 ± 64.51	1553.0 ± 39.41	801.0 ± 28.3
$c = 1.0, m = 1.0 TeV$	7.55 ± 0.18	12.58 ± 0.23	26.0 ± 0.33
$c = 1.0, m = 2.0 TeV$	0.14 ± 0.0033	0.38 ± 0.0054	0.76 ± 0.0076
$c = 1.0, m = 3.0 TeV$	0.0032 ± 0.00012	0.0075 ± 0.00018	0.013 ± 0.00023

Table F.12: Background prediction in SR/CR/SB for Low SB in $3b$ region.

ThreeTag	Sideband	Control	Signal
QCD Est	3797.02 ± 28.24	1395.42 ± 17.15	692.6 ± 11.8
$t\bar{t}$ Est.	825.52 ± 25.8	169.94 ± 11.68	83.07 ± 2.15
$Z + jets$	50.5 ± 15.32	11.21 ± 5.65	0.49 ± 0.49
Total Bkg Est	4673.04 ± 41.2	1576.56 ± 21.5	776.15 ± 12.01
Data	4672.0 ± 68.35	1553.0 ± 39.41	801.0 ± 28.3
$c = 1.0, m = 1.0 TeV$	8.09 ± 0.18	12.58 ± 0.23	26.0 ± 0.33
$c = 1.0, m = 2.0 TeV$	0.17 ± 0.0036	0.38 ± 0.0054	0.76 ± 0.0076
$c = 1.0, m = 3.0 TeV$	0.0039 ± 0.00013	0.0075 ± 0.00018	0.013 ± 0.00023

Table F.13: Background prediction in SR/CR/SB for Large SB in $3b$ region.

ThreeTag	Sideband	Control	Signal
QCD Est	4994.15 ± 29.34	1392.94 ± 17.09	691.4 ± 11.77
$t\bar{t}$ Est.	993.33 ± 28.3	170.09 ± 11.69	83.14 ± 2.15
$Z + jets$	44.81 ± 13.44	11.21 ± 5.65	0.49 ± 0.49
Total Bkg Est	5132.28 ± 42.92	1574.23 ± 21.47	775.03 ± 11.97
Data	5132.0 ± 71.64	1553.0 ± 39.41	801.0 ± 28.3
$c = 1.0, m = 1.0 TeV$	8.63 ± 0.19	12.58 ± 0.23	26.0 ± 0.33
$c = 1.0, m = 2.0 TeV$	0.18 ± 0.0037	0.38 ± 0.0054	0.76 ± 0.0076
$c = 1.0, m = 3.0 TeV$	0.0039 ± 0.00013	0.0075 ± 0.00018	0.013 ± 0.00023

Table F.14: Background prediction in SR/CR/SB for Small SB in $3b$ region.

ThreeTag	Sideband	Control	Signal
QCD Est	2935.02 ± 25.3	1424.16 ± 17.5	706.86 ± 12.05
$t\bar{t}$ Est.	765.58 ± 24.63	166.07 ± 11.41	81.18 ± 2.1
$Z + jets$	28.07 ± 10.31	11.21 ± 5.65	0.49 ± 0.49
Total Bkg Est	3728.68 ± 36.78	1601.44 ± 21.64	788.53 ± 12.24
Data	3728.0 ± 61.06	1553.0 ± 39.41	801.0 ± 28.3
$c = 1.0, m = 1.0 TeV$	7.03 ± 0.17	12.58 ± 0.23	26.0 ± 0.33
$c = 1.0, m = 2.0 TeV$	0.14 ± 0.0033	0.38 ± 0.0054	0.76 ± 0.0076
$c = 1.0, m = 3.0 TeV$	0.0032 ± 0.00012	0.0075 ± 0.00018	0.013 ± 0.00023

The summary of background estimated yields for $2bs$ region can be found in Table F.15, F.16, F.17, F.18, F.19, F.20, F.21, for each variation.

Table F.15: Background prediction in SR/CR/SB for High CR in $2bs$ region.

TwoTag split	Sideband	Control	Signal
QCD Est	17680.28 ± 38.67	6283.4 ± 22.64	3382.9 ± 16.59
$t\bar{t}$ Est.	7700.3 ± 69.5	1629.22 ± 30.95	857.59 ± 22.21
$Z + jets$	69.2 ± 16.9	24.98 ± 9.93	0.13 ± 0.091
Total Bkg Est	25449.78 ± 81.31	7937.59 ± 39.61	4240.62 ± 27.72
Data	25449.0 ± 159.53	8174.0 ± 90.41	4376.0 ± 66.15
$c = 1.0, m = 1.0 TeV$	5.21 ± 0.15	5.91 ± 0.16	10.87 ± 0.22
$c = 1.0, m = 2.0 TeV$	0.21 ± 0.0042	0.34 ± 0.0054	0.6 ± 0.0072
$c = 1.0, m = 3.0 TeV$	0.015 ± 0.00026	0.025 ± 0.00034	0.039 ± 0.00041

Table F.16: Background prediction in SR/CR/SB for Low CR in $2bs$ region.

TwoTag split	Sideband	Control	Signal
QCD Est	16635.37 ± 37.77	7376.46 ± 24.35	3390.48 ± 16.64
$t\bar{t}$ Est.	8026.21 ± 71.28	1385.31 ± 28.45	865.13 ± 22.4
$Z + jets$	55.1 ± 15.01	39.08 ± 12.61	0.13 ± 0.091
Total Bkg Est	24716.68 ± 82.06	8800.86 ± 39.51	4255.74 ± 27.91
Data	24716.0 ± 157.21	8907.0 ± 94.38	4376.0 ± 66.15
$c = 1.0, m = 1.0 TeV$	4.62 ± 0.14	6.5 ± 0.17	10.87 ± 0.22
$c = 1.0, m = 2.0 TeV$	0.17 ± 0.0038	0.38 ± 0.0057	0.6 ± 0.0072
$c = 1.0, m = 3.0 TeV$	0.013 ± 0.00025	0.027 ± 0.00035	0.039 ± 0.00041

Table F.17: Background prediction in SR/CR/SB for Small CR in $2bs$ region.

TwoTag split	Sideband	Control	Signal
QCD Est	17216.91 ± 38.33	4909.25 ± 19.86	3393.56 ± 16.64
$t\bar{t}$ Est.	7852.35 ± 70.3	937.99 ± 23.41	858.27 ± 22.23
$Z + jets$	67.74 ± 16.82	26.28 ± 10.08	0.13 ± 0.091
Total Bkg Est	25137.01 ± 81.82	5873.52 ± 32.31	4251.96 ± 27.77
Data	25137.0 ± 158.55	5999.0 ± 77.45	4376.0 ± 66.15
$c = 1.0, m = 1.0 TeV$	4.79 ± 0.14	3.95 ± 0.13	10.87 ± 0.22
$c = 1.0, m = 2.0 TeV$	0.18 ± 0.0039	0.22 ± 0.0044	0.6 ± 0.0072
$c = 1.0, m = 3.0 TeV$	0.013 ± 0.00025	0.016 ± 0.00026	0.039 ± 0.00041

Table F.18: Background prediction in SR/CR/SB for High SB in $2bs$ region.

TwoTag split	Sideband	Control	Signal
QCD Est	15881.71 ± 37.13	6904.39 ± 23.75	3434.67 ± 16.82
$t\bar{t}$ Est.	8012.21 ± 70.33	1447.3 ± 28.51	836.73 ± 21.67
$Z + jets$	53.46 ± 14.13	26.44 ± 10.08	0.13 ± 0.091
Total Bkg Est	23947.39 ± 80.77	8378.14 ± 38.45	4271.53 ± 27.43
Data	23947.0 ± 154.75	8486.0 ± 92.12	4376.0 ± 66.15
$c = 1.0, m = 1.0 TeV$	4.47 ± 0.14	6.33 ± 0.16	10.87 ± 0.22
$c = 1.0, m = 2.0 TeV$	0.16 ± 0.0037	0.36 ± 0.0056	0.6 ± 0.0072
$c = 1.0, m = 3.0 TeV$	0.012 ± 0.00023	0.027 ± 0.00034	0.039 ± 0.00041

Table F.19: Background prediction in SR/CR/SB for Low SB in $2bs$ region.

TwoTag split	Sideband	Control	Signal
QCD Est	18853.52 ± 39.96	6832.97 ± 23.54	3398.98 ± 16.68
$t\bar{t}$ Est.	7470.01 ± 68.56	1497.44 ± 29.5	865.71 ± 22.42
$Z + jets$	72.2 ± 17.11	26.44 ± 10.08	0.13 ± 0.091
Total Bkg Est	26395.73 ± 81.18	8356.86 ± 39.06	4264.82 ± 27.94
Data	26395.0 ± 162.47	8486.0 ± 92.12	4376.0 ± 66.15
$c = 1.0, m = 1.0 TeV$	5.07 ± 0.15	6.33 ± 0.16	10.87 ± 0.22
$c = 1.0, m = 2.0 TeV$	0.2 ± 0.0041	0.36 ± 0.0056	0.6 ± 0.0072
$c = 1.0, m = 3.0 TeV$	0.014 ± 0.00026	0.027 ± 0.00034	0.039 ± 0.00041

Table F.20: Background prediction in SR/CR/SB for Large SB in $2bs$ region.

TwoTag split	Sideband	Control	Signal
QCD Est	20472.06 ± 41.82	6862.72 ± 23.61	3413.92 ± 16.72
$t\bar{t}$ Est.	8569.73 ± 72.85	1452.54 ± 28.61	839.75 ± 21.75
$Z + jets$	73.9 ± 17.45	26.44 ± 10.08	0.13 ± 0.091
Total Bkg Est	29115.69 ± 85.79	8341.7 ± 38.44	4253.81 ± 27.43
Data	29115.0 ± 170.63	8486.0 ± 92.12	4376.0 ± 66.15
$c = 1.0, m = 1.0 TeV$	5.38 ± 0.15	6.33 ± 0.16	10.87 ± 0.22
$c = 1.0, m = 2.0 TeV$	0.2 ± 0.0042	0.36 ± 0.0056	0.6 ± 0.0072
$c = 1.0, m = 3.0 TeV$	0.015 ± 0.00026	0.027 ± 0.00034	0.039 ± 0.00041

Table F.21: Background prediction in SR/CR/SB for Large SB in $2bs$ region.

TwoTag split	Sideband	Control	Signal
QCD Est	14242.66 ± 34.91	6800.86 ± 23.43	3383.0 ± 16.6
$t\bar{t}$ Est.	6985.79 ± 66.42	1505.96 ± 29.67	870.64 ± 22.55
$Z + jets$	55.33 ± 14.25	26.44 ± 10.08	0.13 ± 0.091
Total Bkg Est	21283.78 ± 76.38	8333.25 ± 39.12	4253.77 ± 28.0
Data	21283.0 ± 145.89	8486.0 ± 92.12	4376.0 ± 66.15
$c = 1.0, m = 1.0 TeV$	4.21 ± 0.13	6.33 ± 0.16	10.87 ± 0.22
$c = 1.0, m = 2.0 TeV$	0.16 ± 0.0037	0.36 ± 0.0056	0.6 ± 0.0072
$c = 1.0, m = 3.0 TeV$	0.012 ± 0.00023	0.027 ± 0.00034	0.039 ± 0.00041

The variation of prediction in SR can be found in Table F.22, F.23 and F.24. The variation in signal-depletion variation is not shown since that will be zero by definition. The variation of background prediction in SR is very small and within statistical uncertainty. This is mainly due to the data-driven background estimation technique we are using.

Table F.22: Variations in Prediction in $4b$ SR region.

FourTag	Prediction	Diff	QCD	ttbar
Nominal	$34.59\% \pm 1.25\%$	$0.011\% \pm 7.23\%$	$0.0021\% \pm 7.59\%$	$0.2\% \pm 5.22\%$
CR High	$34.63\% \pm 1.25\%$	$0.1\% \pm 7.24\%$	$0.3\% \pm 7.62\%$	$-3.73\% \pm 5.01\%$
CR Low	$33.84\% \pm 1.23\%$	$-2.16\% \pm 7.08\%$	$-1.98\% \pm 7.44\%$	$-5.6\% \pm 4.92\%$
CR Small	$34.59\% \pm 1.25\%$	$0.011\% \pm 7.23\%$	$0.0021\% \pm 7.59\%$	$0.2\% \pm 5.22\%$
SB Large	$33.16\% \pm 1.18\%$	$-4.13\% \pm 6.88\%$	$-5.57\% \pm 7.17\%$	$24.0\% \pm 6.46\%$
SB Small	$32.41\% \pm 1.13\%$	$-6.31\% \pm 6.67\%$	$-9.35\% \pm 6.88\%$	$53.41\% \pm 7.99\%$
SB High	$35.89\% \pm 1.31\%$	$3.76\% \pm 7.54\%$	$4.91\% \pm 7.96\%$	$-18.7\% \pm 4.24\%$

Table F.23: Variations in Prediction in $3b$ SR region.

ThreeTag	Prediction	Diff	QCD	ttbar
Nominal	$781.42\% \pm 12.14\%$	$0.00026\% \pm 3.11\%$	$-8.8e-05\% \pm 3.41\%$	$-0.0055\% \pm 5.17\%$
CR High	$779.1\% \pm 12.11\%$	$-0.3\% \pm 3.1\%$	$-0.2\% \pm 3.4\%$	$-1.14\% \pm 5.11\%$
CR Low	$785.83\% \pm 12.2\%$	$0.56\% \pm 3.12\%$	$0.49\% \pm 3.42\%$	$1.23\% \pm 5.24\%$
CR Small	$781.42\% \pm 12.14\%$	$0.00026\% \pm 3.11\%$	$-8.8e-05\% \pm 3.41\%$	$-0.0055\% \pm 5.17\%$
SB Large	$775.03\% \pm 11.97\%$	$-0.82\% \pm 3.07\%$	$-1.45\% \pm 3.36\%$	$4.79\% \pm 5.42\%$
SB Small	$788.53\% \pm 12.24\%$	$0.91\% \pm 3.13\%$	$0.75\% \pm 3.43\%$	$2.32\% \pm 5.29\%$
SB High	$789.26\% \pm 12.27\%$	$1.0\% \pm 3.14\%$	$1.26\% \pm 3.45\%$	$-1.31\% \pm 5.11\%$

Besides the normalization, the variation of QCD shape in SR is also tested, as shown in Figure F.8 and Figure F.9. There are very small variations in terms of QCD shape, and such variation is within QCD shape uncertainty derived from nominal CR.

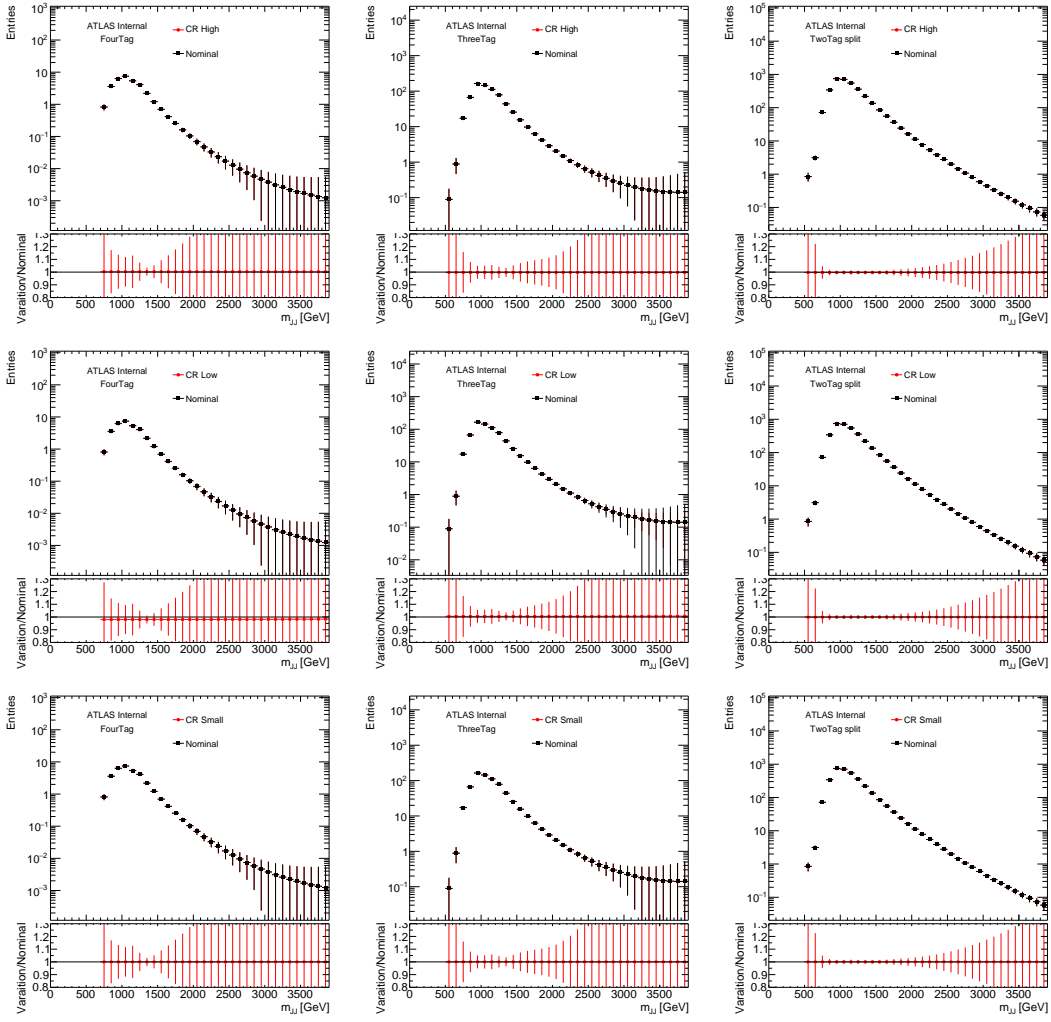


Figure F.8: Comparisons of the nominal QCD shape prediction (black) with the results of control and sideband region variations (red). The ratio of the shape from each variation to the nominal shape is shown in the lower panel. The left column shows the relevant distributions for the $4b$ signal region, the middle column is for the $3b$ signal region, and the left column is for the $2b$ signal region. The top row is for high CR variation, the middle row is for the low CR variation, and the bottom row is for the small CR variation.

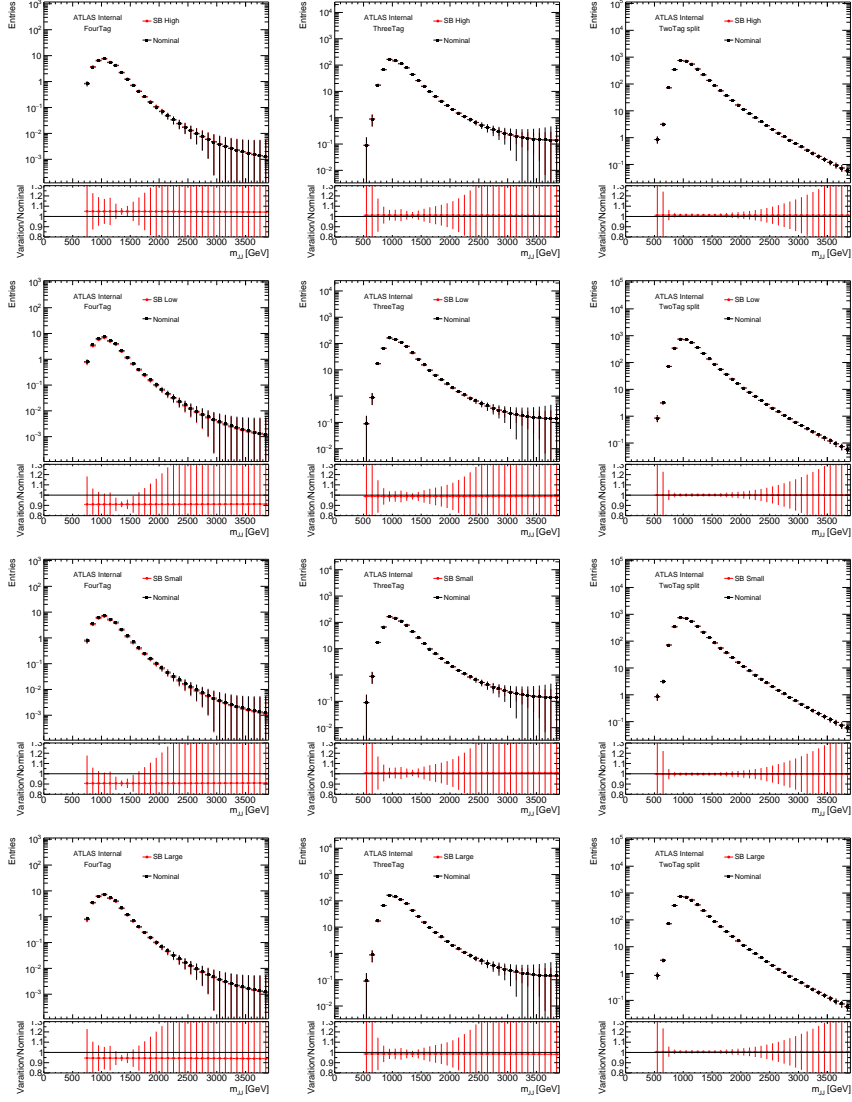


Figure F.9: Comparisons of the nominal QCD shape prediction (black) with the results of control and sideband region variations (red). The ratio of the shape from each variation to the nominal shape is shown in the lower panel. The left column shows the relevant distributions for the $4b$ signal region, the middle column is for the $3b$ signal region, and the right column is for the $2bs$ signal region. The top row is for high SB variation, the second row is for the low SB variation, the third row is for the small SB variation and the large raw is for the large SB variation.

Table F.24: Variations in Prediction in $2bs$ SR region.

TwoTag split	Prediction	Diff	QCD	ttbar
Nominal	4251.96 % \pm 27.77 %	-1.4e-05 % \pm 1.31 %	-8.2e-05 % \pm 0.98 %	-0.00014 % \pm 5.18 %
CR High	4240.62 % \pm 27.72 %	-0.27 % \pm 1.3 %	-0.31 % \pm 0.98 %	-0.079 % \pm 5.18 %
CR Low	4255.74 % \pm 27.91 %	0.089 % \pm 1.31 %	-0.091 % \pm 0.98 %	0.8 % \pm 5.22 %
CR Small	4251.96 % \pm 27.77 %	-1.4e-05 % \pm 1.31 %	-8.2e-05 % \pm 0.98 %	-0.00014 % \pm 5.18 %
SB Large	4253.81 % \pm 27.43 %	0.044 % \pm 1.3 %	0.6 % \pm 0.99 %	-2.16 % \pm 5.07 %
SB Small	4253.77 % \pm 28.0 %	0.043 % \pm 1.31 %	-0.31 % \pm 0.98 %	1.44 % \pm 5.25 %
SB High	4271.53 % \pm 27.43 %	0.46 % \pm 1.3 %	1.21 % \pm 0.99 %	-2.51 % \pm 5.05 %

References

- [1] C. Patrignani et al. Review of Particle Physics. *Chin. Phys.*, C40(10):100001, 2016. doi: 10.1088/1674-1137/40/10/100001.
- [2] David Griffiths. *Introduction to elementary particles*. 2008.
- [3] Christopher G. Tully. *Elementary particle physics in a nutshell*. 2011.
- [4] Matthew D. Schwartz. *Quantum Field Theory and the Standard Model*. Cambridge University Press, 2014. ISBN 1107034736, 9781107034730.
- [5] ATLAS Collaboration. Observation of a new particle in the search for the Standard Model Higgs boson with the ATLAS detector at the LHC. *Phys. Lett. B*, 716:1, 2012. doi: 10.1016/j.physletb.2012.08.020.
- [6] CMS Collaboration. Observation of a new boson at a mass of 125 GeV with the CMS experiment at the LHC. *Phys. Lett. B*, 716:30, 2012. doi: 10.1016/j.physletb.2012.08.021.
- [7] R. Frederix, S. Frixione, V. Hirschi, F. Maltoni, O. Mattelaer, P. Torrielli, E. Vryonidou, and M. Zaro. Higgs pair production at the LHC with NLO and parton-shower effects. *Phys. Lett.*, B732:142–149, 2014. doi: 10.1016/j.physletb.2014.03.026.
- [8] D. de Florian et al. Handbook of LHC Higgs Cross Sections: 4. Deciphering the Nature of the Higgs Sector. 2016. doi: 10.23731/CYRM-2017-002.
- [9] R. Gröber and M. Mühlleitner. Composite Higgs boson pair production at the LHC. *JHEP*, 06:020, 2011. doi: 10.1007/JHEP06(2011)020.
- [10] Roberto Contino et al. Anomalous couplings in double Higgs production. *JHEP*, 08:154, 2012. doi: 10.1007/JHEP08(2012)154.
- [11] Graham D. Kribs and Adam Martin. Enhanced di-higgs production through light colored scalars. *Phys. Rev. D*, 86:095023, 2012. doi: 10.1103/PhysRevD.86.095023.

- [12] Graham D. Kribs, Andreas Maier, Heidi Rzehak, Michael Spannowsky, and Philip Waite. Electroweak oblique parameters as a probe of the trilinear Higgs boson self-interaction. *Phys. Rev.*, D95(9):093004, 2017. doi: 10.1103/PhysRevD.95.093004.
- [13] W.J. Stirling. 7/8 and 13/8 TeV LHC luminosity ratios. 2013. URL http://www.hep.physics.ac.uk/~wstirlin/plots/lhclumi7813_2013_vo.pdf.
- [14] T. D. Lee. A theory of spontaneous t violation. *Phys. Rev. D*, 8:1226–1239, Aug 1973. doi: 10.1103/PhysRevD.8.1226.
- [15] G.C. Branco et al. Theory and phenomenology of two-Higgs-doublet models. *Phys. Rept.*, 516:1, 2012. doi: 10.1016/j.physrep.2012.02.002.
- [16] Kaustubh Agashe, Hooman Davoudiasl, Gilad Perez, and Amarjit Soni. Warped gravitons at the CERN LHC and beyond. *Phys. Rev. D*, 76:036006, 2007. doi: 10.1103/PhysRevD.76.036006.
- [17] Liam Fitzpatrick, Jared Kaplan, Lisa Randall, and Lian-Tao Wang. Searching for the Kaluza-Klein graviton in bulk RS models. *JHEP*, 09:013, 2007. doi: 10.1088/1126-6708/2007/09/013.
- [18] Viviana Cavaliere and Gabriel Facini. Summary of Limits on BSM Models from Diboson Searches. Technical Report ATL-COM-PHYS-2016-1071, CERN, Geneva, Sep 2016. URL <https://cds.cern.ch/record/2203605>.
- [19] ATLAS Collaboration. Search for Higgs boson pair production in the $b\bar{b}b\bar{b}$ final state from pp collisions at $\sqrt{s} = 8$ TeV with the ATLAS detector. *Eur. Phys. J. C*, 75:412, 2015. doi: 10.1140/epjc/s10052-015-3628-x.
- [20] ATLAS Collaboration. Search for Higgs Boson Pair Production in the $\gamma\gamma b\bar{b}$ Final State Using pp Collision Data at $\sqrt{s} = 8$ TeV from the ATLAS Detector. *Phys. Rev. Lett.*, 114:081802, 2015. doi: 10.1103/PhysRevLett.114.081802.
- [21] Georges Aad et al. Searches for Higgs boson pair production in the $hh \rightarrow b\tau\tau, \gamma\gamma WW^*, \gamma\gamma bb, bbbb$ channels with the ATLAS detector. *Phys. Rev.*, D92:092004, 2015. doi: 10.1103/PhysRevD.92.092004.
- [22] Lyndon R Evans and Philip Bryant. LHC Machine. *J. Instrum.*, 3:S08001. 164 p, 2008. URL <https://cds.cern.ch/record/1129806>. This report is an abridged version of the LHC Design Report (CERN-2004-003).

- [23] ATLAS Collaboration. The ATLAS experiment at the CERN Large Hadron Collider. *JINST*, 3:So8003, 2008. doi: 10.1088/1748-0221/3/08/So8003.
- [24] CMS Collaboration. The CMS experiment at the CERN LHC. *Journal of Instrumentation*, 3(08):So8004, 2008. URL <http://stacks.iop.org/1748-0221/3/i=08/a=So8004>.
- [25] LHCb Collaoration. The LHCb Detector at the LHC. *JINST*, 3:So8005, 2008. doi: 10.1088/1748-0221/3/08/So8005.
- [26] ALICE Collaboration. The ALICE experiment at the CERN LHC. *Journal of Instrumentation*, 3(08):So8002, 2008. URL <http://stacks.iop.org/1748-0221/3/i=08/a=So8002>.
- [27] Lyndon Evans. The Large Hadron Collider. *Annual Review of Nuclear and Particle Science*, 61(1):435–466, 2011. doi: 10.1146/annurev-nucl-102010-130438.
- [28] ATLAS Collaboration. Luminosity Determination in $p\bar{p}$ Collisions at $\sqrt{s} = 7$ TeV Using the ATLAS Detector at the LHC. *Eur. Phys. J.*, C 71:1630, 2011. doi: 10.1140/epjc/s10052-011-1630-5.
- [29] Paul Collier for the LHC team. LHC Machine Status. CERN Resource Review Board, 2015. URL <https://cds.cern.ch/record/2063924/files/CERN-RRB-2015-119.PDF>.
- [30] Giulia Papotti for the LHC team. LHC Machine Status Report. CERN Resource Review Board, 2016. URL https://indico.cern.ch/event/563488/contributions/2277292/attachments/1340292/2019570/20160921_LHCC.pdf.
- [31] ATLAS Collaboration. ATLAS Luminosity Public Results, Run 2. 2015. URL <https://twiki.cern.ch/twiki/bin/view/AtlasPublic/LuminosityPublicResultsRun2>.
- [32] ATLAS Collaboration. The ATLAS Experiment at the CERN Large Hadron Collider. *JINST*, 3:So8003, 2008. doi: 10.1088/1748-0221/3/08/So8003.
- [33] ATLAS Collaboration. ATLAS Insertable B-Layer Technical Design Report. CERN-LHCC-2010-013. ATLAS-TDR-19, Sep 2010. URL <https://cds.cern.ch/record/1291633>.
- [34] ATLAS Collaboration. Expected performance of the ATLAS b -tagging algorithms in Run-2. ATL-PHYS-PUB-2015-022, 2015. URL <https://cds.cern.ch/record/2037697>.
- [35] Morad Aaboud et al. Study of the material of the ATLAS inner detector for Run 2 of the LHC. *JINST*, 12(12):P12009, 2017. doi: 10.1088/1748-0221/12/12/P12009.

- [36] ATLAS Collaboration. Performance of the ATLAS Trigger System in 2015. *Eur. Phys. J. C*, 77:317, 2017. doi: 10.1140/epjc/s10052-017-4852-3.
- [37] M. Aaboud et al. Performance of the ATLAS Track Reconstruction Algorithms in Dense Environments in LHC Run 2. *Eur. Phys. J., C77(10):673*, 2017. doi: 10.1140/epjc/s10052-017-5225-7.
- [38] Gavin P. Salam. Towards Jetography. *Eur. Phys. J., C67:637–686*, 2010. doi: 10.1140/epjc/s10052-010-1314-6.
- [39] ATLAS Collaboration. Topological cell clustering in the ATLAS calorimeters and its performance in LHC Run 1. *Eur. Phys. J. C*, 77:490, 2017. doi: 10.1140/epjc/s10052-017-5004-5.
- [40] Matteo Cacciari, Gavin P. Salam, and Gregory Soyez. The Anti-k(t) jet clustering algorithm. *JHEP*, 04:063, 2008. doi: 10.1088/1126-6708/2008/04/063.
- [41] Matteo Cacciari, Gavin P. Salam, and Gregory Soyez. The catchment area of jets. *JHEP*, 04:005, 2008. doi: 10.1088/JHEP04(2008)005.
- [42] ATLAS Collaboration. Jet energy measurement with the ATLAS detector in proton-proton collisions at $\sqrt{s} = 7$ TeV. *Eur. Phys. J. C*, 73:2304, 2013. doi: 10.1140/epjc/s10052-013-2304-2.
- [43] ATLAS Collaboration. Jet Calibration and Systematic Uncertainties for Jets Reconstructed in the ATLAS Detector at $\sqrt{s} = 13$ TeV. ATL-PHYS-PUB-2015-015, 2015. URL <https://cds.cern.ch/record/2037613>.
- [44] Performance of jet substructure techniques in early $\sqrt{s} = 13$ TeV pp collisions with the ATLAS detector. Technical Report ATL-CONF-2015-035, CERN, Geneva, Aug 2015. URL <http://cds.cern.ch/record/2041462>.
- [45] D. Krohn, J. Thaler, and L.-T. Wang. Jet trimming. *JHEP*, 02:084, 2010. doi: 10.1007/JHEP02(2010)084.
- [46] Stephen D. Ellis and Davison E. Soper. Successive combination jet algorithm for hadron collisions. *Phys. Rev. D*, 48:3160, 1993. doi: 10.1103/PhysRevD.48.3160.
- [47] Impact of Alternative Inputs and Grooming Methods on Large-R Jet Reconstruction in ATLAS. Technical Report ATL-PHYS-PUB-2017-020, CERN, Geneva, Dec 2017. URL <http://cds.cern.ch/record/2297485>.

- [48] ATLAS Collaboration. Performance of jet substructure techniques for large- R jets in proton–proton collisions at $\sqrt{s} = 7$ TeV using the ATLAS detector. *JHEP*, 09:076, 2013. doi: [10.1007/JHEP09\(2013\)076](https://doi.org/10.1007/JHEP09(2013)076).
- [49] ATLAS Collaboration. Jet mass reconstruction with the ATLAS Detector in early Run 2 data. ATLAS-CONF-2016-035, 2016. URL <https://cds.cern.ch/record/2200211>.
- [50] ATLAS Collaboration. Optimisation of the ATLAS b -tagging performance for the 2016 LHC Run. *ATL-PHYS-PUB-2016-012*, (ATL-PHYS-PUB-2016-012), Jun 2016. URL <https://cds.cern.ch/record/2160731>.
- [51] ATLAS Collaboration. Performance of b -jet identification in the ATLAS experiment. *JINST*, II:Po4008, 2016. doi: [10.1088/1748-0221/II/04/Po4008](https://doi.org/10.1088/1748-0221/II/04/Po4008).
- [52] Georges Aad et al. Muon reconstruction performance of the ATLAS detector in proton–proton collision data at $\sqrt{s} = 13$ TeV. *Eur. Phys. J.*, C76(5):292, 2016. doi: [10.1140/epjc/s10052-016-4120-y](https://doi.org/10.1140/epjc/s10052-016-4120-y).
- [53] D. J. Lange. The EvtGen particle decay simulation package. *Nucl. Instrum. Meth. A*, 462:152, 2001. doi: [10.1016/S0168-9002\(01\)00089-4](https://doi.org/10.1016/S0168-9002(01)00089-4).
- [54] Torbjorn Sjostrand, Stephen Mrenna, and Peter Z. Skands. PYTHIA 6.4 physics and manual. *JHEP*, 05:026, 2006. doi: [10.1088/1126-6708/2006/05/026](https://doi.org/10.1088/1126-6708/2006/05/026).
- [55] ATLAS Collaboration. Summary of ATLAS Pythia 8 tunes. 2012. URL <http://cdsweb.cern.ch/record/1474107>.
- [56] S. Agostinelli et al. GEANT4: a simulation toolkit. *Nucl. Instrum. Meth. A*, 506:250–303, 2003. doi: [10.1016/S0168-9002\(03\)01368-8](https://doi.org/10.1016/S0168-9002(03)01368-8).
- [57] ATLAS Collaboration. The ATLAS Simulation Infrastructure. *Eur. Phys. J. C*, 70:823–874, 2010. doi: [10.1140/epjc/s10052-010-1429-9](https://doi.org/10.1140/epjc/s10052-010-1429-9).
- [58] S. Dawson, S. Dittmaier, and M. Spira. Neutral Higgs boson pair production at hadron colliders: QCD corrections. *Phys. Rev. D*, 58:115012, 1998. doi: [10.1103/PhysRevD.58.115012](https://doi.org/10.1103/PhysRevD.58.115012).
- [59] T. Plehn, M. Spira, and P.M. Zerwas. Pair production of neutral Higgs particles in gluon-gluon collisions. *Nucl. Phys. B*, 479:46, 1996. doi: [10.1016/0550-3213\(96\)00418-X](https://doi.org/10.1016/0550-3213(96)00418-X). [Erratum: *Nucl. Phys. B* 531 (1998) 655].

- [60] S. Borowka, N. Greiner, G. Heinrich, S. P. Jones, M. Kerner, J. Schlenk, U. Schubert, and T. Zirke. Higgs boson pair production in gluon fusion at NLO with full top-quark mass dependence. *Phys. Rev. Lett.*, 117(1):012001, 2016. doi: 10.1103/PhysRevLett.117.012001.
- [61] S. Borowka, N. Greiner, G. Heinrich, S. P. Jones, M. Kerner, J. Schlenk, and T. Zirke. Full top quark mass dependence in Higgs boson pair production at NLO. *JHEP*, 10:107, 2016. doi: 10.1007/JHEP10(2016)107.
- [62] J. Alwall et al. The automated computation of tree-level and next-to-leading order differential cross sections, and their matching to parton shower simulations. *JHEP*, 07:079, 2014. doi: 10.1007/JHEP07(2014)079.
- [63] Richard D. Ball et al. Parton distributions with LHC data. *Nucl. Phys. B*, 867:244, 2013. doi: 10.1016/j.nuclphysb.2012.10.003.
- [64] A. Carvalho. Gravity particles from Warped Extra Dimensions, predictions for LHC. 2017.
- [65] M. Bahr et al. Herwig++ physics and manual. *Eur. Phys. J. C*, 58:639–707, 2008. doi: 10.1140/epjc/s10052-008-0798-9.
- [66] Hung-Liang Lai, Marco Guzzi, Joey Huston, Zhao Li, Pavel M. Nadolsky, Jon Pumplin, and C. P. Yuan. New parton distributions for collider physics. *Phys. Rev. D*, 82:074024, 2010. doi: 10.1103/PhysRevD.82.074024.
- [67] Pavel M. Nadolsky et al. Implications of cteq global analysis for collider observables. *Phys. Rev. D*, 78:013004, 2008. doi: 10.1103/PhysRevD.78.013004.
- [68] Michael H. Seymour and Andrzej Siódak. Constraining MPI models using σ_{eff} and recent Tevatron and LHC Underlying Event data. *JHEP*, 10:113, 2013. doi: 10.1007/JHEP10(2013)113.
- [69] Simone Alioli, Paolo Nason, Carlo Oleari, and Emanuele Re. A general framework for implementing NLO calculations in shower Monte Carlo programs: the POWHEG BOX. *JHEP*, 06:043, 2010. doi: 10.1007/JHEP06(2010)043.
- [70] Peter Zeiler Skands. Tuning Monte Carlo generators: The Perugia tunes. *Phys. Rev. D*, 82:074018, 2010. doi: 10.1103/PhysRevD.82.074018.
- [71] Michał Czakon and Alexander Mitov. Top++: A program for the calculation of the top-pair cross-section at hadron colliders. *Comput. Phys. Commun.*, 185:2930, 2014. ISSN 0010-4655. doi: 10.1016/j.cpc.2014.06.021.

- [72] Morad Aaboud et al. Search for pair production of Higgs bosons in the $b\bar{b}b\bar{b}$ final state using proton-proton collisions at $\sqrt{s} = 13$ TeV with the ATLAS detector. 2018.
- [73] et al Jon Butterworth. Pdf4lhc recommendations for lhc run ii. *Journal of Physics G: Nuclear and Particle Physics*, 43(2):023001, 2016.
- [74] ATLAS Collaboration. Luminosity determination in pp collisions at $\sqrt{s} = 8$ TeV using the ATLAS detector at the LHC. *Eur. Phys. J. C*, 76(653), 2016. doi: 10.1140/epjc/s10052-016-4466-1.
- [75] ATLAS Collaboration. Jet mass and substructure of inclusive jets in $\sqrt{s} = 7$ tev pp collisions with the atlas experiment. *JHEP*, 05:128, 2012. doi: 10.1007/JHEP05(2012)128.
- [76] Measurement of the Track-Jet b -Tagging Efficiency of the MV1 algorithm in pp Collisions at $\sqrt{s} = 8$ TeV using $e\mu$ Dilepton $t\bar{t}$ events. Technical Report ATL-COM-PHYS-2015-009, August 2015. URL <https://cds.cern.ch/record/1981533>.
- [77] Performance of Track Jet based b -tagging in Monte Carlo at $\sqrt{s} = 8$ TeV with the ATLAS Detector. Technical Report ATL-COM-PHYS-2015-1323, August 2015. URL <https://cds.cern.ch/record/2062412?ln=en>.
- [78] ATLAS Collaboration. Observation of a new particle in the search for the Standard Model Higgs boson with the ATLAS detector at the LHC. *Phys. Lett. B*, 716:1, 2012. doi: 10.1016/j.physletb.2012.08.020.
- [79] Glen Cowan, Kyle Cranmer, Eilam Gross, and Ofer Vitells. Asymptotic formulae for likelihood-based tests of new physics. *Eur. Phys. J. C*, 71:1554, 2011. doi: 10.1140/epjc/s10052-011-1554-0.
- [80] Alexander L. Read. Presentation of search results: The CL_s technique. *J. Phys. G*, 28:2693, 2002. doi: 10.1088/0954-3899/28/10/313.
- [81] ATLAS Collaboration. Search for pair production of Higgs bosons in the $b\bar{b}b\bar{b}$ final state using proton–proton collisions at $\sqrt{s} = 13$ TeV with the ATLAS detector. *Phys. Rev. D*, 94: 052002, 2016. doi: 10.1103/PhysRevD.94.052002.
- [82] Burton Richter. High Energy Colliding Beams; What Is Their Future? *Rev. Accel. Sci. Tech.*, 7:1–8, 2014. doi: 10.1142/9789814651493_0001, 10.1142/S1793626814300011.
- [83] Stephen Hawking and Gordon Kane. Should China build the Great Collider? 2018.